



It is requested that you provide a copy of this report, including the time for reviewing instructions, searching existing data sources, gathering and reviewing the collection of information, and sending comments regarding this burden estimate or any other aspect of this report, including suggestions for reducing the burden, to Washington Headquarters Services, Directorate for Information Operations and Reports, 1215 Jefferson Avenue, Suite 1204, Washington, DC 20543-0121, and to the Office of Management and Budget, Paperwork Reduction Project (0704-0188), Washington, DC 20503.

1. AGENCY USE ONLY (Leave blank)		2. REPORT DATE 10/14/93	3. REPORT TYPE AND DATES COVERED Final Report for 02/15/90 - 2/14/93	
4. TITLE AND SUBTITLE ESTABLISHING THE BASIS FOR VALIDATED PREDICTIONS OF HIGHLY NON-EQUILIBRIUM FLOWS (WITH 9 ATTACHMENTS)			5. FUNDING NUMBERS Grant No. AFOSR 90-0170  2307/AS	
6. AUTHOR(S) Dan Erwin, Joseph Kunc and E. Phillip Muntz				
7. PERFORMING ORGANIZATION NAME(S) AND ADDRESS(ES) Department of Aerospace Engineering University of Southern California 854 W. 36th Pl., RRB 101 Los Angeles, CA 90089-1191			8. PERFORMING ORGANIZATION REPORT NUMBER  AFOSR-TR-93-0842 (2)	
9. SPONSORING/MONITORING AGENCY NAME(S) AND ADDRESS(ES) Dr. Leonides Sakell Air Force Office of Scientific Research Building 410 Bolling AFB D.C., 20332-6448			10. SPONSORING/MONITORING AGENCY REPORT NUMBER  AFOSR-90-0170	
11. SUPPLEMENTARY NOTES				
12a. DISTRIBUTION/AVAILABILITY STATEMENT Approved for public release, distribution unlimited.			12b. DISTRIBUTION CODE DTIC ELECTE NOV 17 1993 S A	
13. ABSTRACT (Maximum 200 words)  A unique iodine vapor hypersonic flow facility for the study of nonequilibrium reacting flows has been developed and used in initial experiments. An important new computationally efficient theoretical approach to describing the energy exchange of iodine and other molecules during collisions has been formulated and applied to iodine. The transport properties of dissociating diatomic molecules have been studied and a potentially very significant phenomena appearing when a gas is partially dissociated has been identified. A Ph.D. thesis has been completed on experiments with the iodine flow facility. Several journal articles and meeting papers on both the experimental and theoretical work have been prepared. A second Ph.D. thesis is nearly complete on the design of parallel flow nozzles for nonequilibrium dissociating, vibrationally active iodine flows.				
14. SUBJECT TERMS code validation; hypersonic, non-equilibrium flows			15. NUMBER OF PAGES	
			16. PRICE CODE	
17. SECURITY CLASSIFICATION OF REPORT UNCLASSIFIED	18. SECURITY CLASSIFICATION OF THIS PAGE UNCLASSIFIED	19. SECURITY CLASSIFICATION OF ABSTRACT UNCLASSIFIED	20. LIMITATION OF ABSTRACT UL	

**Best  
Available  
Copy**

## Introduction and Summary

A unique iodine vapor hypersonic flow facility for the study of nonequilibrium reacting flows has been developed and used in initial experiments. An important new computationally efficient theoretical approach to describing the energy exchange of iodine and other molecules during collisions has been formulated and applied to iodine. The transport properties of dissociating diatomic molecules have been studied and a potentially very significant phenomena appearing when a gas is partially dissociated has been identified. A Ph.D. thesis has been completed on experiments with the iodine flow facility. Several journal articles and meeting papers on both the experimental and theoretical work have been prepared. A second Ph.D. thesis is nearly complete on the design of parallel flow nozzles for nonequilibrium dissociating, vibrationally active iodine flows.

## Experiment: Iodine Hypersonic Wind Tunnel

A pilot scale iodine hypersonic wind tunnel has been operated for about 2 years (Attachments 1, 2). It was used to test the iodine flow cycle and as a means for developing diagnostic techniques for a larger scale iodine flow facility. Based on this information a large scale flow facility (described in Attachments 1, 2) has been designed and largely constructed. The diagnostics development work has been done in the pilot scale facility and is described in great detail in Attachment 3.

The large scale tunnel still remains to be completely assembled. It is necessary to coat the stainless steel shell and condenser section with an iodine resistant material. Originally we had planned to do this with teflon as in the pilot tunnel. However, some problems in the pilot tunnel associated with penetration of the teflon coat were experienced and it was decided to look for alternatives. Unfortunately the alternatives were very expensive. However we did find an inexpensive potential solution, which was to apply boron nitride to the surfaces. This coating comes in the form of a paint with a cost of about \$100/gallon. We have now completed 3 months testing of this coating in an iodine atmosphere at an elevated temperature. It performs very well. Also, it has the admirable property of being easily repaired. We are now in a position to complete the assembly of the full-scale facility.

## Theoretical Studies of Transport Properties and Energy Exchange

New, efficient methods have been developed for obtaining intermolecular potentials of diatomic molecules. Novel issues concerning transport properties of high temperature gases have been investigated.

Original studies of the transport properties of high temperature dissociating gases have been developed (Attachments 4, 5, 6). Very important work has been done on developing computationally efficient methods for obtaining the energy exchange in collisions between diatomic molecules (Attachment 8).



## Navier-Stokes Studies of Vibrationally Relaxing, Dissociating Iodine

Work is nearing completion (Ph.D. thesis) on calculating flows of vibrationally relaxing, dissociating flows of iodine vapor. Several vibrational relaxation models are included. The first application of this development will be to the design of an iodine parallel flow hypersonic nozzle. The thesis should be available in about 6 months. This work is being done by M. Bradley and has been fully supported by his company.

## Other Flow Studies

The experimental results obtained by G. Pham Van Diep (Attachment 3) have recently been used to compare to Monte Carlo simulations. These studies are included here as Attachments 8 and 9.

Accession For	
NTIS	CRA&I
DTIC	TAB
Unannounced	
Justification	
By	
Distribution	
Availability Codes	
Dist	Avail and/or Special
A-1	

DTIC QUALITY INSPECTED 8



**ATTACHMENT 1**

## A Code Validation Strategy and Facility for Nonequilibrium, Reacting Flows

E. P. Muntz,<sup>1</sup> G. Pham Van Diep,<sup>2</sup> M. K. Bradley,<sup>3</sup> D. A. Erwin,<sup>4</sup> and J. A. Kunc<sup>5</sup>

University of Southern California  
Los Angeles, California 90089-1191  
(213) 740-5366

### Introduction

The availability of powerful computers and efficient algorithms with the prospect for continuing rapid progress in both of these areas<sup>1,2</sup> presents new opportunities for experimental research. However, a careful re-thinking of old truths is necessary. Consider the case of hypervelocity air flows. Chemical nonequilibrium is a dominant feature of the flight of slender vehicles (air-breathing or otherwise) in the air-breathing flight corridor and for all higher altitude trajectories. The development of nonequilibrium numerical simulations based on the Navier-Stokes equations or Monte-Carlo techniques has stimulated attempts to establish their detailed validity in gas flows for a wide range of nonequilibrium conditions. There is a need to do this because the kinetic models required by the simulation are complex and difficult. Two principal reasons are at the root of this: 1) the number of atomic and molecular processes taking place in the gas is large, and 2) the collision strengths and transition probabilities for many of the rotational-vibrational-electronic transitions in molecules (even the simplest ones) are either inaccurate or unknown. Approximations are required to include kinetic models in numerical simulations both for reasons of computer limitations and due to a lack of physical knowledge. The first limit will recede, although it is not expected to entirely disappear even with the next generation of massively parallel computing machines (teraflop machines). However the progress in machines and techniques only exposes weaknesses in our physical understanding.

Nonequilibrium, high temperature air flows can currently be simulated but with far more approximations and simplifications than is generally appreciated, a situation that will remain with us for some time. In view of the large user community for hypervelocity, nonequilibrium flow simulations it seems reasonable to suggest that detailed experimental validations of the simulations should be a top priority. This is where re-thinking old truths becomes important.

There are two approaches to validation. Both rely on using the numerical simulations in a laboratory setting to predict laboratory nonequilibrium flows and subsequently comparing experiments to the simulations. It is quite clear that we are a long way from truly experimentally duplicating hypervelocity flow over large, air-breathing flight vehicles; but with careful validations we can afford not to worry too much about ground experimental duplica-

---

<sup>1</sup>Professor, Fellow

<sup>2</sup>Research Assistant, Member

<sup>3</sup>Technical Staff, Rockwell International, Member

<sup>4</sup>Professor, Member

<sup>5</sup>Professor, Associate Fellow

tions and go directly from validated numerical simulations to vehicle design and flight test. The trick is how to accomplish the validations. Generating high enthalpy, hypersonic air flows is a difficult task. High pressure, high enthalpy arc tunnels and shock tunnels (either conventional or piston driven for brief description see discussion in Ref. 3) are the two most popular choices. What is required is that the experimental conditions exercise the chemistry, surface interactions, molecular transport properties and hypervelocity flow properties that will be used in the design of the flight vehicles; although it has to be assumed that this need not all be done in one experiment or you end up with something approaching complete duplication. The facility of choice for hypervelocity nonequilibrium flowfields is at this time the shock tunnel.

The difficulty with high performance shock tunnels is that they produce test times of at most a few milliseconds. Numerous measurements are necessary to really validate nonequilibrium hypervelocity flow simulations such as concentration of  $O_2$ ,  $O$ ,  $NO$ ,  $N_2$ ,  $N$ ,  $OH$ ,  $NO^+$  and other ions,  $e^-$  as well as vibrational and rotational state population distributions, translational temperature and flow velocity. Most of these require non-intrusive optical measurements. For molecules, in order to obtain concentrations from optical measurements in high temperature flows both vibrational and rotational population distribution are necessary. In nonequilibrium flows the vibration in many cases will have a non-Boltzmann distribution, so that a number of vibrational levels have to be probed individually. Either many "simultaneous" laser wavelengths (on order of all wavelengths scanned in say 1 ms) or multiple shock tunnel facility runs are required. Neither alternative is attractive. It is accordingly of some interest to consider alternatives or rather complementary approaches.

Many of the uncertainties in the numerical simulation are related to the adequacy of physical modeling, for instance recipes are used to account for vibrational nonequilibrium in adjusting chemical reaction rates. Another example is the method by which the transport properties of nonequilibrium gases are found. These and similar questions can be investigated in a computationally-rich environment using surrogate gases; not as a tool for the simulation of gases of direct technological interest, but as a convenient test bed for detailed physical descriptions of specific kinetic processes coupled with flow phenomena.

It has been shown<sup>4</sup> that iodine ( $I_2$ ) is a suitable surrogate diatomic gas to use in theoretical studies of chemical nonequilibrium that account for rotational and vibrational as well as electronic processes in a gas. Because of the low temperature at which significant dissociation can be achieved in iodine, it is a particularly attractive candidate for the study of relatively low temperature chemically reacting flows; permitting detailed knowledge of the nonequilibrium populations of translational, rotational, vibrational and electronic energy levels. A pilot iodine facility has been constructed (Figure 1) and operated repeatedly for twelve months. A full scale facility has been designed and is under construction. Both the operating characteristics of the pilot facility and nonequilibrium flow predictions for the full scale facility will be presented. Candidate diagnostic techniques are reviewed and initial LIF results that have been obtained in the pilot facility presented.

Species	Temperature (K)	$\langle \epsilon \rangle$ (eV)	$\Delta E_v$ (eV)	$(\Delta E_v)/\langle \epsilon \rangle$
I <sub>2</sub>	1340	0.17	0.026	0.15
N <sub>2</sub>	5400	0.69	0.292	0.42
O <sub>2</sub>	3530	0.45	0.195	0.43

Table 1: Thermal equilibrium properties of I<sub>2</sub>, N<sub>2</sub>, and O<sub>2</sub> for a degree of dissociation of 50% and pressure of 200 torr (after Kunc et al. 1990).

## 1 Iodine as a Surrogate Gas

### 1.1 Attributes

During the flight of transatmospheric vehicles such as the NASP or the STS orbiter, the temperatures encountered behind a normal shock at an altitude of approximately 50 km are typically 4000 K for a speed of 4 km sec<sup>-1</sup>. At this altitude, the pressure is 1 torr and the most abundant species are molecular oxygen and molecular nitrogen. The Mach number is approximately 12, resulting in a pressure behind the shock of about 200 torr. Table 1 shows a comparison of the temperature required to produce 50% dissociation in iodine, nitrogen and oxygen. Also shown in Table 1 are the ratios of the vibrational energy spacing  $\Delta E_v$  to the average kinetic energy  $\langle \epsilon \rangle = (3/2)kT$ . While 50% dissociation in nitrogen and oxygen is achieved at temperatures of about 3500 and 5400 K, the same degree of dissociation can be produced by heating iodine to approximately 1300 K. The ratio  $(\Delta E_v)/\langle \epsilon \rangle$  is an indication of how close the average kinetic energy of the molecules are to the internal vibrational energy spacing. For all three gases,  $\langle \epsilon \rangle$  is larger than the energy required to excite the molecules to upper vibrational levels resulting in significant population of the vibrational levels. The ratios  $(\Delta E_v)/\langle \epsilon \rangle$  vary by up to a factor of 3. Since the value of  $(\Delta E_v)/\langle \epsilon \rangle$  is smaller for iodine, it is expected that its higher vibrational states will be somewhat more populated than the corresponding vibrational states in nitrogen or oxygen. Because rotational, vibrational and dissociative excitation of the iodine molecule can be achieved at lower temperatures than for oxygen or nitrogen, iodine will be used as a convenient surrogate diatomic gas for the study of chemically reacting gas flows.

The three lowest electronic levels of the I<sub>2</sub> molecule are taken as the ground state X <sup>1</sup>Σ<sub>g</sub><sup>+</sup>, the metastable state B <sup>3</sup>Π<sub>u</sub> and the D <sup>1</sup>Σ<sub>u</sub><sup>+</sup> state energies of the excited states equal to 1.95 and 5.9 eV, respectively.<sup>5</sup> There is also a possibility of existence of another state (A <sup>3</sup>Π<sub>1u</sub>) with energy close to the energy of the B state. In addition, a couple of repulsive molecular states exist with energies between 2 and 5 eV.

The six lowest electronic levels of the O<sub>2</sub> molecule are: X <sup>3</sup>Σ<sub>g</sub><sup>-</sup> and the metastable states a <sup>1</sup>Δ<sub>g</sub>, b <sup>1</sup>Σ<sub>g</sub><sup>+</sup>, c <sup>1</sup>Σ<sub>u</sub><sup>-</sup>, A <sup>3</sup>Σ<sub>u</sub><sup>+</sup> and B <sup>3</sup>Σ<sub>u</sub><sup>-</sup>, with energies 0.98 eV, 1.64 eV, 4.10 eV, 4.39 eV and 6.17 eV, respectively.<sup>5</sup>

Since the dissociation energy of the I<sub>2</sub> molecule is relatively small, only one excited electronic level needs to be considered in kinetic models of nonequilibrium in iodine within the temperature range considered here (however, one should keep in mind uncertainty associated with the A <sup>3</sup>Π<sub>1u</sub> state. In the case of O<sub>2</sub>, 3 or 4 electronic levels must be taken into account

in kinetic considerations. In summary, one can assume that there are only two "active" molecular electronic levels in hot iodine. This assumption allows one to reduce the complexity of the kinetic models by taking into account only the molecular processes involving the ground and the first electronic levels of the  $I_2$  molecule. The fact that there is only one electronic excited state in the  $I_2$  molecule below the molecular dissociation energy, eliminates most of the difficulties (the potential curve crossings, predissociation, etc.) occurring in evaluation and interpretation of the rate coefficients for collisions involving electronically excited molecules.

## 1.2 Safety issues

Iodine has been used in a wide variety of studies. A few examples are; fundamental spectroscopic research,<sup>6,7</sup> investigation of laser induced processes,<sup>8</sup> visualization and probing of supersonic flows.<sup>9,10,11,13</sup> In these studies, iodine was either confined in a static cell or used in trace amounts to seed a flowing carrier gas, usually nitrogen. In either case the amounts of iodine involved were of the order of tens of grams at most. In contrast, the work described in this paper uses quantities of iodine ranging from 500 g to 30 kg. For this reason we gave serious consideration to the corrosive and toxic nature of iodine while designing the facility.

The iodine molecule will react with most metals, the reaction rate depends on the concentration of iodine in contact with the metal. Metals such as aluminum and stainless steel (SS304) are clearly inadequate even at room temperature where the iodine vapor pressure is approximately 0.2 Torr. Aluminum reacts to iodine by forming a large quantity of a light powdery substance which subsequently delays further reaction and can seriously contaminate the pumping system. It was found that the higher the content in nickel, chromium and molybdenum, the better the metal resists iodine corrosion. Stainless steel (SS316) offers a mild resistance to iodine attack at room temperature but cannot be used at higher temperature. Hastelloy (C276), a nickel alloy, was found to be the only commercially available metal that would not significantly corrode for temperatures up to 1000 K. Other non-metallic substances such as Pyrex, ceramics (aluminum-oxides) and Teflon seem to be excellent for use in an iodine environment. For this reason, parts that would ordinarily corrode can either be Teflon coated or anodized. Inert greases for seals and chemically stable pump lubricants are critical for the vacuum integrity of the experiment as well as the longevity of the pumping system. Krytox oils and greases have performed fairly well, until now they have shown very few signs of reaction with iodine.

When inhaled, iodine may cause eye, nose, throat and respiratory tract irritation. If exposure is repeated, bronchitis, skin rashes, loss of appetite and sleep may result. Discontinuation of exposure is necessary to recover from ill effects. The maximum accepted concentration is 0.1 ppm, which corresponds to 1 mg/m<sup>3</sup> at standard atmospheric conditions. Reported lethal doses lie between a few tenths of a gram to more than 20 grams. For the work described in this paper, the quantities of iodine used are of the order of kilograms at pressures above atmospheric, it is therefore absolutely necessary that leaks will only be into the facility and that satisfactory fail-safe features are designed in place.

## 2 Pilot Tunnel Construction and Performance

### 2.1 Operational procedure

The pilot scale hypersonic wind tunnel was conceived so that the methods proposed for handling iodine in the full scale facility could be dealt with in the pilot facility on a scale that would allow easy modifications should design-related failure occur. The corrosive and toxic nature of iodine as well as the wide temperature range encountered in different parts of the facility were the main design considerations. Figure 1 shows a schematic of the vertically mounted prototype wind tunnel. The facility operates intermittently in a closed cycle.

The phase diagram for iodine is presented in Figure 2, with the facility cycle superimposed. During the run phase the boiler is maintained at a temperature that provides the desired stagnation pressure. The saturated iodine vapor from the boiler flows to the stagnation chamber when valve  $V_1$  is opened, where it is superheated to the stagnation temperature. The high temperature iodine in the stagnation chamber expands through a sonic orifice and into a vacuum chamber where optical diagnostics can be performed. A nozzle expansion is not used in the pilot scale tunnel. The iodine flow is pumped using condensation pumping onto two cold traps.

The second phase of operation consists of recycling the iodine from the cold traps used to condense the working gas during the run phase to the supply chamber (boiler). Recirculation is achieved by the vapor pressure differential between the heated cold traps and the facility's heated vacuum envelope, and the cooled boiler. The run time of the pilot wind tunnel is about 20 minutes while the recycling period is of the order of 1 hour. For an orifice diameter of 0.5 mm, a stagnation temperature of 1,000 K and a stagnation pressure of 1 atm., the mass flow rate is approximately 0.1 g/sec. The same mass flow may be obtained with an orifice diameter of 2 mm, a stagnation temperature of 700 K and pressure of 200 torr.

### 2.2 Flow visualization and run time

The flow can be probed in regions where the Mach number ranges from about 5 to 30. Figure 3 a) and b) show photographs of a free jet expansion of iodine for a background pressure of  $10^{-6}$  Torr and 0.1 Torr respectively. Figure 4 shows a photograph of the flowfield around the flat end of a silicone carbide cylinder placed in the iodine jet. In these photographs the bright areas represent fluorescence obtained by excitation with the 5145 Å line of an  $\text{Ar}^+$  laser. The areas downstream of the normal shock waves in the visualizations appear darker because of temperature effects on the populations of the particular rotational lines in resonance with the laser frequency. A normal shock is visible both in the case of a free jet in a high background pressure (Figure 3b) and upstream of the blunt body at a stand-off distance of approximately 2 mm.

Figure 5 shows a time trace of the fluorescence emitted from a point located approximately 25 orifice diameters downstream of exit plane. The sonic orifice diameter was 2 mm, the stagnation temperature and pressure were 700 K and 200 Torr respectively. For this measurement, the 5145 Å line of the  $\text{Ar}^+$  laser was used to excite the  $(X(^1\Sigma_g^+)0'' - B(^3\Pi_{0u}^+)43')$  P13 and R15 transitions of the iodine molecule. Figure 6 shows a top view

of the experiment. The  $\text{Ar}^+$  laser is not represented but was placed parallel to the dye laser. Fluorescence was observed at 5260.25 Å with a SPEX 0.75 m double spectrometer and RCA C31034A02 photomultiplier. The spectrometer slits were adjusted so that the spectral resolution was about 0.4 Å. The laser beam was focused with a 25 cm focal length lens and aimed horizontally through the center of the plume at a position sufficiently far downstream of the orifice exit plane to avoid any quenching effects. Indeed, at a position 25 orifices diameters downstream of the exit plane, the number density drops by 4 orders of magnitude from stagnation conditions,<sup>14</sup> thus significantly reducing collisional deexcitation of molecules in the upper state. The image of the horizontal column of fluorescence emitted from the plume was rotated 90° so that it aligned with the spectrometer entrance slit. Consequently, the signal observed in Figure 5 was integrated radially over a distance in the plume of approximately 1.5 cm. Figure 5 shows a sudden drop in signal intensity during a period of about 2 minutes before the flow conditions become steady. This is caused by the rapid energy loss from the pool of liquid iodine in the boiler due to the net vaporization of  $\text{I}_2$  to make up for the iodine flowing through the orifice when the flow is initiated. The resulting thermal load on the boiler could not be compensated by the boiler heater, which in this case was a simple ceramic oven heater surrounding the boiler but not in direct contact with it. This arrangement resulted in only a moderate control over the boiler temperature of  $\pm 5$  K because of the slow response time of the system. The drop in intensity seen in Figure 5 corresponds to a drop in temperature of about 6 K. A recirculating hot oil bath heater system was subsequently used and resulted in an improved but still insufficient temperature control to within  $\pm 3$  K. It is critical that the boiler temperature be controlled accurately because at 457 K, where the iodine vapor pressure is one atmosphere, a drop of 5 K corresponds in a stagnation pressure decrease of 60 to 70 Torr. Under the present conditions, Figure 5 indicates that a quasi-steady flow can be obtained for run times of the about of 20 minutes. More care in the design of the full system should produce satisfactorily steady stagnation conditions.

When all the iodine supply contained in the boiler has been used, most of the working gas is in principle frozen on the cold traps. At this stage, recycling of the iodine can be performed: the gate valve is closed to protect the pumping units, hot air is blown through the cold traps so that the frozen iodine sublimates (Ref. Figure 2),  $V_2$  (Ref. Figure 1) is opened and the boiler walls are now cooled to  $\text{LN}_2$  temperature. When the iodine evaporates, it flows through the return duct and freezes on the boiler walls. During the recycle phase, it is important that the pressure remains low enough to allow flow of the iodine. Since the pumping system is at this point isolated from the chamber, it is critical that the leak rate of the chamber is reduced to a minimum. With a return duct diameter of cm calculations assuming an incompressible Poiseuille flow within the return duct indicate that the recirculation time should be of the order of a few minutes. The mass flow rate through the recycling duct is described by<sup>15</sup>

$$\dot{m} = \frac{\pi a^4}{8\eta L} \cdot \frac{P^2}{2} \cdot \frac{m}{kT}, \quad (1)$$

where  $a$ ,  $l$ ,  $m$  and  $\eta$  are the radius, length of the tube, the mass of the iodine molecules and the viscosity of the iodine vapor respectively.  $P$  and  $T$  are the pressure and temperature

taken as 2 torr and 323 K respectively. A value of  $14 \times 10^{-6}$  N sec  $m^{-2}$  was selected for the viscosity<sup>16</sup> at 323 K. In practice, we obtain recirculation times less than about 30 min.

In order for the recirculation process to be efficient it is important that all parts of the test section be heated to the temperature corresponding to the vapor pressure necessary to drive the iodine to the boiler. For this purpose, a plexiglas shroud was built around the entire facility and a 5 kW heater is used to blow hot air around it (Ref. Figure 1). If the test facility is nonuniformly heated iodine will condense on its coldest surfaces, thus delaying the recirculation process. Figure 7 shows a photograph of an optical port which was colder than the rest of the test section due to a hot air leak through the shroud. As the iodine crystals of the photograph show, the cryopumping of iodine is a rather efficient process even through temperature gradients of a few degrees.

A subtle but important issue concerning recirculation deals with the accumulation of incondensibles in the boiler. As the iodine vapor condenses on the boiler walls, incondensibles carried with it are separated from the  $I_2$  molecules and over time build up pressure within the boiler, which in turn slows further flow of iodine from the test section. Venting of the incondensibles during the recirculation phase is therefore necessary. This was achieved either by opening  $V_1$  (Ref. Figure 1) during recirculation, or actively pumping on the downstream side of the boiler using a bypass line to the main pumping system. Related phenomena are relatively well known effects to users of cold trapped Macleod gages, it was also used by one of us (E.P.M., who also forgot about it until we had trouble recirculating) to enhance the operation of an isotope separation system.<sup>17,18</sup>

### 3 Nozzle Flow Calculations

The reason for developing an iodine vapor wind tunnel is to study nonequilibrium, reacting flows. In order to verify that flows generated at nominal stagnation conditions of 1500 K and 10 atm. will provide situations where finite rate chemistry effects can be observed, selected nozzle and shock wave calculations have been completed. The nozzle throat used in the calculation is shown in Figure 8. It follows previous nozzle designs reported by a number of authors.<sup>15</sup> The conical section marks the transition to the downstream portion of a hypersonic nozzle where the flow is turned to be approximately parallel at the nozzle exit. Nozzle contours for this downstream section have been investigated. For a conical nozzle formed as an extension of the  $12^\circ$  half angle expansion in Figure 8, a finite rate chemistry, inviscid flow solution was calculated using a One Dimensional Kinetics (ODK) computer program<sup>20</sup> based on the forward reaction rate constant<sup>21</sup> shown in Table 2. These computations resulted in the Mach number, pressure, temperature and degree of dissociation shown in Figures 9a-d. Also shown in the Figure 9c are frozen and equilibrium temperatures for the same nozzle. Note that the flow is fairly close to equilibrium leaving only about a 5% degree of dissociation in the free stream at the nozzle exit.

The calculations were performed for a nozzle geometry and flow conditions summarized in Table 3.

For the same nozzle the sensitivity of the results to stagnation pressure was investigated for pressures of 20 and 2 atm. The results are shown in Fig. 10 for the  $I_2$  mole fraction during



Reaction	$I_2 + I_2 \rightarrow I + I + I_2$
Rate	$1.09 \cdot 10^{17} T^{-0.5} e^{-15800/T}$
Temperature range	(K) $300 < T < 2000$
Units	$\text{cm}^3 \text{mol}^{-1} \text{sec}^{-1}$

Table 2: Reaction rate used in OKD computations.

Working Gas	$I_2$
Stagnation pressure (atm)	10
Stagnation temperature (K)	1500
Downstream pressure (torr)	0.1
Throat radius (mm)	1.778
Nozzle exit radius (cm)	10.16
Area Ratio	3265.3

Table 3: OKD calculation parameters.

the expansion. Similarly vibrational relaxations were investigated in a preliminary way by using a simple relaxation time model for vibrational energy. The results of the calculation for these stagnation pressures at  $T_0 = 1500$  K are shown in Fig. 11. Notice in both Figs. 10 and 11 that  $p_0 = 10$  atm provides a reasonable approach to an equilibrium free stream. A related issue, possible condensation in the free stream has been addressed in a previous paper.<sup>22</sup>

Will there be active chemistry in the flow field at the nozzle exit conditions? To investigate this issue, a normal shock holder was assumed to be placed in the flow. For a frozen flow across the momentum shock, finite rate chemistry calculations were completed as a function of distance behind the shock front. The results are shown in Figure 12 where a relaxation distance of a centimeter is required for the degree of dissociation to come to equilibrium. This would be an ideal distance for measurements of the details of this relaxing, dissociating flow.

A two-dimensional finite rate chemistry method of characteristics computer code was used to calculate the iodine flow for candidate nozzle shapes. This code, the TDK code, is described and is well suited to rapid calculation of chemically reacting nozzle flows. The TDK code also includes a routine to calculate a laminar or turbulent boundary layer during a normal run using the BLM boundary layer code. TDK can optionally be rerun with the wall displaced to account for boundary layer displacement thickness. Two-dimensional inviscid and boundary layer analysis are described in this section.

Chamber conditions and flow chemistry are the same as the conditions used for the one-dimensional analysis reported above. The same design area ratio was also used. The throat contour specified in the previous section was used as a starting point. Various contours were added and the exit flow conditions (Mach number and flow angle) were calculated.

For the first set of computer runs, a cubic polynomial contour was used to connect at the nozzle exit radius (four inches which produces the design area ratio) as indicated in Fig. 13.

Nozzle lengths of 24 through 48 inches were analyzed. Results are shown in Figures 14 and 15. The 48 inch nozzle produced the most uniform Mach number profile, although the 40 inch nozzle had the best profile from a flow angularity standpoint. The 40 inch nozzle was chosen for further parametric studies.

A frozen analysis of the 40 inch nozzle was conducted. The frozen calculation produced a much higher exit Mach number with considerably more distortion. The frozen solution also produced much lower wall pressures. Because frozen chemistry produces significantly higher Mach numbers, with shallower Mach angles, a longer nozzle is necessary to produce the same exit flow quality.

In order to perform the boundary layer analysis, a wall temperature distribution must be assumed. Constant wall temperatures of 500 to 2500 degrees R were analyzed along with an adiabatic wall, and a nominal wall temperature schedule versus length. This schedule has a 2500 degree R wall temperature at the throat and a 500 degree R wall temperature at the nozzle exit with an exponential function used for the distribution. A detailed thermal analysis considering conduction, convection, and radiation would need to be conducted to accurately determine the wall temperature. The boundary layer code was run for these wall temperature cases assuming laminar flow. The boundary layer displacement thickness at the nozzle exit varies significantly with assumed wall temperature. A constant 2500 degree R wall temperature distribution will produce a 1.9 inch boundary layer displacement thickness, which is nearly fifty percent of the four inch exit radius. A boundary layer that thick would certainly invalidate the inviscid plus patched boundary layer approach being used in this analysis. The impact of wall cooling can be determined from these results. Consulting the vapor pressure curve for iodine in Ref. a 500 degree R wall temperature should be sufficient to prevent condensation of iodine on the wall surfaces and produces a displacement thickness of 0.6 in.

The Reynolds number for the nozzle are all quite low, the flow is expected to be laminar as the Reynolds numbers based on displacement and momentum thickness are well below the expected transition number for a flat plate.

From the boundary layer code (BLM), the displacement thickness can be used to adjust the nozzle contour and the inviscid analysis can be repeated. The nozzle exit radius was increased to 4.65 inches and a final angle of 0.8 degrees (instead of 0) was used to account for boundary layer growth, the inviscid analysis was conducted, the boundary layer displacement calculated, the original contour adjusted, and an inviscid analysis conducted on the adjusted contour.

Changing the length of the 12 degree straight section from the nominal length of 0.3 inch to zero and 1.1 inches was investigated. The long 1.1 inch straight section increased exit centerline Mach number by less than 0.05 but held maximum flow angle below 0.5 degrees.

Varying the final angle of the nozzle contour from the nominal value of 0.8 degrees was found to have little effect, except for the flow angle in the vicinity of the wall.

Several runs were made using a skewed parabola instead of a cubic description for the nozzle contour. This did not improve the profiles over the cubic contour runs.

Exit profiles for the "best" analyzed configurations are shown in Fig. 16. The "best" 40 in nozzle, with a 1.1 inch straight section, a 4.65 inch exit radius, and a 0.8 degree final angle

with a cubic contour description. This contour provides an exit Mach number of 9.1 plus or minus 0.5, and a flow angle of less than 0.5 degrees. A more uniform Mach distribution can be obtained by lengthening the nozzle to 48 in.

#### 4 Full Scale Tunnel Design

Figure 17 shows a schematic of the full scale hypersonic facility. The wind tunnel is designed to operate on 50 kg of pure iodine, with a stagnation temperature of 1500 K and pressure of 10 atm. The flow rate will be about  $20 \text{ g sec}^{-1}$  for a total run time of a little over 30 minutes. The hypersonic flow will be achieved by expanding the iodine vapor through a nozzle into a 1 m diameter low pressure dump tank. The open jet nozzle will have a throat diameter of 3.4 mm and an exit diameter of about 20 cm. Pumping of the working gas during the run will be achieved by condensing the iodine on cryogenic panels. The facility will operate on the same basis as its pilot scale counterpart i.e. in a closed cycle for safety reasons and on an intermittent basis. During the recirculation phase, the iodine is transferred from the heated cryogenic pump panels to the cooled walls of the boiler. Mach numbers up to about 10 will be achieved at the nozzle exit. As indicated in Figure 17 the full scale tunnel is mounted vertically with the test section featuring multiple optical access ports about 3 meters from the floor.

The cycle for the full scale tunnel is shown in Figure 18 superimposed on the iodine phase diagram. Based on a tunnel envelope temperature of 450 K the pressure driving the recirculation phase will be about 300 torr. The recirculation lines to the boiler will have a diameter of 2.5 cm and a length of 2 m, resulting in a recirculation time that theoretically should be a few seconds for a recirculating temperature of 450 K. Dropping the temperature to 370 K reduces the pressure to about 30 Torr and increases the recirculation time by two orders of magnitude. This would permit the recycling to proceed without forming liquid iodine. A hastelloy catch basin is incorporated in the condensation pump to hold liquid iodine during recirculation.

The condensation pump is designed for the particular application to the iodine tunnel. The nozzle exit static pressure will be 50 to 100 mtorr. In order to control the condensation pumping at these rather high pressures the condensing surfaces have been arranged as shown in Figure 19. Panels mounted vertically in a star pattern about a central vertical tube are separated from the pressure required for balancing the nozzle flow by a cylindrical surface containing long vertical slits about 7 mm wide. The slits are positioned at the mid point of the outer boundary of the wedge shaped sections formed by the condensing surfaces. Between the slotted cylinder and the pump's outer vacuum boundary the pressure will be close to the nozzle exit pressure. The vertical slots form continuum two-dimensional jets that expand freely into the wedge shaped spaces. The static pressure in these spaces will be  $\leq 10^{-3}$  torr. From the work on 2-D jets by Dupeyrat<sup>23</sup> the shock systems associated with these jets should be about 30 cm downstream of the slits in this particular case (7 mm slits, pressure ratio of 100). Thus the underexpanded jets will impinge directly on the condensing surfaces, both enhancing the efficiency of the surfaces and distributing the condensate in a more uniform manner.

## 5 Diagnostic Considerations

Significant internal energy excitation may be produced by heating the iodine vapor to temperatures ranging from 1000 K to 1500 K.<sup>5</sup> For this reason, we have chosen as an initial study in the pilot facility an underexpanded free jet flow whose stagnation temperature is about 1000 K. At this temperature, approximately 10 vibrational energy levels are significantly populated along with about 200 rotational energy levels within each vibrational state. Because the rate of collisions decreases significantly as the gas expands, nonequilibrium effects are present within the plume. The work reported here is mainly concerned with developing methods for probing the nonequilibrium features of the expansion. These are characterized by a decoupling of the translational and rotational temperature from the vibrational temperature as well as a non-Boltzmann distribution in the vibrational energy levels. With the design run time of the facility being 30 min., emphasis is placed on developing diagnostic techniques which would probe several internal energy states without requiring long integration periods. Previous investigations of iodine expansions have been reported but involved flows of carrier gases seeded with trace amounts of iodine.<sup>9-13</sup> Internal energy state population probing has only been performed on pure iodine in local thermal equilibrium and confined to a static cell using; conventional, discrete resonance (fluorescence) and continuum resonance Raman scattering techniques.<sup>8,24,25</sup> Research on the energy level populations of chemically reacting flows of iodine has to our knowledge never been performed, although measurements of velocity distribution functions in flows of evaporating iodine have been reported.<sup>26</sup>

The iodine molecule has been the subject of many spectroscopic studies over the past two decades because many of its transitions are easily accessible at visible wavelengths.<sup>27-31</sup> For example the  $X^1\Sigma-B^3\Pi\ 0''-43'$  P13, R15 transitions will strongly absorb the 5145 Å radiation of the Ar<sup>+</sup> laser and will fluoresce accordingly. For this reason, this transition is commonly used for visualizing supersonic flows.<sup>13</sup> In the work described here, we probe the population of individual ro-vibrational energy states in a pure flow of iodine molecules whose internal degrees of freedom have been thermally activated. Laser Induced Fluorescence (LIF) was chosen as a diagnostic technique primarily for signal strength considerations and because pumping individual transitions appears possible with a narrow band tunable dye laser. We are however faced with the complication of identifying the numerous transitions that characterize the iodine molecule. Fortunately, molecular constants and Duham expansion parameters describing the  $v' = 0 - 80(B)$ ,  $v'' = 0 - 19(X)$  system have been determined by best fitting Fourier transform absorption spectra.<sup>29,30,31</sup> This enabled us to calculate the energy gap for all possible transitions involving  $v' = 0 - 60$ ,  $v'' = 0 - 6$  and 160 rotational levels for each vibrational level pair, P and R branches were also taken into consideration. Subsequently, only the transitions which could be individually pumped by the laser were considered. This was done by rejecting all transitions which were within 0.05 cm<sup>-1</sup> of any other transition (the laser linewidth being about 0.04 cm<sup>-1</sup>). For the 115,200 transitions calculated, only 12,485 were considered as possible candidates for determining either rotational or vibrational population distributions. By specifying an upper and lower vibrational quantum number we obtained a set of transitions which could be probed to de-

termine rotational energy distributions. Figure 20 gives an example of potential transitions computed for the particular case of  $v' = 0$ ,  $v'' = 17$  and only P transitions were considered. Similarly, by specifying a rotational quantum number, we can determine a two-dimensional set of vibrational quantum numbers (upper and lower levels) which could be used to measure vibrational energy distributions. Figure 21 shows a plot of wavenumbers vs.  $(v'', v')$  pairs having specified a rotational quantum number of 50.

The experiment described in this paper was performed in our pilot scale hypersonic facility described in an earlier paper.<sup>22</sup> The facility operates with 500 gm of pure iodine, on a semi-continuous basis with run times and recycling times of about 30 minutes. The stagnation pressure was maintained at 100 torr and the stagnation temperature 773 K. The iodine vapor was expanded through a 2 mm sonic orifice in a vacuum where the pressure was approximately  $10^{-4}$  torr. To generate a shock in the flowfield, a 7.25 cm diameter cylindrical blunt body was placed 35 mm downstream of the orifice exit plane. The flowfield was probed at five axial positions along the plume center axis. Taking the blunt body leading edge as a reference, the coordinates of the probed positions were 1, 3.5, 6, 11 and 16 mm. Probing was performed by LIF whereby excitation of the transitions was achieved with an excimer pumped dye laser (Lambda Physik FL3002 pumped by EMG 201(Xe Cl)). An intracavity etalon was mounted in the dye laser reducing the laser linewidth from  $0.2 \text{ cm}^{-1}$  to  $0.04 \text{ cm}^{-1}$ . The laser linewidth was checked and optimized using an air spaced Fabry-Perot etalon whose free spectral range was  $0.166 \text{ cm}^{-1}$  and coated for  $5016 \text{ Å}$ . The repetition rate was set to 30 Hz and the dye laser was programmed to scan over a  $1.1 \text{ Å}$  range in about 10 minutes, starting at the  $17'-0''$  P39 transition and proceeding to shorter wavelengths. The laser beam was focused on the probed volume with a 30 cm focal length lens. The LIF signal was collected in a direction perpendicular to the laser beam with two 60 cm focal length lenses (f4.0) and filtered from stray light occurring at the excitation wavelength through a 0.85 m double spectrometer (Spex 1404). The spectrometer was tuned at  $5827 \text{ Å}$  with a resolution of  $20 \text{ Å}$  in order to detect the transitions corresponding to a total vibrational quantum number change of +2. The signal was integrated over 30 samples with a Box Car averager (Stanford Research Systems SRS 250). The gate width was set to 100 ns and centered about the fluorescent signal peak in order for the averaged signal to be insensitive to quenching. Figure 22 shows a series of spectra taken at the axial positions mentioned above. It can be noticed that the further the probed position is from the blunt body, the colder the gas becomes resulting in a weaker response of the transitions involving higher rotational quantum numbers. This is rather well illustrated by the  $18'-0''$  R 101 transition. The transitions chosen to determine rotational distributions are identified in Figure 22. They were selected on the basis of their common lower vibrational state, in this case  $v'' = 0$  and their isolation with respect to other transitions. Transitions with different upper vibrational states were scaled to a reference transition using:

$$\bar{I} = I \left[ \frac{p_{ref} \cdot q_{ref}}{p \cdot q} \right] \quad (2)$$

where  $\bar{I}$  is the scaled transition intensity and  $p$  and  $q$  are the upward and downward Franck-Condon factors computed by Tellinguisen.<sup>32</sup> Resulting rotational population distributions are

shown in Figure 23, where  $\ln(\bar{I}) - \ln(2J + 1)$  is plotted against  $J(J + 1)$  so that the slope of the best linear fits is inversely proportional to the rotational temperature. The temperatures indicated in Figure 23 decrease as the flow is probed at positions further upstream of the blunt body. It may be mentioned that the temperature of 137 K obtained at  $y = 16$  mm matches the temperature prediction of Ashkenas & Sherman<sup>14</sup> for an equivalent axial position in a free jet expansion assuming a specific heat ratio of 9/7 and a stagnation temperature of 773 K. Temperatures vs. axial positions are plotted in Figure 24 where a sharp decrease in temperature taking place over a distance of about two freestream mean free paths shows that probing was performed across a shock. The temperature behind the shock does not reach the flow's stagnation temperature (773 K) because the number density in the plume is low enough for the shock and the disc's boundary layer to be merged.

Saturation has to be considered when dealing with LIF. For pulsed pumping and using a simple 2 level model, the lower and upper state populations  $N_1$  and  $N_2$  are described by the system

$$\frac{dN_2}{dt} = N_1 B_{12} g(\nu) \frac{I(t, x)}{c} - N_2 \left[ B_{12} g(\nu) \frac{I(t, x)}{c} \frac{g_1}{g_2} + \sum_{i < 2} A_{2i} + \sum_{j \neq 2} R_{2j} + D_2 g(\nu) \frac{I(t, x)}{c} \right] \quad (3)$$

$$\frac{dN_1}{dt} = N_2 \left[ B_{12} g(\nu) \frac{I(t, x)}{c} \frac{g_1}{g_2} + A_{21} + R_{21} \right] - N_1 \left[ B_{12} g(\nu) \frac{I(t, x)}{c} + \sum_{j \neq 1} R_{1j} \right] \quad (4)$$

where  $I(t, x)$  is the laser's intensity for an arbitrary pulse shape which should equal the pulse energy once integrated over the pulse length. The laser intensity is kept as a function of physical space because we may need to consider beam attenuation. Equation (3) indicates that the upper state population depends on two competing effects: 1) a laser pumping rate which is a function of the lower state population  $N_1$ , the absorption linestrength  $B_{12}$ , the laser lineshape  $g(\nu)$  and intensity  $I(t, x)$  ( $c$  is the speed of light). 2) a term depopulating the upper level, depending on the stimulated emission linestrength  $B_{21}$  written in Equations (3) and (4) as the product of  $B_{12}$  and the statistical weight  $g_i$ , a spontaneous emission term  $A_{2i}$  and a collisional quenching term  $R_{2i}$ . The term  $D_2$  appears in the depopulating factor to account for molecules being pumped out of level 2 but not repopulating the bottom level, resulting in a net depletion of the probed level's population and thus impeding the saturation process. Such depopulating transitions could be due to multiple photon excitations, photo-dissociation or dissociative quenching reactions which according to several sources can be significant in the case of strong pulsed pumping.<sup>33-35</sup> Taking  $B_{12} = 4 \cdot 10^{18} \text{ m}^3 \text{ J}^{-1} \text{ sec}^{-2}$ ,  $A_{21} = 5 \cdot 10^5 \text{ sec}^{-1}$ ,  $g(\nu) = 1.8 \cdot 10^{-10} \text{ sec}$  and assuming typical experimental conditions, Equations (3) and (4) were solved simultaneously using a laser pulse of Gaussian shape with a 28 nsec width at half maximum. An experimentally determined photo-dissociating cross-section<sup>36</sup> of  $2.4 \cdot 10^{-19} \text{ cm}^2$  was also assumed and resulted in a  $D_2$  dissociative linestrength of  $1.06 \cdot 10^{14} \text{ m}^3 \text{ J}^{-1} \text{ sec}^{-2}$ . The LIF signal being proportional to the population  $N_2$ , the latter was computed for several cases of laser intensities. For reasons that are still unresolved, the signal appears to have an unsaturated behavior, only if the laser input power is set to two orders of magnitude less than the power levels actually used in the experiment.

## 6 Summary

We have conducted an initial investigation into the measurement of rotational and vibrational population distributions in a hypersonic flow of hot iodine vapor. A pilot wind tunnel has been operated successfully for a period of twelve months. It provides run times of about 20 min. Scale up to a larger facility appears feasible. It will provide a 20 cm dia,  $M \simeq 9$  flow of iodine vapor with only small amounts of free stream nonequilibrium. Consideration of the response of the flow to a normal shock wave indicates that significant chemistry will occur in model flow fields in the larger facility.

## Acknowledgment

This work is supported by the United States Air Force Office of Scientific Research as part of the University Research Initiative program and in part by a NASA Training and Research grant. Thane DeWitt, Ken Richards and Mark Trojanowski made important contributions to the development of the pilot tunnel.

## References

- [1] G. Bell. Ultracomputers: a teraflop before its time. *Science*, 256, 64, 1992.
- [2] Anonymous. Massively parallel machines usher in next level of computing power. *Science*, 256, 50, 1992.
- [3] C. Park. Nonequilibrium Hypersonic Aerodynamics. John Wiley, New York, 1990.
- [4] D. A. Erwin, J. A. Kunc, E. P. Muntz. Establishing the Basis for Validated Predictions of Highly Nonequilibrium Flows. Proposal to the University Research Initiative Program. Submitted in response to: BAA Number 89-2, April 1989.
- [5] J. A. Kunc, E. P. Muntz, D. P. Weaver. Model Gases for the Detailed Study of Microscopic Chemical Nonequilibrium in Diatomic Gas Flows. AIAA-90-1662, June 1990, Seattle.
- [6] J. Tellinghuisen. Intensity Factors for the  $I_2$  B X band system. *J. Quant. Spectrosc. Radiat. Transfer*. Vol. 19, pp. 149-161, 1978
- [7] S. Gerstenkorn and P. Luc. Assignments of Several Groups of the Iodine ( $I_2$ ) Lines in the B-X System. *J. Mol. Spectrosc.*, 77, 310-321, 1979.
- [8] D. L. Rousseau and P. F. Williams. Resonance Raman Scattering of Light from a Diatomic molecule. *J. Chem. Phys.* Vol. 64, 9, pp. 3519-37, 1975.
- [9] J. C. McDaniel and D. Baganoff. Density Measurement in Compressible Flows Using Off-Resonant Laser Induced Fluorescence. *Phys. Fluid*, Vol. 25, 7, 1982.
- [10] G. W. McClelland, K. L. Saenger, J. J. Valentini. Vibrational and Rotational Relaxation of Iodine in Seeded Supersonic Beams. *J. Phys. Chem.*, Vol. 83, 8, pp. 947-59, 1979.
- [11] J. C. McDaniel, Investigation of Laser-Induced Fluorescence for the Measurements of Densities in Compressible Flows, Ph.D. thesis, Stanford University, 1982.
- [12] J. Tusa, M. Sulkes, and S. A. Rice. Low Energy Collisional Relaxation of  $I_2$  in He: Evidence for Resonance Enhanced Vibrational Deactivation. *J. Chem. Phys.*, Vol. 70, 6, pp. 3136-37, 1978.

- [13] B. Hiller and R. K. Hanson. Properties of the Iodine Molecule Relevant to Laser-Induced Fluorescence Experiments in Gas Flows. *Exp. Fluids*, 10, 1-11, 1990.
- [14] H. Ashkenas and F. S. Sherman. Structure and Utilization of Supersonic Free Jets in Low Density Wind Tunnels. 4th International Symposium on Rarefied Gas Dynamics. J. H. de Leeuw ed., Vol. 2. Academic Press, 1966, Toronto.
- [15] S. Dushman. Scientific Foundations of Vacuum Technique. John Wiley & Sons, Inc. 1949.
- [16] R. C. Weast. CRC Handbook of Chemistry and Physics. CRC Press, Inc. 1984.
- [17] E. P. Muntz. Partial Pressure Condensation Pump. U. S. Patent No. 4 185 966, January 1980.
- [18] J. Brook, V. Calia, B. Hanel, E. P. Muntz, P. B. Scott and T. Deglow. Jet Membrane Process for Aerodynamic Separation of Mixtures and Isotopes. *AIAA J. Energy*, Vol. 4, No. 5, p. 199, 1980.
- [19] J. C. Sivells. Aerodynamic Design and Calibration of the VKF 50-Inch Hypersonic Nozzle Tunnels. EADC-TDR-62-230, 1963.
- [20] G. R. Nickerson, et al. Two-dimensional Kinetics (TDK) Nozzle Performance Computer Program, NAS8-36863, Software and Engineering Associates, Inc., Carson City, Nevada, 1989.
- [21] N. Davidson. Fundamental data obtained from Shock Tube Experiments. Pergamon Press, 1961. p. 138.
- [22] G. C. Pham-Van-Diep, E. P. Muntz, D. P. Weaver, T. G. Dewitt, M. K. Bradley, D. A. Erwin and J. A. Kunc. An Iodine Hypersonic Wind Tunnel for the Study of Nonequilibrium Reacting Flows. AIAA 92-0566, Reno, NV 1993.
- [23] G. Dupeyrat. Two and Three Dimensional Aspect of a Freejet Issuing from a Long Rectangular Slit. In *Rarefied Gas Dynamics*, S. S. Fisher Ed., p. 812, Progress in Astronautics and Aeronautics. Vol. 74, 1981.
- [24] W. Kiefer and H. J. Bernstein. Vibrational-Rotational Structure in the 5145 Å Excited Anti-Stokes Resonance Raman Spectrum of Iodine Vapor. *J. Chem. Phys.*, Vol. 57, 7, pp. 3017-19, 1972.
- [25] W. Holzer, W. F. Murphy, and H. J. Bernstein. Resonance Raman Effect and Resonance Fluorescence in Halogen Gases. *J. Chem. Phys.*, Vol. 52, 1, pp. 399-408, 1970.
- [26] R. Schilder, G. Adomeit, G. Worthberg. Theoretical and experimental investigation of the Knudsen layer produced by intensive evaporation of iodine. *RGD* 13, pp. 577-84, 1985.
- [27] D. L. Rousseau and P. F. Williams. Resonance Raman Scattering of Light from a Diatomic molecule. *J. Chem. Phys.* Vol. 64, 9, pp. 3519-37, 1975.
- [28] H. W. Schrötter and H. W. Klöckner. Raman Scattering Cross Sections in Gases and Liquids. *Raman Spectroscopy of Gases and Liquids*. Ed. A. Weber. Springer-Verlag Berlin Heidelberg. New York, 1979.
- [29] S. Gerstenkorn and P. Luc. Assignments of Several Groups of the Iodine ( $I_2$ ) Lines in the B-X System. *J. Mol. Spectrosc.*, 77, 310-321, 1979.
- [30] S. Gerstenkorn and P. Luc. Atlas du Spectre d'Absorption de la Molecule d'Iode. Editions du Centre National de la Recherche Scientifique, Paris, 1978.



- [31] S. Gerstenkorn and P. Luc. Description of the absorption spectrum of iodine recorded by means of Fourier Transform Spectroscopy: the (B-X) system. *J. Phys.*, 46 (1985) 867-881.
- [32] J. Tellinghuisen. Intensity Factors for the  $I_2$  B X band system. *J. Quant. Spectrosc. Radiat. Transfer*. Vol. 19, pp. 149-161. 1978
- [33] E. Rabinowitch and W. C. Wood. Dissociation of Excited Iodine Molecules. *J. Chem. Phys.* Vol. 4, pp. 358-362, 1936.
- [34] C. Tai and F. W. Dalby. Nonlinear photodissociation of molecular iodine. *Canadian J. Phys.* Vol. 56, No. 2, pp. 183-190, 1978.
- [35] F. W. Dalby, Gena Petty-Sil, M. H. L. Pryce and C. Tai. Nonlinear Resonant Photoionization Spectra of Molecular Iodine. *Canadian J. Phys.* Vol. 55, No. 12, pp. 1033, 1977.
- [36] F. J. Aoiz, M. M. Oprysko and R. B. Bernstein. Argon Ion Laser Excitation of Supersonic seeded Molecular Beams of  $I_2$ . *Chem. Phys.* 79 (1983) pp. 321-339.

## Figures

**Figure 1:** Schematic of pilot scale hypersonic wind tunnel.

**Figure 2:** Phase diagram of iodine with the facility cycle superimposed.

**Figure 3:** Photograph of a free jet expansion of pure iodine vapor a) high background pressure b) low background pressure.

**Figure 4:** Photograph of flowfield around a cylindrical blunt body.

**Figure 5:** Time trace of fluorescence at an axial position of 25 orifice diameters downstream of the orifice exit plane.

**Figure 6:** Top view of experimental setup.

**Figure 7:** Photograph of iodine condensate on test section optical port.

**Figure 8:** Nozzle throat cross-section.

**Figure 9:** a) Mach number, b) Pressure, c) Temperature, d) Degree of dissociation vs. Area ratio Predictions based on finite rate chemistry.

**Figure 10:**  $I_2$  mole fraction in nozzle expansion for several stagnation pressures.

**Figure 11:**  $I_2$  vibrational temperature freezing in nozzle expansion.

**Figure 12:** Finite rate chemistry calculation of degree of dissociation a) and temperature b) across a normal shock wave.

**Figure 13:** Throat region contour for best 40 inch nozzle—vertical exaggeration.

**Figure 14:** Effect of nozzle length on exit Mach number distribution.

**Figure 15:** Effect of nozzle length on exit flow angle.

**Figure 16:** Nozzle exit flow profile.

**Figure 17:** Schematic of the full scale iodine facility.

**Figure 18:** Pressure temperature diagram for the full scale tunnel operation cycle.

**Figure 19:** Cross-section of the condensation pump.

**Figure 20:** Possible ro-vibrational transitions used for determining rotational population distributions.

**Figure 21:** Possible ro-vibrational transitions to determine vibrational population distributions.

**Figure 22:** LIF emissions at several locations in front of a blunt body in a hypersonic iodine flow.

**Figure 23:** Relative intensity for spectra of Figure 22.

**Figure 24:** Rotational temperatures from Figure 23.

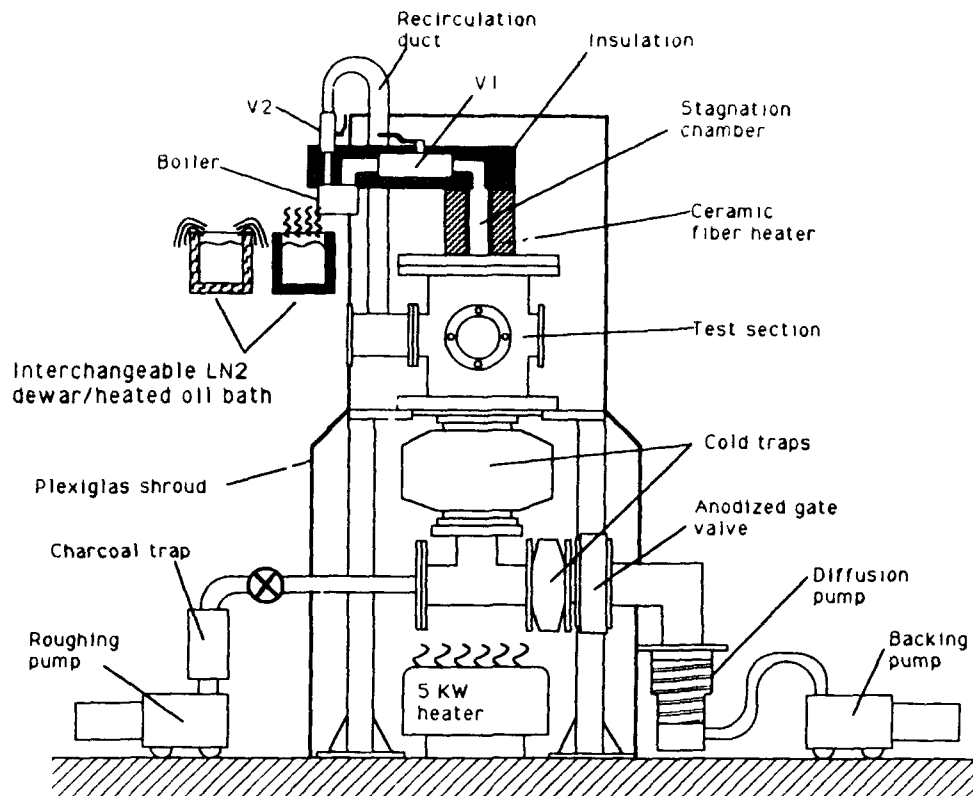


Figure 1: Schematic of pilot scale hypersonic wind tunnel.

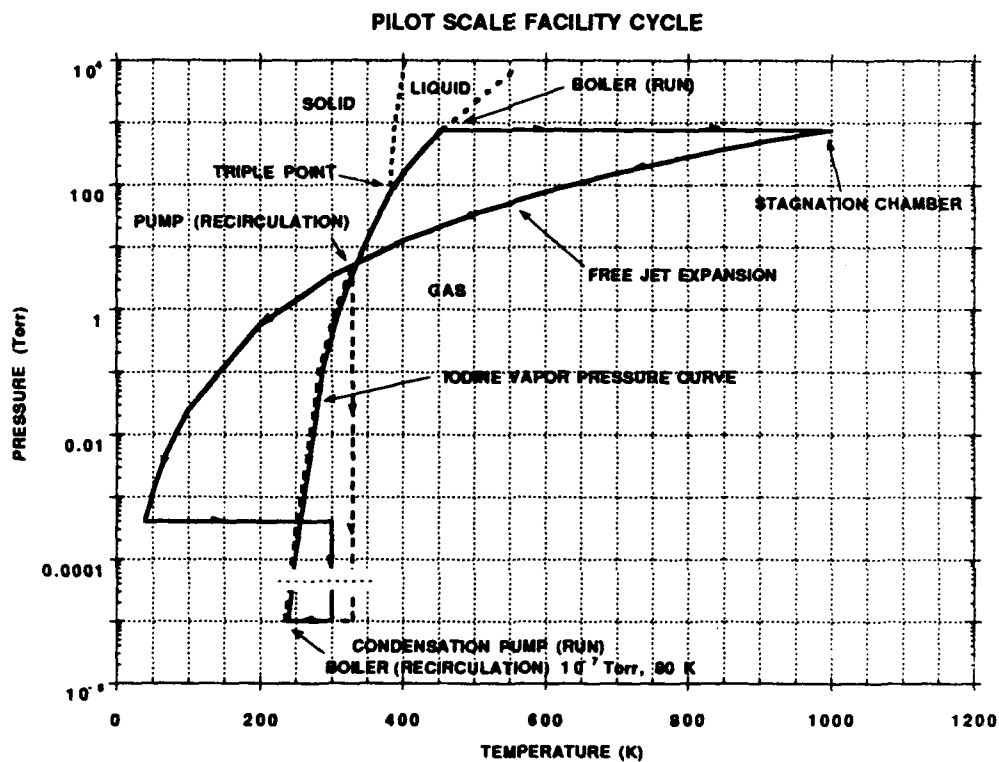
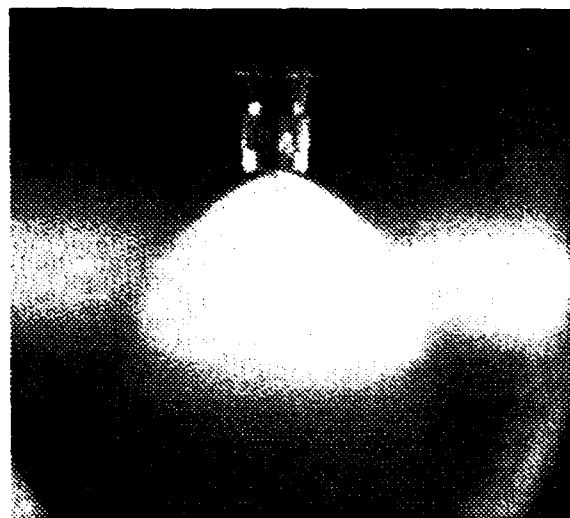


Figure 2: Phase diagram of iodine with the facility cycle superimposed.



a)



b)

Figure 3: Photographs of a free jet expansion of pure iodine vapor a) background pressure = 0.1 Torr b) background pressure =  $10^{-6}$  Torr .

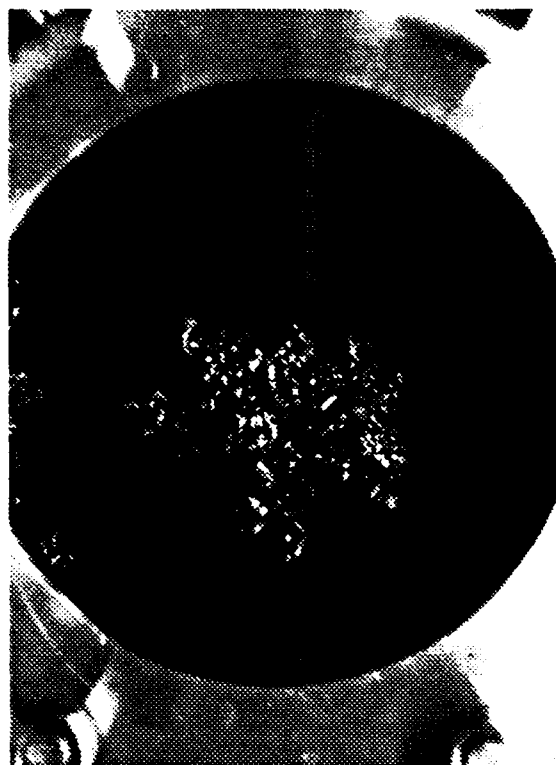
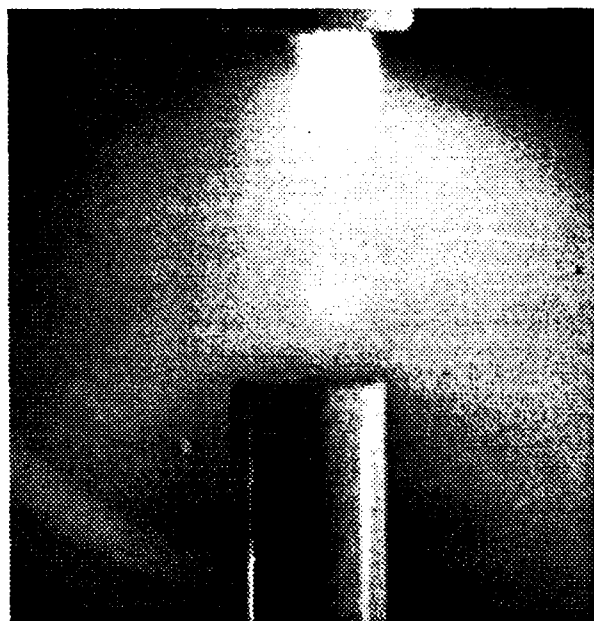
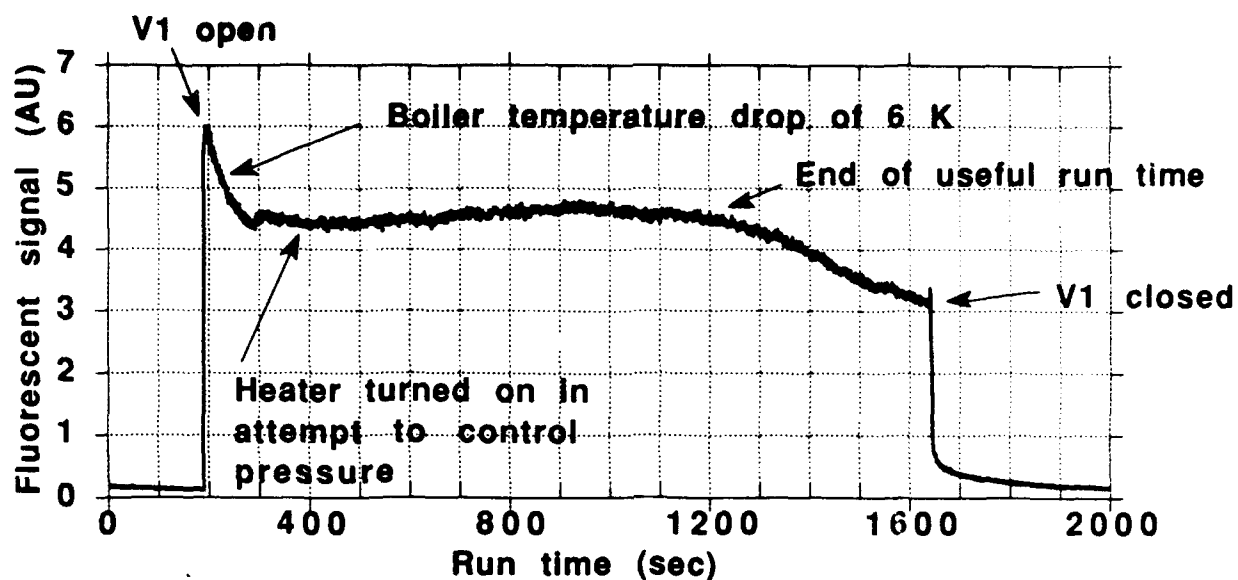


Figure 4: Photograph of flowfield around a cylindrical blunt body.

Figure 7: Photograph of iodine condensate on test section optical port



Run conditions:  $P_0 = 200$  Torr,  $T_0 = 700$  K, Dia = 2 mm

Figure 5: Time trace of fluorescence at an axial position of 25 orifice diameters downstream of the orifice exit plane.

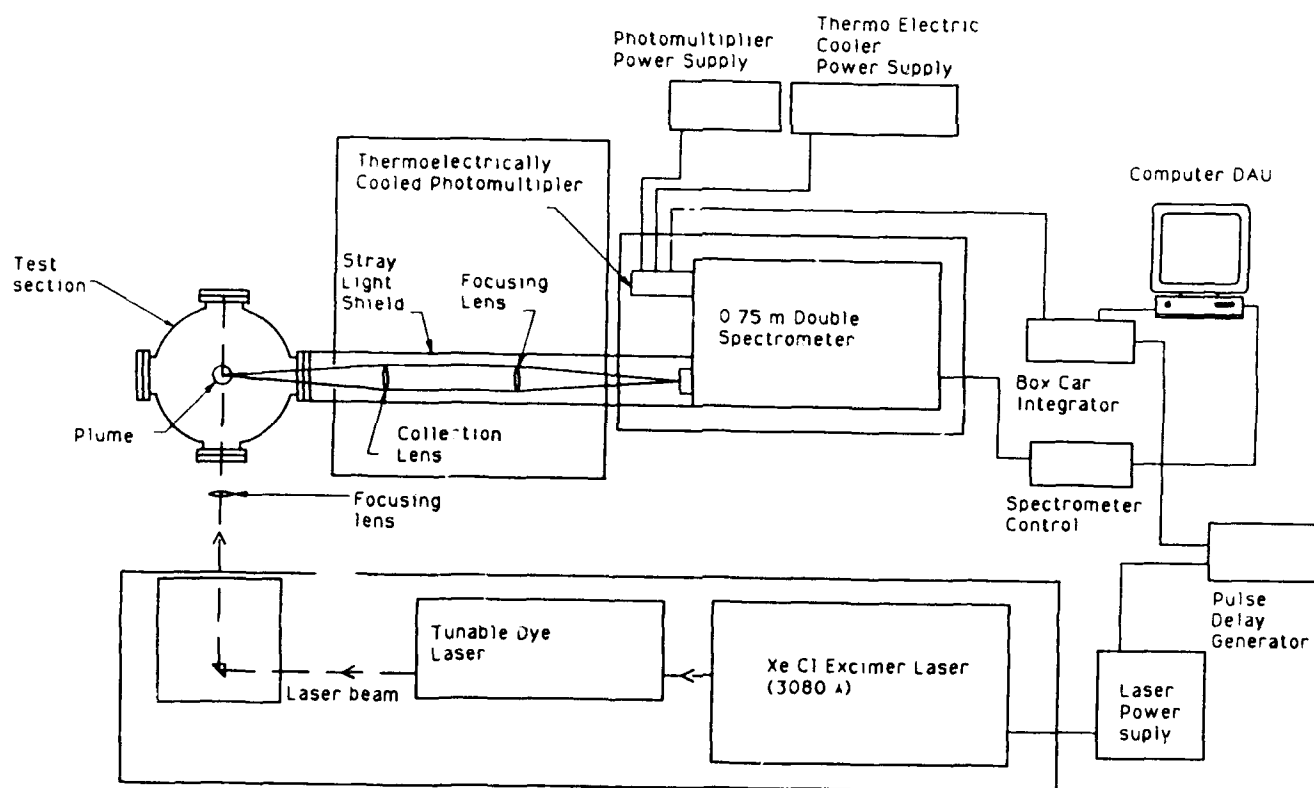


Figure 6: Top view of experimental setup.



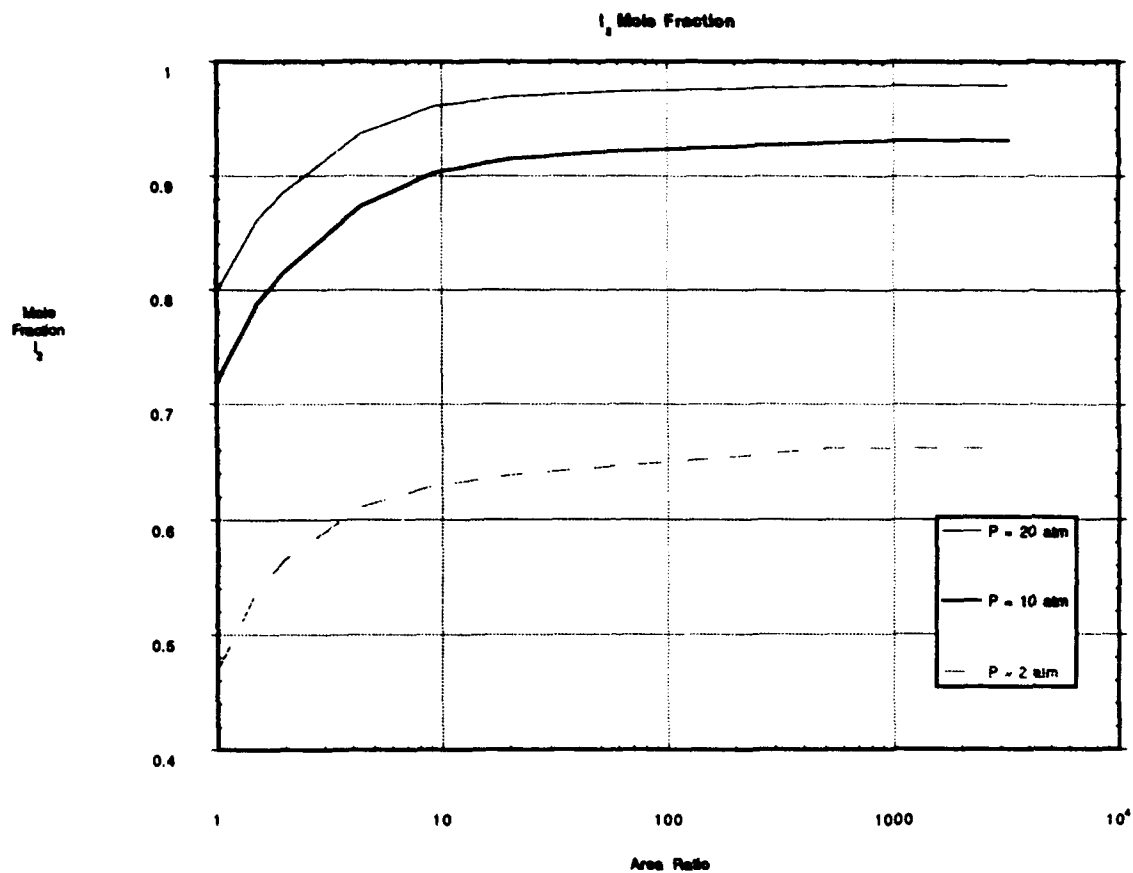


Figure 10:  $I_2$  mole fraction in nozzle expansion for several stagnation pressures.

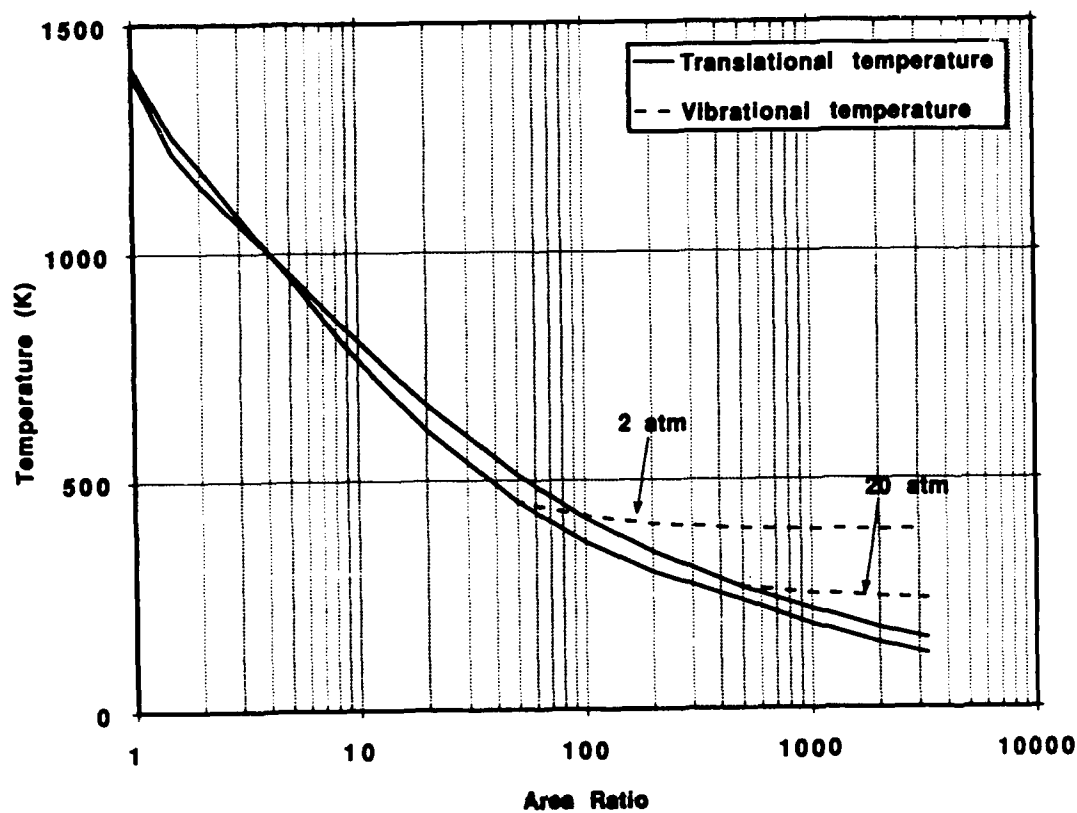


Figure 11:  $I_2$  vibrational temperature freezing in nozzle expansion.



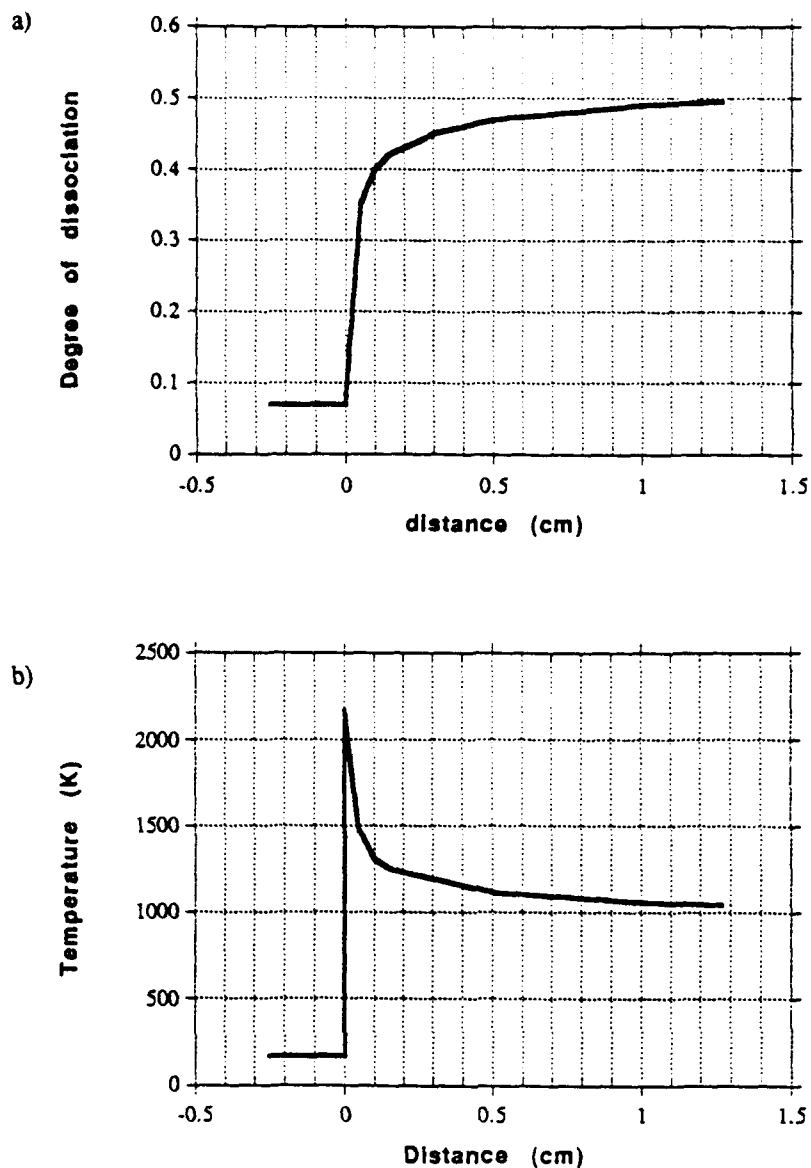


Figure 12: Finite rate chemistry calculation of degree of dissociation a) and temperature b) across a normal shock wave.

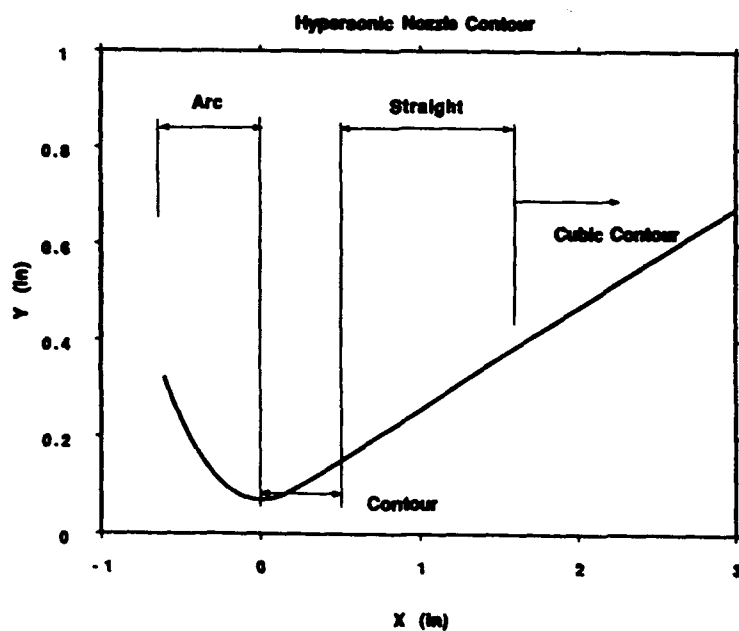


Figure 13: Throat region contour for best 40 inch nozzle—vertical exaggeration.

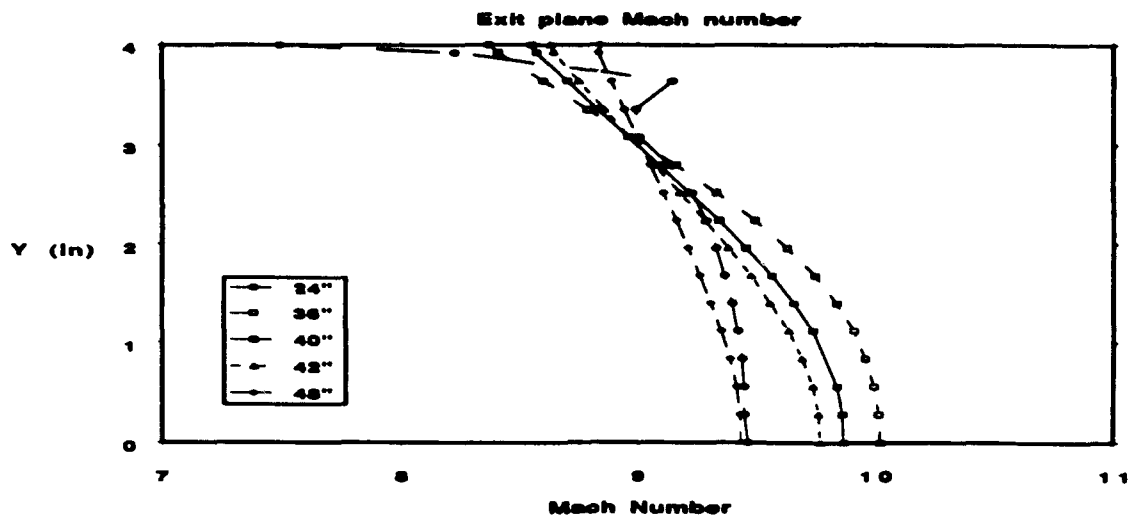


Figure 14: Effect of nozzle length on exit Mach number distribution.

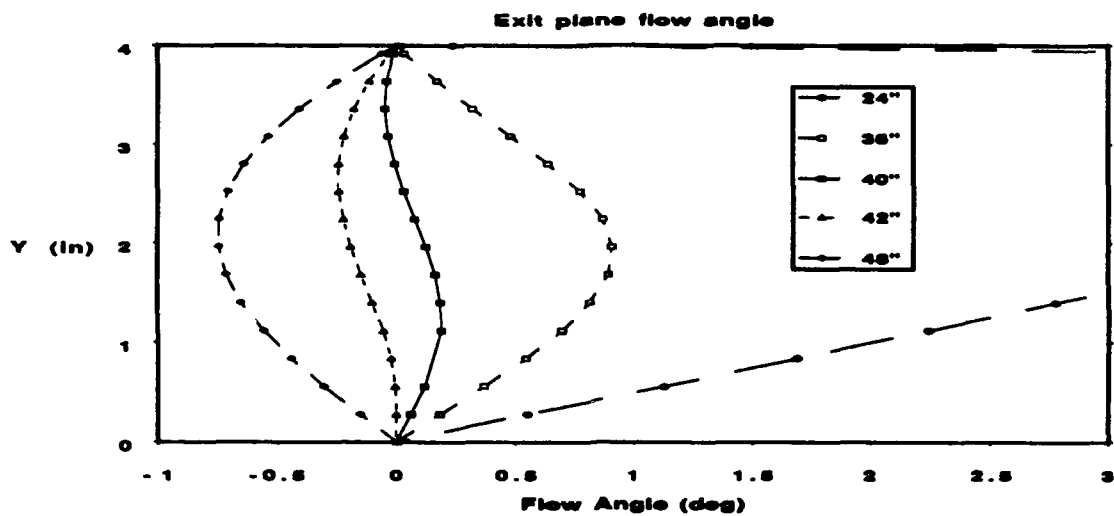


Figure 15: Effect of nozzle length on exit flow angle.

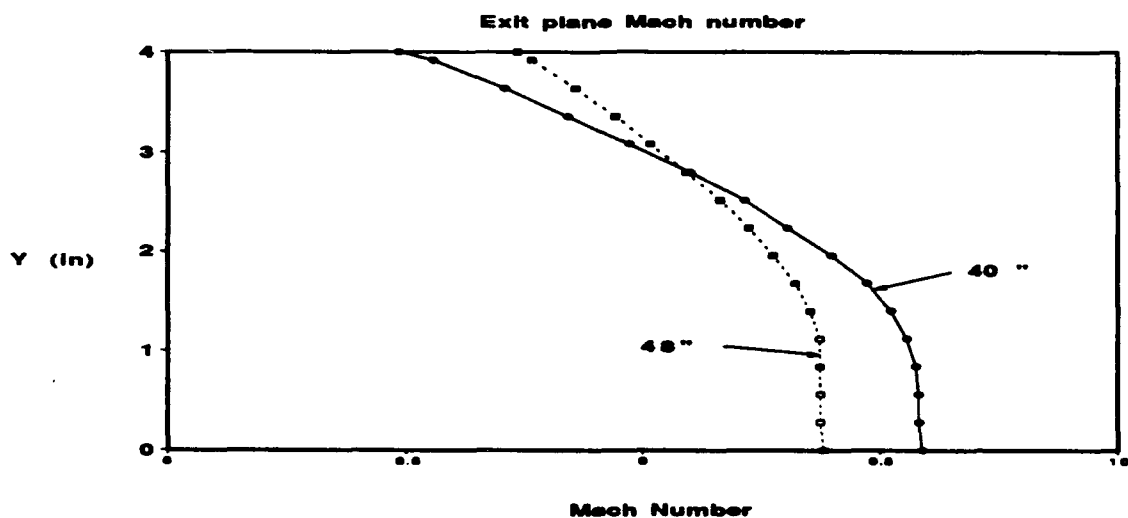


Figure 16: Nozzle exit flow profile.

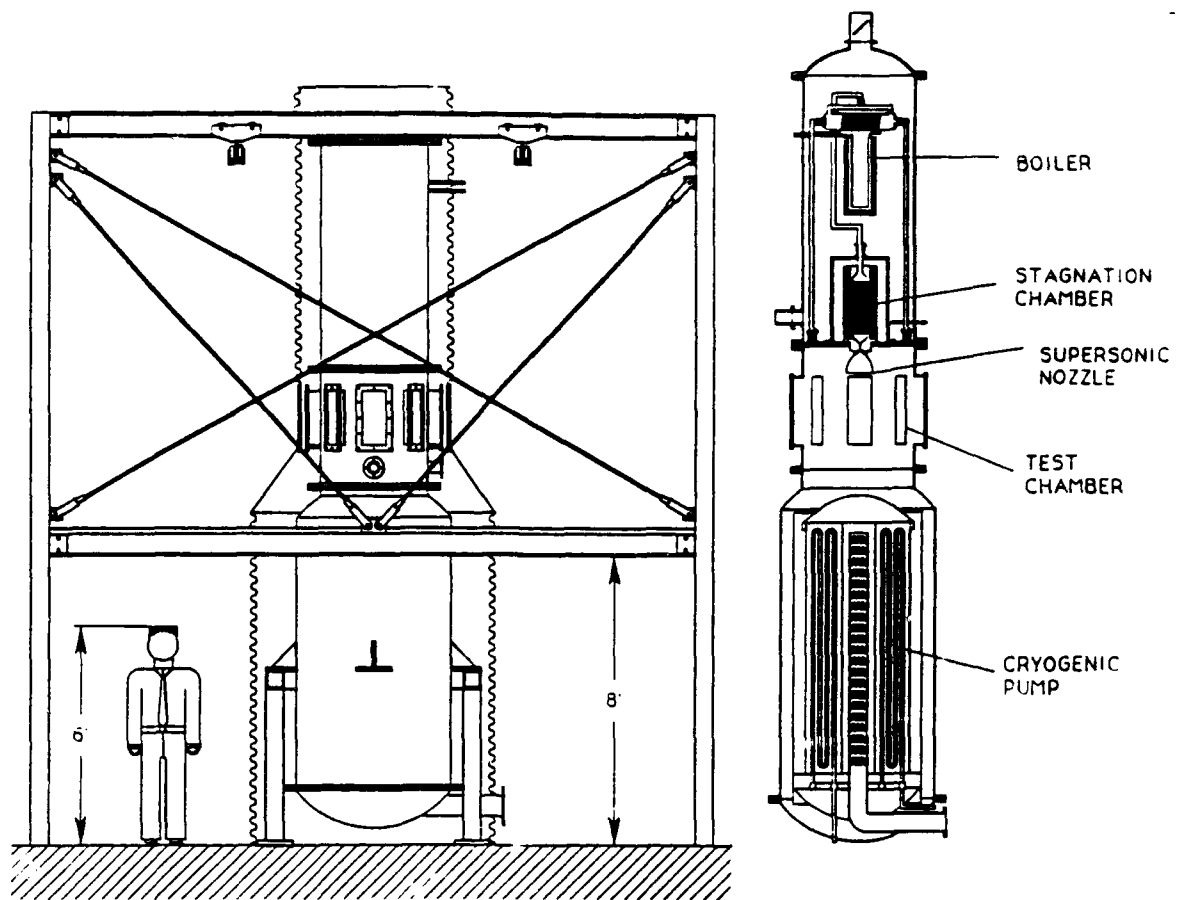


Figure 17: Schematic of the full scale iodine facility.

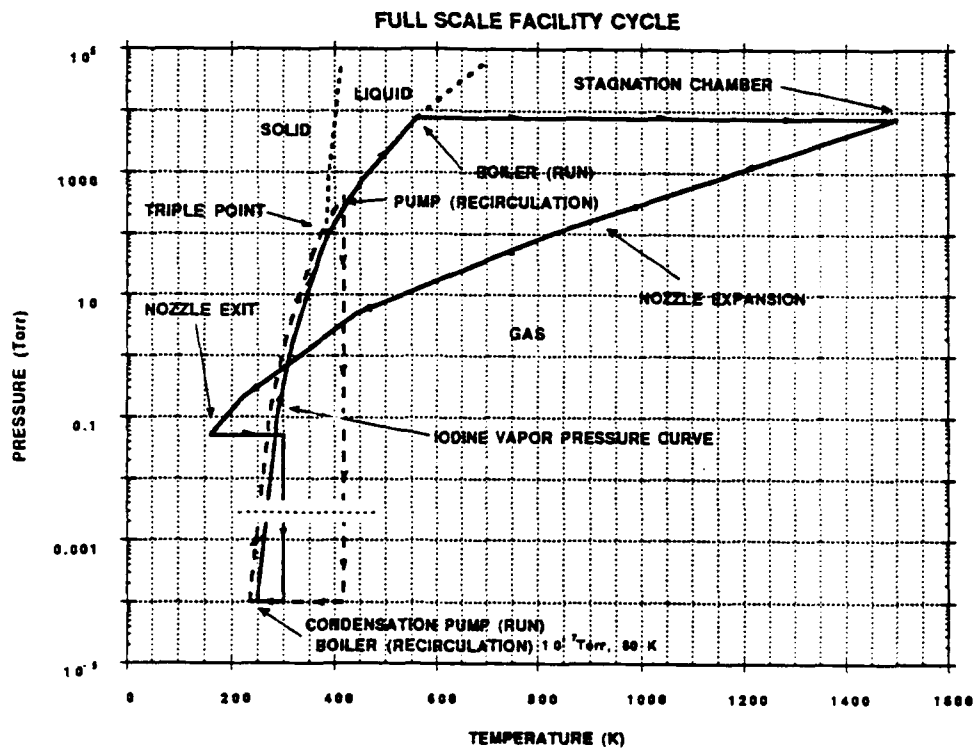


Figure 18: Pressure temperature diagram for the full scale tunnel operation cycle.

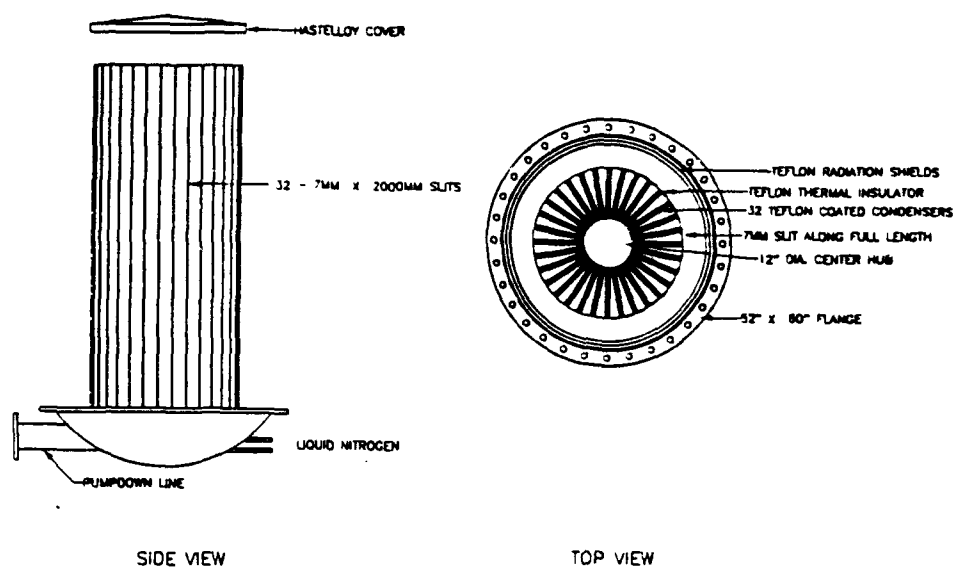


Figure 19: Cross-section of the condensation pump.

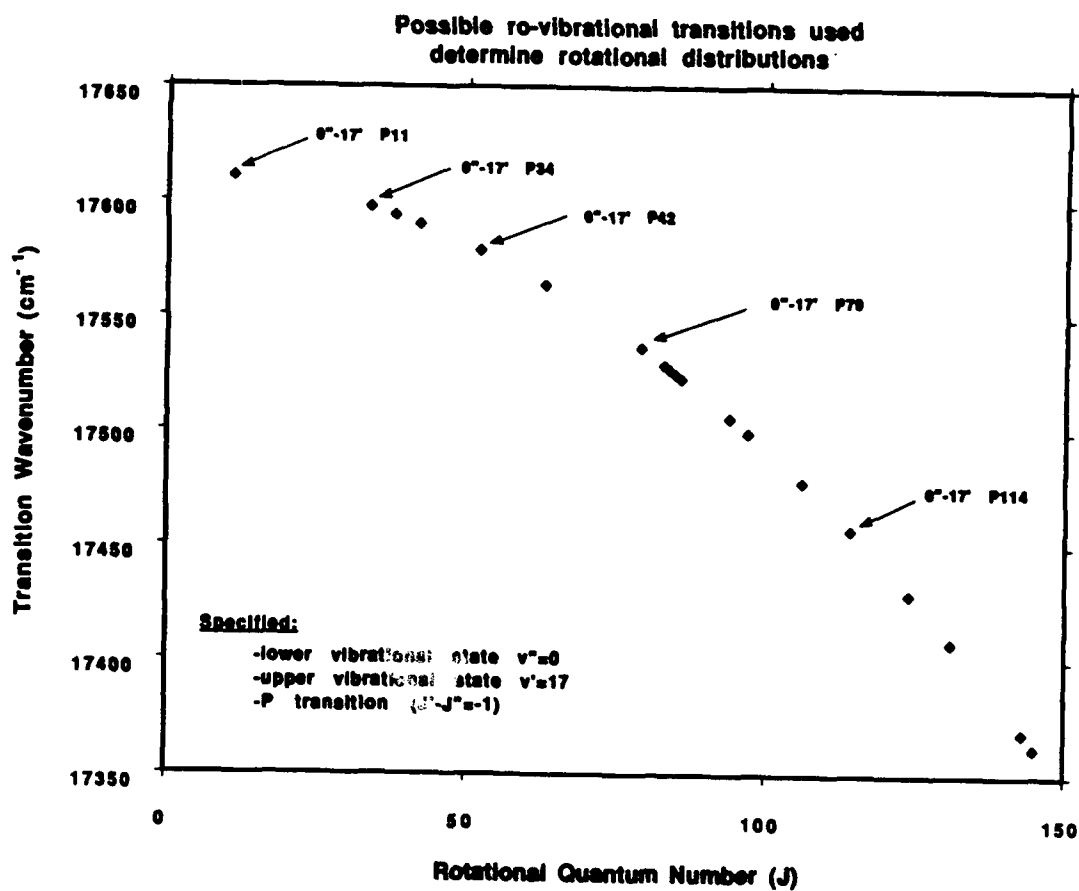
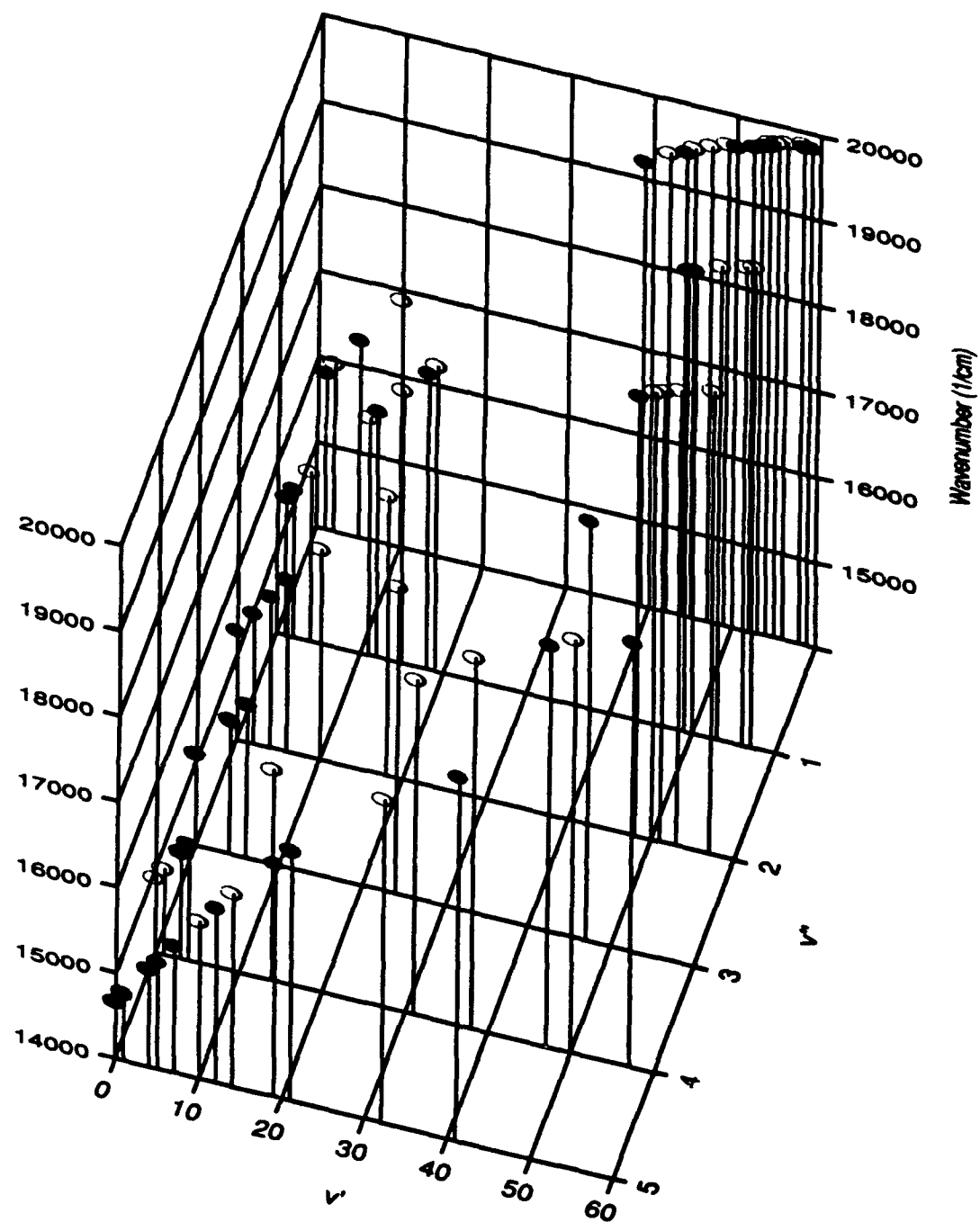


Figure 20: Possible ro-vibrational transitions used for determining rotational population distributions.



open symbols  $j'' = 50$

closed symbols  $j'' = 30$

**Figure 21:** Possible ro-vibrational transitions to determine vibrational population distributions.

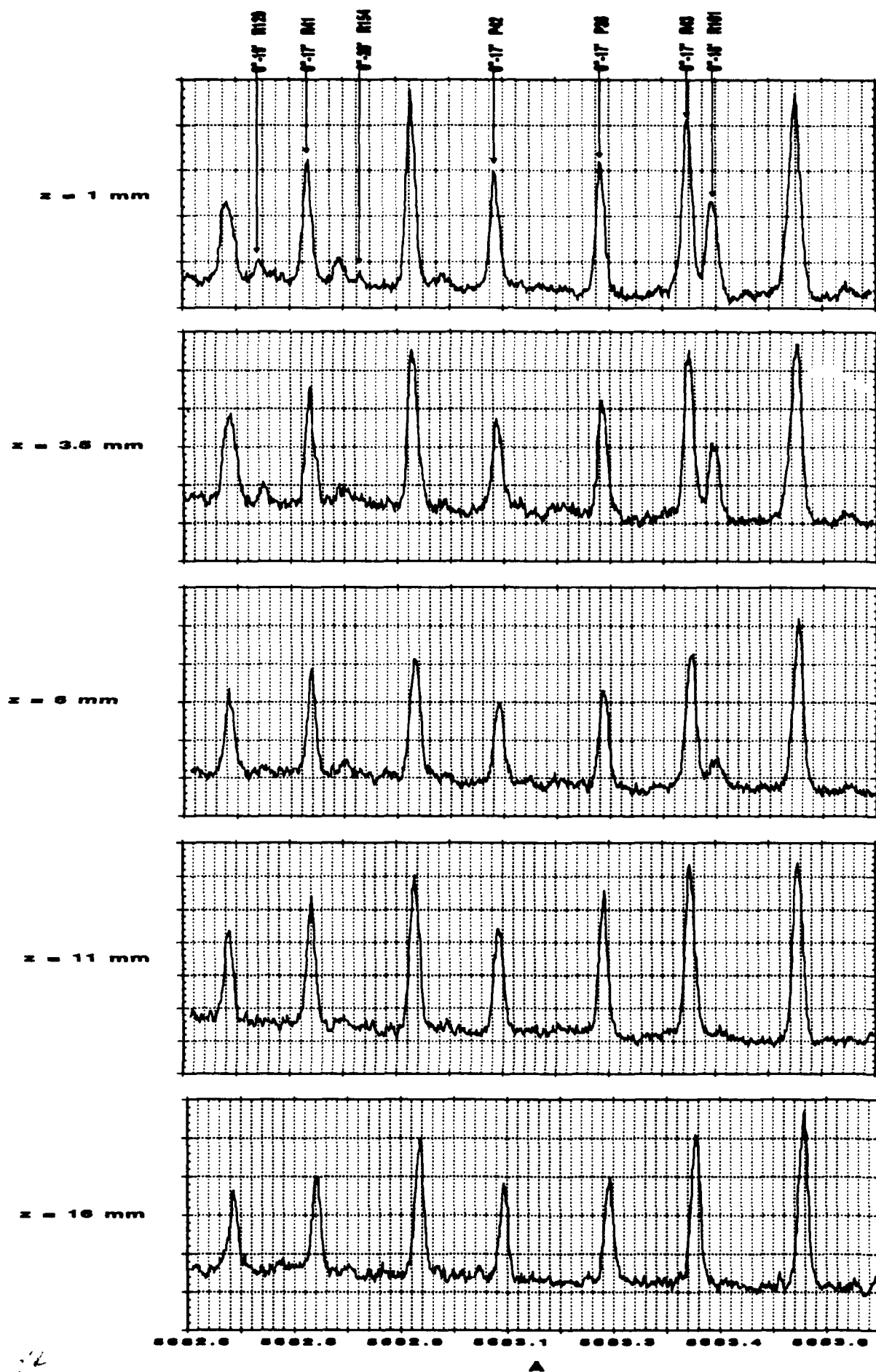


Figure 22: LIF emissions at several locations in front of a blunt body in a hypersonic iodine

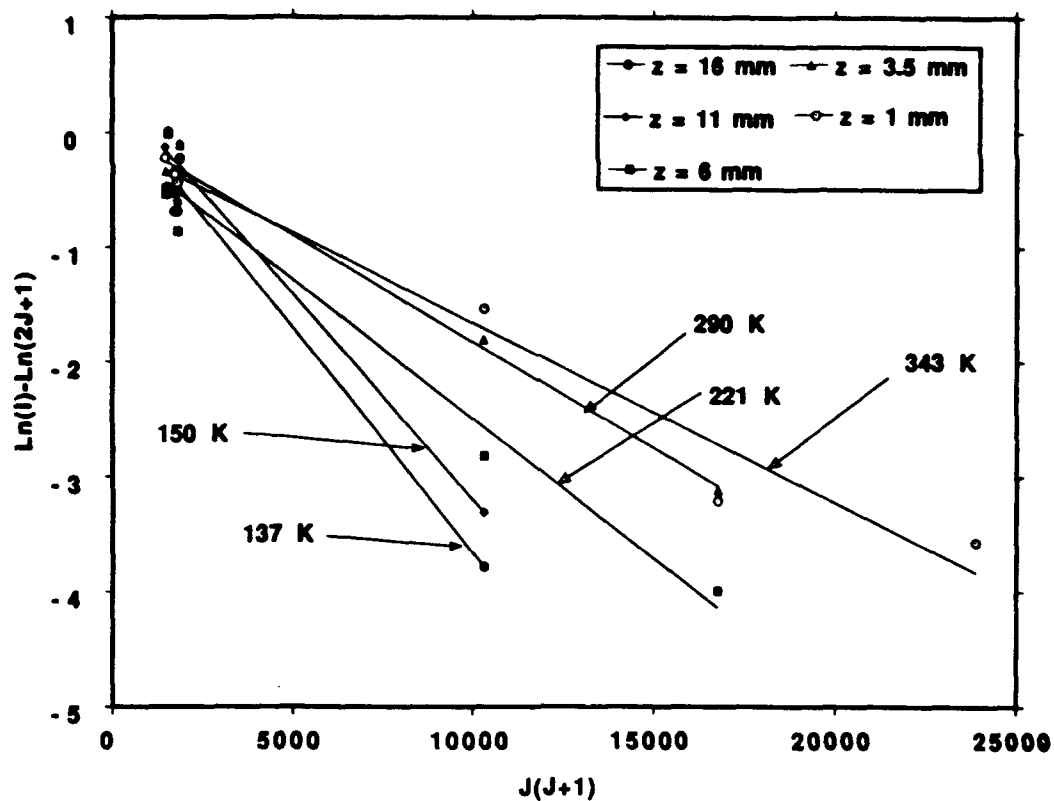


Figure 23: Relative intensity for spectra of Figure 22.

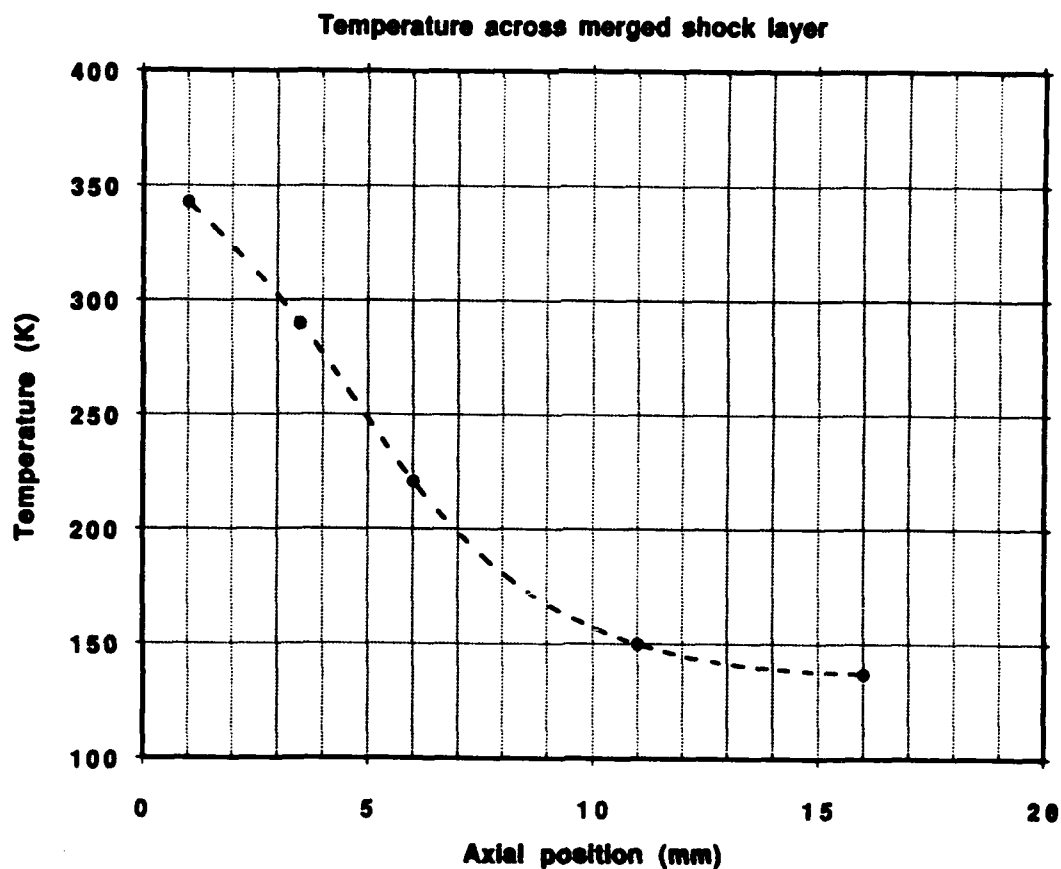


Figure 24: Rotational temperatures from Figure 23.

**ATTACHMENT 2**





**AIAA 92-0566**

## **An Iodine Hypersonic Wind Tunnel for the Study of Nonequilibrium Reacting Flows**

G. C. Pham-Van-Diep<sup>\*</sup>, E. P. Muntz<sup>†</sup>, D. P. Weaver<sup>‡</sup>, T. G.  
Dewitt<sup>\*\*</sup>, M. K. Bradley<sup>††</sup>, D. A. Erwin<sup>‡‡</sup> and J. A. Kunc<sup>\*\*\*</sup>

University of Southern California  
Department of Aerospace Engineering  
University Park  
Los Angeles, California 90089-1191

---

<sup>\*</sup>. Research assistant, Member

<sup>†</sup>. Professor, Fellow

<sup>‡</sup>. Visiting senior scientist, Member

<sup>\*\*</sup>. Laboratory Manager

<sup>††</sup>. Member of Technical staff Rockwell International, Member

<sup>‡‡</sup>. Professor, Member

<sup>\*\*\*</sup>. Professor, Associate Fellow

**30th Aerospace Sciences  
Meeting & Exhibit**  
January 6-9, 1992 / Reno, NV

# An Iodine Hypersonic Wind Tunnel for the Study of Nonequilibrium Reacting Flows

by

G. C. Pham-Van-Diep<sup>\*</sup>, E. P. Muntz<sup>†</sup>, D. P. Weaver<sup>‡</sup>, T. G. Dewitt<sup>+</sup>,  
M. K. Bradley<sup>°</sup>, D. A. Erwin<sup>\*\*</sup> and J. A. Kunc<sup>††</sup>

University of Southern California  
Department of Aerospace Engineering  
University Park  
Los Angeles, California 90089-1191

## Abstract

A pilot scale hypersonic wind tunnel operating on pure iodine vapor has been designed and tested. The wind tunnel operates intermittently with a run phase lasting approximately 20 minutes. Successful recirculation of the iodine used during the run phase has been achieved but can be improved. Relevant issues regarding the full scale facility's design and operation, and the use of iodine as a working gas are discussed. Continuous wave laser induced fluorescence was used to monitor number densities within the plume flow-field, while pulsed laser induced fluorescence was used in an initial attempt to measure vibrational energy state population distributions. Preliminary nozzle flow calculations based on finite rate chemistry are presented.

## 1. Introduction

In two previous papers, we proposed<sup>1,2</sup> iodine as an attractive gas for the detailed experimental study of nonequilibrium, chemically reacting hypersonic flows. In terms of dissociation, a stagnation temperature of 1500 K for iodine is equivalent to about 4000 K for oxygen or 6000 K for nitrogen.<sup>2</sup> An iodine hypersonic flow facility in which detailed measurements of internal state populations are possible, can be used for the validation of flow prediction techniques when nonequilibrium chemistry is important. In this paper we describe the initial implementation of this proposal in a pilot scale hypersonic wind tunnel. A full scale wind tunnel is currently under construction. Design flow periods are up to 30 minutes at stagnation temperatures of 1000 to 1500 K and stagnation pressures up to 10 Atm. Relatively long flow times are desirable to permit the detailed probing of the many energy levels populated within the flow. Three diagnostic techniques; continuum resonance Raman scattering,<sup>4</sup> electron beam fluorescence<sup>5</sup> and laser induced fluorescence<sup>4</sup> have been investigated. Emphasis is on developing techniques capable of measuring nonequilibrium energy state population distributions in the iodine flows. Accurate measurements of the population distributions for the

---

\*. Research assistant, Member

†. Professor, Fellow

‡. Visiting senior scientist, Member

+. Laboratory Manager

°. Member of Technical staff Rockwell International, Member

\*\* . Professor, Member

††. Professor, Associate Fellow

large number of significantly populated levels typical of a dissociating gas, will permit meaningful tests of the basic assumptions about local thermodynamic equilibrium that are made in most predictions involving finite rate chemistry.

## 2. Iodine as a working gas

### 2.1. Attributes of a code validation gas

During the flight of transatmospheric vehicles such as the NASP or the STS orbiter, the temperatures encountered behind a normal shock at an altitude of approximately 50 km are typically 4000 K for a speed of 4 km sec<sup>-1</sup>. At this altitude, the pressure is 1 torr and the most abundant species are molecular oxygen and molecular nitrogen. The Mach number is approximately 12, resulting in a pressure behind the shock of about 200 torr. Table 1 shows a comparison of the temperature required to produce 50% dissociation in iodine, nitrogen and oxygen. Also shown in Table 1 are the ratios of the vibrational energy spacing  $\Delta E_v$  to the average kinetic energy  $\langle \epsilon \rangle = (3/2) kT$ . While 50% dissociation in nitrogen and oxygen is achieved at temperatures of about 3500 and 5400 K, the same degree of dissociation can be produced by heating iodine to approximately 1300 K. The ratio  $(\Delta E_v) / \langle \epsilon \rangle$  is an indication of how close the average kinetic energy of the molecules are to the internal vibrational energy spacing. For all three gases,  $\langle \epsilon \rangle$  is larger than the energy required to excite the molecules to upper vibrational levels resulting in significant population of the vibrational levels. The ratios  $(\Delta E_v) / \langle \epsilon \rangle$  vary by up to a factor of 3. Since the value of  $(\Delta E_v) / \langle \epsilon \rangle$  is smaller for iodine, it is expected that its higher vibrational states will be somewhat more populated than the corresponding vibrational states in nitrogen or oxygen. Because rotational, vibrational and dissociative excitation of the iodine molecule can be achieved at lower temperatures than for oxygen or nitrogen, iodine will be used as a convenient surrogate diatomic gas for the study of chemically reacting gas flows. More detailed considerations of the electronic structure of  $I_2$  and  $I$  further substantiate its suitability as a convenient gas for calculating the properties of inelastic collisions including vibrational transition probabilities and dissociation.<sup>2</sup> An

Species	Temperature (K)	$\langle \epsilon \rangle$ (eV)	$\Delta E_v$ (eV)	$(\Delta E_v) / \langle \epsilon \rangle$
$I_2$	1340	0.17	0.026	0.15
$N_2$	5400	0.69	0.292	0.42
$O_2$	3530	0.45	0.195	0.43

Table 1: Thermal equilibrium properties of  $I_2$ ,  $N_2$  and  $O_2$  for a degree of dissociation of 50% and pressure of 200 Torr (after Kunc *et al.*<sup>2</sup>)

example of this is the recently published work of Kang and Kunc on the viscosity of iodine at elevated temperatures.<sup>3</sup>

### 2.2. Safety issues

Iodine has been used in a wide variety of studies. A few examples are: fundamental spectroscopic research,<sup>6,7</sup> investigation of laser induced processes,<sup>4</sup> visualization and probing of supersonic flows.<sup>8,10,12,9</sup> In these studies, iodine was either confined in a static cell or used in trace amounts to seed a flowing carrier gas, usually nitrogen. In either case the amounts of iodine involved were of the order of tens of grams at

most. In contrast, the work described in this paper uses quantities of iodine ranging from 500 g to 30 kg. For this reason we gave serious consideration to the corrosive and toxic nature of iodine while designing the facility.

The iodine molecule will react with most metals, the reaction rate depends on the concentration of iodine in contact with the metal. Metals such as aluminum and stainless steel (SS 304) are clearly inadequate even at room temperature where the iodine vapor pressure is approximately 0.2 Torr. Aluminum reacts to iodine by forming a large quantity of a light powdery substance which subsequently delays further reaction and can seriously contaminate the pumping system. It was found that the higher the content in nickel, chromium and molybdenum, the better the metal resists iodine corrosion. Stainless steel (SS316) offers a mild resistance to iodine attack at room temperature but cannot be used at higher temperature. Hastelloy (C276), a nickel alloy, was found to be the only commercially available metal that would not significantly corrode for temperatures up to 1000 K. Other non-metallic substances such as Pyrex<sup>®</sup>, ceramics (aluminum-oxides) and Teflon<sup>®</sup> seem to be excellent for use in an iodine environment. For this reason, parts that would ordinarily corrode can either be Teflon coated or anodized. Inert greases for seals and chemically stable pump lubricants are critical for the vacuum integrity of the experiment as well as the longevity of the pumping system. Krytox<sup>®</sup> oils and greases have performed fairly well, until now they have shown very few signs of reaction with iodine.

When inhaled, iodine may cause eye, nose, throat and respiratory tract irritation. If exposure is repeated, bronchitis, skin rashes, loss of appetite and sleep may result. Discontinuation of exposure is necessary to recover from ill effects. The maximum accepted concentration is 0.1 ppm, which corresponds to 1 mg/m<sup>3</sup> at standard atmospheric conditions. Reported lethal doses lie between a few tenths of a gram to more than 20 grams.<sup>12</sup> For the work described in this paper, the quantities of iodine used are of the order of kilograms at pressures above atmospheric, it is therefore absolutely necessary that leaks will only be into the facility and that satisfactory fail-safe features are designed in place.

### 3. Pilot Tunnel Construction and Performance

#### 3.1. Operational procedure

The pilot scale hypersonic wind tunnel was conceived so that the methods proposed for handling iodine in the full scale facility could be dealt with in the pilot facility on a scale that would allow easy modifications should design-related failure occur. The corrosive and toxic nature of iodine as well as the wide temperature range encountered in different parts of the facility were the main design considerations. Figure 1 shows a schematic of the vertically mounted prototype wind tunnel. The facility operates intermittently in a closed cycle.

The phase diagram for iodine is presented in Figure 2, with the facility cycle superimposed. During the run phase the boiler is maintained at a temperature that provides the desired stagnation pressure. The saturated iodine vapor from the boiler flows to the stagnation chamber when valve  $V_1$  is opened, where it is superheated to the stagnation temperature. The high temperature iodine in the stagnation chamber expands through a sonic orifice and into a vacuum chamber where optical diagnostics can be performed. A nozzle expansion is not used in the pilot scale tunnel. The iodine flow is pumped using condensation pumping onto two cold traps.

The second phase of operation consists of recycling the iodine from the cold traps used to condense

the working gas during the run phase to the supply chamber (boiler). Recirculation is achieved by the vapor pressure differential between the heated cold traps and the facility's heated vacuum envelope, and the cooled boiler. The run time of the pilot wind tunnel is about 20 minutes while the recycling period is of the order of 2 to 3 hours. For an orifice diameter of 0.5 mm, a stagnation temperature of 1,000 K and a stagnation pressure of 1 Atm., the mass flow rate is approximately 0.1 g/sec. The same mass flow may be obtained with an orifice diameter of 2 mm, a stagnation temperature of 700 K and pressure of 200 Torr.

### 3.2. Flow visualization and run time

The flow can be probed in regions where the Mach number ranges from about 5 to 30. Figure 3 a) and b) show photographs of a free jet expansion of iodine for a background pressure of  $10^{-6}$  Torr and 0.1 Torr respectively. Figure 4 shows a photograph of the flowfield around the flat end of a silicone carbide cylinder placed in the iodine jet. In these photographs the bright areas represent fluorescence obtained by excitation with the 5145 Å line of an Ar<sup>+</sup> laser. The areas downstream of the normal shock waves in the visualizations appear darker because of temperature effects on the populations of the particular rotational lines in resonance with the laser frequency. A normal shock is visible both in the case of a free jet in a high background pressure (Figure 3 b)) and upstream of the blunt body at a stand-off distance of approximately 2 mm.

Figure 5 shows a time trace of the fluorescence emitted from a point located approximately 25 orifice diameters downstream of exit plane. The sonic orifice diameter was 2 mm, the stagnation temperature and pressure were 700 K and 200 Torr respectively. For this measurement, the 5145 Å line of the Ar<sup>+</sup> laser was used to excite the  $(X(^1\Sigma_g^+) 0^+ - B(^3\Pi_{0u}^+) 43')$  P13 and R15 transitions of the iodine molecule. Figure 6 shows a top view of the experiment. The Ar<sup>+</sup> laser is not represented but was placed parallel to the dye laser. Fluorescence was observed at 5260.25 Å with a SPEX 0.75 m double spectrometer and RCA C31034A02 photomultiplier. The spectrometer slits were adjusted so that the spectral resolution was about 0.4 Å. The laser beam was focused with a 25 cm focal length lens and aimed horizontally through the center of the plume at a position sufficiently far downstream of the orifice exit plane to avoid any quenching effects. Indeed, at a position 25 orifices diameters downstream of the exit plane, the number density drops by 4 orders of magnitude from stagnation conditions,<sup>16</sup> thus significantly reducing collisional deexcitation of molecules in the upper state. The image of the horizontal column of fluorescence emitted from the plume was rotated 90° so that it aligned with the spectrometer entrance slit. Consequently, the signal observed in Figure 5 was integrated radially over a distance in the plume of approximately 1.5 cm. Figure 5 shows a sudden drop in signal intensity during a period of about 2 minutes before the flow conditions become steady. This is caused by the rapid energy loss from the pool of liquid iodine in the boiler due to the net vaporization of I<sub>2</sub> to make up for the iodine flowing through the orifice when the flow is initiated. The resulting thermal load on the boiler could not be compensated by the boiler heater, which in this case was a simple ceramic oven heater surrounding the boiler but not in direct contact with it. This arrangement resulted in only a moderate control over the boiler temperature of  $\pm 5$  K because of the slow response time of the system. The drop in intensity seen in Figure 5 corresponds to a drop in temperature of about 6 K. A recirculating hot oil bath heater system was subsequently used and resulted in an improved but still insufficient temperature control to within  $\pm 3$  K. It is critical that the boiler temperature be controlled accurately because at 457 K, where the iodine vapor pressure is one atmosphere, a drop of 5 K corresponds in a stagnation pressure decrease of 60 to 70 Torr. Under the present conditions, Figure 5 indicates that a quasi-steady flow can be obtained for run times of the about of 20 minutes. More care in the design of the full system should produce satisfactorily steady stagnation conditions.

When all the iodine supply contained in the boiler has been used, most of the working gas is in principle frozen on the cold traps. At this stage, recycling of the iodine can be performed: the gate valve is closed to protect the pumping units, hot air is blown through the cold traps so that the frozen iodine sublimates (Ref. Figure 2),  $V_2$  (Ref. Figure 1) is opened and the boiler walls are now cooled to  $LN_2$  temperature. When the iodine evaporates, it flows through the return duct and freezes on the boiler walls. During the recycle phase, it is important that the pressure remains low enough to allow flow of the iodine. Since the pumping system is at this point isolated from the chamber, it is critical that the leak rate of the chamber is reduced to a minimum. Calculations assuming an incompressible Poiseuille flow within the return duct indicate that the recirculation time should be of the order of 1 hour. The mass flow rate through the recycling duct is described by<sup>17</sup>

$$\dot{m} = \frac{\pi a^4}{8\eta L} \cdot \frac{P^2}{2} \cdot \frac{m}{kT}, \quad (1)$$

where  $a$ ,  $l$ ,  $m$  and  $\eta$  are the radius, length of the tube, the mass of the iodine molecules and the viscosity of the iodine vapor respectively.  $P$  and  $T$  are the pressure and temperature taken as 2 torr and 323 K respectively. A value of  $14 \times 10^{-6}$  N sec  $m^{-2}$  was selected for the viscosity<sup>18</sup> at 323 K. In practice, however, recirculation times are 3 to 4 hours. This is partly due to losses in the recirculation path caused by bends and constrictions.

In order for the recirculation process to be efficient it is important that all parts of the test section be heated to the temperature corresponding to the vapor pressure necessary to drive the iodine to the boiler. For this purpose, a plexiglas shroud was built around the entire facility and a 5 kW heater is used to blow hot air around it (Ref. Figure 1). If the test facility is nonuniformly heated iodine will condense on its coldest surfaces, thus delaying the recirculation process. Figure 7 shows a photograph of an optical port which was colder than the rest of the test section due to a hot air leak through the shroud. As the iodine crystals of the photograph show, the cryopumping of iodine is a rather efficient process even through temperature gradients of a few degrees.

A subtle but important issue concerning recirculation deals with the accumulation of incondensibles in the boiler. As the iodine vapor condenses on the boiler walls, incondensibles carried with it are separated from the  $I_2$  molecules and over time build up pressure within the boiler, which in turn slows further flow of iodine from the test section. Venting of the incondensibles during the recirculation phase is therefore necessary. This was achieved either by opening  $V_1$  (Ref. Figure 1) during recirculation, or actively pumping on the downstream side of the boiler using a bypass line to the main pumping system. Related phenomena are relatively well known effects to users of cold trapped Macleod gages, it was also used by one of us (E.P.M., who also forgot about it until we had trouble recirculating) to enhance the operation of an isotope separation system.<sup>25,26</sup>

## 4. Nozzle Flow Calculations

The reason for developing an iodine vapor wind tunnel is to study nonequilibrium, reacting flows. In order to verify that flows generated at stagnation conditions of 1500 K and 10 atm. will provide situations where finite rate chemistry effects can be observed, selected nozzle and shock wave calculations have been completed. The nozzle throat used in the calculation is shown in Figure 8. It follows previous nozzle designs reported by a number of authors.<sup>27</sup> The conical section marks the transition to the downstream portion of a

hypersonic nozzle where the flow is turned to be approximately parallel at the nozzle exit. Nozzle contours for this downstream section have not been finalized. For a conical nozzle formed as an extension of the 12° half angle expansion in Figure 8, a finite rate chemistry, inviscid flow solution was calculated using a One Dimensional Kinetics (ODK) computer program<sup>19</sup> based on the forward reaction rate constant<sup>29</sup> shown in Table 2. These computations resulted in the Mach number, pressure, temperature and degree of dissociation shown in Figures 9 a) -d). Also shown in the Figure 9 c) are frozen and equilibrium temperatures for the same nozzle. Note that the flow is fairly close to equilibrium leaving only about a 5% degree of dissociation in the free stream at the nozzle exit.

Reaction	$I_2 + I_2 \rightarrow I + I + I_2$
Rate	$1.09 \cdot 10^{17} T^{-0.5} e^{-15800/T}$
Temperature range (K)	$300 < T < 2000$
Units	$\text{cm}^3 \text{mol}^{-1} \text{sec}^{-1}$

Table 2 : Reaction rate used in ODK computations

The calculations were performed for a nozzle geometry and flow conditions summarized in Table 3.

Working Gas	$I_2$
Stagnation pressure (atm.)	10
Stagnation temperature (K)	1500
Downstream pressure (Torr)	0.1
Throat radius (mm)	1.778
Nozzle exit radius (cm)	10.16
Area Ratio	3265.3

Table 3 : ODK calculation parameters

Boundary layer calculations for a similar nozzle indicate a displacement thickness at the exit of about 1.5 cm. The displacement thickness is of course sensitive to the wall temperature which must at all times be controlled so that the corresponding iodine vapor pressure is slightly higher than the local static pressure of the nozzle flow.

The possibility of iodine condensation in the nozzle flow is illustrated in Figure 10 where the finite rate chemistry results are superimposed on the solid-vapor equilibrium line from the iodine phase diagram. The flow only reaches equilibrium saturation at a Mach number of about 6, where the collision frequency is relatively low. We do not expect to encounter serious condensation problems. More details about these calculations will be reported soon by Bradley.<sup>20</sup>

Will there be active chemistry in the flow field at the nozzle exit conditions? To investigate this issue, a normal shock holder was assumed to be placed in the flow. For a frozen flow across the momentum shock, finite rate chemistry calculations were completed as a function of distance behind the shock front.

The results are shown in Figure 11 where a relaxation distance of a centimeter is required for the degree of dissociation to come to equilibrium. This would be an ideal distance for measurements of the details of this relaxing, dissociating flow.

## 5. Full Scale Tunnel Design

Figure 12 shows a schematic of the full scale hypersonic facility. The wind tunnel is designed to operate on 50 kg of pure iodine, with a stagnation temperature of 1500 K and pressure of 10 Atm. The flow rate will be about  $20 \text{ g sec}^{-1}$  for a total run time of a little over 30 minutes. The hypersonic flow will be achieved by expanding the iodine vapor through a nozzle into a 1 m diameter low pressure dump tank. The open jet nozzle will have a throat diameter of 3.4 mm and an exit diameter of about 20 cm. Pumping of the working gas during the run will be achieved by condensing the iodine on cryogenic panels. The facility will operate on the same basis as its pilot scale counterpart i. e. in a closed cycle for safety reasons and on an intermittent basis. During the recirculation phase, the iodine is transferred from the heated cryogenic pump panels to the cooled walls of the boiler. Mach numbers up to about 10 will be achieved at the nozzle exit. As indicated in Figure 12 the full scale tunnel is mounted vertically with the test section featuring multiple optical access ports about 3 meters from the floor.

The cycle for the full scale tunnel is shown in Figure 13 superimposed on the iodine phase diagram. Based on a tunnel envelope temperature of 450 K the pressure driving the recirculation phase will be about 300 Torr. The recirculation lines to the boiler will have a diameter of 2.5 cm and a length of 2 m, resulting in a recirculation time that theoretically should be a few seconds for a recirculating temperature of 450 K. Dropping the temperature to 370 K reduces the pressure to about 30 Torr and increases the recirculation time by two orders of magnitude. This would permit the recycling to proceed without forming liquid iodine. A hastelloy catch basin is incorporated in the condensation pump to hold liquid iodine during recirculation.

The condensation pump is designed for the particular application to the iodine tunnel. The nozzle exit static pressure will be 50 to 100 mTorr. In order to control the condensation pumping at these rather high pressures the condensing surfaces have been arranged as shown in Figure 14. Panels mounted vertically in a star pattern about a central vertical tube are separated from the pressure required for balancing the nozzle flow by a cylindrical surface containing long vertical slits about 7 mm wide. The slits are positioned at the mid point of the outer boundary of the wedge shaped sections formed by the condensing surfaces. Between the slotted cylinder and the pump's outer vacuum boundary the pressure will be close to the nozzle exit pressure. The vertical slots form continuum two-dimensional jets that expand freely into the wedge shaped spaces. The static pressure in these spaces will be  $\leq 10^{-3}$  Torr. From the work on 2-D jets by Dupeyrat<sup>28</sup> the shock systems associated with these jets should be about 30 cm downstream of the slits in this particular case (7 mm slits, pressure ratio of 100). Thus the underexpanded jets will impinge directly on the condensing surfaces, both enhancing the efficiency of the surfaces and distributing the condensate in a more uniform manner.

## 6. Diagnostic considerations

Significant internal energy excitation may be produced by heating the iodine vapor to temperatures ranging from 1000 K to 1500 K.<sup>2</sup> For this reason, we have chosen as an initial study in the pilot facility an underexpanded free jet flow whose stagnation temperature is about 1000 K. At this temperature, approxi-



mately 10 vibrational energy levels are significantly populated along with about 200 rotational energy levels within each vibrational state. Because the rate of collisions decreases significantly as the gas expands, nonequilibrium effects are present within the plume. The work reported here is mainly concerned with developing methods for probing the nonequilibrium features of the expansion. These are characterized by a decoupling of the translational and rotational temperature from the vibrational temperature as well as a non-Boltzmann distribution in the vibrational energy levels. With the design run time of the facility being 30 min., emphasis is placed on developing diagnostic techniques which would probe several internal energy states without requiring long integration periods. Previous investigations of iodine expansions have been reported but involved flows of carrier gases seeded with trace amounts of iodine.<sup>9-12</sup> Internal energy state population probing has only been performed on pure iodine in local thermal equilibrium and confined to a static cell using; conventional, discrete resonance (fluorescence) and continuum resonance Raman scattering techniques.<sup>4,13,14</sup> Research on the energy level populations of chemically reacting flows of iodine has to our knowledge never been performed, although measurements of velocity distribution functions in flows of evaporating iodine have been reported.<sup>15</sup>

We have investigated continuum resonance Raman scattering<sup>4</sup> to evaluate the vibrational and rotational energy state populations within the flows generated in our pilot scale facility. This technique applied to the iodine molecule involves transitions where the probing laser energy is tuned to excite the iodine molecules from the ground  $X(^1\Sigma_g^+)$  state, to the continuum of the  $B(^3\Pi_{0u}^+)$  state. In order to excite the iodine molecule into the dissociative continuum of the  $B$  state, an excitation wavelength of at most 4960 Å is required. Since the energy states of the continuum are non-stationary, the scattering process is fast ( $\leq 10^{-9}$  sec) and thus insensitive to collisional quenching. We have used the 4880 Å radiation of a 1 Watt Ar<sup>+</sup> laser in our c.w. approach. To test signal level intensities, Raman spectra of the fundamental vibrational overtone ( $\Delta v = 1$ ) have been recorded from stagnant iodine contained in the test section at room temperature where the iodine vapor pressure is approximately 200 mTorr. The maximum number of Raman photons detected was typically 100 sec<sup>-1</sup> implying total scanning times of the order of 30 min for the accumulation of reasonable statistics. Figure 15 shows an example of the fundamental vibrational overtone recorded with a spectral resolution of 0.4 Å. Similar measurements have been attempted in the plume of a free jet of iodine where the stagnation temperature and pressure were 800 K and 200 Torr respectively. Number density as a function of time has been recorded, but signal levels were too weak to permit spectral scans. The exceptionally weak signals that are observed in these particular tests are thought to be caused by an unrelated output power loss of the laser. However, in view of the fact that the continuum resonance Raman scattering cross section is  $1.1 \cdot 10^{-28} \text{ cm}^2$  for an excitation wavelength of 4880 Å,<sup>21</sup> (as opposed to  $3 \cdot 10^{-16} \text{ cm}^2$  for fluorescence) the generally weak Raman signal levels observed during this investigation are not surprising.

A pulsed excitation of the Raman transition was investigated. For this purpose, we have used an excimer (XeCl) pumped dye laser tuned to 4880 Å. For a pulsed excitation of the probed molecules, the signal to noise ratio may in principle be increased assuming a reasonable pulse to pulse stability. For the optical efficiency of the collection system used in the experiment, signal levels of the order of  $10^3$  photons per laser pulse should be detected assuming a number density of  $10^{16} \text{ cm}^{-3}$ , a Raman cross section of  $10^{-28} \text{ cm}^2$  and a laser pulse energy of 60 mJ at the excitation wavelength of 4880 Å. In practice however, such signal levels have not been observed for reasons that remain to be identified.

The fluorescence of iodine vapor induced by electron impact was also investigated. We have used a 20 kV electron beam to excite iodine vapor contained in a static cell at a pressure of 200 mTorr. Very little

fluorescence (compared to the  $N_2^+ 1^4$  negative system under similar conditions) could be observed from the resulting transitions. We believe that the excitation caused by electron impact resulted in a large amount of dissociation and very few bound-bound transitions between the  $X$  and  $B$  state, thus inhibiting fluorescence at visible frequencies.

At the present time, the most promising technique for probing the internal energy state populations of the iodine molecule seems to be laser induced fluorescence. This technique has the advantage of providing strong signal levels. Indeed, typical laser induced fluorescence cross sections are of the order of  $3.5 \cdot 10^{-16} \text{ cm}^2$  for pumping at  $5145 \text{ \AA}^{12}$  as opposed  $10^{-28} \text{ cm}^2$  for a Raman transition assuming excitation at  $4880 \text{ \AA}^{21}$ . However, fluorescent signals are by no means a direct measurement of internal state populations. Signal intensities are complicated to interpret due to quenching issues and rely heavily not only on the correct determination of Franck-Condon factors<sup>6</sup> but also require for accurate results knowledge of the variation of the electronic transition probability with vibrational quantum number. Because the technique discussed here requires the pumping frequency to be in resonance with a wide variety of the absorbing transitions, we have used an excimer pumped tunable dye laser with the experiment done in a pulsed mode. Figure 16 shows one spectral scheme we have selected to probe the  $v'' = 2$  level of the  $I_2$  molecule's  $X$  state. Also shown is the present laser line shape which has a full width at half maximum of approximately  $0.2 \text{ cm}^{-1}$  or  $0.05 \text{ \AA}$ . Since all the transitions under the laser profile involve the  $2^{\text{nd}}$  vibrational level of the ground state, it is reasonable to expect that the latter may be successfully probed assuming that the convolution of laser and absorption lineshapes can be computed. Figure 17 shows the absorption spectrum of the iodine molecule in the vicinity of  $5145 \text{ \AA}^7$  with the laser profile position chosen to probe the  $0^{\text{th}}$  vibrational level of the  $X$  state. In this case, we would like to pump the  $(0''-43'')P13/R15$  transition exclusively. Unfortunately, the overlap of the laser profile with the  $(1''-58'')R98$  and  $(1''-50'')P46$  transitions seriously complicates the determination of the population of interest. Pumping of a single transition appears possible by narrowing the laser linewidth to  $0.05 \text{ cm}^{-1}$  which requires the use of an intracavity etalon in the dye laser.

The wavelengths of a large number of absorption lines have been cataloged for iodine<sup>22</sup> but not identified. Identifications do exist near commonly used laser frequencies.<sup>7</sup> However the lack of extensive identifications is a difficulty that will have to be remedied before a complete picture of vibrational and rotational populations are possible from fluorescence measurements.

Issues such as quenching and saturation have to be addressed when dealing with laser induced fluorescence. For pulsed pumping and using a simple 2 level model, the upper state population  $N_2$  is described by

$$\frac{dN_2}{dt} = N_1 B_{12} g(\nu) \frac{I(t, x)}{c} - N_2 \left[ B_{21} g(\nu) \frac{I(t, x)}{c} \left( 1 + \sum_{n \neq 2} P_{2n} \right) + \sum_{i < 2} A_{2i} + \sum_{j \neq 2} R_{2j} \right], \quad (2)$$

where  $I(t, x) = E_p(x)/(A \cdot \tau)$  is the laser's instantaneous intensity,  $A$  is the beam cross section,  $E_p$  the energy per pulse (typically 60 mJ) and  $\tau$  is the pulse duration of 28 nsec. The laser intensity is kept as a function of physical space because we may need to consider beam attenuation. Equation (2) indicates that the upper state population depends on two competing effects: 1) a laser pumping rate which is a function of the lower state population  $N_1$ , the absorption linestrength  $B_{12}$ , the laser lineshape  $g(\nu)$  and intensity  $I(t, x)$  ( $c$  is the speed of light). 2) a term depopulating the upper level, depending on the stimulated emission linestrength  $B_{21}$ , a spontaneous emission term ( $A_{2i}$ ) and a collisional quenching term ( $R_{2j}$ ). The term ( $P_{2n}$ ) appears in the depopulating factor to account for molecules being pumped out of level 2 but not repopulating the bottom

level, thus resulting in a net depletion of the probed level's population. Taking  $B_{12} = 4 \cdot 10^{18} \text{ m}^3 \text{ J}^{-1} \text{ sec}^{-2}$ ,  $A_{21} = 5 \cdot 10^5 \text{ sec}^{-1}$ , and a collisional cross section of  $7.8 \text{ \AA}^2$ ,<sup>12</sup> and assuming typical experimental conditions, the laser pumping term can be estimated at  $10^{33} \text{ sec}^{-1} \text{ m}^{-3}$  which is about 6 orders of magnitude larger than the sum of the spontaneous decay and quenching term. This would indicate that the upper level population is saturated and reaches a steady state value  $N_{2\infty} = N_{1(t=0)} / (1 + g_1/g_2)$ , where  $g_1$  and  $g_2$  are the lower and upper level statistical weights respectively. To calculate the pumping rate discussed above, the sums in eq. (2) were replaced by single terms. The quenching rate was computed for the worst possible case at a pressure of 1 Atm and a temperature of 1000 K. The time it takes  $N_2$  to reach 90% of its saturated value can be calculated with

$$t = \frac{-\ln(0.1) A c \tau}{B_{12} g(v) E_p (1 + g_1/g_2)} \quad (3)$$

A typical response time is of the order of picoseconds which would appear instantaneous on the time scale of the laser pulse. For our purpose, saturation is desired because it has the advantage of making fluorescence insensitive to pulse to pulse fluctuations. However, saturation may be difficult to achieve due to transitions that would depopulate the upper level such as multiple photon excitations, photo-dissociation or dissociative quenching reactions.<sup>23,24</sup>

When the laser pulse ends, the fluorescence decays as

$$\frac{I(t)}{I_0} \propto N_2(0) e^{-\left[\sum_{i=1} A_{2i} + \sum_{j=1} R_{2j}\right] t} \quad (4)$$

where  $N_2(0^+) = N_{2\infty}$  if the upper level is saturated, or  $N_2(0^+) = N_1 B_{12} g(v) E_p / (A \cdot c)$  if weak laser pumping is applied. In both cases, the signal at  $(t = 0)$  is proportional to the lower state population  $N_1$  even though the decay rate becomes independent of  $N_1$  if quenching dominates spontaneous decay. In other words the maximum of a fluorescence time trace is proportional to the lower level population independent of quenching. Of course the signal integrated over all time may be independent of the lower state population if quenching dominates spontaneous emission. The unquenched  $(t = 0)$  signal may be used to measure the relative populations of different vibrational states at several positions on the axis of the free jet expansion.

## 7. Initial results

Figure 18 shows a typical time trace of the fluorescence signal detected 2 orifice diameters downstream of the jet exit plane. The laser was tuned to  $5145 \text{ \AA}$  and fluorescence was observed at  $5260.25 \text{ \AA}$  with a resolution of  $1 \text{ \AA}$ . For this particular experiment the stagnation temperature was 700 K and the stagnation pressure was 200 Torr. The time trace was obtained by scanning a 100 nsec gate across the fluorescent time profile and averaging the signal over 10 pulses. The laser repetition rate was 10 Hz. Similar traces were recorded for different flow conditions. A stagnation temperature of 973 K and stagnation pressure of 10 Torr were selected to extend the jet run time. To determine the peak signal at  $t = 0$  the decaying portion of the time traces were best fit with an exponential function. Time  $t = 0$  was arbitrarily chosen at the center of the laser pulse. Probing was performed at  $z = 2, 3$  and 4 orifice diameters downstream of the exit plane, on the plume centerline. The recorded peak signals are listed in Table 4 and were found to decrease as  $z^{-2}$ . Because this is consistent with number density predictions in free jet expansions,<sup>16</sup> the peak signal does indeed seem to be independent of quenching. The signal decay rate indicates whether collisional deexcitation of the upper level

prevails over radiative decay. Lifetimes based on a  $1/e$  signal decay are listed in Table 4 and are found to increase as  $z$  increases which is consistent with the fact that at positions further downstream the number density and temperature decrease, thus reducing the number of quenching events. The transition's lifetimes are of the order of hundreds of nanoseconds, while the radiative lifetime for the transitions observed is  $2 \mu\text{sec}$ .<sup>12</sup> This would indicate that collisional deexcitation is still effective at the probe positions.

$z$	Fluorescent signal (mV)	Lifetimes (nsec)	Temperature (K)	Number density ( $\text{cm}^{-3}$ )
2	74.4	250	402	$1.2 \cdot 10^{17}$
3	24.5	415	284	$3.7 \cdot 10^{16}$
4	7.85	619	229	$1.7 \cdot 10^{16}$

Table 4 : Fluorescent signal level for several normalized axial positions

Probing the  $v'' = 0, 1, 2$  vibrational levels of the  $X(^1\Sigma_g^+)$  state was attempted using the scheme mentioned in Section 6. Signal levels recorded were reasonable but as indicated in Figures 16 and 17 the laser linewidth of  $0.2 \text{ cm}^{-1}$  was found to be too wide to enable pumping of a single transition at a time, thus making the determination of single level populations impossible. The use of a narrower laser line of  $0.04 \text{ cm}^{-1}$  is planned in the near future. As mentioned earlier, the number of photons available per pulse would indicate that the upper level being pumped by the laser is saturated, thus making the measurement independent of laser power fluctuations. In practice however, the upper level was not saturated because a decrease in laser power by a factor of 3 resulted in a similar decrease in fluorescent signal. This indicates that the upper level population is being depleted by transitions ending in states other than the lower state (i.e. the term  $P_{21}$  in Equation (2) is non negligible). Multiple photon excitation of  $I_2$  resulting in dissociation and ionization of the molecule has been reported in a number of studies<sup>24,30</sup> for a wide range of excitation wavelengths (3600 to 6000 Å). These studies were performed with tunable pulsed lasers at power levels 20 times smaller than the powers used for the present work. For this reason, photo-dissociation and ionization of the probed molecule seem to be a plausible mechanism for depopulating the upper level, thus preventing saturation. Work is proceeding on examining these issues.

## 8. Summary

We are developing a hypersonic wind tunnel in which reacting nonequilibrium flows can be studied. A pilot tunnel has been operated successfully and is being used to develop optical diagnostic techniques. Continuum resonance Raman scattering has been investigated to probe the internal energy population distributions within the flow, but signal levels seem to be too weak to allow an accurate description of energy state populations. Electron beam fluorescence was tested on iodine vapor contained in a static cell. Resulting excitation transitions appear to dissociate or ionize the probed gas, but did not excite strong fluorescence comparable to nitrogen. The most promising diagnostic technique appears to be laser induced fluorescence. Preliminary probing of the first three vibrational levels of the iodine molecules within a supersonic flow has been tested. The technique needs to be improved with the use of a moderately narrower excitation line. Finite rate chemistry calculation indicate that the nozzle flow will be close to equilibrium and that significant chemistry takes place within 1 cm behind the normal shock wave at the nozzle exit conditions.

## 9. Acknowledgment

This work is supported by the United States Air Force Office of Scientific Research as part of the University Research Initiative program and in part by a NASA Training and Research grant.

Ken Richards and Mark Trojanowski made important contributions to the development of the pilot tunnel.

## 10. Bibliography

- 1 D. A. Erwin, J. A. Kunc, E. P. Muntz. *Establishing the Basis for Validated Predictions of Highly Nonequilibrium Flows*. Proposal to the University Research Initiative Program. Submitted in response to: BAA Number 89-2, April 1989.
- 2 J. A. Kunc, E. P. Muntz, D. P. Weaver. *Model Gases for the Detailed Study of Microscopic Chemical Nonequilibrium in Diatomic Gas Flows*. AIAA-90-1662, June 1990, Seattle, WA.
- 3 S. H. Kang and J. A. Kunc. *Viscosity of High Temperature Iodine*. Physical review A, in press.
- 4 D. L. Rousseau and P. F. Williams. *Resonance Raman Scattering of Light from a Diatomic molecule*. J. Chem. Phys. Vol. 64, 9, pp 3519-37, 1975.
- 5 E. P. Muntz. *Electron Beam Fluorescence*. AGARDograph 132, 1968.
- 6 J. Tellinghuisen. *Intensity Factors for the  $I_2$  B X band system*. J. Quant Spectrosc. Radiat. Transfer. Vol. 19, pp 149-161, 1978.
- 7 S. Gerstenkorn and P. Luc. *Assignments of Several Groups of the Iodine ( $I_2$ ) Lines in the B-X System*. J. Mol. Spectrosc., 77, 310-321, 1979.
- 8 J. C. McDaniel and D. Baganoff. *Density Measurement in Compressible Flows Using Off-Resonant Laser Induced Fluorescence*. Phys. Fluid. Vol. 25, 7, July 1982.
- 9 G. W. McClelland, K. L. Saenger, J. J. Valentini. *Vibrational and Rotational Relaxation of Iodine in Seeded Supersonic Beams*. J. Phys. Chem., Vol. 83, 8, pp 947-59, 1979.
- 10 J. C. McDaniel. *Investigation of Laser-Induced Fluorescence for the Measurements of Densities in Compressible Flows*, Ph.D. thesis, Stanford University, 1982.
- 11 J. Tusa, M. Sulkes, and S. A. Rice. *Low Energy Collisional Relaxation of  $I_2$  in He: Evidence for Resonance Enhanced Vibrational Deactivation*. J. Chem. Phys. Vol. 70, 6, pp. 3136-37, 1978.
- 12 B. Hiller and R. K. Hanson. *Properties of the Iodine Molecule Relevant to Laser-Induced Fluorescence Experiments in Gas Flows*. Exp. Fluids. 10, 1-11, 1990.
- 13 W. Kiefer and H. J. Bernstein. *Vibrational-Rotational Structure in the 5145 Å Excited Anti-Stokes Resonance Raman Spectrum of Iodine Vapor*. J. Chem. Phys. Vol. 57, 7, pp. 3017-19, 1972.
- 14 W. Holzer, W. F. Murphy, and H. J. Bernstein. *Resonance Raman Effect and Resonance Fluorescence in Halogen Gases*. J. Chem. Phys., Vol. 52, 1, pp. 399-408, 1970.
- 15 R. Schilder, G. Adomeit, G. Worthberg. *Theoretical and experimental investigation of the Knudsen layer produced by intensive evaporation of iodine*. RGD 13, pp. 577-84, 1985.
- 16 H. Ashkenas and F. S. Sherman. *Structure and Utilization of Supersonic Free Jets in Low Density Wind Tunnels*. 4<sup>th</sup> International Symposium on Rarefied gas Dynamics. J. H. de Leeuw ed. Vol. 2.

Academic Press, 1966, Toronto.

- 17 S. Dushman. *Scientific Foundations of Vacuum Technique*. John Wiley & Sons, Inc. 1949
- 18 R. C. Weast. *CRC Handbook of Chemistry and Physics*. CRC Press, Inc. 1984.
- 19 G. R. Nickerson, *et al.* *Two-dimensional Kinetics (TDK) Nozzle Performance Computer Program*, NAS8-36863, Software and Engineering Associates, inc., Carson City, Nevada, 1989.
- 20 M. K. Bradley. *Nozzle Contour Development for the University of Southern California Hypersonic Iodine Wind Tunnel*. Engineer's Thesis, Univ. So. California, Jan 1992.
- 21 H. W. Schrötter and H. W. Klöckner. *Raman Scattering Cross Sections in Gases and Liquids*. Raman Spectroscopy of Gases and Liquids. Ed. A. Weber. Springer-Verlag Berlin Heidelberg. New York, 1979.
- 22 S. Gerstenkorn and P. Luc. *Atlas du Spectre d'Absorption de la Molecule d'Iode*. Editions du Centre National de la Recherche Scientifique, Paris, 1978.
- 23 . E. Rabinowitch and W. C. Wood. *Dissociation of Excited Iodine Molecules*. J. Chem. Phys. Vol.4, pp 358-362, 1936.
- 24 C. Tai and F. W. Dalby. *Nonlinear photodissociation of molecular iodine*. Canadian J. Phys. Vol.56, No. 2, pp. 183-190, 1978.
- 25 E. P. Muntz. *Partial Pressure Condensation Pump*. U. S. Patent No. 4 185 966, January 1980.
- 26 J. Brook, V. Calia, B. Hanel, E. P. Muntz, P. B. Scott and T. Deglow. *Jet Membrane Process for Aerodynamic Separation of Mixtures and Isotopes*. AIAA J. Energy. Vol. 4, No. 5, p. 199, 1980.
- 27 J. C. Sivells. *Aerodynamic Design and Calibration of the VKF 50-Inch Hypersonic Nozzle Tunnels*, EADC-TDR-62-230, 1963.
- 28 G. Dupeyrat. *Two and Three Dimensional Aspect of a Freejet Issuing from a Long Rectangular Slit*. In Rarefied Gas Dynamics, S. S. Fisher Ed., p. 812, Progress in Astronautics and aeronautics. Vol. 74, 1981.
- 29 N. Davidson. *Fundamental data obtained from Shock Tube Experiments*. Pergamon Press, 1961. p. 138.
- 30 F. W. Dalby, Gena Petty-Sil, M. H. L. Pryce and C. Tai. *Nonlinear Resonant Photoionization Spectra of Molecular Iodine*. Canadian J. Phys. Vol. 55, No. 12, pp. 1033, 1977.

## 11. Figure caption

Figure 1: Schematic of pilot scale hypersonic wind tunnel.

Figure 2: Phase diagram of iodine with the facility cycle superimposed.

Figure 3: Photograph of a free jet expansion of pure iodine vapor a) high background pressure b) low background pressure.

Figure 4: Photograph of flowfield around a cylindrical blunt body.

Figure 5: Time trace of fluorescence at an axial position of 25 orifice diameters downstream of the orifice exit plane.

Figure 6: Top view of experimental setup.

Figure 7: Photograph of iodine condensate on test section optical port.

Figure 8: Nozzle throat cross-section.

Figure 9: a) Mach number, b) Pressure, c) Temperature, d) Degree of dissociation vs. Area ratio Predictions based on finite rate chemistry.

Figure 10: Static pressure in the nozzle flow and iodine vapor pressure vs. temperature.

Figure 11: Finite rate chemistry calculation of degree of dissociation a) and temperature b) across a normal shock wave.

Figure 12: Schematic of the full scale iodine facility.

Figure 13: Pressure temperature diagram for the full scale tunnel operation cycle.

Figure 14: Cross-section of the condensation pump.

Figure 15: Raman spectrum of the first vibrational overtone of stagnant iodine contained in the test section at room temperature.

Figure 16: Absorption spectrum of the iodine molecule<sup>7</sup> around 5288 Å with present laser profile.

Figure 17: Absorption spectrum of the iodine molecule<sup>7</sup> around 5145Å with present laser profile.

Figure 18: Time trace of fluorescence with pulsed pumping at 5145Å.

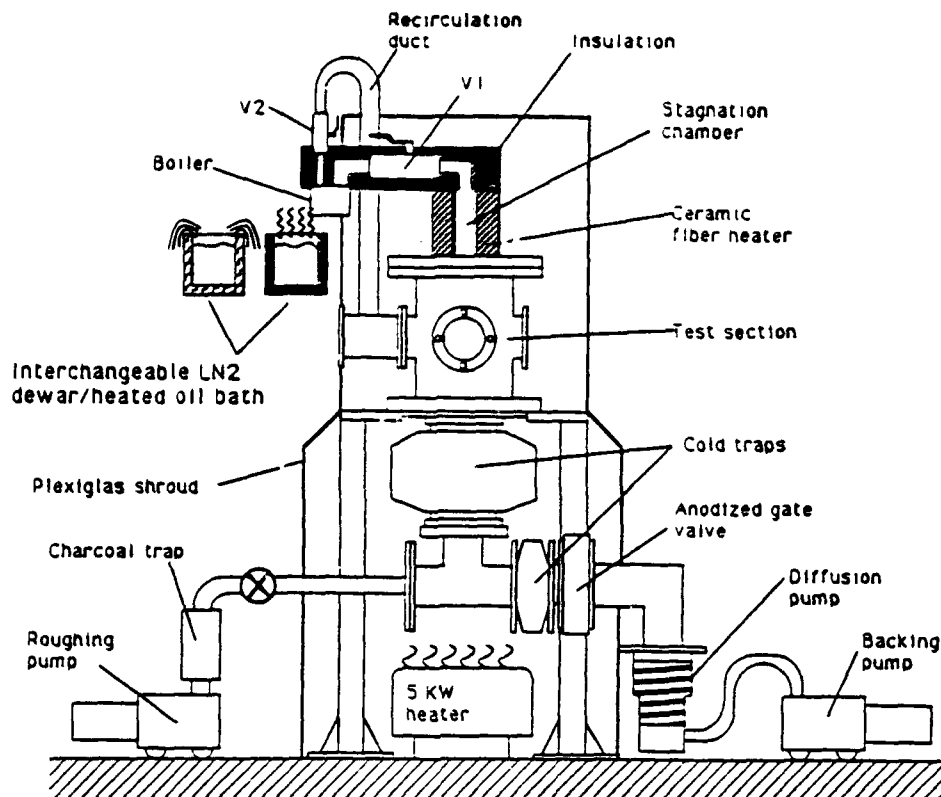


Figure 1: Schematic of pilot scale hypersonic wind tunnel.

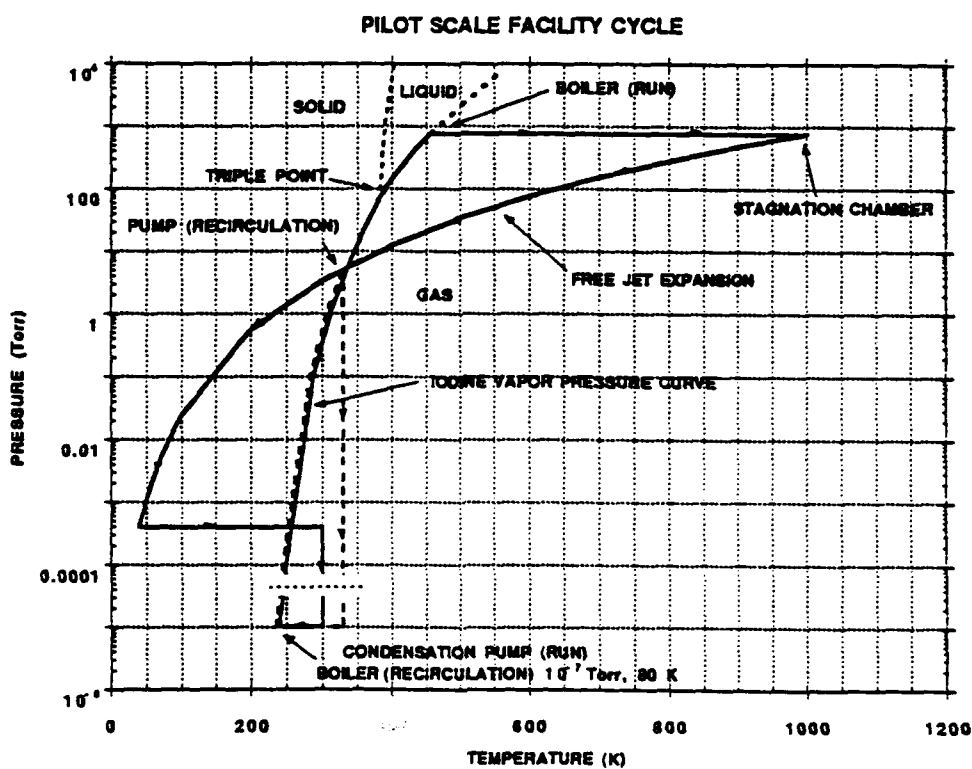
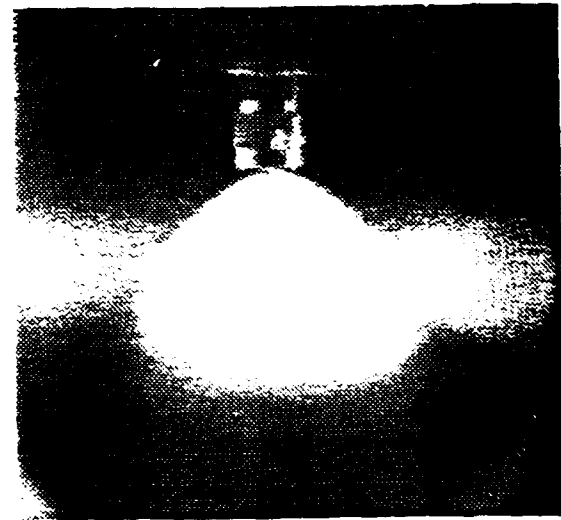


Figure 2: Phase diagram of iodine with the facility cycle superimposed.





a)



b)

Figure 3: Photographs of a free jet expansion of pure iodine vapor a) background pressure =  $10^{-4}$  Torr. b) background pressure =  $10^{-6}$  Torr.

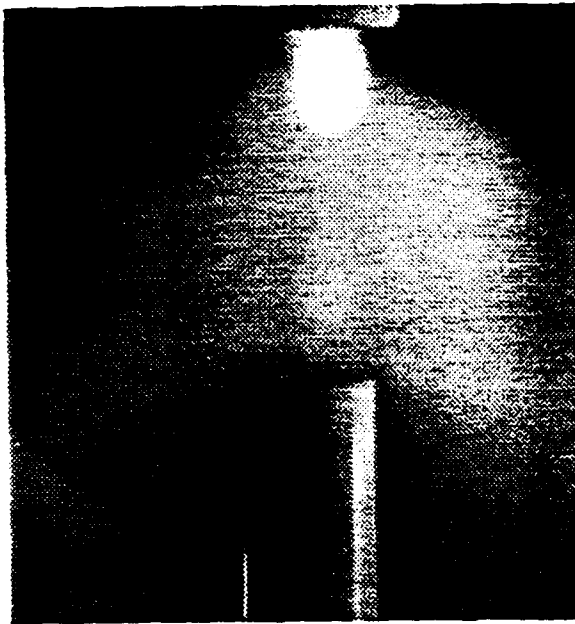
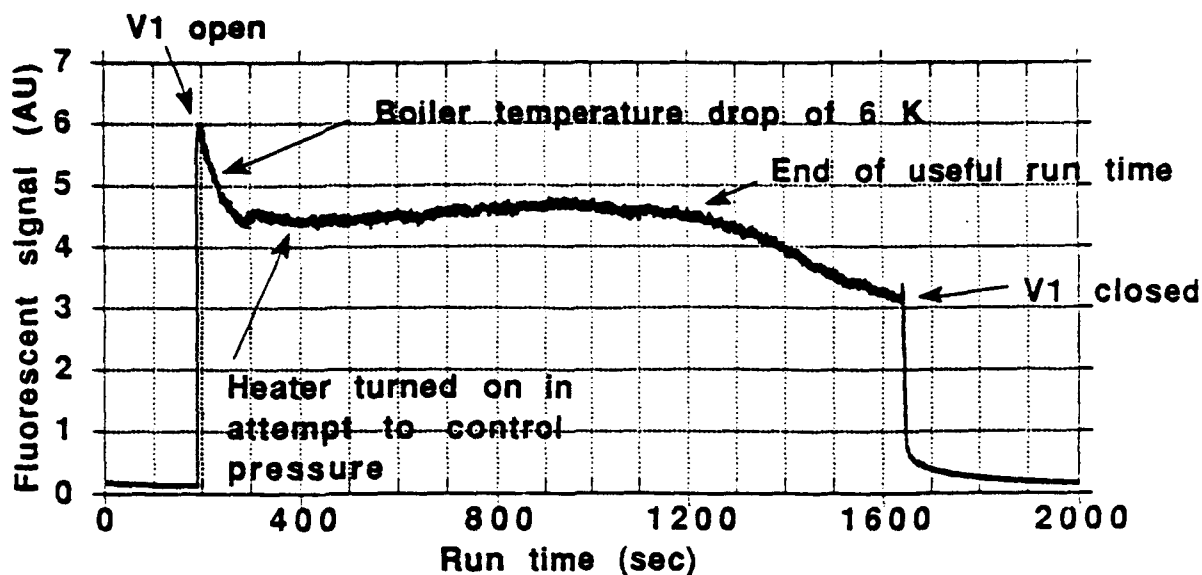


Figure 4: Photograph of flowfield around a cylindrical blunt body.



Figure 5: Photograph of flowfield around a cylindrical blunt body in test section optical port.



Run conditions:  $P_0 = 200$  Torr,  $T_0 = 700$  K, Dia = 2 mm

Figure 5: Time trace of fluorescence at an axial position of 25 orifice diameters downstream of the orifice exit plane.

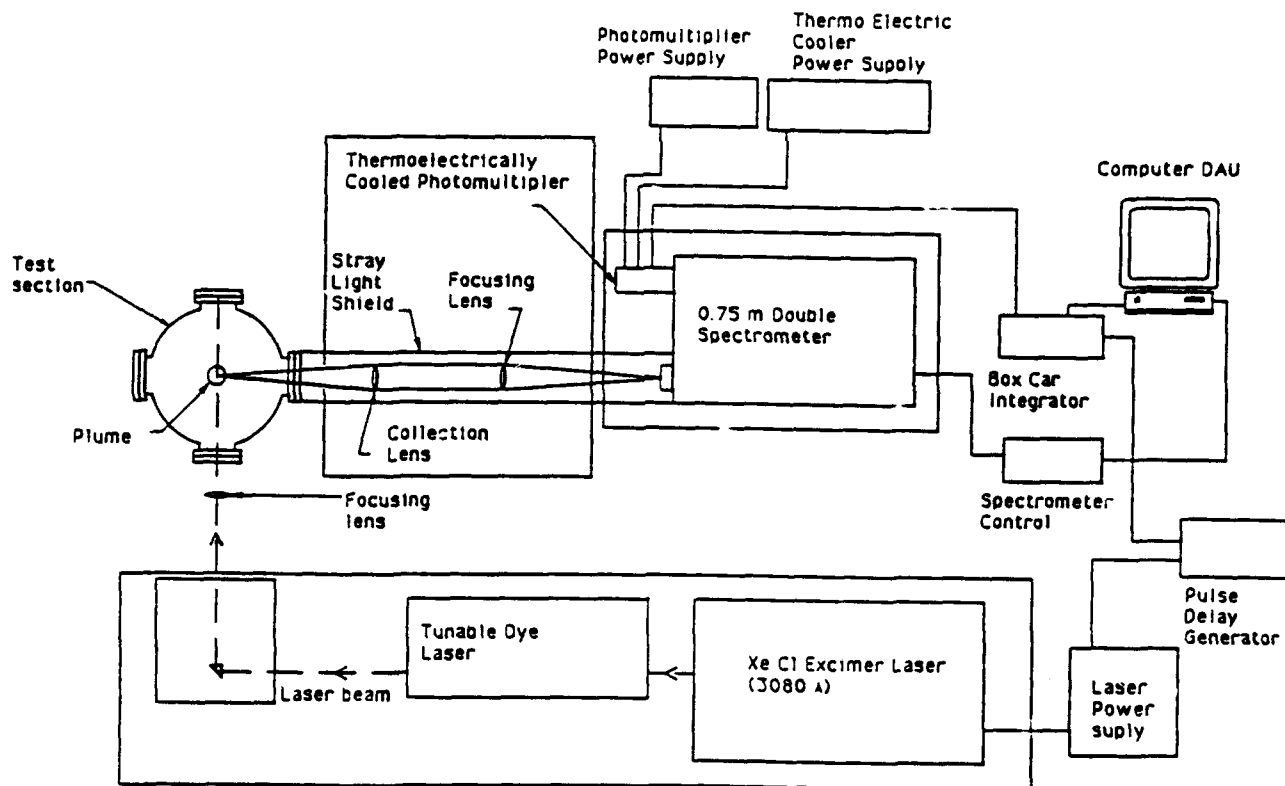


Figure 6: Top view of experimental setup.

Figure 8: Nozzle throat cross-section.

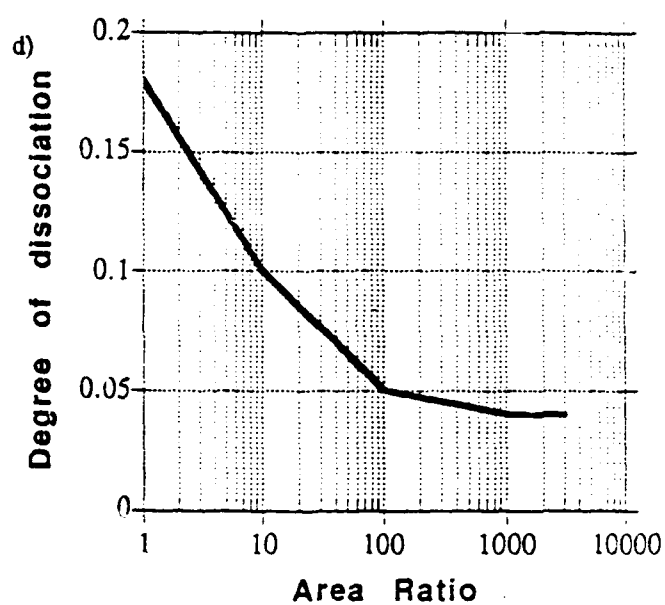
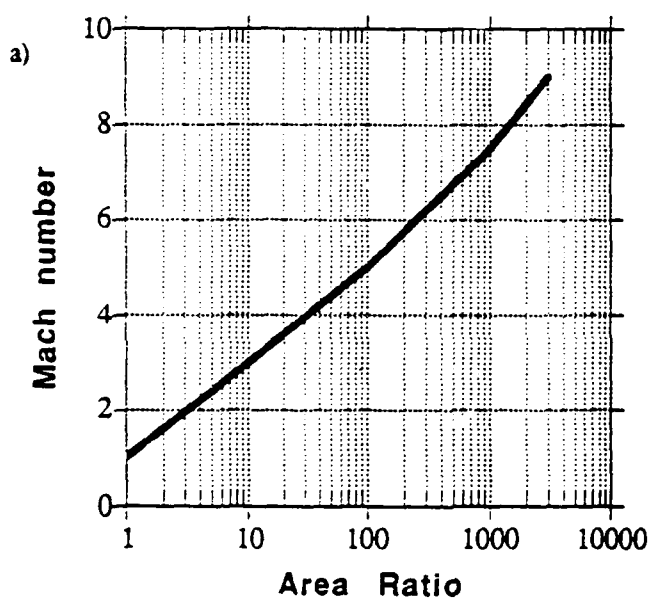
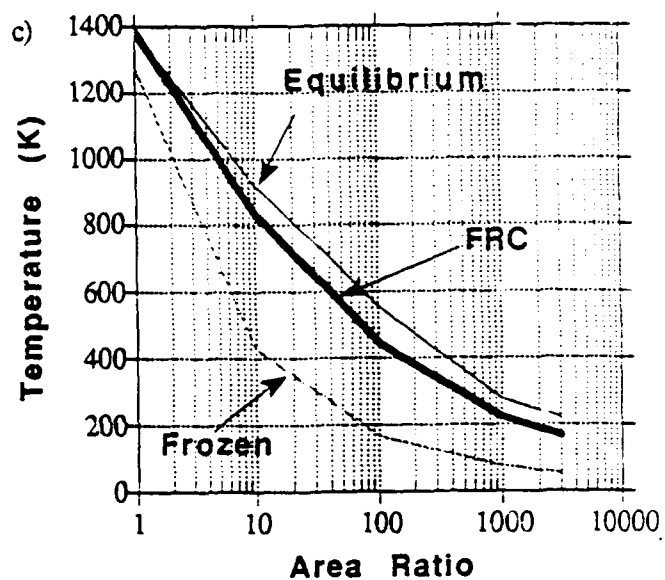
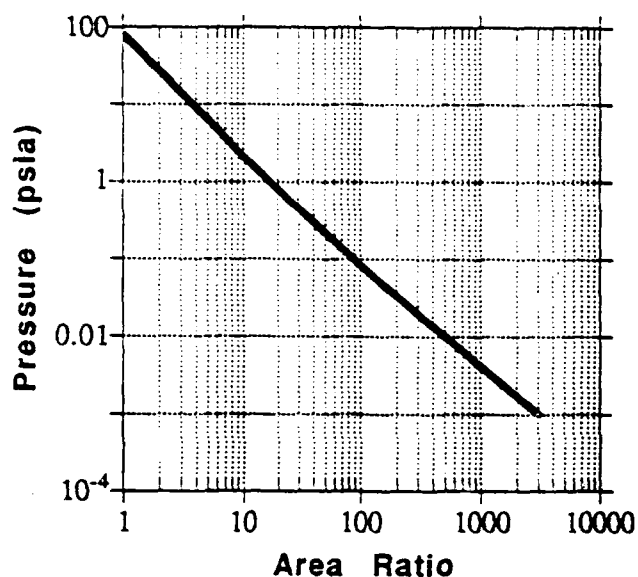
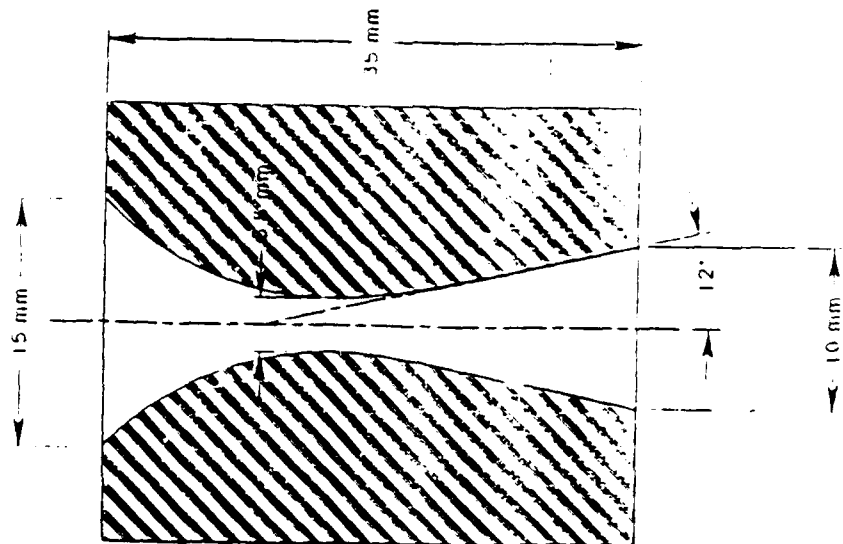
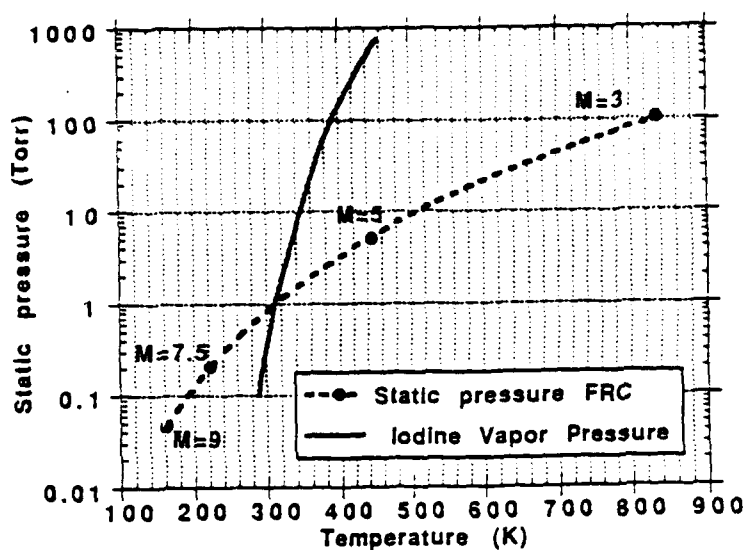


Figure 9: a) Mach number, b) Pressure, c) Temperature, d) Degree of dissociation vs. Area ratio Predictions based on finite rate chemistry.

Figure 10: Static pressure in the nozzle flow and iodine vapor pressure vs. temperature.



a)

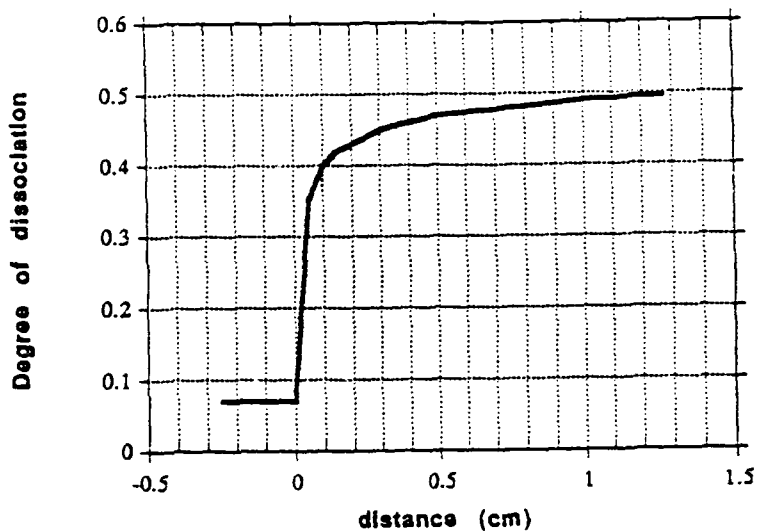
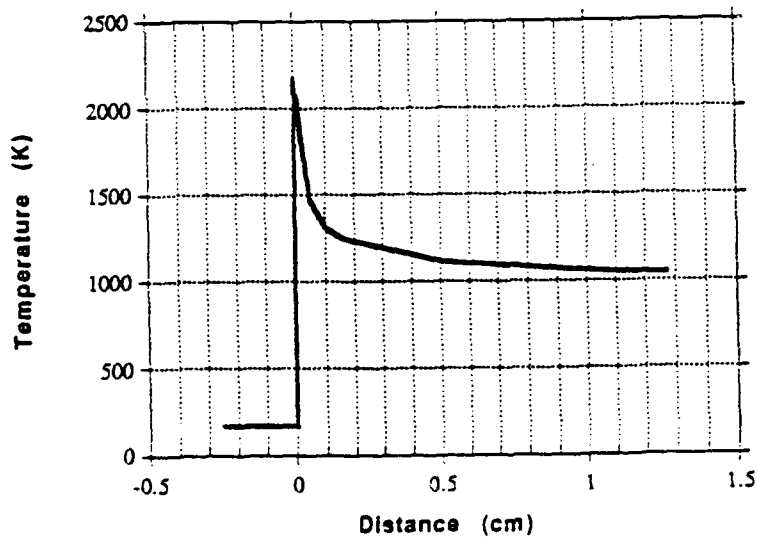


Figure 11: Finite rate chemistry calculation of degree of dissociation a) and temperature b) across a normal shock wave.

b)



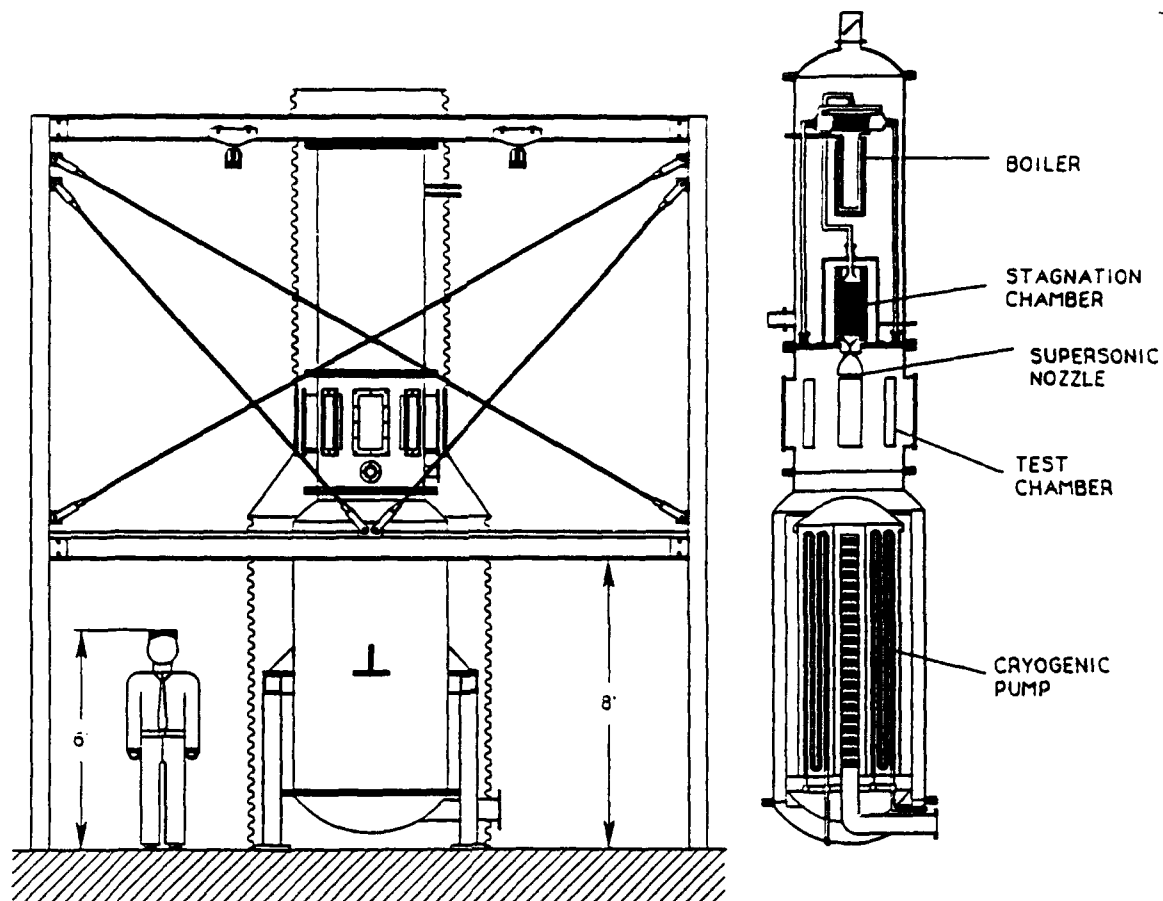


Figure 12: Schematic of the full scale iodine facility.

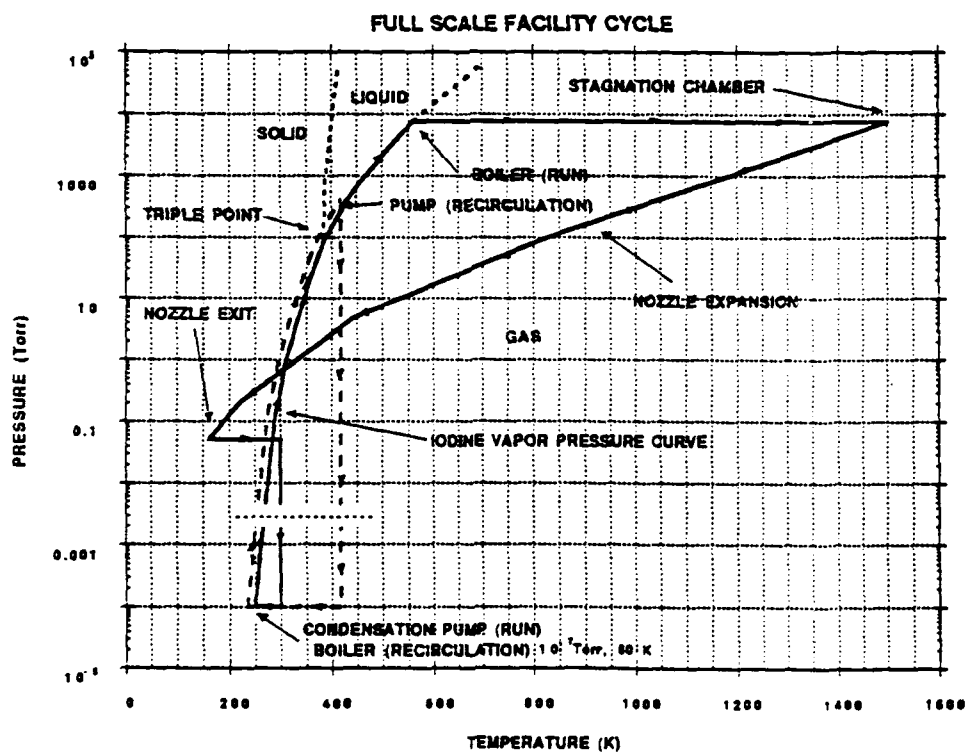


Figure 13: Pressure temperature diagram for the full scale tunnel operation cycle.

Figure 14: Cross-section of the condensation pump.

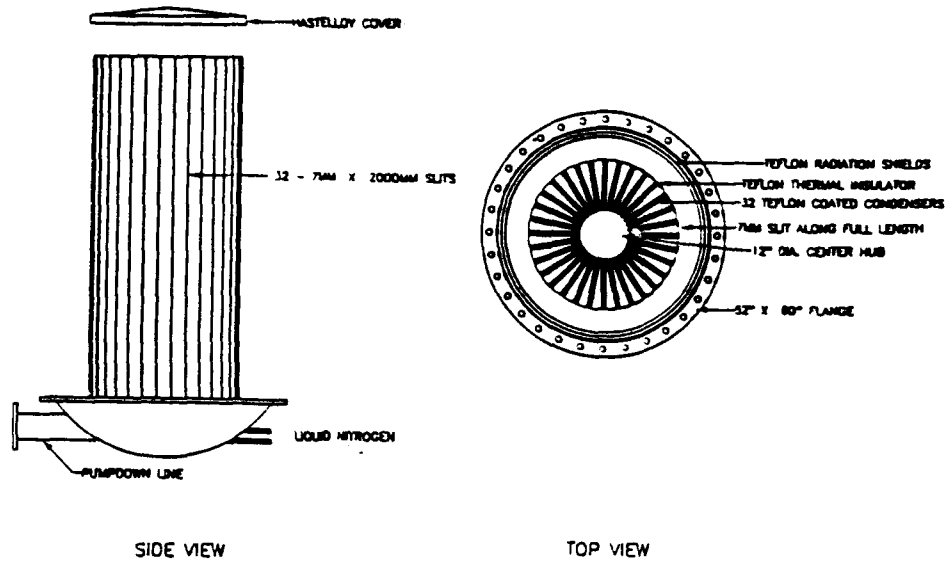


Figure 15: Raman spectrum of the fundamental vibrational overtone of stagnant iodine contained in the test section at room temperature.

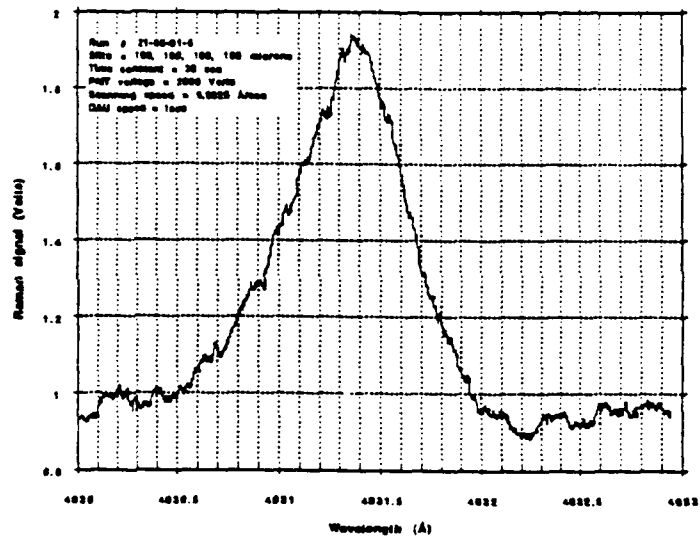
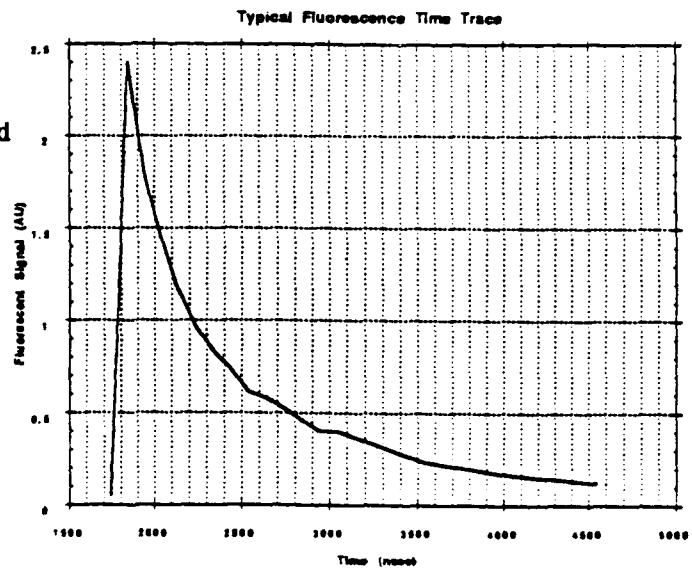


Figure 18: Time trace of fluorescence with pulsed pumping at 5145Å.



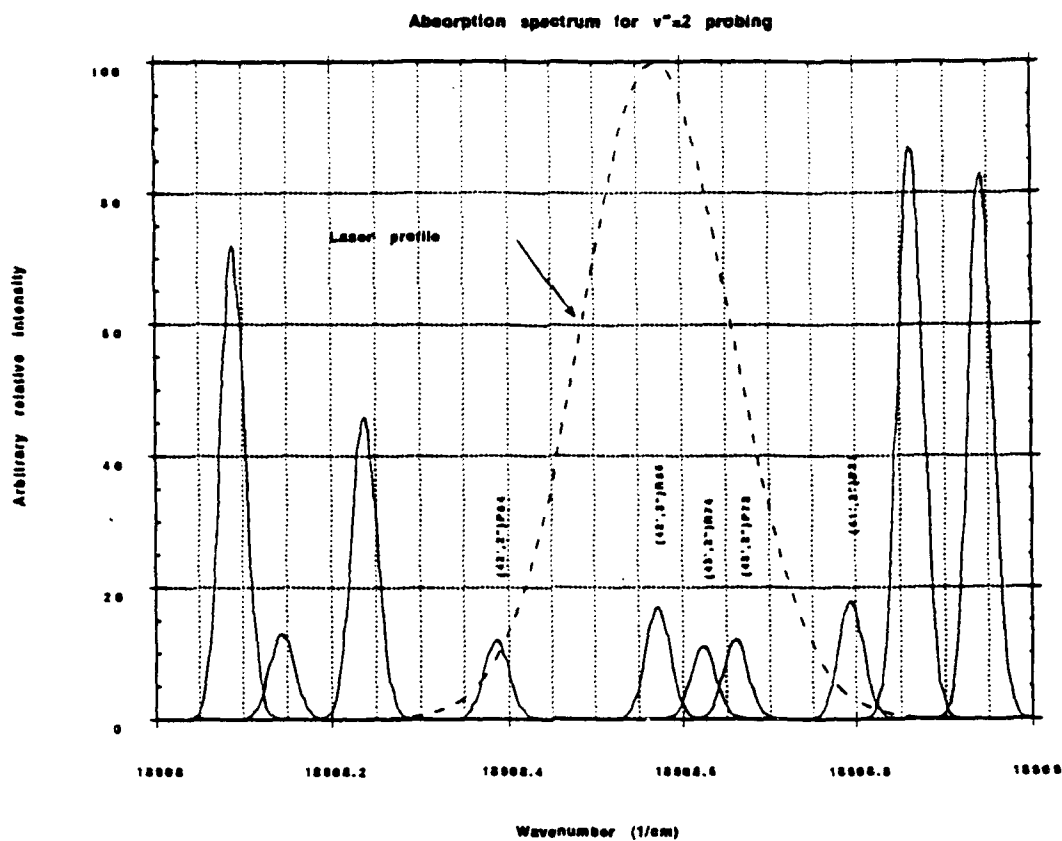


Figure 16: Absorption spectrum of the iodine molecule<sup>7</sup> around 5288 Å with present laser profile.

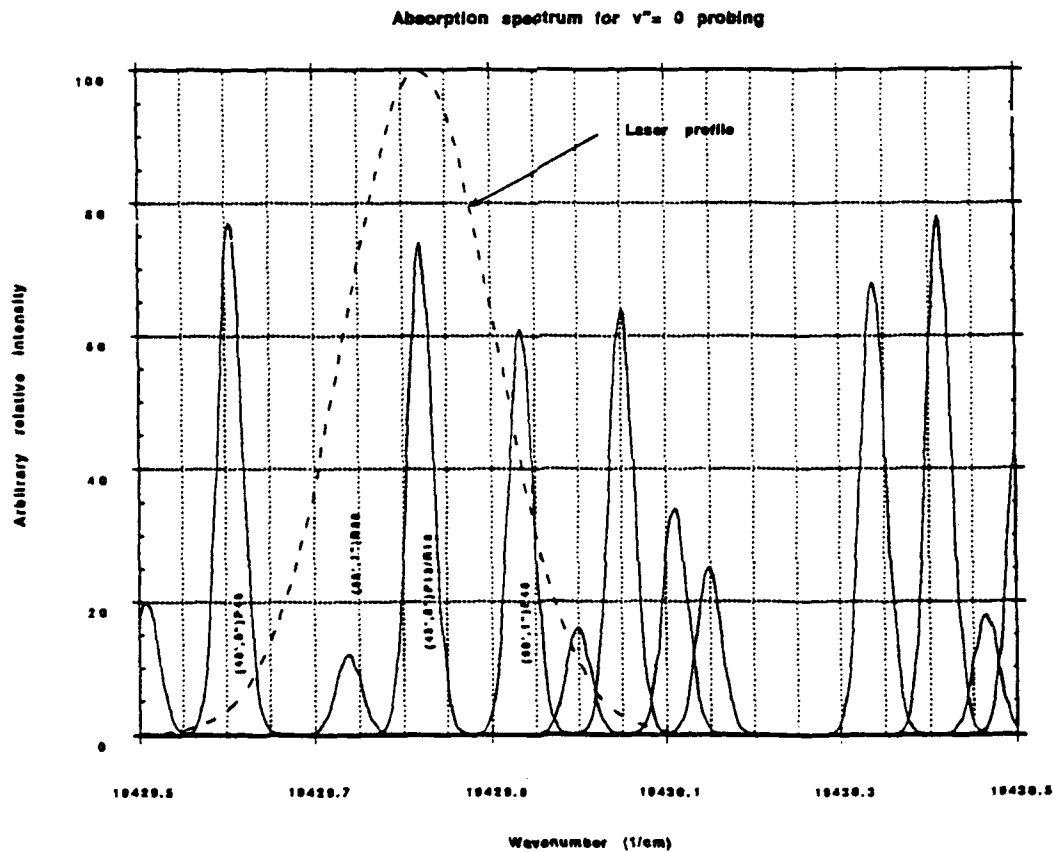


Figure 17: Absorption spectrum of the iodine molecule<sup>7</sup> around 5145 Å with present laser profile.

ATTACHMENT 3

93 11 16 050

93-28111  




Chemically Reacting, Hypersonic Flows of Iodine  
Vapor for the Study of Nonequilibrium Phenomena  
in Diatomic Gases

by

Gérald Christian Pham-Van-Diep

A Dissertation Presented to the  
FACULTY OF THE SCHOOL OF ENGINEERING  
UNIVERSITY OF SOUTHERN CALIFORNIA

In Partial Fulfillment of the  
Requirements for the Degree  
DOCTOR OF PHILOSOPHY  
(Aerospace Engineering)

August 1993

© 1993 Gerald Christian Pham-Van-Diep

## Acknowledgments

I would like to thank my faculty advisor, Professor E. P. Muntz for his guidance, support and patience throughout this research. I feel very fortunate and privileged to have worked with him not only on this project but also on our multiple side endeavors, ski trips included. I would like to express my appreciation to Professor D. A. Erwin, Professor J. A. Kunc and soon to be Dr. David Weaver for their helpful hints and encouragements. Many thanks to Thane Dewitt, Mark Trojanowski and Ken Richards for their most valuable expertise and problem-solving suggestions. I have always felt technicians are never appreciated enough. Many thanks to Stephen Vargo a very valuable work study for patiently rebuilding the great number of vacuum pumps damaged by iodine exposure and for typing in the enormous amount of Franck-Condon factors and R-centroids. Finally, I would like to express my deepest thanks to my wife Martine and my parents for their support, patience and understanding.

This investigation was supported by the United State Air Force Office of Scientific Research as part of the University Research Initiative program and in part by a NASA Training and Research grant.

*"Happiness is a straight line on a Log plot..."*

Otto Hagen

## Table of Contents

Acknowledgments.....	ii
Table of content.....	iv
Tables.....	vi
Figures.....	vii
Abstract.....	ix
<b>Chapter 1 Introduction</b>	
1.1 Background and motivations.....	1
1.2 Velocity distribution functions for low stagnation temperature shock waves.....	6
1.3 High temperature gas flow measurement.....	10
<b>Chapter 2 Choice of Iodine as a Representative Gas</b>	
2.1 Properties of the iodine molecule.....	14
2.2 Spectroscopic constants of the iodine molecule.....	15
<b>Chapter 3 Transient Laser Induced Fluorescence (TLIF)</b>	
3.1 General principle.....	19
3.2 Upper state population response to pulsed pumping.....	20
3.3 Identification and choice of transitions.....	29
3.3.1 Identification of transitions.....	29
3.3.2 Choice of transitions.....	29
3.4 Prediction LIF spectral intensities.....	36
3.4.1 Einstein <i>A</i> and <i>B</i> coefficients.....	37
3.4.2 Transition line strength.....	38
3.4.3 Alteration of rotational intensities due to nuclear statistics.....	39
3.4.4 Population in a rovibrational level.....	40
3.4.5 Absorption of molecules to the <i>B</i> state.....	40
3.4.6 Emission intensity.....	42
3.5 Diagnostic considerations.....	47
3.5.1 Laser beam attenuation.....	47
3.5.2 Laser beam .....	50
3.5.3 Lineshape broadening.....	52
3.5.4 Predissociation.....	54
3.5.5 Quenching.....	57
<b>Chapter 4 The Pilot Scale Wind Tunnel</b>	
4.1 Introduction.....	60

4.2 The boiler and stagnation pressure measurement.....	62
4.3 The stagnation chamber.....	65
4.4 Pumping of iodine and incondensibles.....	69
4.5 Recycling.....	69
4.6 Material considerations.....	71
4.7 Safety considerations.....	73
4.8 Free jet expansion of high temperature iodine.....	73
4.8.1 Properties of free jet expansions.....	73
4.8.2 Nonequilibrium effects.....	78
4.8.3 Effects of clusters.....	80
<b>Chapter 5 Experiment</b> .....	
5.1 Introduction.....	84
5.2 Experimental set-up.....	84
5.3 Experimental tasks.....	87
5.3.1 Test Flows.....	87
5.3.2 Spectral regions probed and data analysis procedure.....	87
5.3.3 Laser pulse shape determination.....	91
5.3.4 Linear dependence of fluorescent signal.....	92
5.3.5 Laser linewidth monitoring.....	93
5.4 Experimental results.....	93
5.4.1 Rotational population distributions.....	93
5.4.2 Vibrational population distributions.....	98
5.4.3 Error estimates.....	108
5.5 Discussion and recommendations.....	109
5.5.1 Rotational data.....	109
5.5.2 Vibrational data.....	110
5.5.3 Recommendations for future work.....	112
<b>Chapter 6 Conclusions</b> .....	116
<b>Appendix A Dunham Expansion Coefficients for the Iodine Molecule (<math>V'' = 0-19</math>, <math>V' = 0-80</math>)</b> .....	119
<b>Appendix B Rates and absorption coefficients associated with the transitions studied in this work.<sup>12</sup></b> .....	122
<b>Bibliography</b> .....	124

## Tables

Table 1: Thermal equilibrium properties of iodine, nitrogen and oxygen for a degree of dissociation of 50% and a pressure of 200 Torr.

Table 2: Spectroscopic constants of the iodine molecule (Hertzberg<sup>30</sup>).

Table 3: Iodine properties at 1,000 K.

Table 4: Alloys used in the injector assembly and their compositions.

Table 5: Flow conditions used in this study.

Table 6: Spectral regions and quantum levels probed.

Table 7: Transitions in the 6120 Å range and corresponding transition probabilities.

Table 8: Transitions in the 5683 Å range and corresponding transition probabilities.

Table 9: Transitions in the 5208 Å range and corresponding transition probabilities.

## Figures

Figure 1: Parallel velocity distribution functions for a normal shock in helium at  $M = 25$  and  $\tilde{n} = 0.285$ .

Figure 2: Inverse maximum shock thickness vs. Mach number for normal shocks in argon (Shock tube experiments).

Figure 3: Schematic of the intermolecular potentials of  $I_2$  involved in the pulsed LIF process.

Figure 4: Two level system used to analyze population responses under pulsed excitation.

Figure 5: Normalized upper level populations and laser pulse time history for several transitions.

Figure 6: Time response of the population  $N_2$  of the  $B$  state under a Gaussian pulse shape laser pumping for the transition (39, 0) R55 and laser energies per pulse of  $7 \cdot 10^{-7}$ ,  $7 \cdot 10^{-6}$  and  $7 \cdot 10^{-5}$  J.

Figure 7: Time response of the sum  $N_1 + N_2$  under a Gaussian pulse shape laser pumping for the transition (39, 0) R55 and laser energies per pulse of  $7 \cdot 10^{-7}$ ,  $7 \cdot 10^{-6}$  and  $7 \cdot 10^{-5}$  J.

Figure 8: Energy of vibrational levels of the  $X$  state ( $J = 0$ ). Difference between standard method and Gerstenkorn's prediction.

Figure 9: Energy of vibrational levels of the  $B$  state ( $J = 0$ ). Difference between standard method and Gerstenkorn's prediction.

Figure 10: ( $B \leftrightarrow X$ ) transitions for  $V'' = 0$  to 5,  $V' = 0$  to 59 and  $J'' = 0$  to 159 between 16200 and 16600  $\text{cm}^{-1}$ .

Figure 11: ( $B \leftrightarrow X$ ) transitions for  $V'' = 0$  to 5,  $V' = 0$  to 59 and  $J'' = 0$  to 159 between 16200 and 16600  $\text{cm}^{-1}$ . The transitions which cannot be resolved with a laser linewidth of 0.05  $\text{cm}^{-1}$  have been filtered.

Figure 12: Franck-Condon factors for the transitions of the ( $B \leftrightarrow X$ ) band. ( $0 \leq V'' \leq 19$ ,  $0 \leq V' \leq 59$ ,  $J'' = 0$ )

Figure 13: Laser pumping wavelength for the transitions of the ( $B \leftrightarrow X$ ) band. ( $0 \leq V'' \leq 19$ ,  $0 \leq V' \leq 59$ ,  $J'' = 0$ )

Figure 14: Fabry-Perot trace taken from the laser linewidth narrowed with an intra-cavity etalon.

Figure 15: Predicted and measured emission spectra for a spectral range of 60 Å. (Predicted spectrum calculated with a laser FWHM = 0.1 Å).

Figure 16: Predicted and measured emission spectra for a spectral range of 1.6 Å. (Predicted spectrum calculated with a laser FWHM = 0.01 Å).

Figure 17: Radial density profile and laser intensity attenuation for the (39, 0) R55 and (45, 1) P74 transition.

Figure 18: Schematic of the pilot scale hypersonic wind tunnel operating on iodine.

Figure 19: Pressure-Temperature diagram for the pilot scale wind tunnel.

Figure 20: Iodine vapor pressure gauge calibration curves for different ambient temperatures.

Figure 21: Degree of dissociation in the stagnation chamber versus equilibrium temperature for stagnation pressures of 30, 100 and 760 Torr.

Figure 22: Free jet nomenclature and laser sheet configuration.

Figure 23: Mach number, normalized number density, temperature and pressure on centerline of free jet expansion for  $\gamma = 9/7$  and  $\gamma = 7/5$ .

Figure 24: Viscosity of iodine vs. Temperature.

Figure 25: Vapor pressure curve for iodine<sup>62</sup> compared to isentropes for  $\gamma = 9/7$  and  $\gamma = 7/5$ .

Figure 26: TLIF scattering experiment.

Figure 27: Schematic of free jet assembly, blunt body and laser sheet.

Figure 28: Example typical Boltzmann plot.

Figure 29: Measured and best fitted laser pulse shape.

Figure 30: Fluorescence signal dependence on laser power.

Figure 31: Boltzmann plots for  $z =$  a) 5, b) 7, c) 9, d) 10, e) 20, f) 24, g) 25, h) 26 mm.

Figure 32: Rotational temperature along free jet centerline for  $T_0 = 773$  K,  $P_0 = 30$  Torr and 100 Torr.

Figure 33: Rotational temperature along free jet centerline for  $T_0 = 1000$  K,  $P_0 = 30$  Torr and 100 Torr.

Figure 34: Rotational temperatures obtained by probing transitions requiring laser pumping at 5683 Å compared to rotational temperatures obtained by probing at 5208 Å.

Figure 35: Vibrational population distribution  $T_0 = 1000$  K,  $P_0 = 100$  Torr for  $z =$  a) 5, b) 10, c) 15, d) 20, e) 24 mm.

Figure 36: Vibrational population distribution  $T_0 = 1000$  K,  $P_0 = 30$  Torr for  $z =$  a) 5, b) 10, c) 15, d) 20, e) 24 mm.

Figure 37: Vibrational population distribution  $T_0 = 773$  K,  $P_0 = 100$  Torr for  $z =$  a) 5, b) 10, c) 15, d) 20, e) 24 mm.

Figure 38: Vibrational population distribution  $T_0 = 773$  K,  $P_0 = 30$  Torr for  $z =$  a) 5, b) 10, c) 15, d) 20, e) 24 mm.

Figure 39: Vibrational temperature profiles for  $T_0 = 1000$  K,  $P_0 = 100$  and 30 Torr.

Figure 40: Vibrational temperature profiles for  $T_0 = 773$  K,  $P_0 = 100$  and 30 Torr.



## Abstract

Nonequilibrium flows are important phenomena in many technological and natural settings. In this study, a representative gas is used to validate models and computer simulations describing nonequilibrium flows of diatomic molecules. One way to study the physics of such flows is to generate a chemically reacting hypersonic flow of pure iodine vapor and to probe the internal energy population distributions within this flow. For the purposes of this study the properties of a free jet expansion impinging on a disk were examined. This thesis is mainly experimental and is composed of two parts: 1) Development of a pilot scale hypersonic flow facility operating with pure iodine as a working gas. The wind tunnel has run times of approximately 1/2 hour and operates on a semi-continuous basis. The stagnation conditions are such that significant internal energy excitation can be achieved in the flowfields generated by the facility. Issues regarding the design of the wind tunnel, corrosion resistance and appropriate operating procedures are discussed. 2) Development of a diagnostic technique to probe the internal energy state population distributions within the nonequilibrium flows. Transient Laser Induced Fluorescence (TLIF) was selected for detailed study. Both rotational and vibrational distribution functions have been measured at different positions along the free jet expansion's center axis for different stagnation pressure and temperature conditions.

# Chapter 1

## Introduction

### 1.1 Background and motivations

Highly nonequilibrium, chemically reacting, radiating gas flows are observed in numerous natural phenomena as well as technological settings. Of particular interest to the aerospace engineering community are the problems associated with the significant thermal and chemical nonequilibrium effects encountered in the flow over a large portion of the NASP flight corridor<sup>1,2</sup> and more generally the severe nonequilibrium chemistry which occurs in the flowfields of a spacecraft entering Earth's or other planets' atmosphere. Also of interest to the engineering community are nonequilibrium phenomena encountered in material processing schemes such as the growth of films by cluster or plasma assisted deposition, the kinetics of gases within micromechanisms, plasma containment flowfields encountered in rapid energy release fusion schemes, chemical rocket and electric propulsion engine exhaust plumes, plasma rail guns and high power gas discharges. In nature, highly nonequilibrium reacting flows occur in stellar coronas, flowfields around comets and meteorites, and other astrophysical plasmas.

The development of Navier-Stokes and Direct Simulation Monte-Carlo (DSMC)<sup>3</sup> computational techniques for the prediction of nonequilibrium flows, has stimulated efforts to establish their validity for a wide range of flow conditions. Kinetic models for nonequilibrium flows are usually extremely complex because the number of atomic and molecular processes occurring in the gas is significant, and transition probabilities are either inaccurate or unknown. A criti-

cal need to validate both analytical and computational prediction techniques is presently being felt because of the increasing interest and activity in phenomena involving nonequilibrium gas flows.

Detailed agreement is needed between laboratory scale experiments and theory or computational techniques before predictions can be considered sufficiently reliable to expand their usefulness in applications to flight or industrial scales. The prediction of low-energy, viscous, turbulent flowfields has traditionally been approached with the use of ideal gas computations calibrated and validated by sub-scale experiments. Flight scale performances can then be determined by extrapolation using scaling laws based on Mach and Reynolds number. Similar scaling for nonequilibrium reacting phenomena is extremely difficult except for very simple cases. Any extrapolation from laboratory models to flight scales must be made on the basis of sufficient knowledge of the detailed atomic and molecular characteristics such as internal energy distributions and transfers that are crucial for the description of nonequilibrium flows. Validation on a laboratory scale of prediction schemes based on basic physical inputs such as transition probabilities and intermolecular potentials, will permit application of these techniques for predicting flight scale flow properties. Significant progress in the fields of transatmospheric flight, processing of advanced materials and the fundamental physics of nonequilibrium flow phenomena may be expected if validations of prediction schemes become available.

The work described here is primarily experimental and is aimed at probing the internal energy state population distributions in a far from equilibrium chemically reacting gas flow. To achieve detailed probing of the energy states, a

flow facility with relatively long flow times is required. The many drawbacks encountered in transient facilities such as shock tubes and tunnels may be avoided by experimenting in a wind tunnel; for example, flow property measurements requiring relatively long integration times such as the measure of molecular velocity distribution functions with the electron beam fluorescence technique investigated by Muntz<sup>4</sup> is difficult to perform in anything but a continuous flow facility. More generally, fluorescence or light scattering measurements requiring scanning across a certain frequency spectrum, may it be performed with a spectrometer or an etalon, requires that the observed flow properties remain uniform for time intervals of the order of minutes. Some steady state quantities of nonequilibrium flows such as shock wave density and temperature profiles are more conveniently measured in wind tunnels because the boundary conditions of the shock is easily controlled in such experiments, while the measurement of the same quantities in shock tubes is often times affected by the non-steady nature of the experiment.<sup>5</sup> Therefore, in view of the unavoidable disadvantages encountered in transient facilities, a semi-continuous prototype hypersonic wind tunnel has been developed to operate on iodine. This project was intended to serve as proof of the concept that such a facility can indeed operate with reliability as well as provide the basis for the design of a larger scale wind tunnel for the study of nonequilibrium reacting gas flows. The study described here is composed of two parts:

- 1) Design of a pilot scale hypersonic wind tunnel including investigation of the appropriate materials as well as manufacturing procedures, and importantly a study of optimal operating procedures. The pilot scale facility has been used as the foundation for the design of a larger scale wind tunnel.

2) Development and application of a diagnostic technique to probe the non-equilibrium flows obtained in the pilot scale facility. Both vibrational and rotational relative population distributions are measured by means of pulsed laser induced fluorescence.

A previous study performed by Kunc *et al.*<sup>5</sup> has established that molecular iodine ( $I_2$ ) can be conveniently used as a working gas to achieve significant rotational and vibrational excitation as well as dissociation, by heating the gas to temperatures easily achieved in a laboratory. The relatively low temperatures at which significant internal modes of the iodine molecule may be excited and the desirable long flow times are the reasons for the use of a wind tunnel operating with iodine as a working gas and in a semi-continuous regime, allowing for run times of approximately 30 minutes. The iodine molecule has rotational and vibrational states which are relatively easy to populate by heating the gas to temperatures of the order of 1000 K.<sup>6</sup> Because of this, the iodine molecule has been the object of numerous and extensive studies aimed at analyzing its spectral properties under various temperature and pressure conditions.<sup>7-12</sup> In these studies, pure iodine contained in a static cell was probed with either laser induced fluorescence or Raman scattering techniques. More recent investigations<sup>13,14</sup> have examined rotational and vibrational energy transfers in supersonic flows of carrier gases seeded with iodine. Iodine as a seed in gas flows is a widely used technique; it allows measurement of the temperature and density of a carrier gas (usually nitrogen) by laser induced fluorescence<sup>15</sup> provided the energy exchange between the carrier gas and the seed is efficient and that the densities are low enough so that quenching effects are negligible. Research on the energy level populations of chemically reacting flows of pure iodine has to our knowledge never been performed, although there are sev-

eral measurements of velocity distribution functions performed on flows of evaporating iodine,<sup>16</sup> and more recently, a comprehensive study of vibrational energy distributions of iodine molecules within iodine chemical laser injectors has been conducted.<sup>21</sup>

The convenient spectral properties of iodine in principle allow very accurate and detailed measurements of the energy state populations of the excited iodine gas. In the context of this study, probing by means of Transient Laser Induced Fluorescence (TLIF) sometimes called pulsed discrete resonance Raman scattering,<sup>10</sup> is investigated; in particular, this study focuses on measuring relative rotational and vibrational population distributions within the flowfield of a free jet expansion of iodine vapor impinging on a disk. This particular experimental case enables the study of both the expansion and compression regions of the flowfield.

The corrosive and toxic nature of iodine at the typical temperatures encountered in the flow system studied here is one of the major parameters driving the design of the flow facility and presents several technological challenges; its impact on the materials used in the wind tunnel components, particular manufacturing principles, safety precautions and operating procedures were investigated in this study.

Major improvements are expected in computing memory and speed within the next decade, for this reason, a prediction technique such as the Direct Simulation Monte Carlo method (DSMC)<sup>3</sup> which is based on a particulate approach for the description of nonequilibrium flows in rarefied regimes looks very promising. The present treatment of chemistry and inelastic collisions by the DSMC technique assumes small departures from thermodynamic equilibrium,<sup>17</sup>

this assumption may be valid for the rotational energy of the simulated molecules but is certainly unrealistic for vibrational and electronic excitation. In the present work, we investigate the relaxation of both rotational and vibrational degrees of freedom in a nonequilibrium flow of iodine. The initial information acquired in the investigation will be the basis for more extensive studies. These will not only help validate or improve some existing prediction techniques, but also enable determination of the prevailing kinetic processes as well as how much microkinetic detail must be included in the DSMC and Navier-Stokes simulation techniques to predict macroscopic and microscopic nonequilibrium flow properties with arbitrary accuracy. A similar approach has been adopted in the past for monatomic gases and has been the subject of several papers.<sup>18-22</sup> The validation procedure applied to the  $I_2$  molecule may in principle be applied to the  $O_2$  and  $N_2$  molecules which constitute the bulk of the species in the Earth's upper atmosphere. The present work will contribute to the larger effort taking place in the Aerospace Engineering department of USC aimed at developing and validating prediction techniques for highly nonequilibrium reacting flows based on fundamental physical inputs such as interatomic potentials and transition probabilities.

### **1.2 Velocity distribution functions for low stagnation temperature shock waves**

The approach proposed in this work has been successfully used in previous studies for the validation of prediction techniques describing the properties of normal shock waves in monatomic gases.<sup>18-22</sup> In these studies, the validation was based on a detailed comparison of predicted and measured velocity distribution functions. The predictions were performed by DSMC method and compared to velocity distribution functions measured at various positions within normal shock waves of

different strengths.

Molecular velocity distribution functions were measured using the Electron Beam Fluorescence (EBF) technique<sup>4</sup> across normal shock waves in flows of argon and helium for Mach numbers ranging from 1.5 to about 25.<sup>23,24</sup> The measurement of molecular motion with the EBF technique consists of spectrally resolving with a Fabry-Perot etalon or a spectrometer the intensity profiles of the predominantly Doppler-broadened emission lines excited by an electron beam with a diameter of  $\sim 1$  mm, an energy of 20 KeV and an intensity of approximately 10 mA. In typical continuous steady-state EBF experiments, the electron density in the probed volume is small enough that Stark broadening of the profiles may be neglected, however the combination of instrument and lifetime broadening is usually more of the order of the Doppler broadening and thus, cannot be ignored. The spectral profiles obtained by such a technique can be transformed from wavelength or frequency space to velocity space using the Doppler relation. The resulting profiles are actually simple moments of the velocity distribution functions because the excitation by the electrons is broad-band and the velocity is resolved in the direction of the optical axis of the detection system so that the molecular motion in the direction normal to the observation axis is not seen. Figure 1 shows the velocity distribution function measured with the EBF technique in the direction parallel to the flow. The distribution function was measured across a normal shock wave in helium where the freestream Mach number and static temperature were 25 and 1.5 K respectively. The experiment generating the shock wave was performed in a low density wind tunnel and has been described in a previous publication.<sup>18</sup> The particular position within the shock, at which distribution functions are recorded may be expressed in terms of the normalized number density  $\bar{n}$  across



the shock defined as  $\bar{n} = (n - n_1)/(n_2 - n_1)$ , where the subscripts 1 and 2 represent the freestream and downstream conditions respectively.

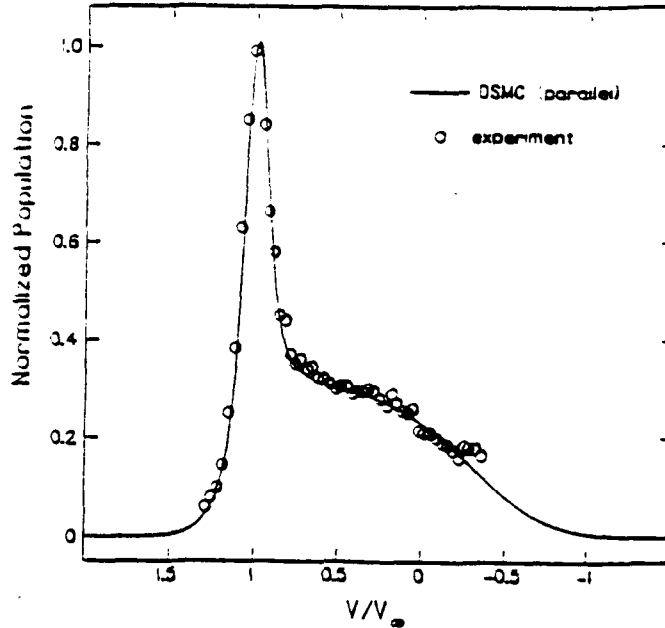


Figure 1: Parallel velocity distribution functions for a normal shock wave in helium at  $M = 25$  and  $\bar{n} = 0.285$ .

The distribution function shown in Figure 1 was taken at  $\bar{n} = 0.285$  and were peak normalized. Of interest in this figure is the bimodal form of the distribution function where an equilibrium upstream distribution “blends” with a downstream equilibrium distribution function shifted by the change of flow velocity across the shock. This bimodal character of the distribution functions is typical of nonequilibrium flows and has, to our knowledge never been directly observed in any other study. In the experiment reported here, the combination of instrument and lifetime broadening was small and equivalent to approximately 2 K. The corresponding instrument profile was convolved with the predicted velocity distribution profiles

before a legitimate comparison to the experimental data could be made. The agreement between experiment and prediction is excellent, in particular, the DSMC method seems to be very good at predicting the population of scattered molecules with velocities intermediate between those of the upstream and those of the downstream equilibrium distributions.

When the DSMC technique was originally developed,<sup>3</sup> it treated binary collisions between simulated molecules as variable hard sphere scattering (VHS) from inverse power potentials whose parameters were determined so that experimental viscosities could be reproduced at least for the temperature range encountered in the shock. The DSMC calculations mentioned here are based on differential scattering from the Maitland-Smith (Aziz)<sup>26</sup> intermolecular potential for the helium atom whose distance parameter and well depth are 2.976 Å and 10.9 K respectively. The cut-off angle below which a molecular interaction was not taken into account was chosen as 0.1 rad. The value of this cut-off angle was shown to have some minor significance in the prediction of distribution functions.<sup>27</sup> Although the differential scattering technique described here is computationally less efficient than the VHS scattering technique, it presents the advantage of being more realistic both in terms of the simulated molecules and the mimicked molecular interactions. Moreover, it was shown in a previous publication<sup>19</sup> that the microscopic properties of shock waves are more accurately predicted with differential scattering from the Maitland-Smith potential than with any other collision simulation schemes currently implemented in the DSMC technique.

In summary, experiments enabling the probing of microscopic properties within nonequilibrium flows such as velocity distributions functions were suc-

cessfully performed in low density wind tunnels.<sup>23,24</sup> The resulting experimental data were used by a number of studies<sup>18,20</sup> as a benchmark to validate a modified version of the DSMC (VHS) technique for the prediction of microscopic properties within normal shock waves in monatomic gases. These validations, however, are only applicable to monatomic gas flows at relatively low temperatures; for the case of helium at Mach 25 and argon at Mach 7 the upstream static temperature was 1.5 K and 16 K respectively, and in both cases the stagnation temperature did not exceed 300 K. In view of the previous success measuring and validating microscopic properties of flows out of equilibrium, an attempt to extend the same approach to higher temperature diatomic gases seems a logical following step.

### **1.3 High temperature gas flow measurements**

High temperature, nonequilibrium gas flow diagnostics have traditionally been made in shock tube and tunnel experiments where stagnation temperatures up to several thousand degrees K may be reached. Electron beam fluorescence,<sup>4</sup> laser induced fluorescence as well as Raman and Rayleigh scattering techniques have been used to diagnose macroscopic properties of flows generated in shock tubes. Extensive measurements of macroscopic properties such as shock wave thicknesses have been the object of numerous studies, the culmination of which may be represented by density measurements made with the electron beam attenuation technique by Alsmeyer.<sup>5</sup> His measurements of inverse maximum slope thicknesses of shock waves in argon for Mach numbers ranging from 1.75 to about 11 are shown in Figure 2. Maximum slope shock thicknesses have traditionally been used to characterize the size of shock waves in rarefied conditions, they are often times normalized by the Chapman-Enskog freestream mean free path defined as

$$\lambda_1 = \frac{16}{5} \sqrt{\frac{5}{6\pi}} \frac{\eta_1}{\rho_1 a_1} \quad (1)$$

where  $\eta_1$ ,  $\rho_1$  and  $a_1$  are the freestream viscosity, density and speed of sound respectively. Also shown in Figure 2 are predictions using the DSMC technique based on differential scattering from the Maitland-Smith (Aziz)<sup>26</sup> potential for argon whose well depth and distance parameters are 141.55 K and 3.756 Å respectively. As may be noticed, shock thickness predictions are relatively accurate for Mach numbers below about 5, while an increasing discrepancy between the predictions and the experimental data may be observed for Mach numbers above 5.

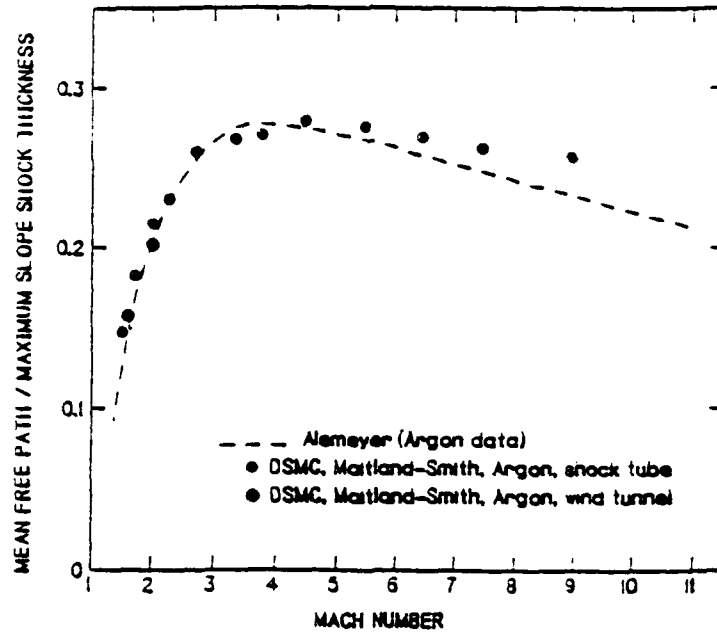


Figure 2: Inverse maximum shock thickness vs. Mach number for normal shocks in argon (Shock tube experiments)

This disagreement may be due to either the repulsive part of the Maitland-Smith

(Aziz) potential being inaccurate at high temperatures, or the experiment being questionable at higher Mach numbers. A previous paper<sup>22</sup> discusses the probable causes for the disagreement and suggests a few self consistent modifications of the intermolecular potential to improve the prediction technique. These modifications seemed however, not adequate to yield a satisfying agreement between experiments and predictions. While the cause of the discrepancy still remains an open issue, it seems that a better understanding of the kinetic processes involved in high stagnation temperature shocks may cast some light on the problem. The present study is aimed at developing a diagnostic technique that would allow detailed probing the energy state populations of flows in nonequilibrium which in turn will provide a better understanding of the dominant kinetic processes in such flows.

In shock tube experiments as well as in wind tunnel experiments, the determination of macroscopic quantities such as density is usually nearly instantaneous and does not require long integration times, however, fluorescent signals are in some cases weak enough to require relatively long integration periods for the determination of microscopic properties such as velocity distribution functions or energy state population distributions. The transient nature of shock tube experiments usually does not allow probing of the microscopic properties of the flow that requires averaging times of the order of seconds while typical diagnostic windows in shock tubes are more of the order of  $\mu\text{sec}$  or  $\text{msec}$  at best. Consequently, if microscopic properties of an out of equilibrium flow have to be determined, it seems that the generation of such flows has to be done in a wind tunnel facility where run times are usually of the order of tens of minutes in semi-continuous closed facilities or even several hours in continuous circuit wind tunnels. In addition to the relatively long flow times, wind tunnel experiments have the advantage

of providing more control on the boundary conditions of the flow and thus, have a higher degree of repeatability than shock tube experiments. Several attempts have been made to create high stagnation temperature supersonic flows facilities<sup>28</sup> operating on nitrogen, but results from these investigation are either inconclusive or not yet known. The concept of a wind tunnel operating on iodine has been motivated by the success of the past and above mentioned wind tunnel experiments for the probing of the microscopic properties of low temperature hypersonic flows in monatomic gases as well as the rather advantageous properties of iodine at relatively low temperatures. To our knowledge, the only accurate measurements of vibrational and rotational level distribution functions and specie concentrations in high speed flows have been obtained from wind tunnel facilities. Very recently, however, measurements of nonequilibrium vibrational populations in nitrogen have been measured in shock tubes experiments using spontaneous Raman spectroscopy.<sup>29</sup>

## Chapter 2

### Choice of Iodine as a Representative Gas

#### 2.1 Properties of the iodine molecule

During the reentry of transatmospheric vehicles such as the NASP or the STS orbiter, a shock will typically form in the vicinity of the hull. The temperatures encountered behind the shock at an altitude of approximately 50 km are typically of the order of 4000 K for a reentry speed of 4 km sec<sup>-1</sup>. At this altitude, the number density is typically 1 torr and the most abundant species are molecular oxygen and molecular nitrogen. The Mach number is approximately 12 for these flight conditions resulting in a pressure behind the shock of about 200 torr. Table 1 shows a comparison of the temperature required to produce about 50% dissociation in iodine, nitrogen and oxygen. Also shown in Table 1 are the ratios of the vibrational energy spacing  $\Delta E_v$  to the average kinetic energy  $\langle \epsilon \rangle = (3/2) kT$ . As may be noticed, while 50% dissociation in nitrogen and oxygen is achieved at temperatures of about 4000 to 5000 K, the same degree of dissociation can be produced by heating iodine to approximately 1000 K. The ratio  $(\Delta E_v) / \langle \epsilon \rangle$  is an indication of how close the average kinetic energy of the molecules are to the internal vibrational energy spacing. For all three gases,  $\langle \epsilon \rangle$  is larger than the energy required to excite the molecules to upper vibrational levels resulting in significant population of the vibrational levels. Since the value of  $(\Delta E_v) / \langle \epsilon \rangle$  is smaller for iodine, it is expected that its higher vibrational states will be more populated than the corresponding vibrational states in nitrogen or oxygen. Consequently, because rotational, vibrational and dissociative excitation of the iodine molecule can be achieved at lower temperatures than for oxygen or nitrogen, iodine may be used as a convenient sur-

rogate diatomic gas for the study of chemically reacting gas flows.

Species	Temperature (K)	$\langle \epsilon \rangle$ (eV)	$\Delta E_v$ (eV)	$(\Delta E_v)/\langle \epsilon \rangle$
$I_2$	1340	0.17	0.026	0.15
$N_2$	5400	0.69	0.292	0.42
$O_2$	3530	0.45	0.195	0.43

Table 1: Thermal equilibrium properties of iodine, nitrogen and oxygen for a degree of dissociation of 50% and a pressure of 200 Torr.

## 2.2 Spectroscopic constants of the iodine molecule

Table 2 summarizes some spectroscopic constants of the iodine molecule in the  $(X^1\Sigma_g^+, V=0)$  state,<sup>30</sup> which might be useful in the determination of gas properties as well as computation of approximate transition energies.

Symbol	Description	Units	values
$M$	Molecular weight	$\text{g mol}^{-1}$	253.8
$\omega_e$	Vibrational constant	$\text{cm}^{-1}$	214.57
$\omega_e x_e$	Vibrational constant (1 <sup>st</sup> unharmonicity)	$\text{cm}^{-1}$	0.61
$\omega_e y_e$	Vibrational constant (2 <sup>nd</sup> unharmonicity)	$\text{cm}^{-1}$	-0.000895
$B_e$	Rotational constant	$\text{cm}^{-1}$	0.037
$\alpha_e$	Vibration-rotation constant	$\text{cm}^{-1}$	0.000117
$r_e$	Equilibrium internuclear distance	$\text{\AA}$	2.666
$D_0$	Molecular dissociation energy	eV	1.54
$E_{m.i.}$	Excitation energy of the 1 <sup>st</sup> electronic level ( $B^3\Pi_u$ )	eV	5.09

Table 2: Spectroscopic constants of the iodine molecule (Hertzberg<sup>30</sup>).



Symbol	Description	Units	values
$E_{m,2}$	Excitation energy of the 2 <sup>nd</sup> electronic level ( $D^1\Sigma_g^-$ )	eV	9.31
$U_m$	Molecular ionization energy	eV	9.31
$\theta_r$	Characteristic rotational temperature	K	0.053
$\theta_v$	Characteristic vibrational temperature	K	308
$\theta_d$	Characteristic dissociation temperature	K	17894

Table 2: Spectroscopic constants of the iodine molecule (Hertzberg<sup>30</sup>).

One may note that the iodine molecule is relatively large and heavy compared to the nitrogen or oxygen whose interatomic separation is more of the order of 1 Å.

Table 3 shows a few properties of the iodine gas in equilibrium at a temperature of 1000 K. This particular temperature was chosen to correspond to a temperature conveniently obtained in laboratory.

Symbol	Description	Units	Values
$J_p$	Most probable rotational quantum number	dimensionless	95
$\Delta E_r$	Energy gap between rotational levels $J_p$ and $J_p+1$	eV	0.0009
$\Delta E_v$	Energy gap between the ground and 1 <sup>st</sup> vibrational level	eV	0.026
$\langle \epsilon \rangle$	Mean translational energy	eV	0.08
$\lambda$	Ratio of number of molecules in $V = 1$ to $V = 0$ vibrational level	dimensionless	0.73

Table 3: Iodine properties at 1000 K

Symbol	Description	Units	Values
y	Degree of dissociation	dimensionless	
	$n = 10^{16}\text{cm}^{-3}$ $n = 10^{19}\text{cm}^{-3}$		0.65 0.03
x	Degree of ionization	dimensionless	
	$n = 10^{16}\text{cm}^{-3}$ $n = 10^{19}\text{cm}^{-3}$		$3.6 \cdot 10^{-22}$ $1.9 \cdot 10^{-23}$

Table 3: Iodine properties at 1000 K

Noting that the most probable rotational quantum number  $J_p$  equals 95, it may be remarked that significant rotational excitation of the iodine molecule is easily achieved at 1000 K. This is because the typical energy gap between levels  $J_p$  and  $J_p-1$ ,  $\Delta E_r$ , equals 0.0009 eV while the average translational energy  $\langle \epsilon \rangle$  at 1000 K is about 2 orders of magnitude larger. Vibrational excitation is also significant at the temperature considered here since the average translational energy is of the same order as the energy gap between the ground and 1<sup>st</sup> vibrational level; the ratio  $\lambda$  of the number of molecules in the  $V = 1$  to  $V = 0$  vibrational level is indeed of the order of unity. The degree of dissociation at 1000 K may be obtained using the law of mass action assuming that the gas is in complete thermal equilibrium. More details on the determination of the degree of dissociation for a given temperature is covered in Section 4.3. For the temperature (1000 K) and pressure (1 Atm or  $n = 10^{19}\text{cm}^{-3}$ ) of interest here, one may note that the degree of dissociation is about 3% while the degree of ionization determined by the Saha relation and taking into account the contribution of atomic and molecular ionization is of the order of  $10^{-23}$ . Compared to another halogen gas such as chlorine, the energy levels of the iodine molecule are more easily populated. For example, at 1000 K the most probable rotational quantum number for chlorine is 37 as opposed to 95 for iodine; the ratio  $\lambda$  for chlorine is 44% while it is 73% for iodine and the degree of dissociation

expected at 1 Atm for chlorine is 0.0024% compared to 3% for iodine.

To summarize, the decision to use iodine as a working gas is mainly justified by the fact that rotational and vibrational levels of the iodine molecule can be populated at temperatures easily reachable in laboratory. The temperature of concern here is approximately 1000 K where it is expected that significant rotational and vibrational excitation of the molecule will occur and this, in turn, will enable the study of rotational and vibrational relaxation or nonequilibrium phenomena. At least 3% dissociation can be expected, but the number of dissociated molecules being quite sensitive to temperature and pressure, the dissociation can easily be increased by raising the temperature or decreasing the pressure. The presence of dissociated molecules will in principle enable examination of chemical reactions which will not be affected by free electrons since the degree of ionization is negligible.

## Chapter 3

### Transient Laser Induced Fluorescence (TLIF)

#### 3.1 General principle

Transient or pulsed laser induced fluorescence was selected for this study because it produces relatively strong signals compared to other scattering techniques such as Raman scattering.<sup>10</sup> Provided the tunable pulsed laser linewidth is small and stable enough to excite single transitions at a time, the chosen probing technique is robust, repeatable and has the advantage of being quenching insensitive under the condition that only the early portion of the fluorescent pulse is detected.

Figure 3 shows a schematic of the  $I_2$  potentials involved in the excitation and fluorescence processes. The laser excites the  $I_2$  molecules from a rovibrational level ( $V''$ ,  $J''$ ) of the ground electronic state  $X(^1\Sigma_0^+)$  to a rovibrational level ( $V'$ ,  $J'$ ) of the  $B(^3\Pi_{0,u})$  state. Emission spectra are obtained by scanning the laser wavelength, i. e. successively exciting levels of the  $X$  state to levels of the  $B$  state. The fluorescence signal is observed through a wide spectral window of a spectrometer whose main purpose is to filter out scattered photons at the laser frequency.

The laser wavelength  $\lambda_0$  corresponding to a transition  $(B, V', J') \leftarrow (X, V'', J'')$  enables probing of the populations in level  $(X, V'', J'')$  by exciting these molecules to a level  $(B, V', J')$ . Subsequently, the molecules in level  $(B, V', J')$  transition to several lower levels  $(X, V_i'', J_i'')$ , and in doing so emit photons at wavelengths  $\lambda_i$ . Only the wavelengths located in the spectrometer band pass are detected. Several rovibrational levels of the  $X$  state can be probed by sweeping the laser wave-

length  $\lambda_0$ . The intensity of the fluorescent signal for a given laser frequency is a measure of the population in the level  $(X, V'', J'')$  initially excited. The probing method described here has been extensively used to measure the vibrational distributions of  $I_2$  in chemical laser injectors.<sup>31</sup> In this study the probing laser was a ring-dye CW laser, while the work described here used a pulsed dye laser whose linewidth was narrowed with an intra-cavity air spaced etalon.

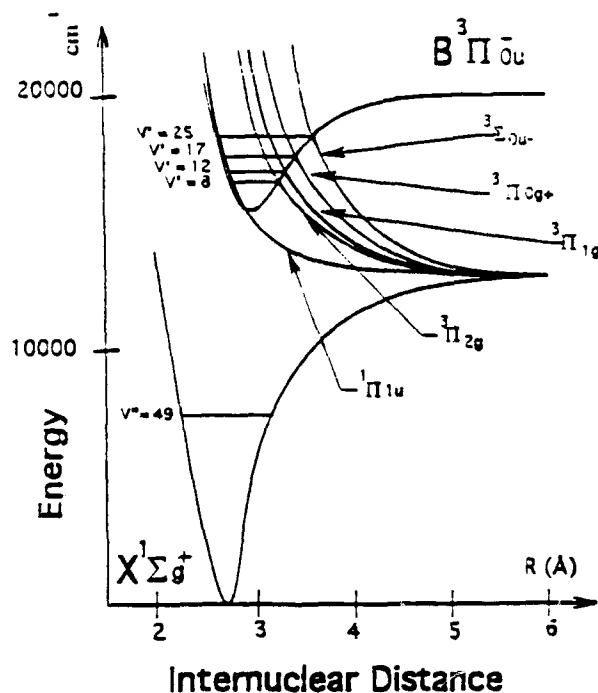


Figure 3: Schematic of the intermolecular potentials of  $I_2$  involved in the TLIF process

### 3.2 Upper state population response to pulsed pumping

The pulsed nature of the work described here raises issues dealing with the unsteadiness of the populations being probed. In this section it is of interest to describe the time dependence of the population  $N_1$  of the  $X$  state being excited by the laser and the population  $N_2$  in the  $B$  state. Let us examine a simple two level sys-

tem illustrated in Figure 4 and modeled by the pair of rate equations:

$$\frac{dN_1}{dt} = N_2 (P_{21} + A_{21} + \sum_{i=1} R_{i1}) - N_1 (P_{12} + \sum_{i<1} A_{1i} + \sum_{i=1} R_{1i} + P_{dis}) \quad (2)$$

$$\frac{dN_2}{dt} = N_1 (P_{12}) - N_2 (P_{21} + \sum_{i<2} A_{2i} + \sum_{i=2} R_{2i} + A_{pdis}) \quad (3)$$

where  $P_{ij} = B_{ij} g(v_L) E_p(t)/(Ac)$  is the pumping rate from level  $i$  to level  $j$ ,  $A_{ij}$  is the spontaneous emission coefficient from level  $i$  to  $j$ ,  $B_{ij}$  is the stimulated emission or stimulated absorption factor depending on whether levels  $i$  and  $j$  are upper or lower levels,  $R_{ij}$  is the decay rate due to collisional deexcitation,  $g(v_L)$  is the laser line shape,  $E_p(t)$  is the laser energy delivered to the probed volume per unit time,  $A$  is the laser beam cross-sectional area and  $c$  is the speed of light. Finally  $P_{dis}$  is the pumping rate which depopulates level 1 by direct absorption to the dissociative state  $^1\Pi_{1u}$ .<sup>32,33</sup>  $P_{dis}$  has the same form as  $P_{ij}$ , with the only difference being that  $B_{ij}$  is replaced by an absorption coefficient  $B_{dis}$  consistent with a dissociative reaction. Spontaneous predissociation, whereby a molecule is initially absorbed into the  $B$  state and subsequently spontaneously dissociates by transitioning to the  $^1\Pi_{1u}$  state, has been taken into account in Equation (3) with the spontaneous decay term  $A_{pdis}$ . Direct absorption and spontaneous predissociation to other dissociative states such as  $^3\Pi_{2g}$ ,  $^3\Pi_{1g}$ ,  $^3\Pi_{0g}$ ,  $^3\Sigma_{0u}$ , or  $^3\Delta_{3u}$  are ignored in this analysis because their contribution has been found to be minimal compared to the  $^1\Pi_{1u}$  state.<sup>33</sup> Experimental evidence will show however that these states may be responsible for some anomalies observed in this study (see discussion in Section 5.5). For the purpose of this analysis, the collisional quenching rates  $R_{ij}$  are ignored because the pressures at the points of diagnostics are usually not more than a few Torr and collisional quenching at these pressures is usually neglected.<sup>31</sup> For higher stagnation pressure regimes collisional quenching may not be neglected. However, as shown in Sec-

tion 3.5.5, since detection of the fluorescent signal is performed for a short time during the early part of the signal pulse, the technique is insensitive to quenching and hence, the term  $R_{ij}$  may still be neglected. For the sake of notation, the sum  $\sum_{i=2} A_i$  is replaced by  $A_2$  and since a two level system is considered and level 1 is the lowest level,  $\sum_{i=1} A_i$  can be replaced by 0.

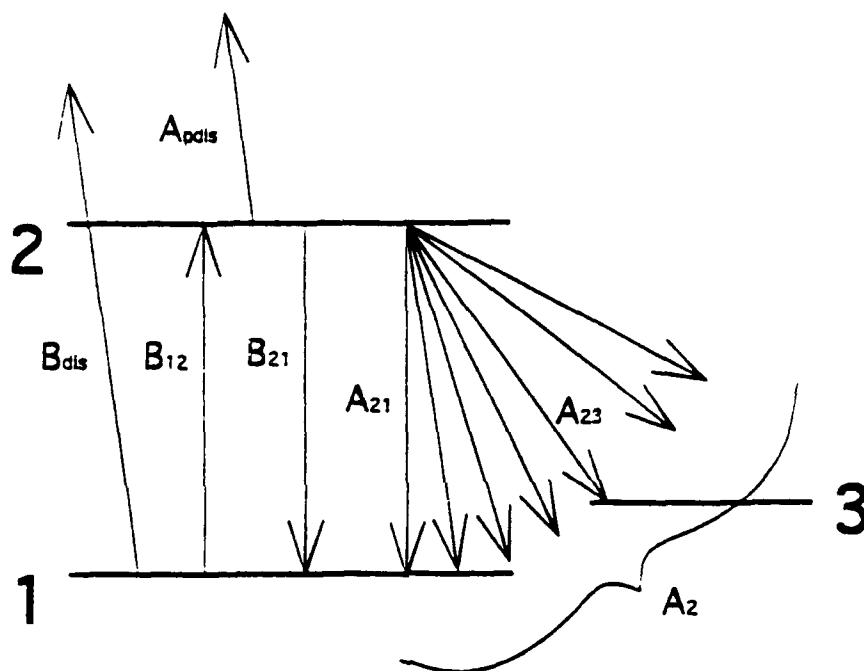


Figure 4: Two level system used to analyze population responses under pulsed excitation.

As an example, we choose the (39, 0) R55 transition which requires laser pumping at approximately 5208 Å. Capelle and Broida<sup>34</sup> report a total rate depopulating the upper state (due to radiation and predissociation) of approximately  $7 \cdot 10^5 \text{ sec}^{-1}$ . Of this total rate,  $2.5 \cdot 10^5$  transitions per second are purely radiative and  $4.5 \cdot 10^5 \text{ sec}^{-1}$  are predissociative. This results in an Einstein absorption coefficient  $B_{12}$  of  $9.26 \cdot 10^{17} \text{ m}^3 \text{ J}^{-1} \text{ sec}^{-2}$  calculated using expression

$$A_2 = \alpha \cdot \sum_{V''} v^3 FC(V', V''), \quad (4)$$

where

$$\alpha = \frac{64\pi^4}{3hc^3} \cdot \frac{1}{4\pi\epsilon_0} \cdot \frac{HL(J', J'')}{2J' + 1} \cdot |\mu(R_c)|^2 \quad (5)$$

and Equations (18) and (15).  $FC(V', V'')$ ,  $HL(J', J'')$  and  $\mu(R_c)$  are respectively the Franck-Condon, Höln-London factors and the dipole moment defined in Section 3.4.2. In order to obtain Equations (4) and (5) several assumption have been made:

- 1) The rotational transition probability  $HL(J', J'')$  is independent of vibrational transition probability.
- 2) The vibrational transition probability may be decomposed into two parts: an overlap integral of vibrational wavefunctions  $FC(V', V'')$  usually called Franck Condon factor, and an average electronic transition moment  $|\mu(R_c)|^2$ .
- 3) The average electronic transition moment can be represented by the electronic transition moment at an average internuclear distance  $R_c$  called the R-centroid. This is the R-centroid approximation<sup>35</sup> (Ref. Section 3.4.2).
- 4) The R-centroid which in principle depends on vibrational quantum number has for the purpose of this example been considered constant.

Although the last assumption has been used for convenience in a number of past studies,<sup>36,37</sup> it was found in this work that it may result in overestimating the decay rates and absorption coefficients by up to 15% for the (17, 0) R42 for instance. For



the purpose of developing the probing technique concerned in this work, an error of the order of 10% is tolerable. However, the precise determination of absorption coefficients and decay rates is certainly required if a precise determination of population distributions is desired. In this case the variation of the electronic transition moment with vibrational quantum number has to be taken into account and evaluation of Equation (4) has to be done by including the term  $|\mu(R_v)|^2$  in the summation.

$A_2$ , the total radiative rate of  $2.5 \cdot 10^5 \text{ sec}^{-1}$  from the upper  $(B, V', J')$  state to several  $(X, V'', J'')$  states, has been calculated with relative accuracy<sup>32</sup> and is the value used to determine the absorption coefficient  $B_{12}$ . In order to calculate the latter one needs  $A_{21}$  which can be calculated by first computing the summation in Equation (4) using the Franck Condon factors and frequencies determined by Martin *et al.*,<sup>12</sup> second determining  $\alpha$  by equating Equation (4) to the measured rate  $A_2$ ,<sup>34</sup> and finally computing  $A_{21} = \alpha \nu^3 FC(2', 1'')$ , which for this example comes out to be  $16175 \text{ sec}^{-1}$ . An absorption coefficient  $B_{12}$  of  $9.26 \cdot 10^{17} \text{ m}^3 \text{ J}^{-1} \text{ sec}^{-2}$  may then be calculated using expressions (15) and (18). A predissociation rate  $A_{\text{predis}}$  of  $4.5 \cdot 10^5 \text{ sec}^{-1}$  as measured by Capelle and Broida<sup>34</sup> was assumed, this value is consistent with a rate of  $5.7 \cdot 10^5 \text{ sec}^{-1}$  measured by another group for a neighboring transition at  $5277 \text{ \AA}$ .<sup>32</sup>  $B_{12}$  was taken as 20% of the total absorption or 25% of  $B_{12}$  as suggested by Brewer and Tellinghuisen.<sup>32</sup> Appendix B summarizes rates and absorption coefficients for the transitions of interest in this work.

The case of an excitation laser pulse with Gaussian shape is considered. Its full-width-at-half-maximum (FWHM) is  $\tau = 28 \text{ nsec}$  and an energy per pulse  $E_p$  of  $0.0007 \text{ mJ}$  is selected taking into account that the laser beam is fanned into

a 26 mm wide sheet of 1.5 mm thickness. This results in a probed volume having the shape of a small cylinder of diameter 1.5 mm (corresponding to the diameter of the orifice at the spectrometer entrance, see Section 5.2) and 1.5 mm length. The laser pulse is assumed to be of the form:

$$E_p(t) = \alpha e^{-\beta^2(t-t_0)^2} \quad (6)$$

where  $t_0$  is chosen equal to  $2\tau$  and  $\alpha$  and  $\beta$  are chosen so that the pulse's FWHM equals  $\tau$  and  $\int_0^\infty E_p(t) dt = E_p$ . Figure 5 shows the normalized excited state population growth  $N_2/N_{2\infty}$  as a function of time as well as the normalized pulse power time history. The time response is shown for a duration of approximately 100 nsec which corresponds to the gate width  $GW$  during which the signal is detected and averaged.

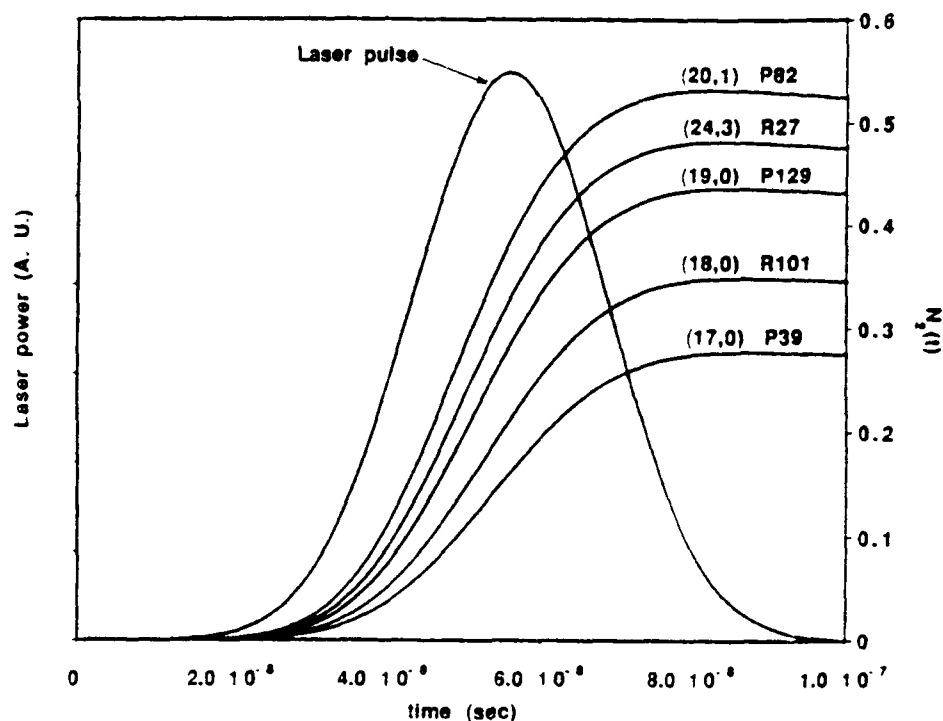


Figure 5: Normalized upper level populations and laser pulse time history for several transitions.

The reason for solving for  $N_2(t)$  is that the fluorescent signal strength is proportional to the product  $A_{21} \int_{\omega} N_2(t) d\omega$ . If one wants to determine the population  $N_1$  from the fluorescence intensities, it is crucial to know how the upper level populations behaves with time under pulsed laser excitation.  $N_{2\infty}$  is the population in the upper level as  $t \rightarrow \infty$  and  $\tau \rightarrow \infty$ :

$$N_{2\infty} = \frac{N_1(0) + N_2(0)}{(1 + g_1/g_2)} \quad (7)$$

In Equation (7)  $g_i$  is the statistical weight of level  $i$ . The values of the statistical weights for the  $X$  and  $B$  levels are defined in Section 3.4. For the example described here,  $g_1(X) = 1$ ,  $g_2(B) = 3$ ,  $N_1(0)$  is taken as 1 and  $N_2(0)$  assumed equal to 0. This gives  $N_{2\infty}/N_1(0) = 3/4$ . To find the solution  $N_2(t)$  the laser spectral lineshape  $g(\nu_L)$  was chosen to be constant at  $9 \cdot 10^{10}$  sec because the laser profile is broader than the absorption profile. Indeed, the laser lineshape is  $0.05 \text{ cm}^{-1}$  at best while the absorption profile is mostly Doppler broadened and of the order of  $0.01 \text{ cm}^{-1}$ . Figure 5 shows that the population in the upper level does not reach the saturated population  $N_{2\infty}$ . This is mainly due to the relatively low laser energy levels used in this experiment. One may then surmise that an increase in laser power would saturate the population in level 2, however this does not seem to be the case as illustrated in Figure 6 where the time response of the population in level 2 is shown for three laser power levels where  $E_p = 7 \cdot 10^{-7}$ ,  $7 \cdot 10^{-6}$  and  $7 \cdot 10^{-5}$  Joules. As may be noticed from this figure, a stronger laser pulse does not necessarily result in an increase in signal. In fact even for the stronger pulse case one may notice that the saturated ratio  $N_{2\infty}/N_1(0) = 3/4$  is still not reached and the population in level 2 tends to decrease even as laser power increases. This is caused by the  $B_{12}$  term in Equation (2) which depopulates the lower level and consequently creates a net de-

pletion of total molecules in the system as illustrated by Figure 7. Consequently, in the low laser power mode the upper state population is not saturated because of lack of pumping power, this is in fact the regime in which we operate; and if the laser power is increased the molecules in the lower level are directly absorbed in the  $\Pi_{1u}$  dissociative state, ultimately impeding the pumping of molecules to the upper  $B$  state.

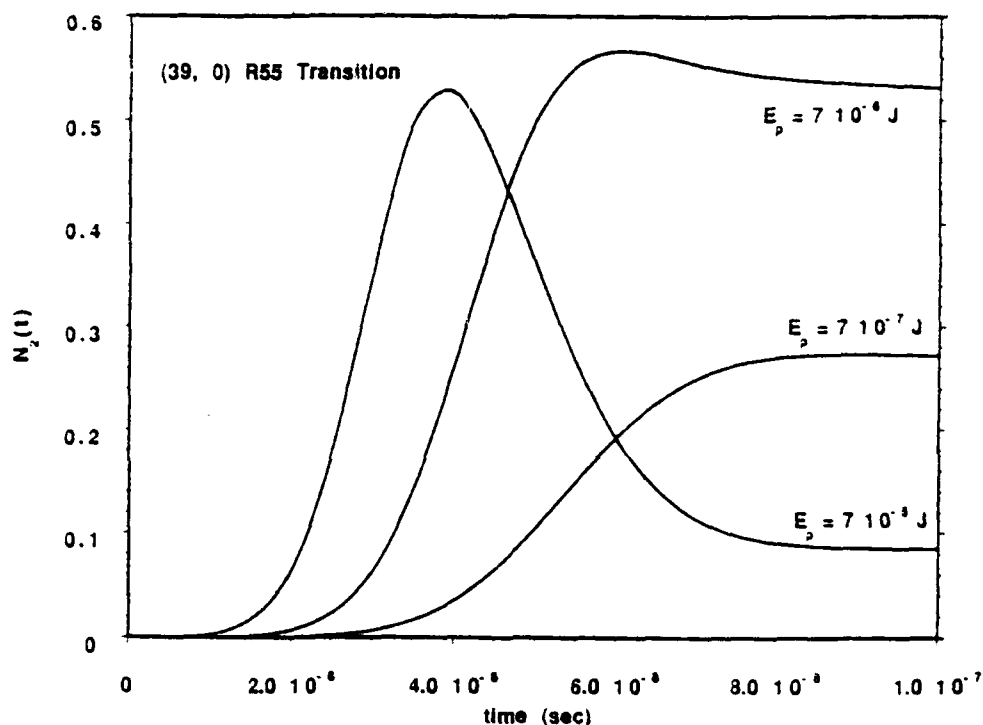


Figure 6: Time response of the population  $N_2$  of the  $B$  state under a Gaussian pulse shape laser pumping for the transition (39, 0) R55 and laser energies per pulse of  $7 \cdot 10^{-7}$ ,  $7 \cdot 10^{-6}$  and  $7 \cdot 10^{-5}$  J.

In summary, it would seem that saturating the population in the upper level is difficult to achieve, as was verified experimentally in this work. Whether the laser power be weak or strong, the fluorescence signal remains dependent on laser power and cannot saturate. In practice, this means that because of the type of pulsed excitation applied in this probing technique, it is important that the signal intensity

as well as laser power be recorded and that the signal intensity be linear with laser power.

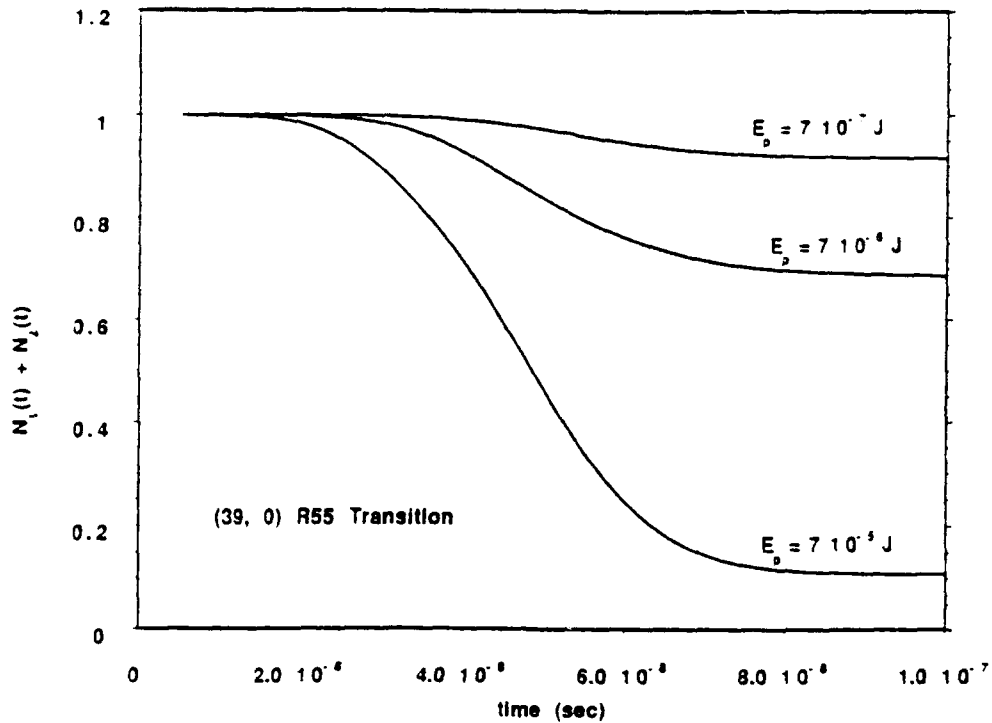


Figure 7: Time response of the sum  $N_1+N_2$  under a Gaussian pulse shape laser pumping for the transition (39, 0) R55 and laser energies per pulse of  $7 \times 10^{-7}$ ,  $7 \times 10^{-6}$  and  $7 \times 10^{-5}$  J.

The solutions shown in Figure 5 through Figure 7 were computed taking into account the attenuation of the laser sheet as it penetrates in to the flowfield and photons are absorbed. This results in a net depletion of laser power at the point being probed. How strong this attenuation is depends on the transition being excited and the number density distribution in the flowfield. A more complete description of how attenuation is calculated can be found in Section 3.5.1.

### 3.3 Identification and choice of transitions

#### 3.3.1 Identification of transitions

The spectral position of all possible rovibrational transitions between the 6 first vibrational energy levels of the ground  $X(^1\Sigma_0^+)$  and the 60 first vibrational states of the  $B(^3\Pi_{0-2})$  states of the iodine molecule have been computed using Dunham expansion coefficients determined by Gerstenkorn and Luc.<sup>11</sup> These coefficients are valid for  $0 \leq V'' \leq 19$  and  $0 \leq V' \leq 80$  and were obtained by best fitting the absorption spectrum of iodine between 11000 and 20040  $\text{cm}^{-1}$  recorded by means of Fourier Transform Spectroscopy. The energy  $E(V'', J'')$  of the lower level  $X(^1\Sigma_0^+)$  may be calculated with

$$E(V'', J'') = E(V'', 0) + B_{V''}K - D_{V''}K^2 + H_{V''}K^3, \quad (8)$$

where  $K = J(J+1)$  and  $E(V'', 0) = G(V'') - G(0)$ . The value of  $G(V'')$ ,  $B_{V''}$ ,  $D_{V''}$  and  $H_{V''}$  are defined as follows:

$$\sum y_{il} (V'' + 1/2)^i, \text{ where} \quad (9)$$

$l = 0$  and  $i = 1, 2, \dots$  for  $G(V'')$

$l = 1, 2, 3, \dots$  and  $i = 0, 1, 2, \dots$  for  $B_{V''}, D_{V''}, H_{V''}$ .

Similarly the energy  $E(V', J')$  of the upper level  $B(^3\Pi_{0-2})$  may be calculated using

$$E(V', J') = E_{V'}(V', 0) + B_{V'}K - D_{V'}K^2 + H_{V'}K^3 + L_{V'}K^4 + M_{V'}K^5, \quad (10)$$

where  $K$  and  $B_{V'}$  are the same as above, and  $E(V', 0) = G(V') - G(0) + T_{0,0} = G(V') + 15661.9408 \text{ cm}^{-1}$ .  $T_{0,0}$  being the distance between the ground level  $V'' = 0, J'' =$

0 of the  $X$  state and the level  $V'' = 0, J'' = 0$  of the  $B$  state. The values of  $D_{V'}$ ,  $H_{V'}$ ,  $L_{V'}$  and  $M_{V'}$  are defined as follows:

$$D_{V'} = \exp \left\{ \sum_{i=1} c_{di} (V' + 1/2)^{i-1} \right\} \quad (11)$$

$$-H_{V'} = \exp \left\{ \sum_{i=1} c_{hi} (V' + 1/2)^{i-1} \right\} \quad (12)$$

$$-L_{V'} = \exp \left\{ \sum_{i=1} c_{li} (V' + 1/2)^{i-1} \right\} \quad (13)$$

$$-M_{V'} = \exp \left\{ \sum_{i=1} c_{mi} (V' + 1/2)^{i-1} \right\}. \quad (14)$$

The constants  $y_{il}$ ,  $c_{di}$ ,  $c_{hi}$ ,  $c_{li}$ ,  $c_{mi}$  are listed in appendix A. Effective constants  $M_{V'}^* = k M_{V'}$  were used to account for the neglected  $N_{V'}$ ,  $O_{V'}$ ... An empirical scaling factor  $k$  equal to 2.2 was used in the calculations presented here. A total of 115,200 transitions were calculated; these included  $V'' = 0$  to 5,  $V' = 0$  to 59,  $J'' = 0$  to 159 and a  $P$  and  $R$  branch for each rovibrational transition. Note that there are no  $P$  branches for transitions with  $J'' = 0$ . A more comprehensive description of the  $X(^1\Sigma_0^-)$  ground and  $B(^3\Pi_0^-)$  state was performed by Martin *et al.*<sup>12</sup> Their study determined the Dunham coefficients and Franck-Condon factors for vibrational levels up to  $V'' = 113$  of the ground  $X$  electronic state and  $V' = 71$  of the  $B$  state. The transition energies calculated from these coefficients showed virtually no difference when compared to transitions calculated with Gerstenkorn's coefficients. Franck-Condon transition probabilities for the  $B \leftrightarrow X$  band ( $0 \leq V'' \leq 5$ ,  $0 \leq V' \leq 67$ ) were also calculated by Tellinghuisen<sup>38</sup> and showed to be different from Martin *et al.*'s factors by no more than 1% for the range of vibrational levels of interest in this study. For the purpose of predicting emission spectra in this study, the Dunham coefficients of Gerstenkorn<sup>11</sup> and the Franck-Condon factors of Tellinghuisen<sup>38</sup> were used.

In order to identify transitions of the  $B \leftrightarrow X$  system, it is necessary to

predict the energy involved in a transition with an accuracy that is equivalent or better than the laser spectral resolution. Since the laser linewidth is about  $0.05 \text{ cm}^{-1}$  when fitted with an intracavity etalon, the transition wavenumber has to be determined with an accuracy which only Gerstenkorn<sup>11</sup> and Martin *et al.*<sup>12</sup> are able to produce. The standard techniques for predicting transition energies such as that outlined by Hertzberg<sup>30</sup> result in significant errors particularly for transitions involving higher vibrational levels. Figure 8 and Figure 9 illustrate the discrepancy  $\nu_{\text{Stand}} - \nu_{\text{Gerst}}$  between a standard computation of vibrational energy and that produced by Gerstenkorn's coefficients for levels of the *X* and *B* state respectively. All the wavenumbers are computed for the  $0^{\text{th}}$  rotational level in each vibrational state. Discrepancies are of the order of unity for the *X* state and  $10^2 \text{ cm}^{-1}$  for the *B* state. This makes the standard method clearly inadequate for transition identification.

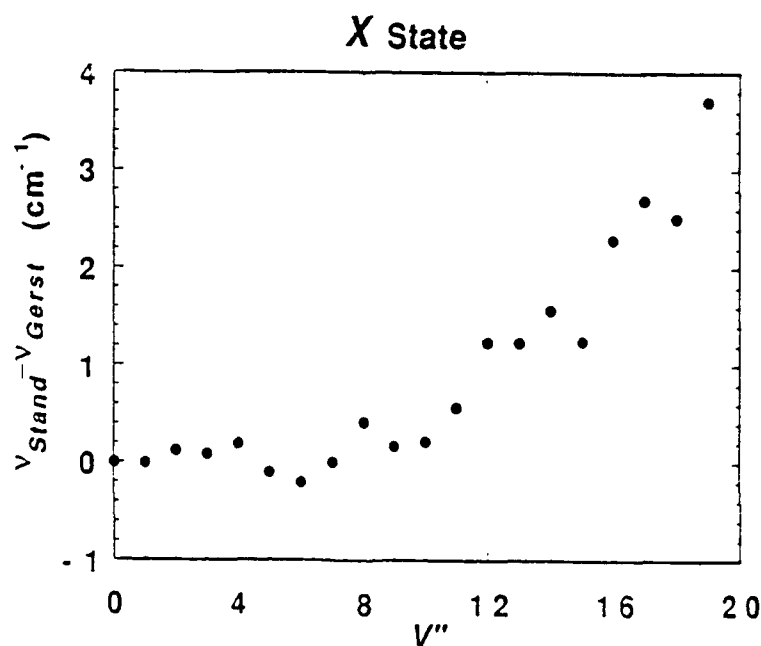


Figure 8: Energy of vibrational levels of the *X* state ( $J = 0$ ). Difference between standard method and Gerstenkorn's prediction.



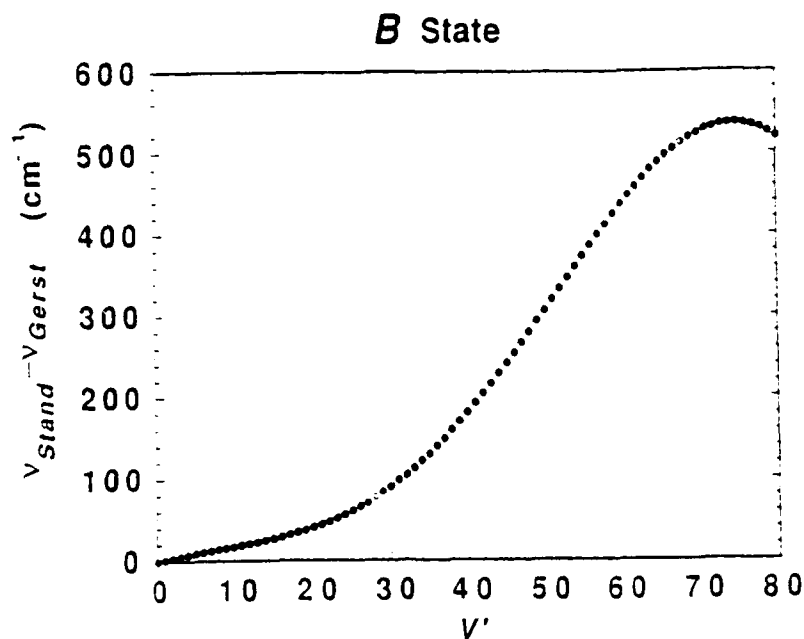


Figure 9: Energy of vibrational levels of the *B* state ( $J = 0$ ). Difference between standard method and Gerstenkorn's prediction.

### 3.3.2 Choice of transitions

The Dunham expansion coefficients determined by Gerstenkorn<sup>11</sup> were used to calculate the wavenumber of all possible transitions for  $V'' = 0$  to 5,  $V' = 0$  to 59 and  $J'' = 0$  to 159. An example of possible transitions between 16200 and 16600  $\text{cm}^{-1}$  is shown in Figure 10 where transitions with different lower vibrational levels are represented with different symbols. The transitions are plotted as rotational quantum number vs. wavenumber to show that a wide range of rotational quantum numbers ( $0 \leq J'' \leq 100$ ) and vibrational quantum number between 0 and 5 may be probed with spectral scans of about 150  $\text{cm}^{-1}$ . Figure 11 shows only the transitions that can be resolved with a laser linewidth of 0.05  $\text{cm}^{-1}$ , in other words, all transitions which have a neighbor transition closer than 0.05  $\text{cm}^{-1}$  have been filtered. It

may be seen from this figure that although many transitions cannot be resolved by the laser, a large enough number of transitions may still be used for determining population distributions.

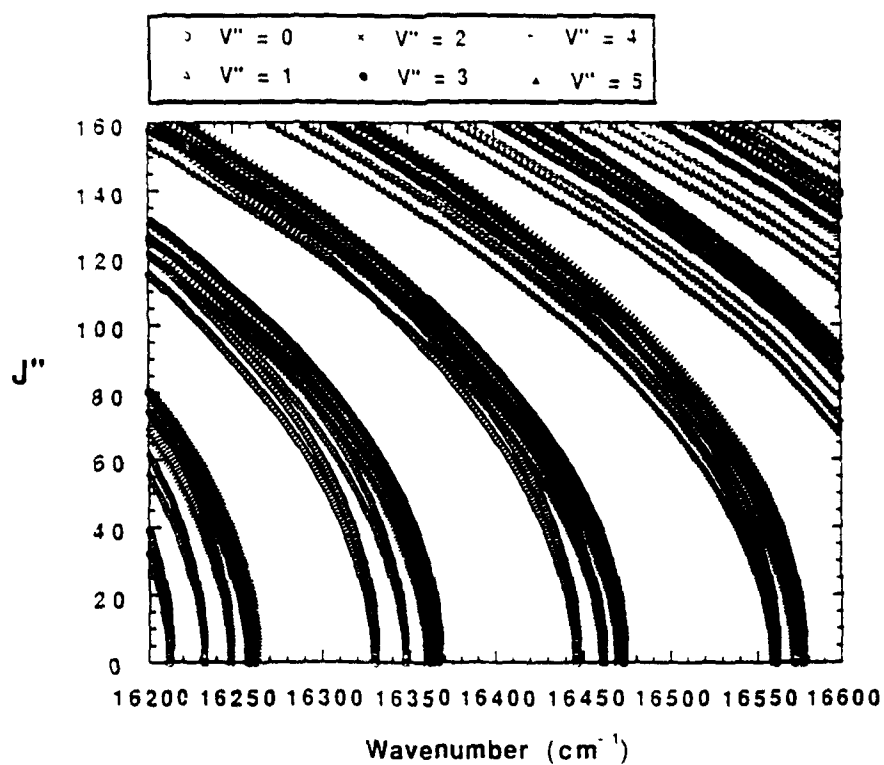


Figure 10: ( $B \leftrightarrow X$ ) transitions for  $V'' = 0$  to  $5$ ,  $V' = 0$  to  $59$  and  $J'' = 0$  to  $159$  between  $16200$  and  $16600 \text{ cm}^{-1}$ .

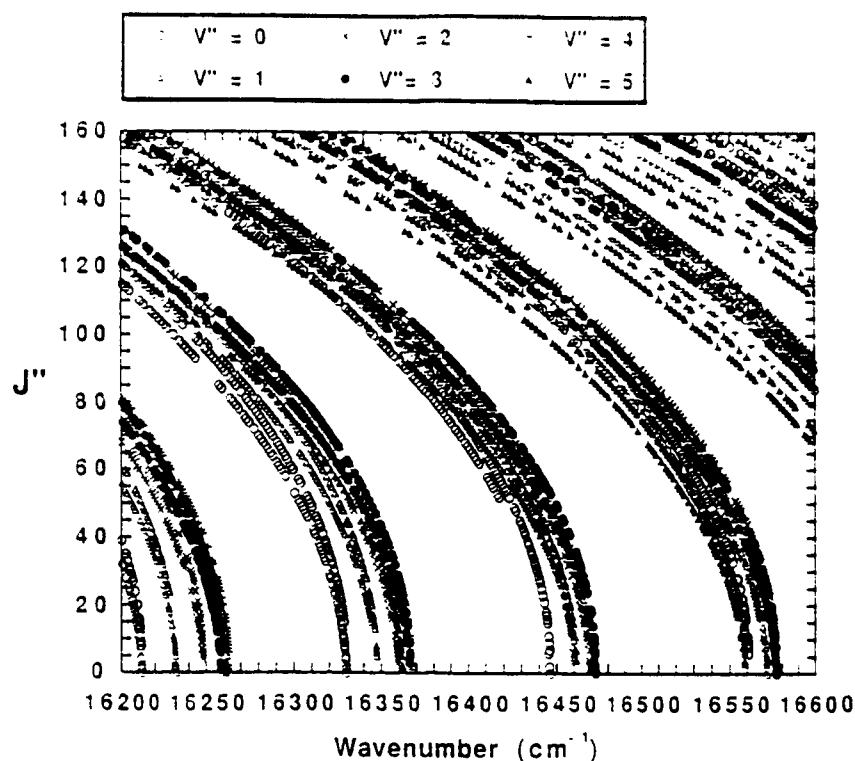


Figure 11: ( $B \leftrightarrow X$ ) transitions for  $V'' = 0$  to 5,  $V' = 0$  to 59 and  $J'' = 0$  to 159 between 16200 and 16600  $\text{cm}^{-1}$ . The transitions which cannot be resolved with a laser linewidth of 0.05  $\text{cm}^{-1}$  have been filtered.

Franck-Condon factors computed by Martin *et al.*<sup>12</sup> are presented for  $0 \leq V'' \leq 19$ ,  $0 \leq V' \leq 59$  and  $J'' = 0$  in Figure 12 along with a plot of the approximate laser wavelength required to excite a transition of the type  $V' \leftarrow V''$  shown in Figure 13. The wavelengths shown in latter figure were calculated with Equations (8) and (10) for  $J'' = J' = 0$ . Note that this type of transition ( $\Delta J = 0$ ) is in principle forbidden because the Höln-London factor for  $Q$  transitions is zero (Ref. Section 3.4.2). However, for the purpose of determining an approximate transition wavelength, this is considered adequate. Figure 12 shows an interesting pattern, namely that the strongest Franck-Condon factors are found within the range  $0 \leq V' \leq 20$

for the entire  $V''$  range. This means that in order to probe a wide range of vibrational levels of the  $X$  state ( $V''$ ) and at the same time maximize signal strengths, the laser wavelength to be used is about 5300 Å for  $V'' = 0$  and progresses towards longer wavelengths for higher  $V''$ .

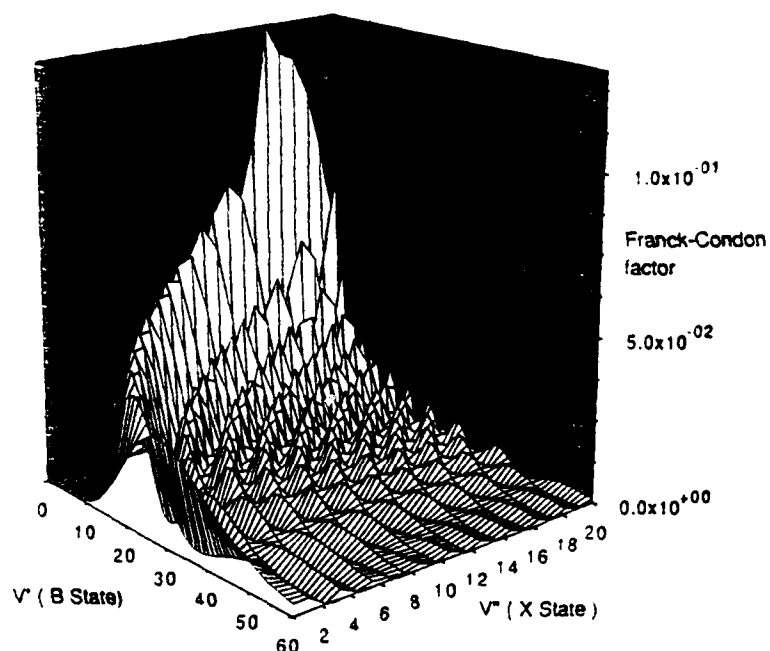


Figure 12: Franck-Condon factors for the transitions of the ( $B \leftrightarrow X$ ) band.<sup>12</sup> ( $0 \leq V'' \leq 19$ ,  $0 \leq V' \leq 59$ ,  $J'' = 0$ )

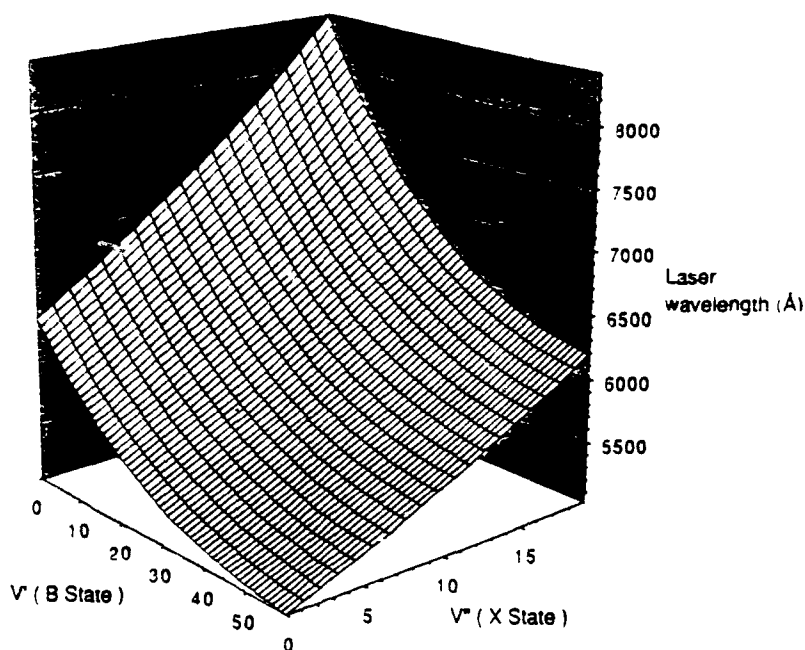


Figure 13: Laser pumping wavelength for the transitions of the ( $B \leftrightarrow X$ ) band. ( $0 \leq V'' \leq 19$ ,  $0 \leq V' \leq 59$ ,  $J'' = 0$ )

For the purpose of this study, the transitions chosen for probing are those already identified at common laser frequencies by Gerstenkorn and Luc.<sup>25</sup> However, the analysis in this section enables identification of any transitions for  $0 \leq V'' \leq 19$  and  $0 \leq V' \leq 80$ . Consequently, any transition can in principle be used for the determination of population distributions provided the transition is strong enough.

### 3.4 Predicted LIF spectral intensities

In this section, an expression for the intensity of the LIF emission spectra is derived assuming thermodynamic equilibrium of both rotational and vibrational lev-

els. This expression will in turn be used to generate synthetic spectra which once compared to experimental spectra, enable the unambiguous identification of the transitions involved.

### 3.4.1 Einstein A and B coefficients

For the following analysis, a simple two level system is assumed. The nomenclature is the same as in Section 3.2. The Einstein coefficients are defined as follows:

- Coefficient of spontaneous emission:  $A_{21} = -\frac{\Delta N_2}{N_2 \cdot \Delta t}$  .
- Coefficient of stimulated emission:  $B_{21} = -\frac{\Delta N_2}{N_2 \cdot \Delta t \cdot \rho(\nu)}$  , where  $\rho(\nu)$  is the spectral energy density of the incident laser light.
- Coefficient of absorption from 1 to 2:  $B_{12} = -\frac{\Delta N_1}{N_1 \cdot \Delta t \cdot \rho(\nu)}$  .

The stimulated absorption and emission coefficients are related by

$$B_{12} \cdot g_1 = B_{21} \cdot g_2 \text{ ,} \quad (15)$$

where  $g_1$  and  $g_2$  correspond to the  $X$  and  $B$  electronic levels respectively and have the values:

$$g_1 = 2J'' + 1 \quad (16)$$

$$g_2 = 3(2J' + 1) \text{ .} \quad (17)$$

Note that although the  $B$  state has a  $\Lambda$  value of 1, it does not have any  $\Lambda$  splitting because it has an  $\Omega = \Lambda + \Sigma$  value of 0.

The spontaneous emission and stimulated emission coefficient are related by

$$\frac{A_{21}}{B_{21}} = \frac{8\pi h \nu^3}{c^3} \text{ ,} \quad (18)$$

where  $\nu$  is the frequency corresponding to a transition between 1 and 2. The coefficient of spontaneous emission can be written as:

$$A_{21} = \frac{64\pi^4\nu^3}{3hc^3} \cdot \frac{1}{4\pi\epsilon_0} \cdot \frac{S(V', J', V'', J'')}{2J' + 1}, \quad (19)$$

where  $S$  is the strength of the transition starting from the upper rovibrational level  $(B, V', J')$  to the lower level  $(X, V'', J'')$ . The factor of  $2J' + 1$  takes into account the degeneracy of the state. Combining Equations. (18) and (19) the absorption coefficient can be written as:

$$B_{12} = \frac{8\pi^3}{3h^2} \cdot \frac{1}{4\pi\epsilon_0} \cdot \frac{g_2}{g_1} \cdot \frac{S(V', J', V'', J'')}{2J' + 1}. \quad (20)$$

### 3.4.2 Transition line strength

Assuming that the dipole moment  $\mu(R_e)$  varies slowly with internuclear distance  $R$  and that this distance is constant during an electronic transition, the line strength can be decomposed as the product of a rotational, vibrational and electronic transition probability.

$$S(V', J', V'', J'') = HL(J', J'') \cdot |\langle \mu(R_e) \rangle|^2 \cdot FC(V', V''), \quad (21)$$

where  $FC(V', V'')$  is the Franck Condon factor or square of the overlap integral:

$$FC(V', V'') = |\langle \Psi_{v'} | \Psi_{v''} \rangle|^2. \quad (22)$$

Franck-Condon Factors have been calculated by Tellinghuisen<sup>38</sup> for  $0 \leq V' \leq 67$  and  $0 \leq V'' \leq 5$  and lately by Martin *et al.*<sup>12</sup> for  $0 \leq V' \leq 72$  and  $0 \leq V'' \leq 108$ . The spectra calculated in this study are based of Tellinghuisen's factors.

$HL(J', J'')$  is the Höln-London factor or rotational line strength given for absorption by:<sup>31</sup>

$$HL_P(J, J'') = J'' \quad (23)$$

$$HL_Q(J, J'') = 0 \quad (24)$$

$$HL_R(J, J'') = J'' + 1 \quad (25)$$

The subscripts  $P$ ,  $Q$  and  $R$  denote transitions where  $\Delta J = J' - J'' = -1, 0, 1$  respectively.

In Equation (21)  $|\langle \mu(R) \rangle|$  is the average dipole moment taken at a given internuclear distance  $R$ . In the  $R$ -centroid approximation,<sup>38</sup>  $|\langle \mu(R) \rangle|$  is considered as the dipole moment taken at an average internuclear distance  $\langle R \rangle$  called the  $R$ -centroid  $R_c$ . In other words,  $|\langle \mu(R) \rangle|$  may be replaced by  $|\mu(\langle R \rangle)| = |\mu(R_c)|$ .  $R$ -centroids are a function of the vibrational and rotational quantum numbers involved in the transition and have been calculated by Tellinghuisen<sup>38</sup> for the particular case of the  $B-X$  transitions in iodine and later, more extensively by Martin *et al.*<sup>12</sup> In summary the transition line strength may be written:

$$S(V', J', V'', J'') = HL(J', J'') \cdot |\mu(R_c)|^2 \cdot FC(V', V'') \quad (26)$$

### 3.4.3 Alternation of rotational intensities due to nuclear statistics

In a homonuclear diatomic molecule, nuclear spin causes energy levels to be degenerate. This results in an alternation of the intensity of rotational transitions depending on  $J''$ . The statistical weight for an even  $J''$  is  $(2I+1)I$  and for an odd  $J''$  is  $(2I+1)(I+1)$ . The value for the nuclear spin  $I = 5/2$ , which means that  $g_{J''(\text{odd})} = 7$  and  $g_{J''(\text{even})} = 5$ . In deriving an expression for line intensities, nuclear spin is taken into account by means of a "spin" factor  $SP(J'')$  which will be equal to 7 for odd  $J''$  and 5 for even  $J''$ .



### 3.4.4 Population in a rovibrational level

The absorption intensity of a rovibrational transition  $(B, V', J') \leftarrow (X, V'', J'')$  is proportional to the population in the absorbing level  $N(V'', J'')$ . For the spectra generated in this portion of the study, thermodynamic equilibrium was assumed with the provision that the vibrational temperature  $T_{vb}$  may be decoupled from the rotational temperature  $T_{rot}$ . The total population in a rovibrational level  $(V, J)$  is given by:

$$N(V, J) = N(V) \cdot N(J) = \frac{e^{-\frac{E(V)}{kT_{vb}}}}{Q_{vb}} \cdot \frac{(2J+1) e^{-\frac{E(J)}{kT_{rot}}}}{Q_{rot}} \quad (27)$$

where:

- $(2J+1)$  is the statistical weight of rotational level  $J$ .
- $Q_{vb}$  and  $Q_{rot}$  are the vibrational and rotational state sums respectively.
- $E(V)$  is the energy of vibrational level  $V$  and  $E(J)$  is the energy of rotational level  $J$  within vibrational level  $V$ .

### 3.4.5 Absorption of molecules to the $B$ state

The populations in the lower level  $(X, V'', J'')$  are being pumped by the laser at frequency  $\nu_L$  to an upper level  $(B, V', J')$ . The quantity which we want to measure is the number density in the lower level is  $N_1(V'', J'')$  defined in the previous section in the case of thermodynamic equilibrium. The number of molecules  $N_2(V', J')$  being excited to the upper level per unit time is given by

$$N_2(V', J') = N_1(V'', J'') \cdot B_{12} \cdot g(\nu_L) \cdot \rho_{\nu_L} \cdot SP(J'') \quad (28)$$

where  $\rho_{\nu}$  is the energy density in Joules  $m^{-3}$  which may be replaced by  $E_p(t)/(Ac)$

as seen in Section 3.2. The rest of the terms in Equation (28) are defined in Section 3.2 and Section 3.4.1. The population  $N_2$  is time dependent because excitation is done in a pulsed mode. A description of this time dependence is critical for accurate population determination (Ref. Section 3.2), however, for the sole purpose of transition identification, it is sufficient to assume that  $N_2$  is constant with time.

In the experiment described here, the laser lineshape  $g(\nu_L)$  has a width of about  $0.05 \text{ cm}^{-1}$  while the absorption linewidth is mainly Doppler broadened and has a width of approximately  $0.01 \text{ cm}^{-1}$ . The laser linewidth was reduced from its original value of  $0.2 \text{ cm}^{-1}$  to  $0.05 \text{ cm}^{-1}$  with the use of an air spaced intracavity etalon of Free Spectral Range (FSR)  $0.5 \text{ cm}^{-1}$ . The laser linewidth was subsequently measured with an air spaced Fabry-Perot etalon of FSR  $1/6 \text{ cm}^{-1}$ . An example of such measurement is shown in Figure 14. Since the absorption linewidth is considerably smaller than the laser linewidth, it is the latter which will be taken into account for the generation of spectra.

It is of interest to predict the absorption spectrum for iodine in thermodynamic equilibrium, the absorption intensity  $I_{abs}$  is proportional to  $N_2$  but in this case it is more appropriate to convolve the discrete absorption distribution by the pumping laser profile  $g(\nu_L)$ .  $I_{abs}$  may then be written

$$I_{abs}(\nu) \propto [N_1(V'', J'') \cdot SP(J'') \cdot B_{12}] \otimes g(\nu) , \quad (29)$$

where the  $\otimes$  symbol stands for the convolution operator. Note that since we are interested in relative intensity distributions the proportional sign and omission of the power density  $\rho_\nu$  are acceptable.

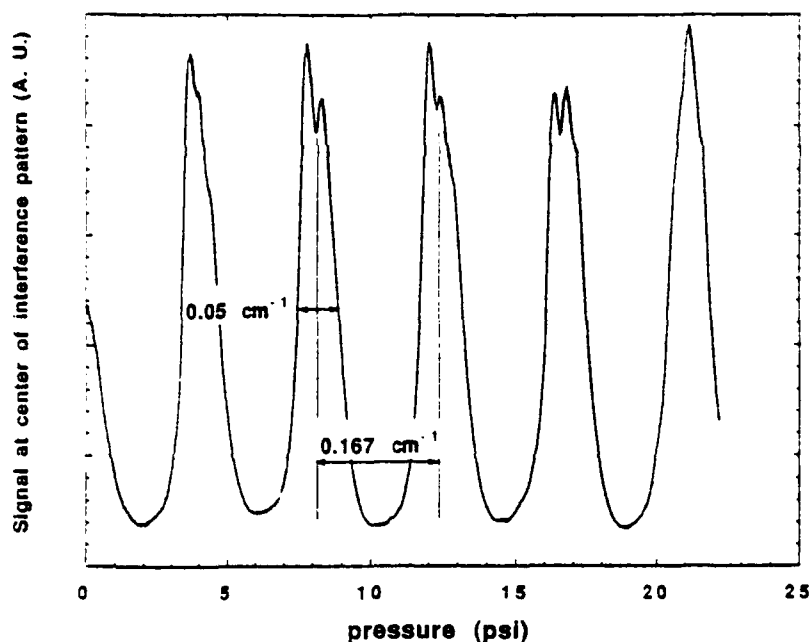


Figure 14: Fabry-Perot trace taken from the laser linewidth narrowed with an intracavity etalon.

The laser intracavity etalon was scanned by pressure tuning

### 3.4.6 Emission intensity

In a general manner the incident laser light excites molecules of one or several lower levels  $(X, V_i'', J_j'')$  to different upper level  $(B, V_i', J_j')$ . For simplicity, we shall consider the case where the laser linewidth is thin enough and the absorption profile is isolated from other transitions so that pumping of a single transition is achieved. In this case, a single upper level  $(B, V', J')$  is being populated and its population is proportional to  $I_{abs}(\nu)$  given by Equation (29). The total fluorescent intensity from level  $(B, V', J')$  is given by the sum of the spontaneous decays to the final lower levels  $(X, V_i'', J_j'')$ :

$$I_{fluo}(\nu) \propto \eta(V', J') \cdot I_{abs}(V', J', V'', J'') \cdot \sum_{V'', J''} A_{21}(V', J', V'', J'') \quad (30)$$

where  $\eta(V', J')$  is an efficiency factor accounting for the portion of the population in the upper level which undergo deexcitation through a non radiative process such as collisional deexcitation or predissociation.  $A_{23}(V', J', V_i'', J_i'')$  is the radiative rate for one transition of the type  $(B, V', J') \rightarrow (X, V_i'', J_i'')$  and is given by Equation (19) where the subscript 1 has been replaced by 3 to avoid confusion between the initial (1) and final (3) lower state. In the context of this study, Equation (30) may be simplified because the emission intensity is observed through a wide spectral window of approximately 20 Å centered around a specified vibrational overtone (usually the first, which corresponds to  $\Delta V = V''_{\text{final}} - V''_{\text{initial}} = 2$ ). The spectral band pass enables detection of all active rotational transitions within a single vibrational band and rejection of scattered photons at the laser frequency. Equation (30) then becomes

$$I_{fluor}(\nu) \propto [N_1(V'', J'') \cdot SP(J'') \cdot B_{12} \cdot A_{23}] \otimes g(\nu) \quad (31)$$

where  $B_{12}$  and  $A_{23}$  are respectively, the absorption and emission rates for a single rovibrational transition. For practicality, we shall assume that the molecules in the upper level  $(X', J')$  are not deexcited by collisions nor predissociate by transitioning to repulsive states. This is shown in Equation (31) by setting  $\eta(V', J')$  to 1. In addition, if one makes the assumption that the electronic transition moment varies slowly with internuclear distance and takes into account that the Höln-London factors are normalized by rotational statistical weights making  $HL(J', J'')/(2J+1) \approx 1/2$  for large  $J$ , Equation (31) becomes

$$I_{fluor}(\nu) \propto [N_1(V'', J'') \cdot SP(J'') \cdot FC(V', V''_1) \cdot FC(V', V''_3)] \otimes g(\nu) \quad (32)$$

where the subscripts 1 and 3 correspond to the initial and final lower states respectively. Note that in Equation (32) the  $\nu^3$  dependence of  $A_{23}$  has been omitted be-

cause the spectral recognition of transitions is usually done over a small wavelength range, typically of the order of 1 Å.

Using Equation (32) and Franck Condon factors determined by Tellin-ghuisen,<sup>38</sup> the relative intensities of all transitions for  $V''' = 0$  to 5,  $V' = 0$  to 59 and  $J'' = 0$  to 159 were calculated for a gas in thermodynamic equilibrium at room temperature (300 K). The generated synthetic spectra were then compared to experimental spectra in order to calibrate the laser and unambiguously identify the transitions being pumped by the laser. Figure 15 shows a predicted and recorded emission spectrum for iodine contained in a static cell maintained at room temperature. The scan had spectral range of 60 Å. For the simulation, an equilibrium temperature of 300 K and a laser FWHM of 0.1 Å were assumed (the laser was scanned without intracavity etalon). The figure shows that transitions for the iodine molecule are abundant because what appears to be noise in the figure are indeed individual transitions. Figure 16 shows a comparison between predicted and measured emission spectra for the same conditions as above but with a laser FWHM of 0.01 Å (the laser was scanned with a synchronized intracavity etalon). The scan had a total spectral range of 1.6 Å. The figure shows a fairly good agreement between experiment and prediction. Although the spectra do not match perfectly, the relative intensities and their spectral positions are close enough to enable identification of a great majority of transitions and establish which transitions are isolated enough to permit their use in the determination of population distributions. The small discrepancies observed in Figure 16 may be due, on the experimental side, to spectral jitter of the line narrowing etalon or, on the prediction side, to the omission of direct dissociation or predissociation in the model.

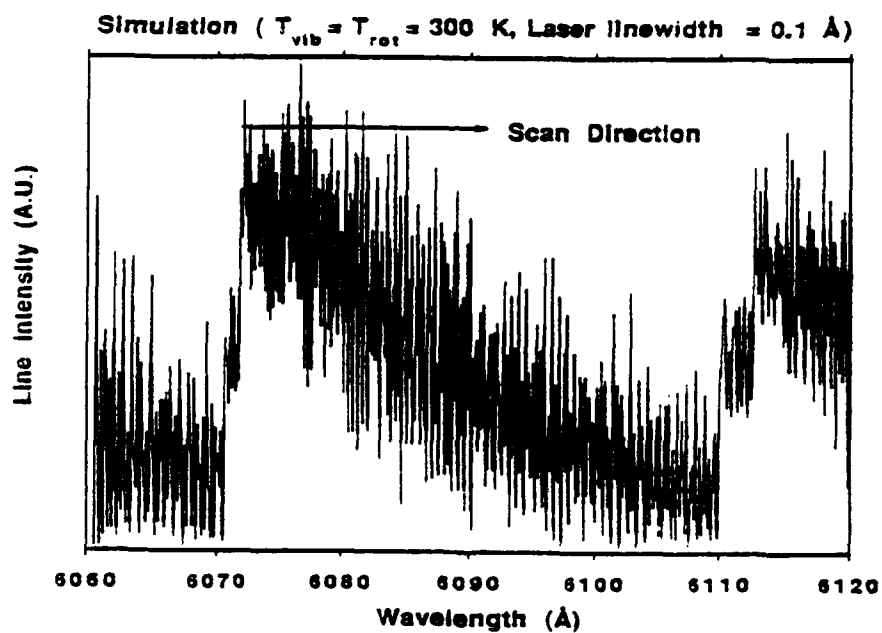
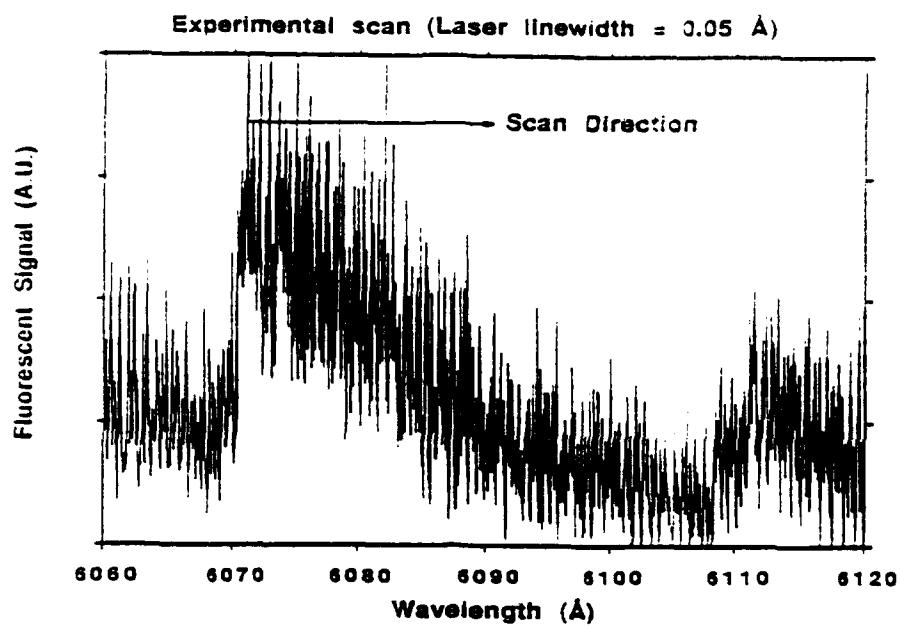


Figure 15: Predicted and measured emission spectra for a spectral range of 60 Å. (Predicted spectrum calculated with a laser FWHM = 0.1 Å).

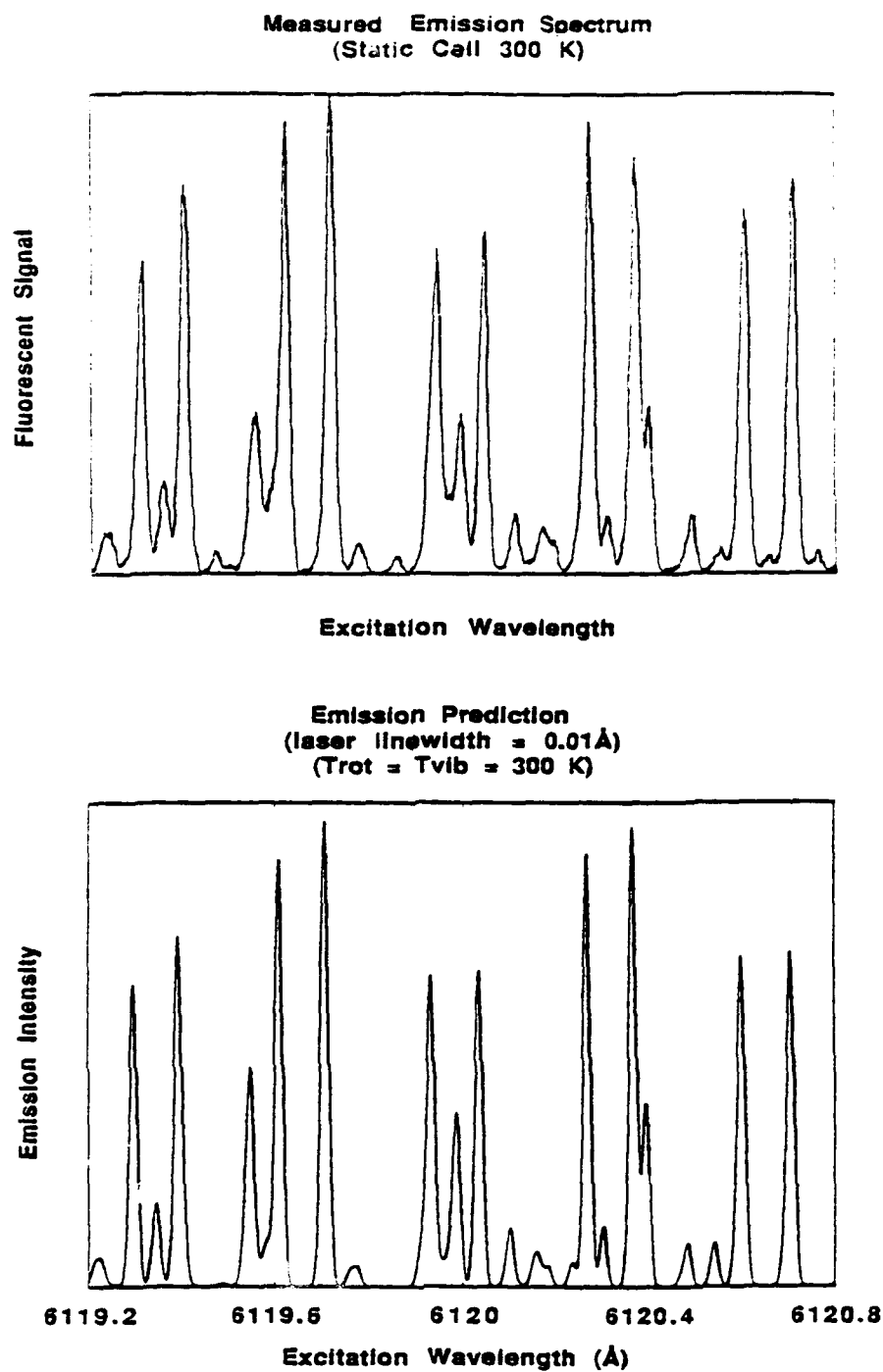


Figure 16: Predicted and measured emission spectra for a spectral range of 1.6 Å. (Predicted spectrum calculated with a laser FWHM = 0.01 Å).

### 3.5 Diagnostic considerations

#### 3.5.1 Laser beam attenuation

As the laser sheet penetrates into the flowfield, photons are absorbed along the laser beam path. Depending on the strength of the transition and the population in the level being probed, this may result in a non negligible attenuation of the laser beam intensity by the time it reaches the point of diagnostics. To investigate this issue, we shall examine the example where the laser sheet illuminates the free jet expansion transversely as illustrated in Figure 22. A position located two orifice diameters downstream of the exit plane, a stagnation pressure of 100 Torr, and a stagnation temperature of 1000 K should correspond to the most critical condition in terms of attenuation. We shall assume a beam energy variation in physical space is described by the following equation:

$$\frac{dP}{P} = -n(z, r) \sigma dr, \quad (33)$$

where  $P$  is the laser beam power,  $n(z, r)$  the number density as a function of axial ( $z$ ) and radial ( $r$ ) coordinate.  $\sigma$  is the absorption cross section given by<sup>39</sup>

$$\sigma = \frac{B_{12} h g(\nu)}{\lambda}. \quad (34)$$

$B_{12}$  is the absorption coefficient defined in Section 3.4.1. As in Section 3.2 we have chosen the (39, 0) R55 transition for which  $B_{12} = 9.26 \cdot 10^{17} \text{ m}^3 \text{ J}^{-1} \text{ sec}^{-2}$ ,  $h$  equals Planck's constant,  $\lambda$  is the transition wavelength equal to 5208 Å and  $g(\nu)$  is the laser spectral profile assumed to be wide compared to the absorption profile and therefore approximated by  $1/\Delta\nu = 9 \cdot 10^{-10} \text{ sec}$ . This gives an absorption cross section  $\sigma$  of  $1.33 \cdot 10^{-14} \text{ cm}^2$  assuming that the absorption coefficient is increased by 25% to account for direct absorption to the repulsive state  $^1\Pi_{1u}$ . (Ref. Section 3.2)



The number density within the plume is given by<sup>52</sup>

$$n(z, r) = N(J)N(V)n(z) \left\{ \cos \left[ \arctan \left( \frac{r}{z} \right) \right]^2 \right\} \left[ \cos \frac{\pi \cdot \arctan \left( \frac{r}{z} \right)}{2\phi} \right]^2, \quad (35)$$

where  $N(J)$  is the number of molecules in a given rotational level  $J$  divided by the total number of molecules in the vibrational level that  $J$  belongs to, and  $N(V)$  is the number of molecules in vibrational level  $V$  normalized by the total number of molecules. Assuming an equilibrium temperature of 340 K,  $N(J) = 1.1 \cdot 10^{-2}$  and  $N(V) = 0.59$ .  $\phi$  is taken as 1.888 and  $n(z)$  is the number density at axial position  $z$  and a radial position of zero given by

$$n(z) = n_0 \left( 1 + \frac{\gamma - 1}{2} M^2(z) \right)^{\frac{1}{1-\gamma}}. \quad (36)$$

$n_0$  is the stagnation number density which is about  $9.6 \cdot 10^{23} \text{ m}^{-3}$  for a stagnation pressure and temperature of 100 Torr and 1000 K respectively.  $M(z)$  is the Mach number at the axial position  $z$  given by Equation (55).  $\gamma = 9/7$  is used under the assumption that both rotational and vibrational degrees of freedom are activated.

Equation (33) is solved for  $P$  for the specified normalized axial position  $z/d = 2$  and the number density field described by Equation (35). The solution  $P(r)$  is shown in Figure 17 along with the number density profile to be expected at this axial position. It may be noticed that the absorption cross section for this particular transition is rather large and results in a substantial absorption of the laser beam, approximately 57% as opposed to only 4% for the (45,1) P74 transition also shown in Figure 17 for which  $N(J) = 9.8 \cdot 10^{-3}$  and  $N(V) = 0.24$  and the absorption coefficient  $B_{12} = 1.17 \cdot 10^{17} \text{ m}^3 \text{ J}^{-1} \text{ sec}^{-2}$ . In summary, attenuation of the laser beam by absorption of photons along the beam path may be significant depending on the transition being pumped. This effect varies the amount of laser power being deliv-

ered to the probed volume and should be taken into account during the determination of populations from observed fluorescence intensities.

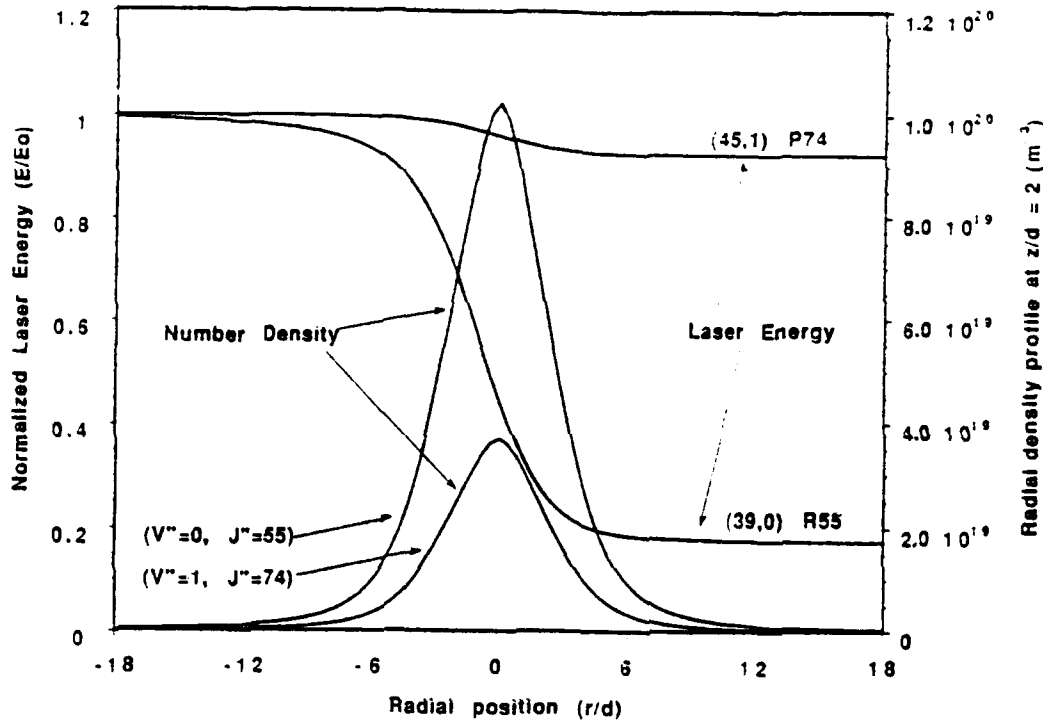


Figure 17: Radial density profile and laser intensity attenuation for the (39, 0) R55 and (45, 1) P74 transitions.

One way to avoid this problem is to reduce the difference in attenuation between transitions by choosing transitions which have a strong absorption for the higher vibrational quantum levels where the populations are generally small, and weak transitions for lower vibrational quantum levels where the populations are large. In practice however, one is never sure that the same degree of attenuation applies to all the probed transitions and therefore, it seems more prudent to avoid the attenuation issue by choosing transitions that are all weak enough, or by probing regions of the flowfield where the number density is low. Another way to minimize attenuation in regions of high number density is to design an experiment where the

laser beam has to travel short distances through the flowfield before it reaches the probed volume. In practice, region of high density are located downstream of the shock system created by a model placed in the flow. Attenuation could then be minimized by introducing the laser beam into the flowfield through the model.

### 3.5.2 Laser beam intrusion

Gas molecules within the region of a focused laser beam may have a different energy distribution than the molecules outside the focal region. Holzer *et al.*<sup>7</sup> have reported a temperature increase of up to 130% due to laser beam heating. Their work was performed with bromine vapor contained in a static cell at a pressure of 160 Torr probed by a continuous wave (CW) 1 W argon ion laser beam tuned at 4880 Å. This raises the question of whether the probing technique of interest here is indeed non intrusive. Because of the pulsed nature of the technique studied here, the available laser energy of approximately  $10^{-4}$  mJ (Ref. Section 3.2) is compressed in a light burst lasting approximately 30 nanosecond. The typical transit time of a molecule in the probed volume is of the order of one  $\mu$ sec, therefore the laser pulse is virtually instantaneous on the time scale of the molecules transiting in the probed volume. Two conditions have to be met before significant heating of the flow by the incident laser beam occurs and the technique be considered intrusive: 1) Heating of the target gas is particularly significant if the laser excitation is tuned close to an absorption band and if the radiative lifetime of the resulting transition is of the same order or larger than the time between collisions. Indeed, heating will occur if the excited molecules transfer their energy through collisions before they have the chance to radiate spontaneously. Under these circumstances not only does the laser beam modify the energy distributions within the flow, but

the fluorescent signal is no longer directly representative of the populations in the probed states since the upper states are deexcited through collisions. 2) The first condition being met, the second requirement is that the energy deposited in the gas be significant enough to change its thermodynamic properties.

Consider how the molecules' radiative lifetime  $\tau_r$  and the time between collision  $\tau_c$  compare to create conditions where beam heating is important. Take the case where  $\tau_r$  is 1.45  $\mu\text{sec}$  for the (39, 0) R55 transition while  $\tau_c$  can vary widely depending on the position within the plume. For instance, at a position close to the orifice, say 2 orifice diameters downstream of the exit plane, the intercollision time is approximately  $(c_0 n \sigma)^{-1} \approx 0.4 \mu\text{sec}$  assuming a local temperature of 500K, a number density  $n$  of  $1.4 \cdot 10^{16} \text{ cm}^{-3}$  and a collision cross section  $\sigma$  approximated by a typical self-quenching cross section<sup>42</sup> equal to  $6 \cdot 10^{-15} \text{ cm}^2$ ,  $c_0 \approx 200 \text{ m sec}^{-1}$  is the mean thermal speed  $\sqrt{(8kT)/(\pi m)}$ . Therefore, the intercollision time being smaller than the radiative lifetime, the first condition for intrusiveness is met. Let us now check if the energy transferred to the molecules is significant enough to perturb the flow. We estimate the energy transferred to the molecules using the results of Section 3.5.1 where about 43% of the laser beam is absorbed by the gas for the (39, 0) R55 transition. Recall that the assumed stagnation temperature and pressure were 1000 K and 100 Torr respectively and that a position of  $z/d = 2$  was chosen to correspond to the worst condition in terms of beam attenuation. In such conditions it may be shown that the laser energy available on the plume centerline at the location of the probed volume is  $3 \cdot 10^{-7} \text{ J}$  and that 7% of that energy is added to the gas contained in the probed volume. This energy produces an increase in gas temperature of only 12 K assuming a specific heat  $c_p$  of  $0.1 \text{ J g}^{-1} \text{ K}^{-1}$ .<sup>40</sup> The temperature increment  $\Delta T$  was calculated using

$$\Delta T = \frac{\Delta E}{c_p \cdot m}, \quad (37)$$

where  $m$  is the total mass of  $I_2$  contained in the probed volume and the volume is a small cylinder 0.15 mm diameter by 0.15 mm length. Further downstream of the orifice exit plane, the number density and temperature decrease relatively fast which has the effect of increasing the intercollision time and hence reduce intrusion of the laser beam. In summary, situations where laser beam heating may pose a problem is when  $\tau_i > \tau_c$  and the energy added to the flow is enough to change the temperature of the flow. About 2% increase in temperature is expected when the number density is of the order of  $10^{16} \text{ cm}^{-3}$ , the local temperature 500 K and the transition is strong with a  $B_{12}$  coefficient  $\approx 10^{18} \text{ m}^3 \text{ J sec}^{-2}$ . Consequently, in the context of this study, we shall consider that the laser beam is non intrusive. It is conceivable that for high enough number density, significant heating of the gas will occur. In this case, it is possible to narrow the observation window so that the fluorescent photons detected are unaffected by collisions.

### 3.5.3 Lineshape broadening

During the LIF process, the emitted photon is considered independent of the absorbed photon and therefore, the scattered radiation lineshape will be subject to lifetime broadening. Since the excited state lifetimes are relatively long ( $10^{-5}$ – $10^{-7}$  sec), the emitted photons is subject to collisional or pressure broadening.

Let us now evaluate the extent to which different broadening mechanisms may affect the spectral distribution of the LIF photons. Pressure and Doppler broadening are expected to be the most significant close to the orifice. The pressure broadened lineshape width is given by

$$\Delta\nu = \frac{125D^2P}{\sqrt{MT}} \text{ (Mhz)}, \quad (38)$$

where  $D$  is the molecule diameter in Å.  $P$  the pressure in Torr,  $M$  the molecular weight and  $T$  the temperature in K. The width of a Doppler broadened may be expressed as

$$\Delta\nu = \frac{214}{\lambda_i} \sqrt{\frac{T}{M}} \text{ (Mhz)}, \quad (39)$$

where  $\lambda_i$  is the incident wavelength expressed in  $\mu\text{m}$ . Taking the extreme pressure of 1 Atm. and the maximum temperature encountered in the facility of 1000 K, one gets a pressure broadened lineshape width of 0.01 Å and a Doppler broadened profile width of  $7 \cdot 10^{-3}$  Å assuming laser pumping at 5145 Å. Therefore, Doppler and pressure broadening of the emitted radiation are too small to pose a resolution problem. Similarly, lifetime broadening can be considered negligible. For a transition of lifetime  $\tau$  the spectral linewidth of the emitted photons is  $(2\pi\tau)^{-1}$ . Choosing a short transition lifetime of  $10^{-8}$  sec results in a linewidth of about  $10^{-4}$  Å for a pumping laser wavelength of about 5000 Å. Predissociation may in certain conditions reduce the lifetime of a transition,<sup>34</sup> however observed predissociation rates are of the same order or smaller than purely radiative rates. Consequently, predissociation produces broadening effects that are of the same order or smaller than lifetime broadening effects and therefore can be neglected.

To summarize, it seems that lifetime and predissociation broadening effects are very small compared to Doppler and pressure broadening which start being of the order of the laser linewidth ( $\sim 0.01$  Å) for regions of the flow where the temperature is above 1000 K and the pressure is higher than 1 Atm. In the context of this work, the laser linewidth is larger than any of the widths resulting from the aforementioned broadening mechanisms. Consequently, the emission spectra are

expected to display peak widths which correspond to the laser linewidth.

### 3.5.4 Predissociation

As mentioned in Section 3.2 molecules pumped into the  $B(^3\Pi_{g,u})$  suffer natural predissociation by transitioning to the repulsive  $^3\Pi_{g,u}$  state (Ref. Figure 3). Predissociation plays a significant role in the determination of the population within a rovibrational level because its magnitude may vary according to the transition being pumped by the laser. It is conceivable that two transitions which are adjacent in wavelength have upper states with completely different quantum numbers and therefore, different predissociation characteristics. In such a case predissociation affects the emission characteristics of both transitions differently and if this difference is unknown or not measured, the relative lower state populations cannot be determined. In this section, it is of interest to investigate the extent to which predissociation may affect LIF measurements and how its effects may be minimized.

Typically the total spontaneous decay rate can be written

$$\frac{1}{\tau_{tot}} = \frac{1}{\tau_{rad}} + \frac{1}{\tau_{nr}} \quad (40)$$

where  $\tau_{tot}^{-1}$ ,  $\tau_{rad}^{-1}$  and  $\tau_{nr}^{-1}$  are the total, radiative and non radiative (due to predissociation) decay rates respectively. Tellinghuisen surmised that the non radiative decay rate is a function of both the excited state vibrational and rotational quantum number:<sup>41</sup>

$$\frac{1}{\tau_{nr}} = \kappa(V) \cdot J'(J'+1) \quad (41)$$

Capelle and Broida<sup>34</sup> measured total spontaneous decay rates ( $\tau_{tot}^{-1}$ ) of the  $B$  state

by direct decay method using a relatively broad band (FWHM  $\approx 1\text{--}10\text{ \AA}$ ) pulsed laser. As a result, their lifetime measurements are not state specific since the observed fluorescence is the result of the spontaneous decay of several excited states. Nevertheless, their measurements showed a few interesting features: 1) A long range variation of the predissociative rate corresponding to the variation in overlap integral of the  $B$  and  ${}^1\Pi_{1u}$  states' wavefunctions. 2) A rather significant scatter thought to be due to the rates' dependence on rotational quantum number. 3) Predissociation rates are similar in magnitude as the purely radiative decay rates. More recently, Paisner and Wallenstein<sup>42</sup> and later Broyer *et al.*<sup>43</sup> repeated Capelle and Broida's experiment with a narrow band laser which enabled excitation of individual rovibrational states. Their study indicates that Capelle and Broida's measurements are off by an average of about 15% and that the predissociative rates are indeed dependent on the upper states vibrational and rotational quantum number for  $V' \leq 18$  as anticipated by Tellinghuisen. Their values of  $\kappa(V')$  are smaller than Tellinghuisen's by a factor about ten. A clear explanation for this discrepancy remains to be produced.

Traditionally, focus has been placed on the  ${}^1\Pi_{1u}$  state because it is mainly responsible for the direct dissociation ( $1u \leftarrow X$ ) of ground state molecules being directly absorbed in the dissociative state during the pumping process. Approximately 10–50% of the total absorption may go into direct dissociative transitions.<sup>32</sup> As mentioned in the previous paragraph the  ${}^1\Pi_{1u}$  state is also a major contributor in the predissociation ( $1u \leftarrow B \leftarrow X$ ) of the  $B$  state. Its relative position to the  $B$  state is fairly well known; the  ${}^1\Pi_{1u}$  state's repulsive branch lies above and parallel to the inner limb of the  $B$  state, and crosses it at a fairly low vibrational level  $V' \approx 24^1$  (Ref. Figure 3). There are however other dissociative states crossing



the  $B$  state on its outer limb. These are the  ${}^3\Pi_{2g}$ ,  ${}^3\Pi_{1g}$ ,  ${}^3\Pi_{0g}$ ,  ${}^3\Sigma_{0u}$ , and the  ${}^3\Delta_{3u}$  states according to Steinfeld<sup>44</sup> while Mulliken believes the  ${}^3\Pi_{0g}$  state may indeed be the  ${}^3\Sigma_{0u}$  state.<sup>33</sup> Very little attention has been given to the effect these states may have on predissociation rates. Since these levels cross the outer limb of the  $B$  state, one would expect a significant increase in predissociative reactions when the laser becomes resonant with a transition whose upper level matches the crossing point energy. A similar argument has been used by Mulliken in order to identify dissociative states which play a significant role in magnetic predissociation.<sup>33</sup> This sudden increase in predissociative rate has not yet been observed experimentally. Even Broyer *et al.*<sup>43</sup> who were able to measure radiative lifetimes of individual rovibrational transitions with the use of two independent methods, could not show evidence of that phenomenon. Their study however, was performed by exciting a limited number of transitions which most probably did not correspond to crossing points. Steinfeld<sup>44</sup> attempts to determine the vibrational levels of the  $B$  state which correspond to crossing points, these are shown in Figure 3, but there is enough uncertainty both in the position of the repulsive states and their identity that a precise determination of the crossing point energy and internuclear distance is virtually impossible. A more systematic study, where the lifetime of subsequent rotational transitions within the same vibrational state is measured, is in order if predissociation from crossing states is to be investigated. The experiment conducted in the present study shows some evidence that predissociation from other states than the  ${}^1\Pi_{1u}$  state may play a significant role if individual rovibrational transitions are excited. This will be discussed in Section 5.5.

In summary, predissociation of the upper state involved in the pulsed LIF process of interest here is significant and cannot be neglected. Most of the pre-

dissociation is caused by the  ${}^1\Pi_u$  state. Its effects can however be quantified because many studies have been dedicated to determining decay rates of the rovibrational levels of the  $B$  state. However, complications may arise from other dissociative states crossing the  $B$  state on its outer limb because predissociation induced by these states has not been examined in detail. In order to avoid any potential problems related to these states, it is recommended that levels suspected of being close to a crossing point be avoided. Another way to avoid this problem would be to systematically measure, under well defined experimental conditions, the lifetime of each upper state being used in the technique.

### 3.5.5 Quenching

The previous paragraph showed how the upper excited state  $B({}^3\Pi_0 - u)$  may be depopulated by predissociative reactions. Another mechanism by which the upper state can relax is collisional deexcitation. This would correspond to the term  $R_2$  in Equation (3) becoming of the same order as the spontaneous radiative decay term  $A_2$  and the predissociative rate  $A_{\text{dis}}$ . This phenomenon, more commonly known as quenching, occurs when the molecules excited to the  $B$  state are deexcited by means of energy transfer during collisions with other molecules rather than by emitting a photon. Under this condition, the upper state population and consequently the fluorescent intensity (integrated over the excited state's lifetime) become independent of the lower state population. Quenching becomes significant when the intercollision time  $\tau_c$  based on a quenching cross section  $\sigma_q$  is of the same order as the radiative lifetime  $\tau_{\text{rad}}$ . The argument is similar to the one developed in analyzing the intrusiveness of the laser beam, (Ref. Section 3.5.2) but this time a quenching cross section is used instead of a collision cross section. Quenching

cross sections for a variety of transitions and quenching partners have been reported.<sup>42</sup> A typical self quenching cross section is approximately  $60 \text{ \AA}^2$ . As mentioned in Section 3.2, most of the pressures conditions encountered in the flowfields examined in this work are low enough that quenching may be neglected. However, taking the extreme flow conditions of the example in Section 3.5.2, it can be shown that the intercollision time is of the same order as the radiative lifetime. This implies that at least for these conditions, quenching effects may be significant enough to prevent the accurate measurement of populations. Moreover, future experiments will probably be performed at higher pressures where quenching effects are definitely significant. In the subsequent paragraphs, we shall examine what may be done to the probing technique so that it is not sensitive to quenching effects.

The fluorescent trace produced by a short laser pulsed has a maximum that is proportional to  $N_2(0^+)$  the population in the excited state immediately after the laser pulse. The laser pulse width is assumed smaller than the intercollision time based on a quenching cross section. For the sake of argument, let us for now ignore all the depopulating terms of Equation (3), in such a case  $N_2(0^+)$  can be approximated by

$$N_2(0^+) = N_1 B_{12} g(\nu_L) \frac{E_p}{Ac}, \quad (42)$$

where all the terms have been defined in Section 3.2. After the pulse, the fluorescence decays as

$$N_2(t) = N_2(0^+) e^{-\left(A_{rad} + \sum A_{21} + \sum R_{21}\right)t}, \quad (43)$$

where all the terms have been defined in Section 3.2. Noting that the quenching

rate  $R_2$  may be written as the product of the lower state population  $N_1$ , a quenching cross section  $Q_2$  and an average relative velocity  $V_r$ .  $N_2(t)$  may be rewritten as

$$N_2(t) = N_1 B_{12} g(v_L) \frac{E_p}{Ac} e^{-\left(A_{pdis} + \sum A_{2i} + \frac{N_1}{N(V'')N(J'')} \sum V_r Q_{2i}\right)t}, \quad (44)$$

where it is assumed that the total population  $N_0$  in the  $X$  state is proportional to the population  $N_1$  in the rovibrational level being excited by the laser:

$$N_1 = N(V'')N(J'')N_0, \quad (45)$$

where  $N(V'')$  and  $N(J'')$  have been defined in Section 3.5.1. The fluorescence signal integrated over time is:

$$I_{fluor} = \int_0^\infty N_2(t) dt = \frac{N_1 B_{12} g(v_L) E_p}{Ac \left[ A_{pdis} + \sum A_{2i} + \frac{N_1}{N(V'')N(J'')} \sum V_r Q_{2i} \right]}. \quad (46)$$

If quenching becomes important, the predissociation and spontaneous decay terms may be ignored and Equation (46) becomes

$$I_{fluor} = \frac{N_1 B_{12} g(v_L) E_p N(V'') N(J'')}{Ac N_1 \sum V_r Q_{2i}}, \quad (47)$$

which is independent of  $N_1$ . So in the quenched limit, the peak of the LIF signal is directly proportional to  $N_1$ , while the integral is not. Based on this fact, we detect fluorescence only at the peak of the fluorescent pulse. This is achieved by gating the detection with a 100 nsec window centered around the laser pulse maximum. Since most of the upper states used in this work are long lived ( $\tau_{rad} \approx 1-2 \mu\text{sec}$ ), it is reasonable to assume that a 100 nsec gate detects only the photons emitted at the maximum of the fluorescent pulse. The gate width is chosen to be small compared to the radiative lifetime, but wide enough to minimize noise induced by laser jitter.

## Chapter 4

### The Pilot Scale Hypersonic Wind Tunnel

#### 4.1 Introduction

The pilot scale hypersonic wind tunnel was conceived so that difficulties in handling iodine could be dealt with on a scale that would allow easy and inexpensive modifications of the facility should design-related failure occur. A semi-continuous operation of the wind tunnel does not only serve as a proof of concept, but is also used as the basis for the design of a larger scale wind tunnel also operating on iodine but running at about ten times the flow rate of the facility described here. The corrosive nature of iodine and the wide temperature range encountered in different components of the facility are the two main design considerations. Because very little data can be found on materials resisting corrosion from high temperature iodine, the pilot scale wind tunnel described here is ideal to test the few corrosion resistant candidates as well as preliminary operational procedures.

A schematic of the vertically mounted prototype wind tunnel facility is shown in Figure 18. The facility is a closed circuit for safety reasons regarding the toxic nature of iodine (Ref. Section 4.7), it operates on a semi-continuous basis with a run time of roughly 1/2 hour and a recirculation time of about 2 hours. During the run phase, high temperature iodine stored in the boiler is expanded through a sonic orifice and into a vacuum chamber where optical diagnostics are performed. The iodine flow is pumped using condensation shields in the cold traps mounted in series for better protection of both the diffusion pump and the roughing pump. The second phase of the operation consists of recycling from the cold

traps used to condense the iodine during the run phase, to the supply chamber (boiler) cooled to liquid nitrogen temperature. Recirculation is achieved by the pressure differential between the heated cold traps and the cooled boiler walls.

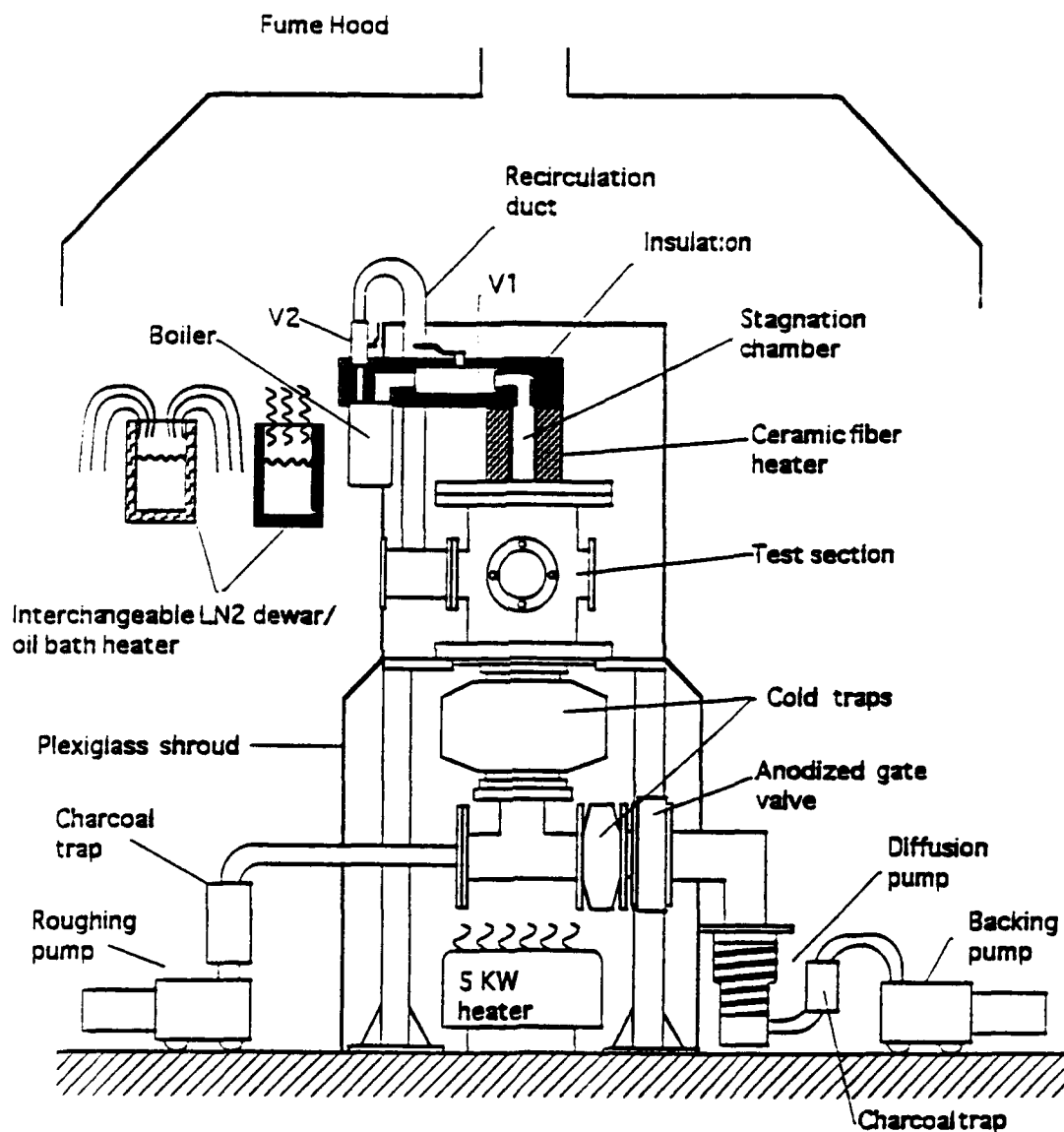


Figure 18: Schematic of the pilot scale hypersonic wind tunnel operating on pure iodine.

Figure 19 shows a pressure-temperature diagram for the facility used in his work. Note that the stagnation temperature and pressure represented correspond to the extreme case of 1000 K and 760 Torr, respectively. Typical flow conditions for the

data presented in this work are 1000 K and 100 Torr.

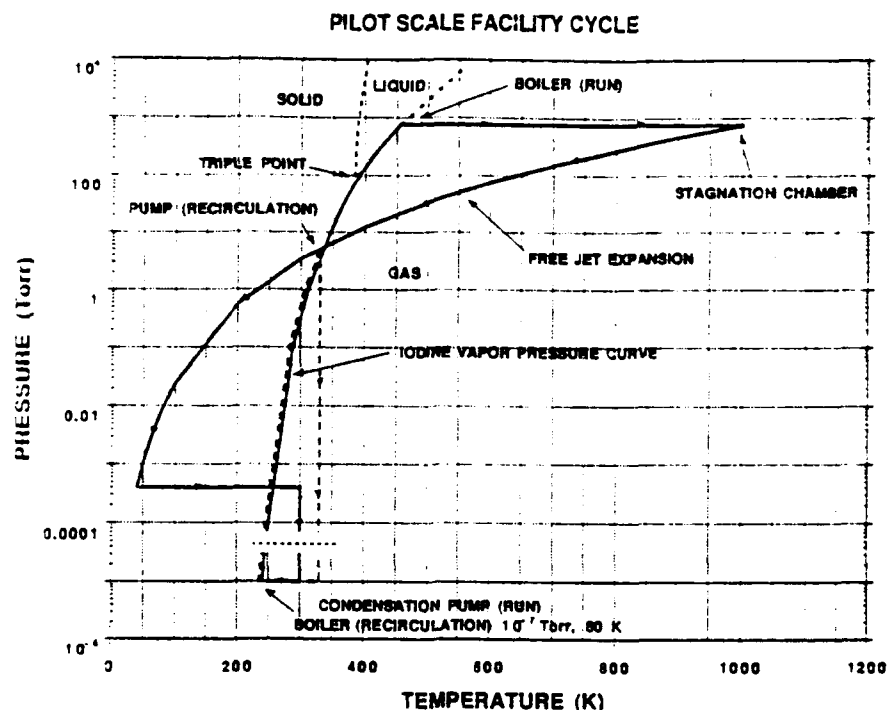


Figure 19: Pressure-temperature diagram of the pilot scale wind tunnel cycle.

Preliminary calculations indicate that for a stagnation pressure of 100 Torr, an orifice diameter of 2 mm and a stagnation temperature upstream of the orifice of about 1000 K, the mass flow rate during the run phase is  $0.15 \text{ g sec}^{-1}$  (Ref. Equation (48)). If a total mass used per run is fixed at 1 kg, the run phase will last approximately 30 minutes. The following sections will describe the work that has been done on the construction of the pilot scale flow facility. Design considerations, problems encountered, solutions and suggestions are outlined.

#### 4.2 The boiler and stagnation pressure measurement

During the run phase, the supply of iodine is heated so that the iodine vapor pressure corresponds to the stagnation pressure desired for the run. For example, in

order to obtain a stagnation pressure of 100 Torr, the boiler temperature has to be regulated to about 390 K. The vapor pressure curve of iodine is shown in Figure 25. The pressure in the injection portion of the wind tunnel (i.e. just upstream of the sonic orifice) is expected to remain at the boiler pressure since the transfer duct between the boiler and the stagnation chamber has an inner diameter which matches that of the stagnation chamber. The stagnation chamber and transfer duct are made of Hastelloy® (C276) which was found to be the only commercially available alloy capable of resisting iodine corrosion at high temperatures. The transfer duct is heated by four 500 Watts mica band heaters and insulated with mineral wool to minimize heat losses and hence prevent crystallization of the iodine on the duct's inner wall. For the same reason the 3.5 cm I.D. ball valve V1 separating the stagnation chamber from the boiler is heated with heat bands and insulated. All the ball valve surfaces in contact with iodine are made of SS 316 and the ball seat material is virgin Teflon®. The boiler is one of the most critical part to design because it has to be heated as uniformly as possible in order to avoid cold spots on which the iodine would condense. Moreover, the boiler has to withstand temperatures up to 455 K (where the iodine vapor pressure is about 760 Torr) during the run phase and has to be cooled to liquid nitrogen temperatures during the recycling period. For the facility to have a rapid turn around time, the boiler has to be thermally cycled quite rapidly (from 455 K to 70 K) in minutes without loss of vacuum integrity. For this reason, the boiler is entirely made of Hastelloy and welded together to avoid seal degradation during thermal cycling. Heat to the boiler is provided by a bath of recirculated hot synthetic oil for uniform and better heat conduction. In the latter part of the project, this heating scheme was replaced with three 1250 Watts mica band heaters in direct contact with the boiler circumference and ther-



mally isolated from the ambient air with mineral wool.

Pressure in the boiler was determined by measuring the deflection of a previously calibrated Hastelloy bellows. The bellows is capped on one end and the remaining open end is welded to a 2.5 cm hole drilled between the boiler and V1. A cylindrical guide allows the bellows to expand and contract along a single axis without significant friction. Figure 20 shows calibration curves obtained by evacuating the boiler until the pressure is about  $10^{-3}$  Torr, then slowly introducing air in the boiler while recording both the pressure and the corresponding bellows deflections. Although the procedure was repeated for several temperatures (20, 120, 180° C), it was found that the bellows deflection is relatively temperature independent. The curves shown in Figure 20 indicate that iodine pressures from 20 Torr to 760 Torr can be measured with an accuracy ranging from 10% at 20 Torr to about 4% at 760 Torr.

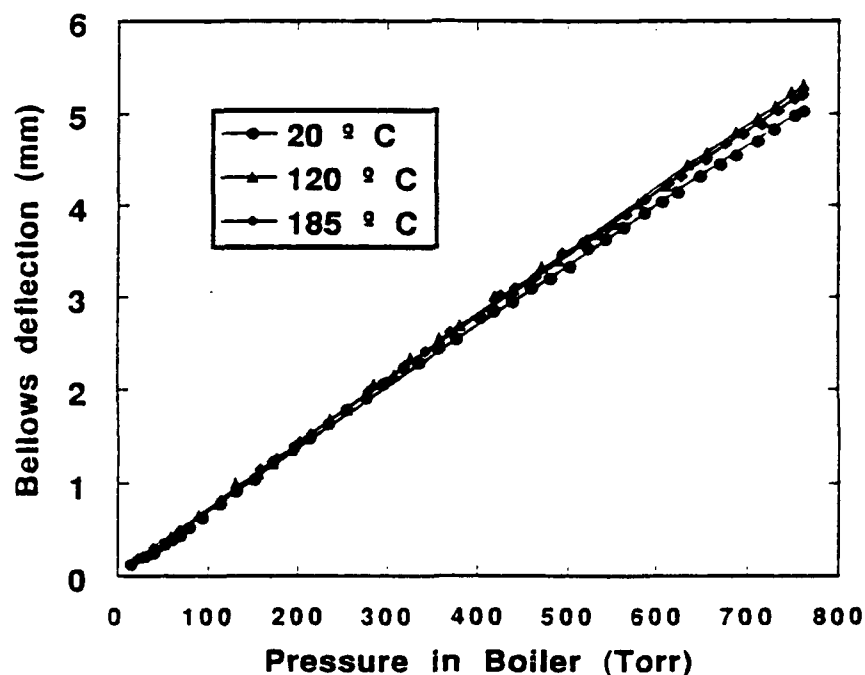


Figure 20: Iodine pressure gauge calibration curves for different temperatures.

### 4.3 The stagnation chamber

The primary purpose of the stagnation chamber is to superheat the iodine from the boiler temperature of about 400 K to the stagnation temperature desired for the run which is usually of the order of 1000 K. The stagnation chamber being the hottest component of the entire flow facility, special attention had to be given to its design to prevent corrosion from iodine and minimize heat losses. The central body of the stagnation chamber assembly is made of a 3.5 cm I.D. Hastelloy cylinder welded at one end to a transfer tube connected to V1, and threaded at the other end to allow easy replacement of the sonic orifice assembly. The data presented in this work was obtained with an orifice assembly consisting of a Monel® plug in which a 2 mm orifice was drilled. The orifice's aspect ratio  $L/D$  is about 0.5. The orifice assembly can easily be interchanged with another orifice of different size or a nozzle if the plume properties need to be changed. The interchangeability of the nozzle assembly may also allow convenient inspection of the stagnation chamber interior for traces corrosion or deposits.

The mass flow exiting the stagnation chamber may be calculated using

$$\dot{m} = \frac{A^* P_0}{\sqrt{\frac{kT_0}{m}}} \sqrt{\gamma} \left( \frac{2}{\gamma+1} \right)^{(\gamma+1)/(2(\gamma-1))} \quad (48)$$

where  $P_0$ ,  $T_0$  are the stagnation pressure and temperature respectively.  $A^*$  is the cross sectional area of the throat,  $m$  is the mass of the iodine molecule equal to  $4.22 \cdot 10^{-25}$  kg and  $k$  is Boltzmann constant.  $\gamma$  is the specific heat ratio taken as 9/7 under the assumption that both rotational and vibrational degrees of freedom are activated. If the stagnation pressure is tuned to 100 Torr and the stagnation temperature to 1000 K, the mass flow rate is about  $0.15 \text{ g sec}^{-1}$  for a 2 mm diameter

orifice. And the resulting run time is about 30 minutes for a total supply of iodine of 1 kg.

To minimize heat losses from the stagnation assembly to the test section, a 2 mm thick Hastelloy membrane is welded to the bottom of the stagnation chamber and connects it to the test section. Assuming a linear decay of temperature through the membrane, and a thermal conductivity of  $0.2 \text{ W cm}^{-1} \text{ K}^{-1}$  (typical value for nickel alloys), the maximum power loss through the membrane is approximately 140 W. The membrane will also confine losses due to black body radiation from the nozzle or orifice assembly and its immediate vicinity. Preliminary calculations indicate that at most 80 W would be lost assuming ideal black body radiation and a radiating surface of approximately  $10 \text{ cm}^2$ . Because the Hastelloy membrane is thin, it does not counteract any axial loads due to the difference of pressure between the interior and the outside of the chamber. To prevent the stagnation chamber from collapsing in the test section, four small vertical winglets are welded to the top of the stagnation chamber and rest on a platform which can be adjusted in height. The winglets are designed with point contacts to the platform to minimize heat losses due to conduction. The stagnation chamber is heated with two 500 Watts ceramic fiber heaters whose body is molded in ceramic fiber material for thermal insulation.

The iodine supplied by the boiler diffuses to the stagnation chamber at a pressure of approximately 100 Torr and a temperature of 390 K. The purpose of the stagnation chamber is to transfer enough energy to the iodine to raise the gas from boiler temperature to the desired stagnation temperature of about 1000 K. The dimensions of the stagnation chamber are chosen so that the transit time of

the iodine in the chamber is large enough to allow equilibration of the iodine temperature to the wall temperature. Let us assume a mass flow rate of  $0.1 \text{ g sec}^{-1}$  and a specific heat for iodine of  $0.15 \text{ J g}^{-1} \text{ K}^{-1}$ , the power required to heat the gas from 390 K to 1000 K is approximately  $P_{\text{req}} = 8 \text{ W}$ . Taking the local coefficient of heat transfer  $H$  for turbulent flow as  $0.334 \cdot 10^{-4} \text{ J sec}^{-1} \text{ cm}^{-2} \text{ K}^{-1}$ ,<sup>45</sup> the length  $L$  of the stagnation chamber required to heat the iodine may be obtained by equating power required to power transferred from the chamber walls:

$$L = \frac{P_{\text{req}}}{H\pi D\Delta T} \quad (49)$$

where  $D$  is the diameter of the stagnation chamber and  $\Delta T$  is the logarithmic mean of the temperature increase of the gas. Using Equation. (49), a length  $L$  of 27 cm is obtained for a tube diameter  $D$  of 3.8 cm. The actual length of the stagnation chamber is about 30 cm.

The determination of the degree of dissociation of the  $I_2$  molecules in the stagnation chamber is of importance if chemistry is to be studied in the plume downstream of the expansion throat. An estimate of the degree of dissociation may be obtained by assuming thermodynamic equilibrium of an ideal dissociating gas in the stagnation chamber. By combining the law of mass action:<sup>46</sup>

$$\frac{\alpha^2}{1-\alpha} = \frac{p_d}{p} e^{-\epsilon_d/T} \quad (50)$$

and the ideal dissociating gas law

$$p = \frac{2Pm}{(1+\alpha)kT} \quad (51)$$

one can solve for the degree of dissociation  $\alpha$

$$\frac{\alpha^2}{1-\alpha^2} = \frac{p_d}{2mP} kT e^{-\epsilon_d/T} \quad (52)$$

where  $\theta_d$ ,  $P$  and  $T$  are the characteristic temperature of dissociation taken as 17894 K, the pressure and the temperature on the gas respectively,  $k$  is the Boltzmann constant and  $m$  the mass of the iodine atom equal to  $2.1 \cdot 10^{-25}$  kg.  $\rho_d$  is a characteristic dissociation density<sup>46</sup> defined as:

$$\rho_d = m \left( \frac{\pi m k}{h^2} \right)^{3/2} \theta_r \sqrt{T} (1 - e^{-(\theta_v/T)}) \frac{(Q_{el}^a)^2}{Q_{el}^{aa}}, \quad (53)$$

where  $\theta_r$  and  $\theta_v$  are the characteristic temperature for rotation and vibration taken as 0.0542 K and 308.8 K respectively and  $Q_{el}^a$  and  $Q_{el}^{aa}$  are the electronic partition functions of the atom and of the molecule taken as 4 and 1 respectively,  $h$  is Planck's constant,  $m$ ,  $k$  and  $T$  have been defined earlier. Figure 21 shows the degree of dissociation one would expect to find in the stagnation chamber as a function of stagnation temperature for stagnation pressures of 30, 100 and 760 Torr.

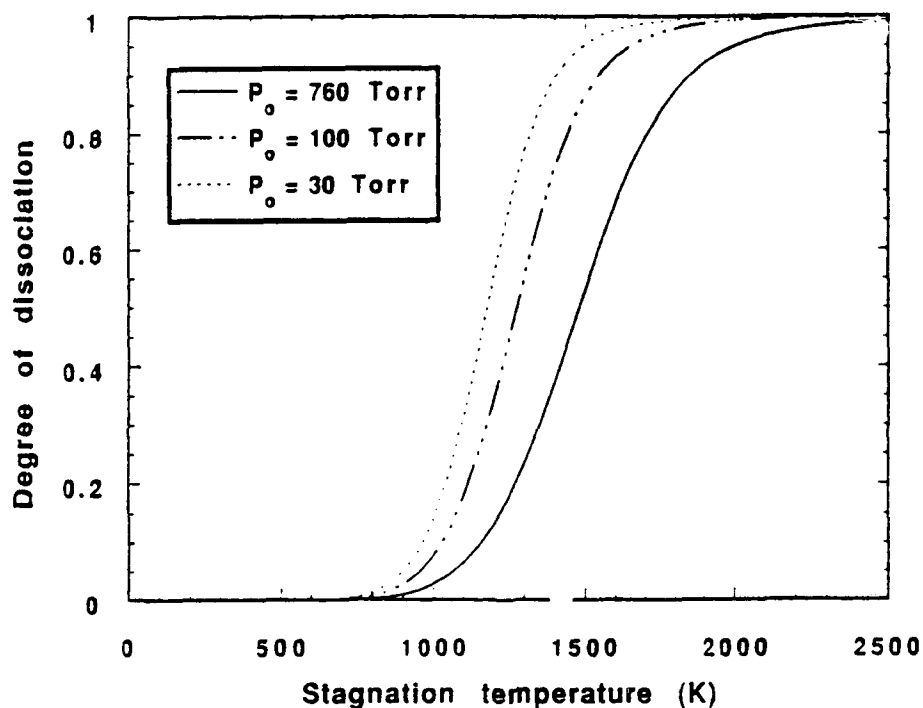


Figure 21: Degree of dissociation in the stagnation chamber versus equilibrium temperature for stagnation pressures of 30, 100, 760 Torr.

#### 4.4 Pumping of iodine and incondensibles

During the run phase, the iodine flows through the sonic orifice or nozzle, expands in the test section where diagnostics are performed and is subsequently pumped by condensation on two cold traps mounted in series. The cold traps are Teflon coated and have a combined cryogenic surface of approximately 600 cm<sup>2</sup> yielding a pumping capacity of about 1 g sec<sup>-1</sup> assuming a total accommodation of the iodine molecule after one hit on the cryogenic surface, a pressure of 500 mTorr and room temperature (saturation of the shields has been neglected). Pumping of the incondensibles during the run phase is undertaken by a diffusion pump with a pumping capacity of about 1000 liters sec<sup>-1</sup> able to maintain the background pressure at 10<sup>-4</sup> Torr. It is important that the diffusion pump and its roughing pump be isolated from the iodine, for this reason, the cold traps are always kept at liquid nitrogen temperature during the run phase. Krytox® diffusion pump oil was found to be the only low vapor pressure oil that does not react with iodine. All hydrocarbon based diffusion pump oils showed some reaction with iodine and consequently, could not be used. In a general manner Krytox pump oils and vacuum grease proved to be rather inert in an iodine environment.

#### 4.5 Recycling

When all the iodine supply contained in the boiler has been used, most of the working gas is in principle frozen on the cold traps. At this stage, recycling of the iodine can be performed: the gate valve is closed to protect the pumping units, hot air is blown through the cold traps so that the frozen iodine sublimates (Ref. Figure 19), V<sub>2</sub> (Ref. Figure 18) is opened and the boiler walls are now cooled to LN<sub>2</sub> temperature. During this phase, the cold traps are heated to about 330 K where the

iodine vapor pressure is about 3 Torr (Ref. Figure 19). When the iodine evaporates, it flows through the return duct and freezes on the boiler walls. During the recycle phase, it is important that the pressure remains low enough to allow flow of the iodine. Since the pumping system is at this point isolated from the chamber, it is critical that the leak rate of the chamber is reduced to a minimum. Calculations assuming an incompressible Poiseuille flow within the return duct indicate that the recirculation time should be of the order of 1 hour. The mass flow rate through the recycling duct is described by<sup>47</sup>

$$\dot{m} = \frac{\pi a^4}{8\eta L} \cdot \frac{P^2}{2} \cdot \frac{m}{kT}, \quad (54)$$

where  $a$ ,  $l$ ,  $m$  and  $\eta$  are the radius, length of the tube, the mass of the iodine molecules and the viscosity of the iodine vapor respectively.  $P$  and  $T$  are the pressure and temperature taken as 2 torr and 323 K respectively. A value of  $14 \cdot 10^{-6}$  N sec  $m^{-2}$  was selected for the viscosity<sup>48</sup> at 323 K. In practice, however, recirculation times are 2 to 3 hours. This is partly due to transients in heating the cold traps and losses in the recirculation path caused by bends and constrictions.

In order for the recirculation process to be efficient it is important that all parts of the test section be heated to the temperature corresponding to the vapor pressure necessary to drive the iodine to the boiler. For this purpose, a plexiglass shroud was built around the entire facility and a 5 kW heater is used to blow hot air around it (Ref. Figure 18). If the test facility is nonuniformly heated, iodine will condense on its coldest surfaces, thus delaying the recirculation process.

A subtle but important issue concerning recirculation deals with the accumulation of incondensibles in the boiler. As the iodine vapor condenses on the

boiler walls, incondensibles carried with it are separated from the  $I_2$  molecules and over time build up pressure within the boiler, which in turn slows further flow of iodine from the test section. Venting of the incondensibles during the recirculation phase is therefore necessary. This was achieved either by opening V1 (Ref. Figure 18) during recirculation, or actively pumping on the downstream side of the boiler using a bypass line to the main pumping system. Related phenomena are relatively well known effects to users of cold trapped Macleod gauges. It was also used by Muntz to enhance the operation of an isotope separation system.<sup>49,50</sup>

#### 4.6 Material considerations

As may have been noticed in the preceding sections, the use of high temperature iodine as a working gas makes the choice of the materials used in the construction of the wind tunnel critical. The corrosive nature of iodine particularly at high temperatures is one of the main considerations in the design of the flow system. Very little data was found on materials resisting iodine corrosion, for this reason, the pilot scale wind tunnel can also be viewed as a means of testing materials whose adequacy for use in an iodine environment is questionable. Table 4 gives a summary of the metals we feel are good candidates for use in the flow system along with their composition. As may be seen from this table, a higher content of nickel and molybdenum seems to be a decisive factor in resisting iodine corrosion. When the use of non metallic materials is required, for example when gaskets or coatings are required, it was found that Teflon and fluocarbon provide excellent resistance to iodine corrosion. More recently 3M® produced an elastomer registered as Aflas® which supposedly has the same corrosion resistant characteristics as Teflon and therefore would be a very good candidate for use in an iodine environment. Sim-



ilarly. Dupont<sup>®</sup> produces a perfluoroelastomer registered as Kalrez<sup>®</sup> which also exhibits excellent inertness to iodine. Pyrex<sup>®</sup> and porcelain are also very adequate materials to use in contact with iodine, but they obviously cannot be used as gaskets and are difficult to use as coating materials. The ability of a material to resist corrosion is often times measured in length of penetration of the corroder per year of exposure at a given temperature. Given the time frame of the pilot scale iodine wind tunnel project which is about two years, some materials were used even though they only offer moderate resistance, with the idea of replacing the corroded parts when erosion can no longer be tolerated. During some preliminary testing of current materials used in laboratories, it was found that copper, aluminum, SS 304 are not suitable for use in an iodine environment while Hastelloy, Monel, SS 316, Pyrex and Teflon are more suited to resist iodine corrosion.

Alloy	C	Mg	Si	P	S	Cr	Ni	Mo	Cu	Fe	Mn
SS 316	0.1	2	1	0.04	0.03	16-18	4-10	2-3			
Monel						17	53	19		6	
Hastelloy							67		30	1.5	1

Table 4: Alloys used in the injector assembly and their compositions.

Since the stagnation chamber and boiler assembly are the parts of the flow system in contact with iodine at high temperature, the choice of metals used for the design of the iodine injecting assembly was given particular attention. All the parts composing the boiler, transfer ducts and stagnation chamber, were made of Hastelloy which is by far the best choice for resisting iodine corrosion. Unfortunately, the ball valves V1 and V2 could not be obtained in Hastelloy, and therefore were made of SS 316. Other coating processes may be used in order to resist

iodine corrosion, these include hard anodizing aluminum, Teflon coating and Hastelloy plasma coating.

#### **4.7 Safety considerations**

When inhaled, iodine may cause eye, nose, throat and respiratory tract irritation. If exposure is repeated, bronchitis, skin rashes, loss of appetite and sleep may result. Discontinuation of exposure is necessary to recover from ill effects. The maximum accepted concentration is 0.1 ppm, which corresponds to  $1 \text{ mg/m}^3$  at standard atmospheric conditions. Reported lethal doses lie between a few tenths of a gram to more than 20 grams.<sup>39</sup> For the work described in this paper, the quantities of iodine used are of the order of kilograms at pressures of approximately 100 Torr, it is therefore absolutely necessary that leaks will only be into the facility and that satisfactory fail-safe features are designed in place.

#### **4.8 Free jet expansion of high temperature iodine**

For the purposes of this study, a free jet expansion impinging on a disk was used. Free jets have the advantage of being relatively simple and have been studied in detail in the past.<sup>52</sup> In addition, a free jet is ideal for the present work if freezing of the molecules' internal energy is to be observed. A disk was placed in the free jet flowfield to generate a normal shock and consequently create a high temperature region downstream of the shock where nonequilibrium effects may be observed.

##### **4.8.1 Properties of free jet expansions**

Free jets have been used extensively in the past to obtain high speed flows in the

study of molecular beam, formation of clusters, nonequilibrium phenomena, internal energy relaxation, isotope separation, etc... For the purpose of this study, we use a free jet expansion for the generation a high speed flow of pure iodine molecules whose internal energy modes are thermally excited from stagnation conditions. A diverging nozzle flow may be used in future work, but for simplicity, this work will only deal with a free jet expansion. Diagnostics will be performed non-intrusively in the plume of the expansion to probe the internal energy states of the molecules composing the flow. For this to be possible, a preliminary knowledge of the plume characteristics is necessary. For example, the number density at different positions within the plume determines whether collisional quenching effects are significant, how much light scattering may be expected and what broadening mechanisms are dominant. Other phenomena have to be considered in the design of the experiment, for instance, the formation of clusters could significantly affect the light scattering intensity since the latter is proportional to the 6<sup>th</sup> power of the particle size (as long as the particle dimension is smaller than 5% of the incident wavelength).<sup>51</sup> The freezing and decoupling of translational, rotational and vibrational temperatures is also of concern here because it is a direct result of nonequilibrium phenomena within the plume.

A comprehensive study conducted by Ashkenas *et al.*<sup>49</sup> gives a rather concise and practical guide to determine properties of inviscid to slightly viscous flow in the central core of a supersonic free jet. Figure 22 shows the nomenclature which we shall adopt to define various quantities related to a sonic orifice flow-field. The Mach number increase along the free jet centerline may be described by

$$M = A \left( \frac{z-z_0}{D} \right)^{\gamma-1} - \frac{1}{2} \left( \frac{(\gamma+1)/(\gamma-1)}{A \left( (z-z_0)/D \right)^{\gamma-1}} \right), \quad (55)$$

where  $z_0/D = 0.85$  and  $A = 3.96$  are constants determined by comparison to the solution of characteristics.

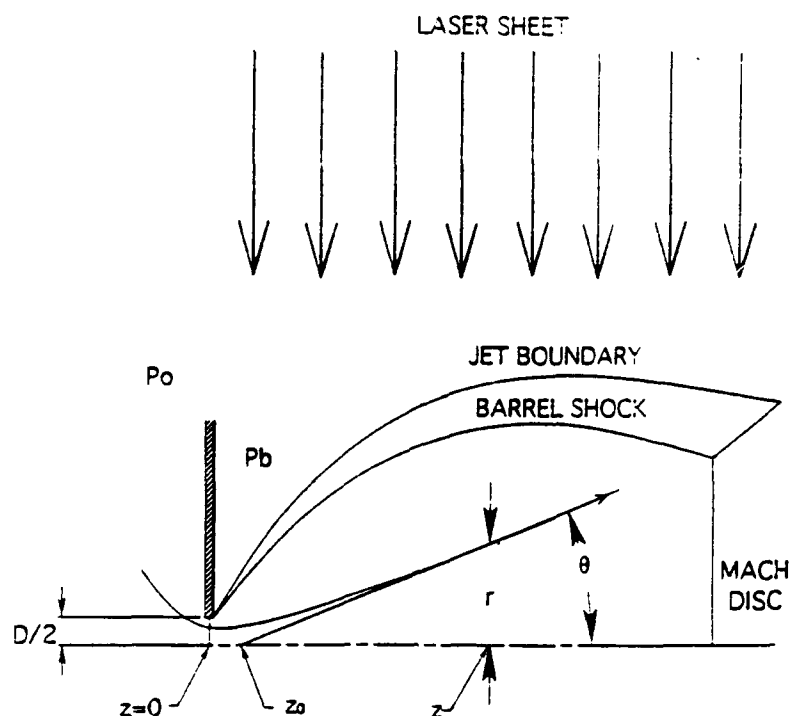


Figure 22: Free jet expansion nomenclature and laser sheet configuration.

In Equation (55),  $D$  is the orifice diameter and  $\gamma$  equals  $9/7$ . This particular value of the specific heat ratio is used because the iodine molecules are assumed to be vibrationally and rotationally excited due to the relatively elevated stagnation temperature. The pressure, number density and temperature within the plume of the free jet may be estimated by assuming that the expansion is isentropic and using the usual isentropic flow relation between Mach number, stagnation and static conditions. Figure 23 shows the Mach number, normalized number density, pressure and translational temperature along the plume centerline for specific heat ratios of  $7/5$  and  $9/7$ . The Mach number curve was obtained from Equation (55) while the temperature, density and pressure curves were derived from the isen-

tropic flow relations. So far, we have taken  $\gamma = 9/7$  because the vibrational and rotational degrees of freedom are assumed activated due to the elevated stagnation temperature. However, as may be seen from Figure 23, the static temperature drops very fast downstream of the orifice. It is therefore reasonable to assume that the specific heat ratio varies within the expansion. The difference between the two specific heat ratio cases is not negligible, for example, at an  $x/D = 100$  the Mach number is about 14 for  $\gamma = 9/7$  while it is 50% higher for  $\gamma = 7/5$ .

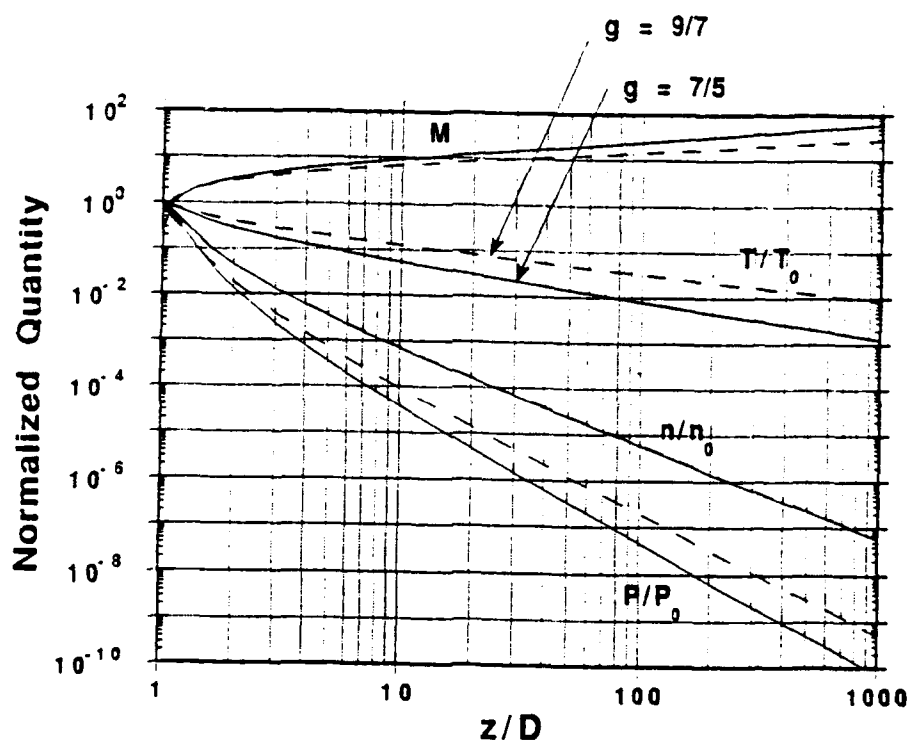
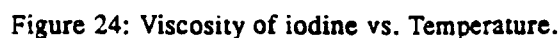


Figure 23: Mach number, normalized number density, temperature and pressure on centerline of free jet expansion for  $\gamma = 9/7$  and  $\gamma = 7/5$ .

The above prediction of free jet expansion properties assumes that the flow is inviscid or slightly viscous. If the stagnation conditions are such that the boundary layer thickness at the orifice wall is of the same order of magnitude as the orifice diameter, the flow at the orifice and further on downstream will be af-

### Dissociating I<sub>2</sub> Viscosity



77

which would justify an inviscid analysis of the flow. It must be noted, however, that if a diverging nozzle is used instead of a sonic orifice, viscous effects will have to be taken into account in the prediction of flowfield properties. This is because as the gas expands in the nozzle, the number density decreases quite quickly and so does the Reynolds number.

#### 4.8.2 Nonequilibrium effects

The stagnation conditions of interest in this work are such that many internal energy modes of the iodine molecule are excited and that the unexpanded gas may partially be dissociated. When the gas expands in a free jet, the thermal energy of random molecular motion stored in the stagnation chamber, is converted into directed kinetic energy. As a result, the number density and hence, the number of collisions decreases dramatically during the expansion. Internal energy adjustments that are necessary for the molecules to reach equilibrium have to be made by means of collisions. However, if the time between collision is of the same order of magnitude as the time for a typical molecule to travel a characteristic distance of the flow, nonequilibrium effects are to be expected. Let us define  $\tau_c$  as the time between collision for a typical binary encounter, and  $\tau_f$  as the time required for a molecule to travel a characteristic distance of the flowfield. If the flow conditions are such that  $\tau_c$  is of the same order as  $\tau_f$ , the flow will depart from equilibrium which may modify the flow pattern and complicate its analysis. If  $\tau_c \ll \tau_f$ , molecules undergo a large number of collisions during the time they spend in the field of interest, in this case the flow may be considered in local thermal equilibrium. On the other hand if  $\tau_c \gg \tau_f$ , internal adjustment of the molecules does not happen because very few collisions occur while the molecule transits through the field of

observation. In the latter case, the flow is considered frozen. Typically, dissociation freezes first in the expansion, then molecular vibration, rotation and finally translation freezes in this order further downstream. This particular freezing order may be explained as follows. Dissociation is usually first to freeze because a dissociated molecule requires the occurrence of a three body collision in order to recombine. While translational energy requires about one collision to be transferred from one molecule to another, rotational and vibrational energy require an increasing number of collisions. Therefore, while vibrational modes may be frozen, rotational and translational energy exchanges may still be occurring at the same plume location. By the same token, rotational states may be locked while translational energy adjustments may still be occurring.

Chemical nonequilibrium and freezing effects in expansion flows have been the object of several analytical studies. Several models have been developed to describe the freezing of dissociation and internal energy in supersonic flows. Bray<sup>54</sup> proposed the sudden-freezing (S-F) model whereby the nonequilibrium flow is represented by an upstream equilibrium branch and a downstream frozen branch, joined together at a "freezing point". Bray defined a "freezing criterion" as the point where convective rates and reaction rates become equal. Good agreement between results using the S-F model and exact numerical solutions for conical and hyperbolic nozzles, have been reported.<sup>54</sup> During his study of weakly ionized gas flows, Smith<sup>55</sup> found that a modification of the S-F model was necessary. He suggested that the downstream frozen branch of the S-F model be replaced by a branch governed by the recombination rate. This model is referred to as the equilibrium-recombination (E-R) model. Blythe<sup>56</sup> conducted a study considering chemical as well as vibrational nonequilibrium in a nozzle flow for an ideal



dissociating gas; he reports that both S-F and E-R models are found to be inadequate for the description of vibrational nonequilibrium in nozzle flows. In Blythe's analysis, the ratio  $T/\theta_d$  is assumed much smaller than unity, where  $T$  is a reference translational temperature and  $\theta_d$  is the characteristic dissociation temperature of the gas as defined in Table 2. Another assumption in Blythe's work is that the degree of dissociation is small and consequently the rate equation is decoupled from other conservation equations. It is because of this assumption that Blythe's model disagrees with both the S-F and E-R models except for the prediction of the degree of dissociation far downstream of the nozzle. Cheng and Lee<sup>57,58</sup> adopted the same approach as Blythe, but their model includes coupling of the chemical reactions with the thermodynamics of the flow. Their assumption of strong coupling relies on the fact that for small ratios  $T/\theta_d$ , the Arrhenius factor defined as  $e^{(-\theta_d/T)}$  controls the dissociation rate and is very sensitive to even minor changes in temperature. Cheng determines two regimes which may be of interest for the work described here: the weak interaction regime whereby  $(\theta_d \alpha)/T \leq O(T/\theta_d)$ , where  $\alpha$  is the degree of dissociation. In this regime, the thermodynamics of the flow are only slightly affected by chemical reactions, however the coupling still has to be taken into account owing to the sensitivity of the Arrhenius factor to small temperature perturbations. In the second regime we have the following condition:  $(\theta_d \alpha)/T \geq O(1)$  which results in a strong coupling between the conservation equations and the rate equation.

#### 4.8.3 Effects of clusters

When a laser beam interacts with the iodine molecules, in addition to fluorescence, part of the scattered light occurs at the laser frequency. This component of scat-

tered light is called Rayleigh scattering, it is proportional to the sixth power of the scattering particle size.<sup>51</sup> Therefore Rayleigh scattering signals are very sensitive to the presence of clusters in the flow field. For example, using the simplistic view that a dimer is twice as large as a monomer, only 1.5% dimer in the flow will essentially double the scattering signal. In addition, it is not known what the fluorescent response of a polymer might look like. Direct Rayleigh scattering is filtered by detecting fluorescence usually two vibrational quanta ( $\Delta V'' = 2 = 1''$  overtone) on the Stokes (longer wavelength) side of the laser wavelength. This however does not mean that the fluorescence from potential clusters is filtered. It is, therefore important to know whether clusters are likely to form within the plume for the regimes applied in this work.

To our knowledge, no work has been done either on the formation of clusters in iodine expansions or fluorescence from iodine clusters. However, several investigations have been reported on the formation of clusters in sonic orifice expansion flows for gases different than iodine.<sup>59-61</sup> Hagena and Obert<sup>61</sup> studied the effect of pressure, temperature, nozzle size and test gas on the size and points of formation (onset points) of clusters made of *Ne*, *Ar*, *Kr*, *Xe*, *N<sub>2</sub>*, *CO<sub>2</sub>* molecules. Their study reveals a good agreement between their prediction and mass spectrometric measurements. More importantly, they develop scaling laws based on intermolecular potential parameters resulting in a non-dimensionalization of stagnation pressure, temperature and orifice size, subsequently, allowing extrapolation of the validated theories to uncharted gases. Figure 25 represents the pressure-temperature phase diagram for the condensation of iodine in a free jet expansion corresponding to a stagnation pressure  $P_0 = 1$  Atm and a stagnation temperature  $T_0 = 1000$  K. In the free jet plume, the gas will expand isentropically fol-

lowing the isentrope passing through  $P_0$  and  $T_0$  until it meets the vapor pressure line.<sup>52</sup> The isentrope is defined by the relation

$$\frac{P_0}{P} = \left( \frac{T_0}{T} \right)^{\frac{\gamma}{\gamma-1}} \quad (56)$$

Note that Figure 25 shows two isentropes for  $\gamma = 7/5$  and  $9/7$ , this is because although it is quite certain that internal energy modes are excited near the orifice, it is not known how fast the internal energy of the molecules will relax or freeze, thus preventing specification the specific heat ratio. Nonetheless, representation of both isentropes allows us to estimate where the intersection with the vapor pressure curve occurs. When the gas continues to expand after the crossing point, it follows the "dry" isentrope into the supersaturated region until the onset point where the formation of clusters leads to the collapse of the supersaturated state. At this point, the expansion returns to the equilibrium vapor pressure line. Figure 25 shows that the isentrope-vapor pressure crossing occurs at about 350 K which corresponds to approximately 2 to 2.5 nozzle diameters downstream of the orifice, however, clusters will typically start forming at a distance an order of magnitude greater.<sup>60</sup> So, one would expect the onset point to be at about 30 orifice diameters downstream of the exit plane. This location is well beyond the range being probed in this work and consequently, the presence of clusters in the flowfields diagnosed here is highly improbable.

In the context of future work where clusters might be present, the formation of polymers may be delayed or sometime avoided by decreasing the stagnation pressure to decrease the number density in the plume hence reducing the number of collisions or increase the stagnation temperature so that the energy involved in a binary encounter is large enough to prevent the colliders from "stick-

ing" together. Another alternative, is to decrease the orifice diameter thus reducing the number density at a given absolute position within the expansion.

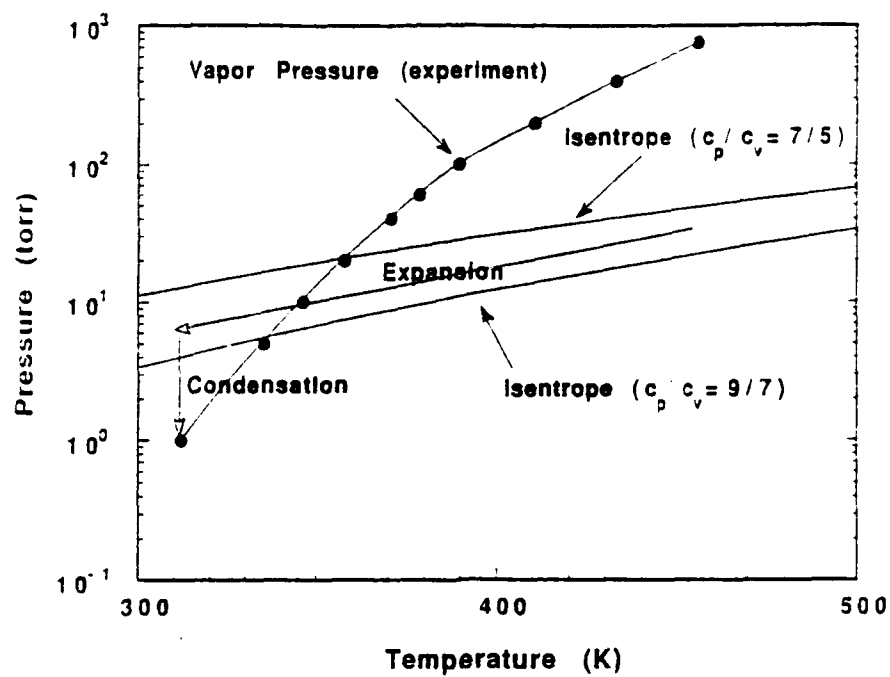


Figure 25: Vapor pressure curve for iodine<sup>62</sup> compared to isentropes for  $\gamma = 9/7$  and  $\gamma = 7/5$ .

## Chapter 5

### EXPERIMENT

#### 5.1 Introduction

The experiment described in this chapter has two main purposes: 1) Develop a pilot scale hypersonic facility operating on iodine vapor in order to generate flows where nonequilibrium effects can be observed. This part of the experiment has been described in Chapter 4, it establishes optimal operating procedures and provides the foundation for the design of larger scale wind tunnel. For the purposes of the work described here a free jet impinging on a disk was studied. 2) Develop a diagnostic technique to probe the rotational and vibrational population distributions and possibly measure the degree of dissociation within the flows generated in both the pilot scale and full scale facilities. The following sections describe the experiment designed to measure both vibrational and rotational population distributions within the flows generated in the pilot scale wind tunnel. Results are presented and discussed.

#### 5.2 Experimental set-up

A top view of the experiment used in this work is shown in Figure 26. It is configured like a standard light scattering experiment. The incident laser beam is provided by an excimer laser (Lambda Physik EMG 201 MSC) emitting radiation at 3080 Å and delivering approximately 500 mJ per pulse. The excimer laser pumps a tunable dye laser (Lambda Physik FL 3002E) equipped with a synchronized air spaced intracavity etalon reducing the laser linewidth from 0.2  $\text{cm}^{-1}$  to 0.05  $\text{cm}^{-1}$ . A portion of the dye laser beam is diverted through a 1/8 m monochromator whose

output is fed into a PMT for monitoring the pulse to pulse laser energy.

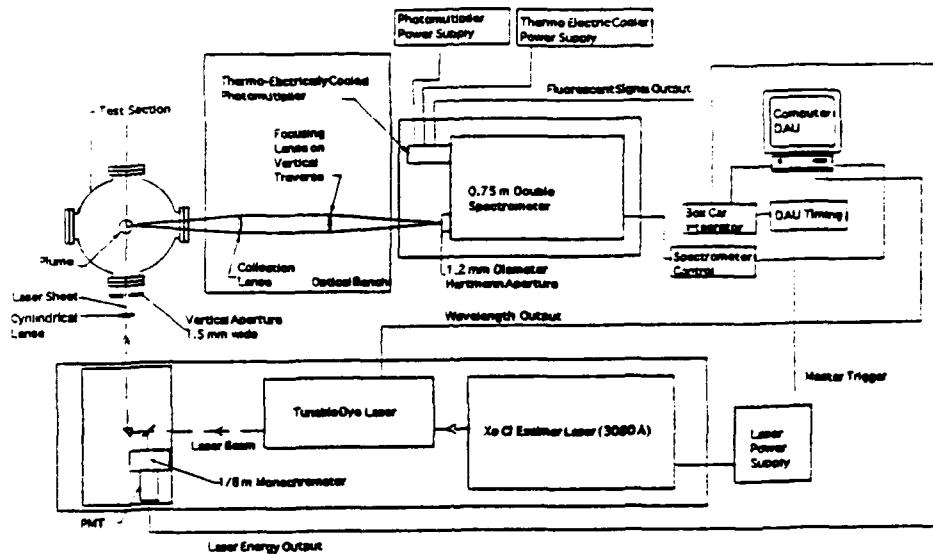


Figure 26: TLIF scattering experiment.

The main part of the dye laser beam is fanned and trimmed into a sheet 1.5 mm thick before it enters the test section where it illuminates the entire flowfield between the blunt body and the orifice exit. This is illustrated in Figure 27. The fluorescent signal is collected with two 60 cm focal length  $f/1.6$  lenses. The collection lens is placed 60 cm away from the plume centerline and the focusing lens can be translated vertically in order to probe various plume axial positions. The traversing mechanism is however not represented in Figure 26. The focusing lens is placed on the collection optics axis so that the probed volume is imaged with a magnification of 1. The image of the probed volume is focused onto the entrance of a 0.85 m double spectrometer (SPEX 1401) used to reject photons at the laser frequency as well as the fluorescent overtones other than the first ( $\Delta V'' = 2$ ). A small 1.5 mm diameter orifice is placed at the focusing lens focal point at entrance of the spectrometer. This determines the diameter of the probed volume which is

assumed to be a small cylinder 1.5 mm diameter 1.5 mm long.

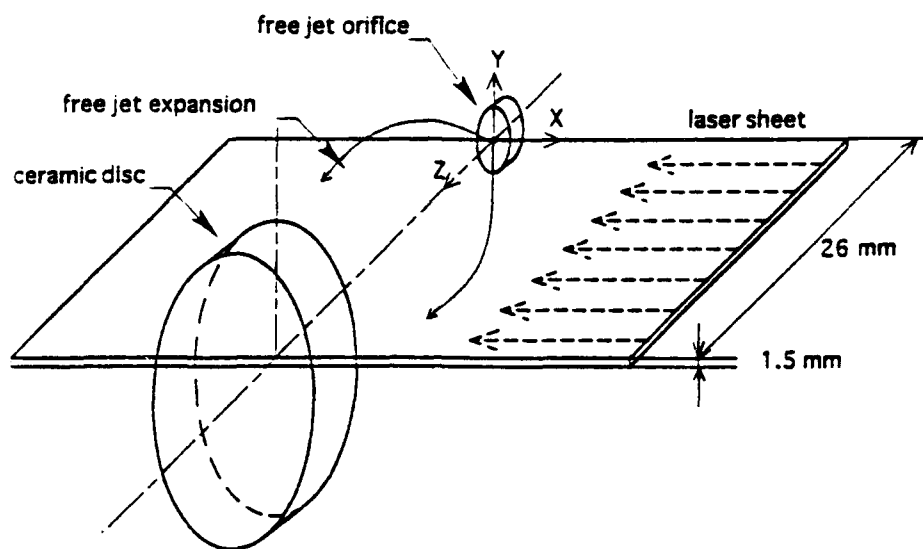


Figure 27: Schematic of free jet assembly, blunt body and laser sheet.

The fluorescent signal occurring at the overtone of interest is detected with a thermocooled photomultiplier tube (RCA C31034A02). Data acquisition and averaging is done with a boxcar integrator (Stanford Research System SR250) and recording achieved by computer (Macintosh IIx) operating with the software package Labview II®. A/D conversion is achieved with National Instrument card NB-MIO-16H-9 sampling at a maximum rate 0.1 Mhz. Both fluorescent signal and pulse to pulse laser energy are recorded and averaged through 2 independent boxcar channels using the same gate width of 100 nsec. Timing is performed by a digital delay generator (Stanford Research DG535). The data presented here is taken with a laser repetition rate of 30 Hz and the fluorescent pulses are averaged over 30 samples.

### 5.3 Experimental Tasks

#### 5.3.1 Test flows

In this study, measurements were taken on four different sets of flow conditions summarized in Table 5. Also indicated in this table is the degree of dissociation expected in the stagnation chamber for the corresponding flow conditions.

	Case 1	Case 2	Case 3	Case 4
Orifice diameter (mm)	2	2	2	2
Blunt body position (mm)	26	26	26	26
Boiler temperature (K)	328	389	328	389
Stagnation temperature (K)	773	773	1000	1000
Stagnation Pressure (Torr)	30	100	30	100
Degree of dissociation in stagnation chamber (%)	< 1	< 1	14.1	7.7

Table 5: Flow conditions used in this study.

#### 5.3.2 Spectral regions probed and data analysis procedure

Three parts of the visible spectrum were probed, they are listed in Table 7 through Table 9 in Appendix B, where the transitions have been arranged in order of increasing wavelengths. The rate and absorption coefficients are defined in Figure 4, and were determined according to the analysis of Section 3.2. The transitions' wavenumber are taken from Gerstenkorn's identification of absorption intensities observed by Fourier transform spectroscopy.<sup>25</sup> The transitions were selected on the basis of the strength of their intensity and in order to avoid complications arising from overlapping lines, only the transitions which are sufficiently isolated (i.e. at least  $0.05 \text{ cm}^{-1}$  apart) are considered. Although the analysis of Section 3.3 allows



identification of a wide range of arbitrary transitions, we narrow the range of transitions used in this work to transitions already identified by Gerstenkorn.<sup>25</sup>

In order to measure rotational distributions, one would ideally want to probe transitions with the same lower and upper vibrational levels and at the same time cover a wide range of rotational quantum numbers. In such case the measured intensities are a direct measurement of rotational population distributions. This, however is difficult to achieve because systematic probing of a wide range of rotational levels keeping the vibrational transitions the same requires wide and high resolutions scans while, in practice, high resolution scans may only be performed over a total range of the order of 1 Å. The small scan limitation is due to the slow laser scanning speed required to produce spectra with enough resolution, combined with the constraints of the facility's run time. It is also due to the detuning of the intracavity etalon which occurs over the span of relatively long scans (larger than 3 Å). In order to avoid the requirement of long range scans, one may release the constraint that the upper vibrational level remain the same for all observed transitions. In such a case, for rotational distributions to be determined, one has to a priori know the transition probability for both excitation ( $B_{12}$ ) and radiative ( $A_{21}$ ) phases. A method for determining these coefficients is developed in Section 3.2 and specific transition probabilities for the transitions used in this study are tabulated in Appendix B. Once the intensity of a transition  $I_{\lambda_{uv}}(\nu)$  is recorded, it is normalized by laser power and corrected according to Equation (31) in order to obtain a measurement of the population  $N_1(V'', J'')$ . Since the lower vibrational level  $V''$  remains the same (usually  $V'' = 0$ ),  $N_1(V'', J'') = N_1(V'') \cdot N_1(J'') = \text{Constant} \cdot N_1(J'')$  and the relative population in level  $J''$  is finally computed using the correction:

$$N_1(J'') = \frac{I_{fluor}(v)}{B_{12}A_{23}SP(J'')} \quad (57)$$

The relative populations in a number of rotational levels are plotted on a Boltzmann plot where  $\ln(N_1(J'')/(2J''+1))$  is plotted versus  $J''(J''+1)$ . In this work, it is found that plotted in such manner, the data can easily be linearly fitted. This indicates that the rotational energy is in equilibrium and that a rotational temperature  $T_{rot}$  can be determined based on the slope of the best linear fit and the characteristic rotational temperature  $\theta_r$ .

Relative vibrational distributions are obtained in a similar fashion as the rotational distributions. In this case however, the transitions probed are not limited to those having the same lower initial vibrational state. To determine the vibrational population distribution at a given position in the flow, the rotational population  $N_1(J'')$  has to a priori be determined at that same position. This is done using Equation (27) and the rotational temperature  $T_{rot}$  determined as described in the preceding paragraph. The relative vibrational population may then be determined by correcting the transition intensity with:

$$N_1(V'') = \frac{I_{fluor}(v)}{B_{12}A_{23}SP(J'')N_1(J'')} \quad (58)$$

An example of a Boltzmann plot is shown in Figure 28. The flow conditions for this particular plot are a stagnation pressure and temperature of 100 Torr, and 773 K respectively. Probing was performed at an axial position of  $z/d$  of 2.5. The slope obtained by linearly best fitting the data points is  $2.3 \cdot 10^{-4}$  resulting in a rotational temperature of 234 K assuming a characteristic rotational temperature  $hcB/k = 0.05375$  K.

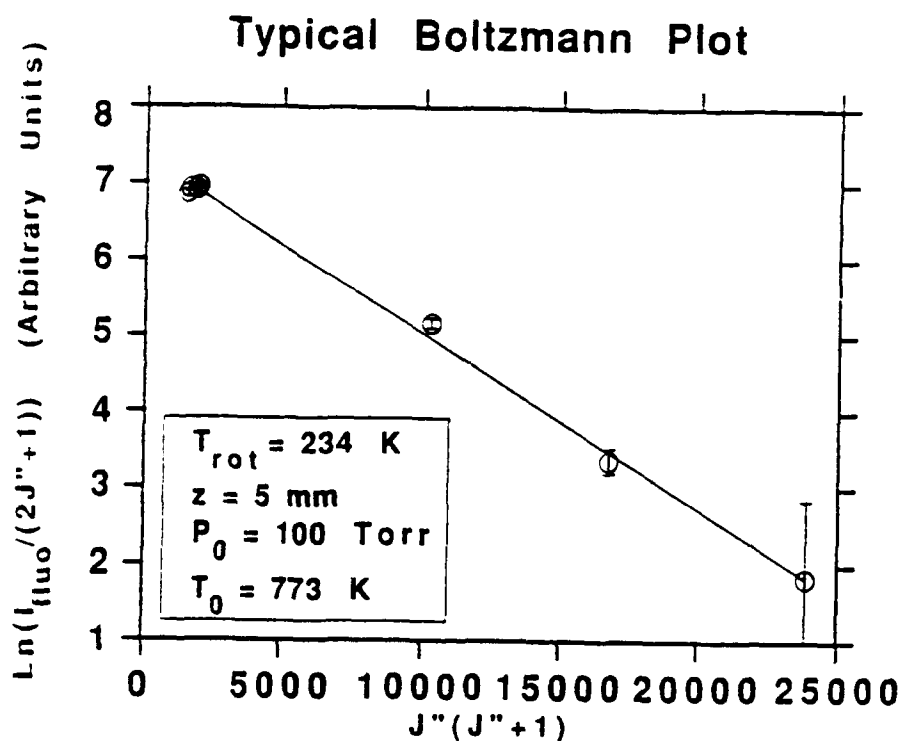


Figure 28: Typical Boltzmann plot.

Certain spectral intervals are more suited to the determination of rotational populations, others, more appropriate to measure vibrational distributions. For example, referring to Appendix B, transitions in the 6120 Å range allow population measurements of the vibrational levels  $V'' = 1$  to 4. On the other hand, transitions in the 5683 Å range enable probing of rotational levels  $J''$  between 40 and 150 all belonging to the same lower vibrational level  $V'' = 0$ . Transitions in the neighborhood of 5208 Å are used to both verify the rotational populations measured with transitions in the 5683 Å range and determine the relative vibrational populations of  $V'' = 0$  and 1 in order to complete the set of measurements performed in the 6120 Å range. Table 6 gives a summary of the vibrational and rotational quantum levels used in this work and the spectral regions in which they

can be accessed.

Probed regions	5208 Å	5683 Å	6120 Å
$J''$ probed belonging to $V'' = 0$	55, 74	38, 39, 42, 43, 101, 129, 154	None
$V''$ probed	0, 1	0, 1, 3	1, 2, 3, 4

Table 6: Spectral regions and quantum levels probed.

### 5.3.3 Laser pulse shape determination

As mentioned in Section 3.2 the laser pulse temporal shape  $E_p(t)$  has to be known in order to compute the time response of the upper level population  $N_2(t)$ .

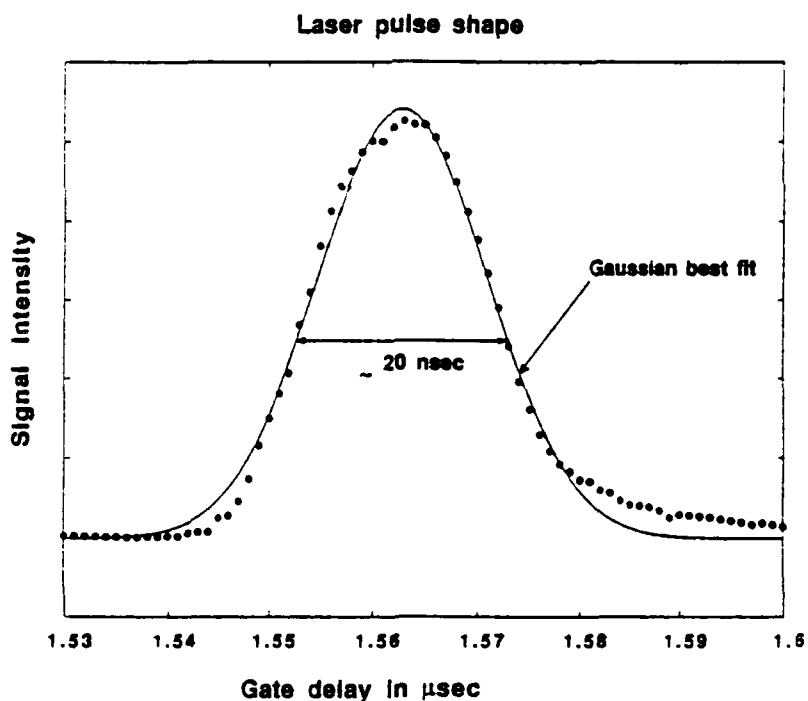


Figure 29: Measured and best fitted laser pulse shape.

The pulse shape was determined experimentally by measuring the light intensity scattered at the laser frequency as the boxcar gate delay is scanned across the laser

pulse. The gate width was tuned to about 1 nsec so that the pulse shape could be determined with enough resolution. The resulting laser pulse shape is shown in Figure 29 along with a Gaussian best fit indicating that the pulse's FWHM is about 20 nsec.

#### 5.3.4 Linear dependence of fluorescent signal

As mentioned in Section 3.2 dissociation and predissociation reactions occurring during the pulsed pumping process make it virtually impossible to saturate a transition. Because of this, it is important that the laser power be tuned so that the fluorescence signal varies linearly with laser intensity. Figure 30 shows the variation of fluorescent signal as the laser beam intensity is progressively attenuated.

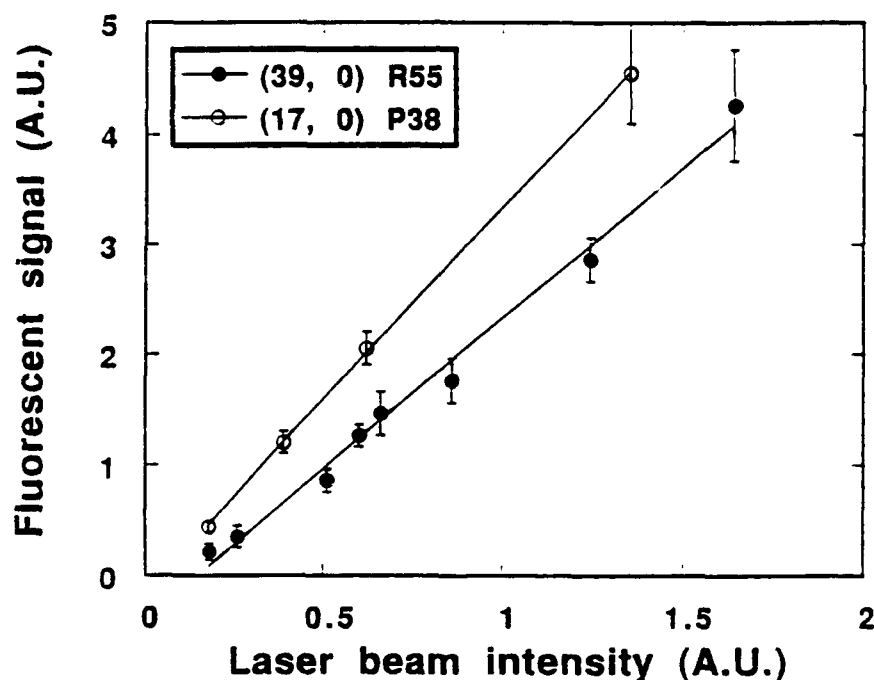


Figure 30: Fluorescence signal dependence on laser power.

The measurement is performed in the free jet expansion for three different transi-

tions: (17, 0) P38 at 5683 Å and (39, 0) R55 at 5208 Å. These transitions were chosen because they have a relatively strong absorption coefficient; clearly if a strongly absorbing transition produces a signal that varies linearly with laser power, so do weaker transitions.

### 5.3.5 Laser linewidth monitoring

As mentioned in Section 3.4.5 the laser linewidth is estimated by measuring the intensity variation through a 0.25 mm dia. pin hole placed at the center of the interference pattern generated with an air spaced Fabry-Perot etalon as the laser is slowly scanned. The Fabry-Perot etalon has a FSR of  $1/6 \text{ cm}^{-1}$  and a finesse of about 150 for a nominal reflectivity of 98%. Figure 14 indicates that the laser linewidth is about  $0.05 \text{ cm}^{-1}$  which corresponds to its advertised performance. It is found however, that the laser linewidth is very sensitive to ambient temperature and can easily detune itself over time periods of the order of tens of minutes. Consequently, the interference pattern is frequently checked for best contrast and the intracavity etalon retuned when necessary.

## 5.4 Experimental results

### 5.4.1 Rotational population distributions

Rotational population distributions are represented on Boltzmann plots in Figure 31 a)-h) for several positions along the center axis of the free jet expansion. The flow conditions are those corresponding to Case 4 of Table 5 and the transitions used are those tabulated in Table 8 of Appendix B. As indicated in Table 6, the spectral region best suited to the determination of rotational population is the 5683 Å range.

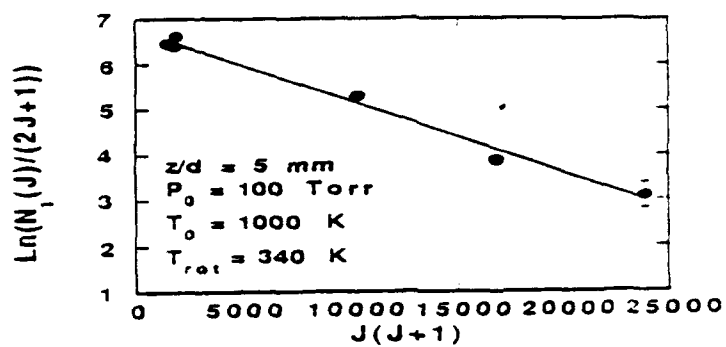


Figure 31 a)

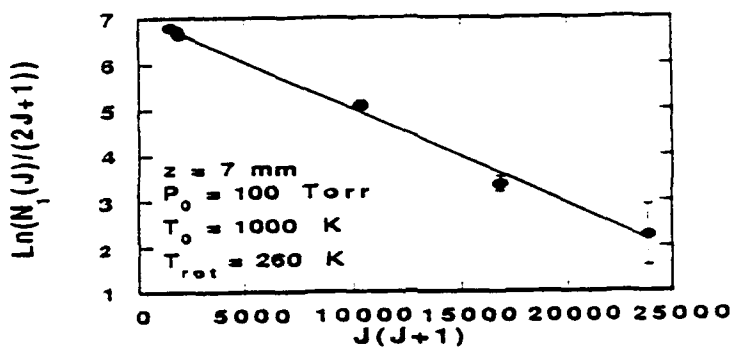


Figure 31 b)

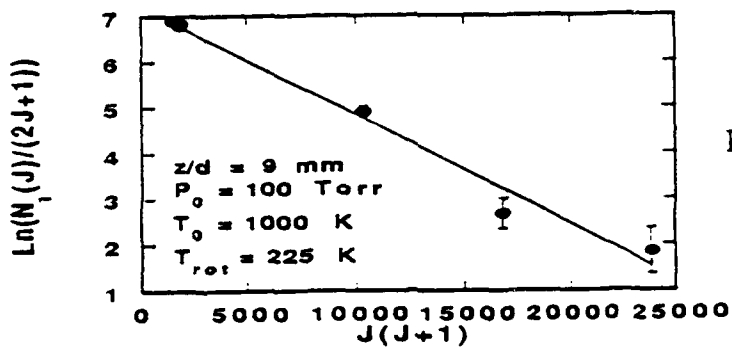


Figure 31 c)

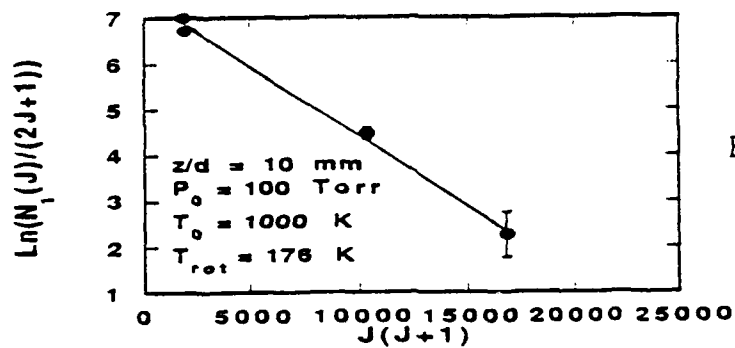


Figure 31 d)

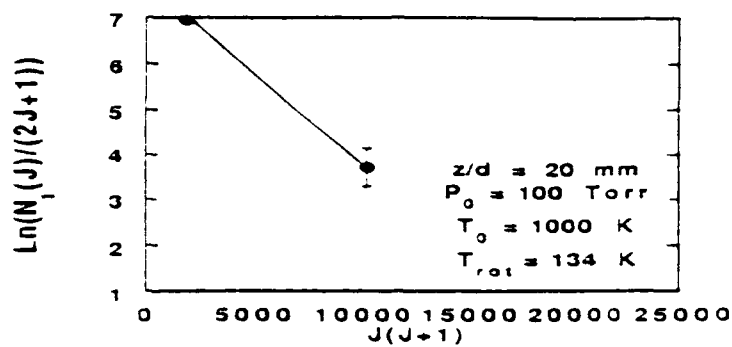


Figure 31 e)

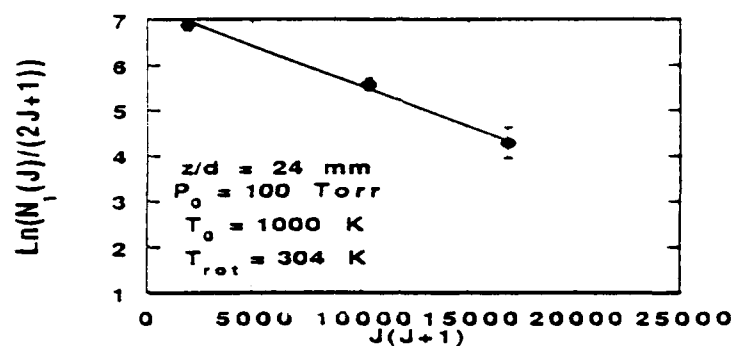


Figure 31 f)

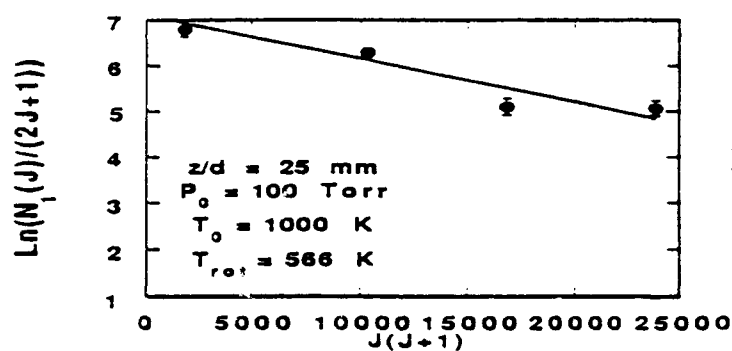


Figure 31 g)

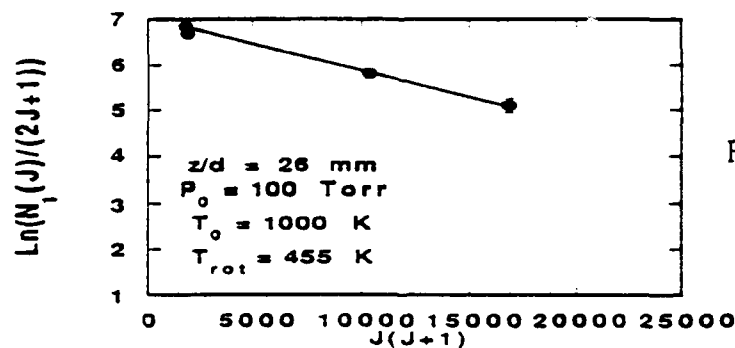


Figure 31 h)

Figure 31: Boltzmann plots for  $z =$  a) 5, b) 7, c) 9, d) 10, e) 20, f) 24, g) 25, h) 26 mm.



The plots indicate that at least within the resolution of the measuring technique, the rotational energy distributions at each axial positions are in equilibrium. Consequently, a rotational temperature may be computed for each axial position probed. These are shown in Figure 32 for a stagnation temperature of 773 K and stagnation pressures of 30 Torr and 100 Torr (Cases 1 & 2 of Table 5).

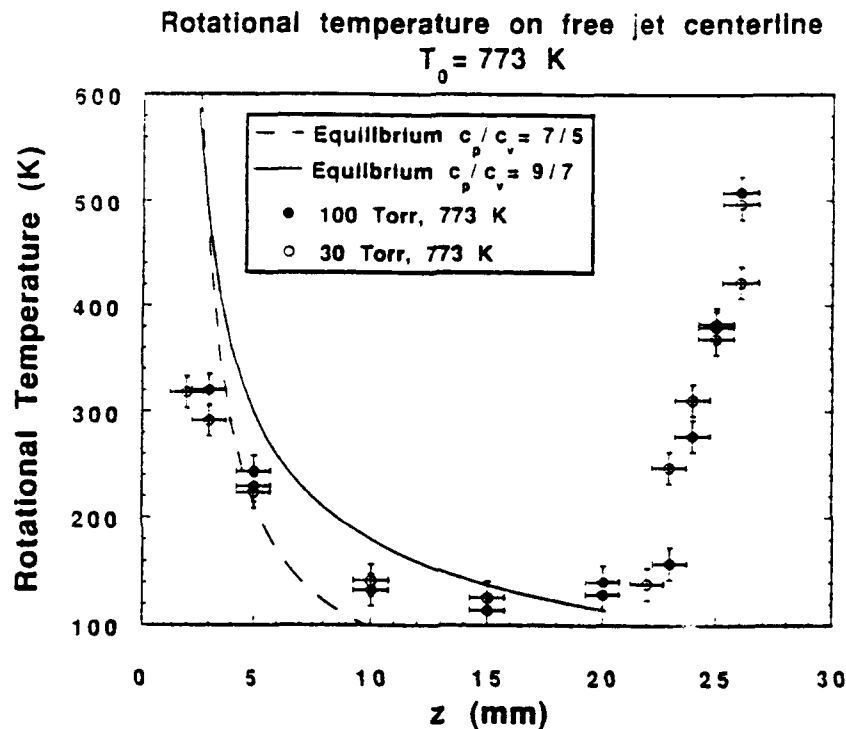


Figure 32: Rotational temperature along free jet centerline for  $T_0 = 773$  K,  $P_0 = 30$  Torr and 100 Torr.

Figure 33 shows similar rotational temperature plots for the same couple of stagnation pressures but for a stagnation temperature of 1000 K (Cases 3 & 4 of Table 5). Also indicated in the two latter figures are the translational temperatures computed under the assumption that the expansion is isentropic.<sup>52</sup> Two different cases of specific heat ratios are taken into consideration: one where the vibrational degree of freedom is frozen ( $\gamma = 7/5$ ), the other where rotational and vibrational degrees of freedom are active ( $\gamma = 9/7$ ).

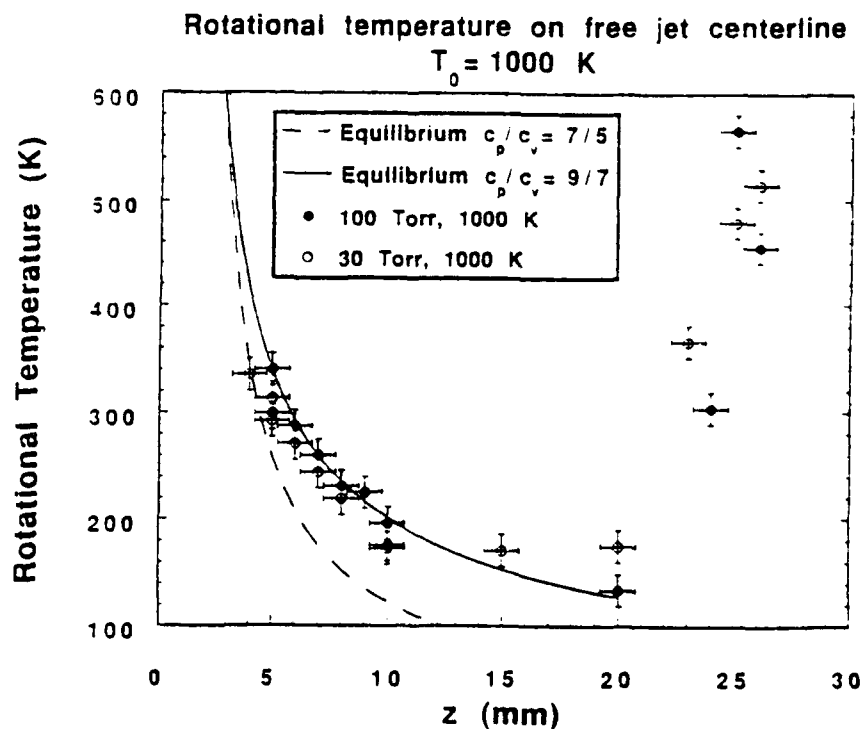


Figure 33: Rotational temperature along free jet centerline for  $T_0 = 1000 \text{ K}$ ,  $P_0 = 30 \text{ Torr}$  and  $100 \text{ Torr}$ .

In order to verify the general adequacy of the probing technique and the data analysis procedure, rotational distributions were obtained by probing transitions in another part of the visible spectrum. These transitions require laser pumping at about  $5208 \text{ \AA}$  and are listed in Table 9 of Appendix B. Resulting rotational temperatures are plotted in Figure 34 and compared to rotational temperatures obtained by probing transitions listed in Table 8 of Appendix B (i.e. in the vicinity of  $5683 \text{ \AA}$ ).

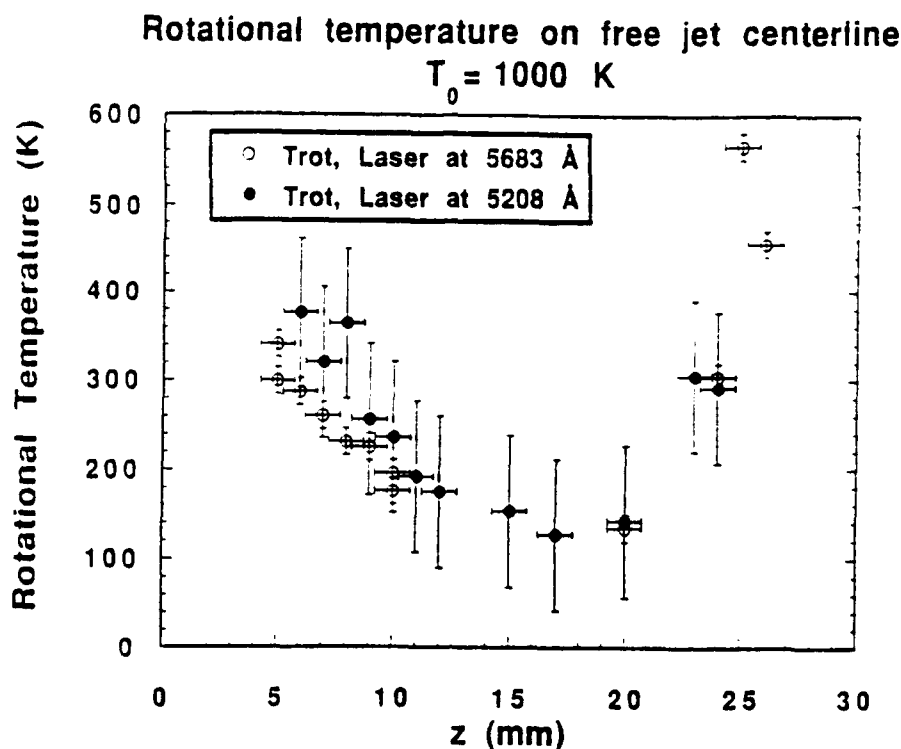


Figure 34: Rotational temperatures obtained by probing transitions requiring laser pumping at 5683 Å compared to rotational temperatures obtained by probing at 5208 Å.

#### 5.4.2 Vibrational population distributions

Rotational temperatures determined in the previous section are used along with Equation (58) to obtain vibrational the population  $N_1(V'')$  for several axial positions  $z = 5, 10, 15, 20$  and  $24 \text{ mm}$ . These are shown in Figure 35 through Figure 38 for flow conditions corresponding from Case 1 through Case 4 of Table 5. The vibrational populations are represented on Boltzmann plots where  $\ln(N_1(V''))$  is plotted versus  $V''$  so that any deviation from equilibrium conditions may be shown. As indicated in Table 6 the spectral region that is most appropriate for the probing of upper vibrational states is the  $6120 \text{ Å}$  range. The transitions used for this part of the study are tabulated in Table 7 of Appendix B. In Figure 35, the pop-

ulations in  $V'' = 0$  and 1 are obtained by probing at shorter wavelengths (5208 Å, Ref. Table 6) and the transitions used are listed in Table 9 of Appendix B. This is because the zero<sup>th</sup> vibrational level cannot be probed by exciting the iodine in the 6120 Å range. So Figure 35 shows populations at  $V'' = 1, 2, 3$  and 4 obtained by probing in the 6120 Å range and populations at  $V'' = 0$  and 1 determined by probing in the 5208 Å range. The two population intervals are plotted by best matching the population at  $V'' = 1$ .

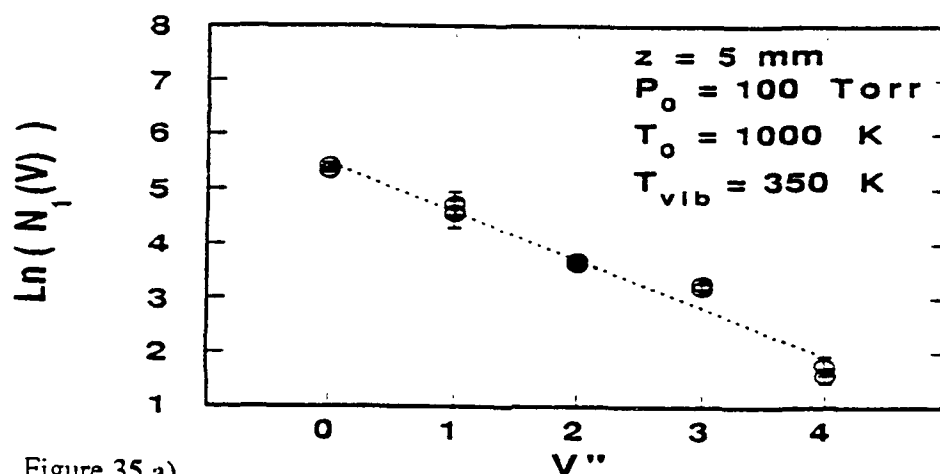


Figure 35 a)

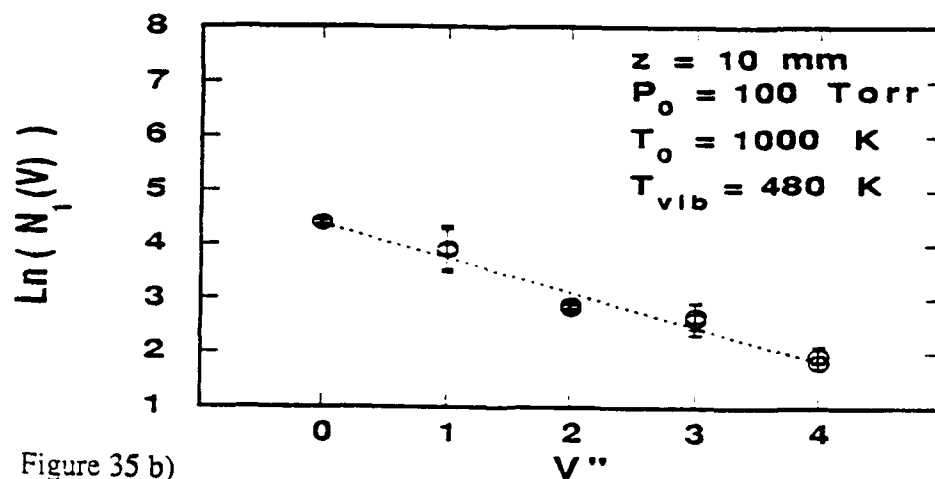


Figure 35 b)

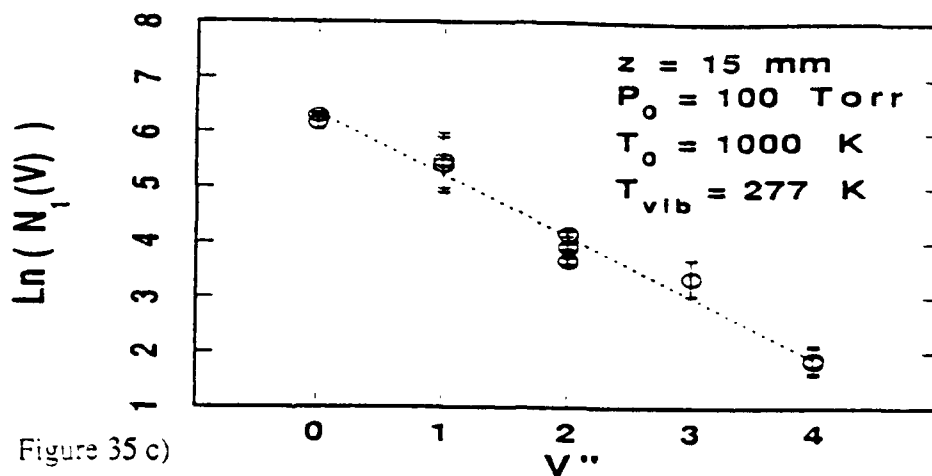


Figure 35 c)

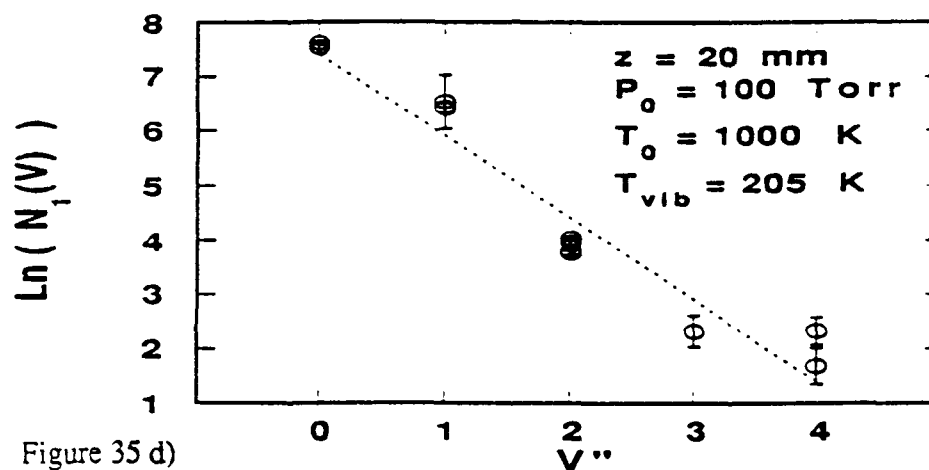


Figure 35 d)

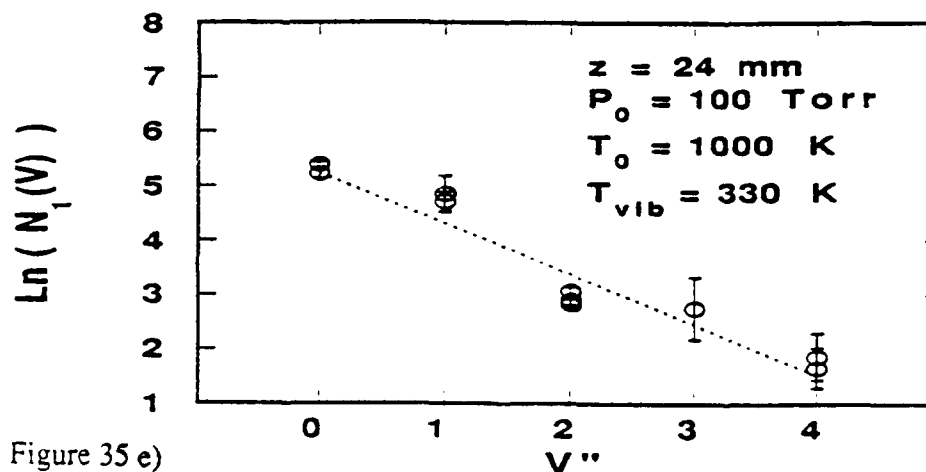


Figure 35 e)

Figure 35: Vibrational population distribution  $T_0 = 1000 \text{ K}$ ,  $P_0 = 100 \text{ Torr}$  for  $z =$  a) 5, b) 10, c) 15, d) 20, e) 24 mm.

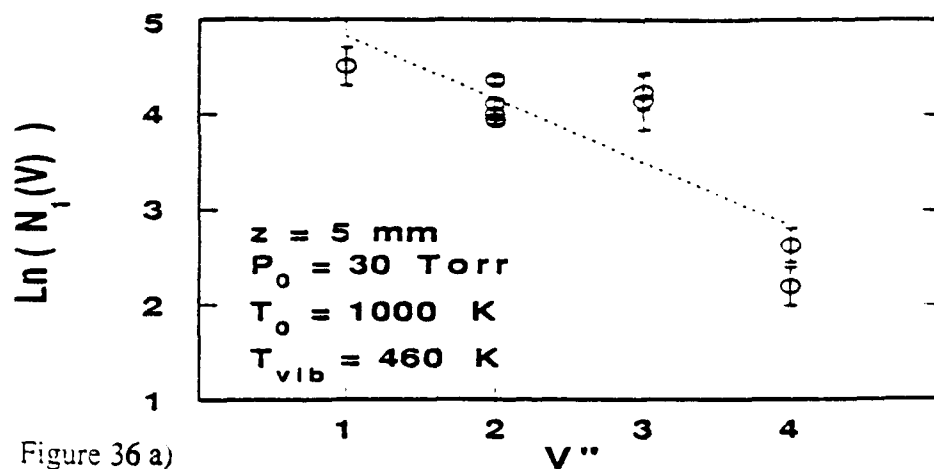


Figure 36 a)

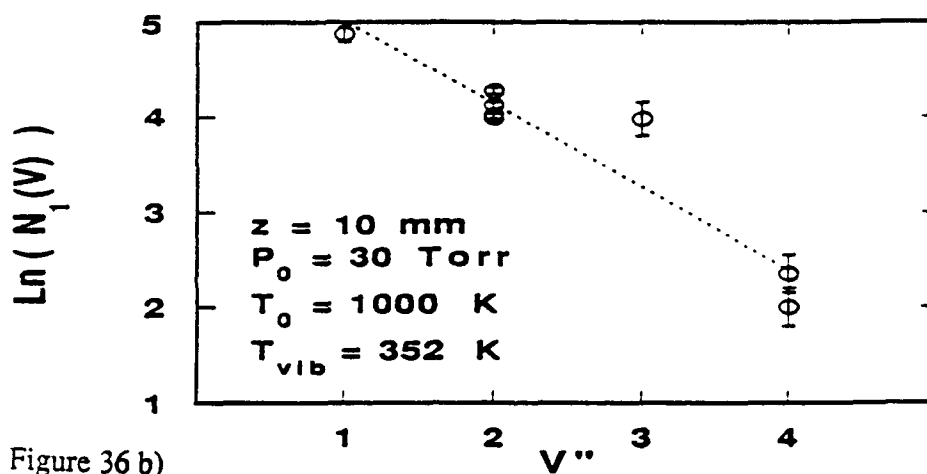


Figure 36 b)

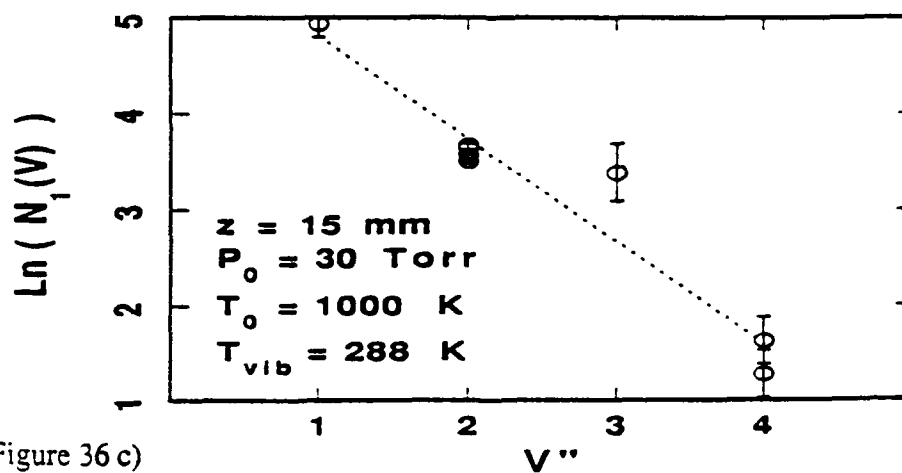


Figure 36 c)

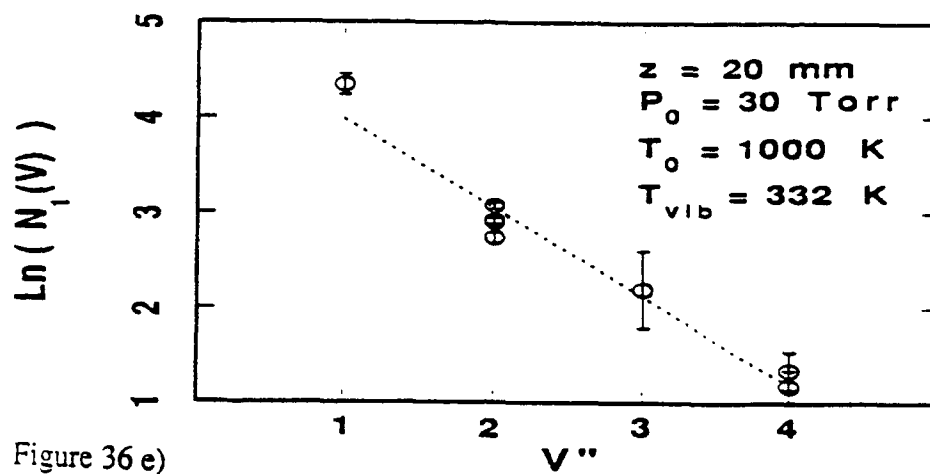


Figure 36 e)

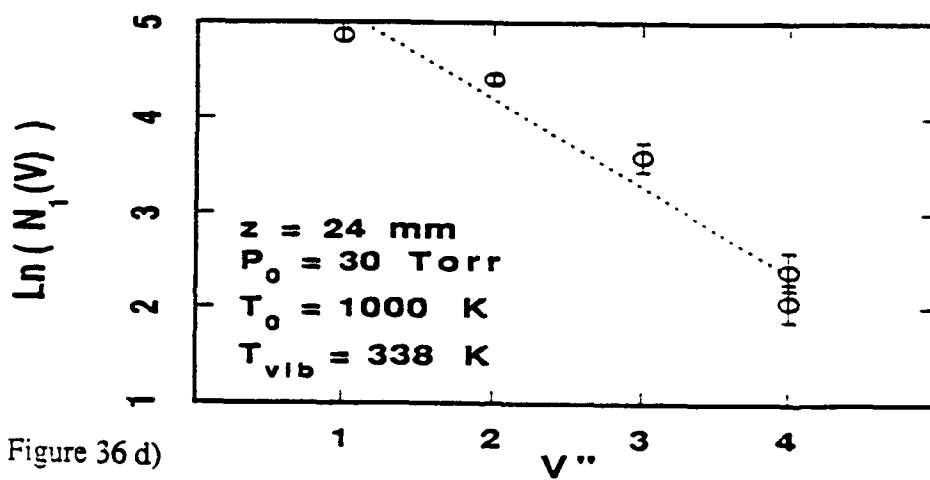


Figure 36 d)

Figure 36: Vibrational population distribution  $T_0 = 1000$  K,  $P_0 = 30$  Torr for  $z =$  a) 5, b) 10, c) 15, d) 20, e) 24 mm.

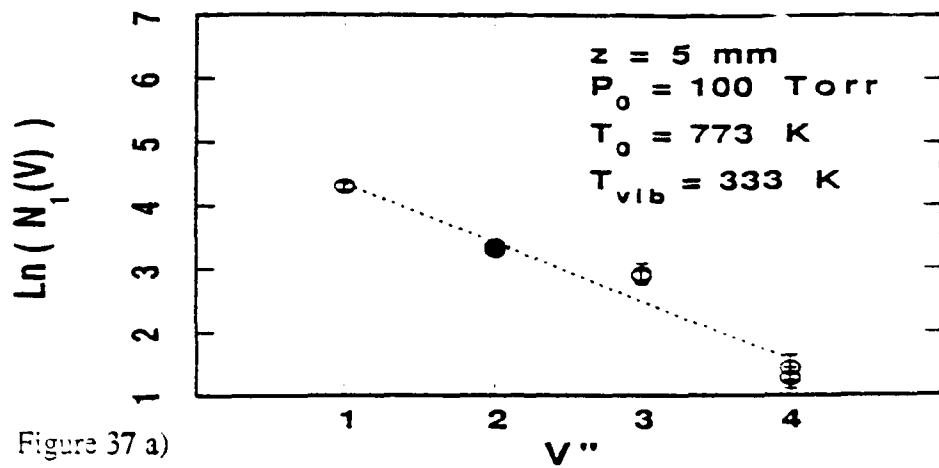


Figure 37 a)

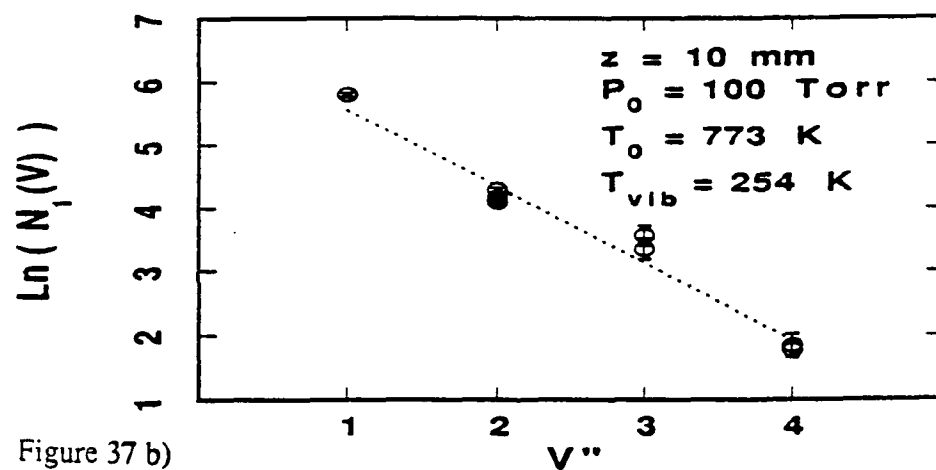


Figure 37 b)

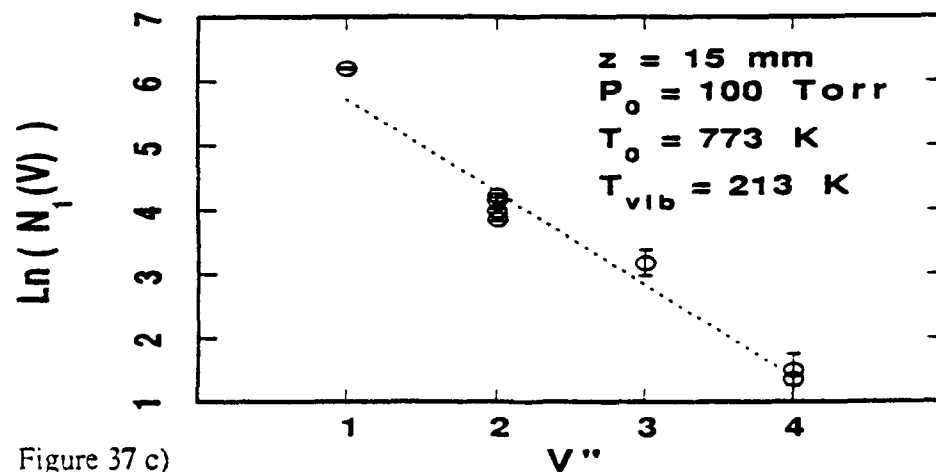


Figure 37 c)



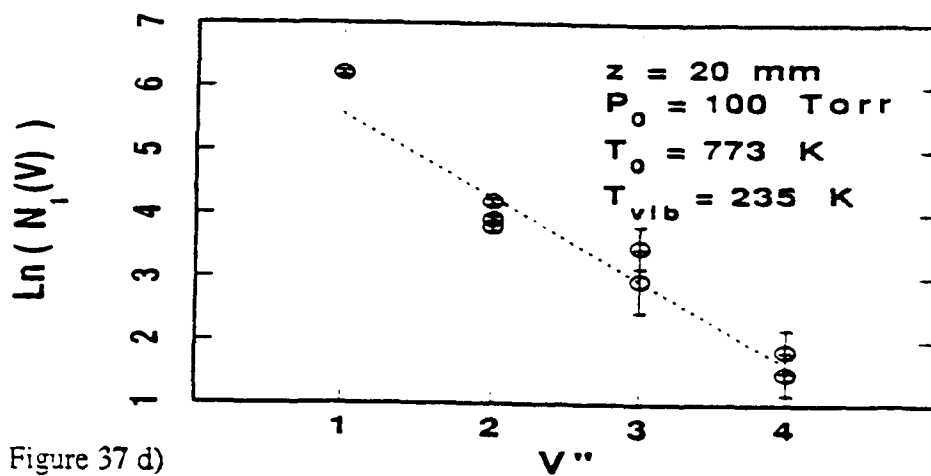


Figure 37 d)

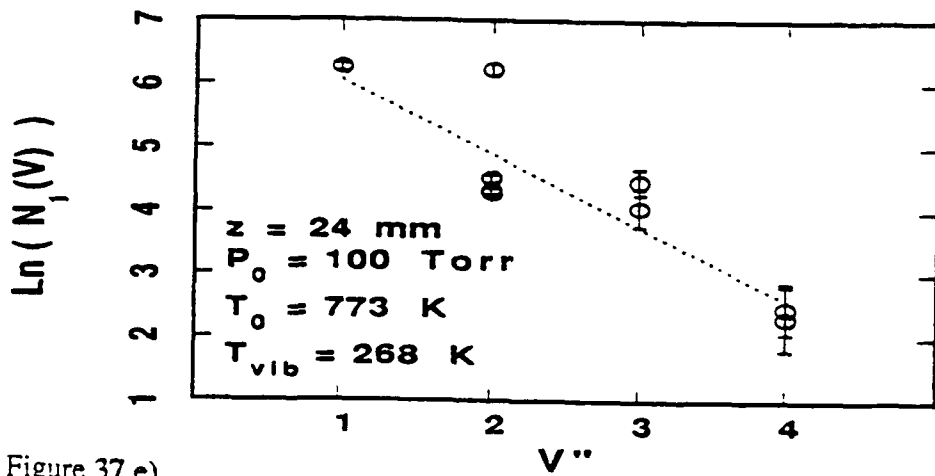


Figure 37 e)

Figure 37: Vibrational population distribution  $T_0 = 773$  K,  $P_0 = 100$  Torr for  $z =$  a) 5, b) 10, c) 15, d) 20, e) 24 mm.

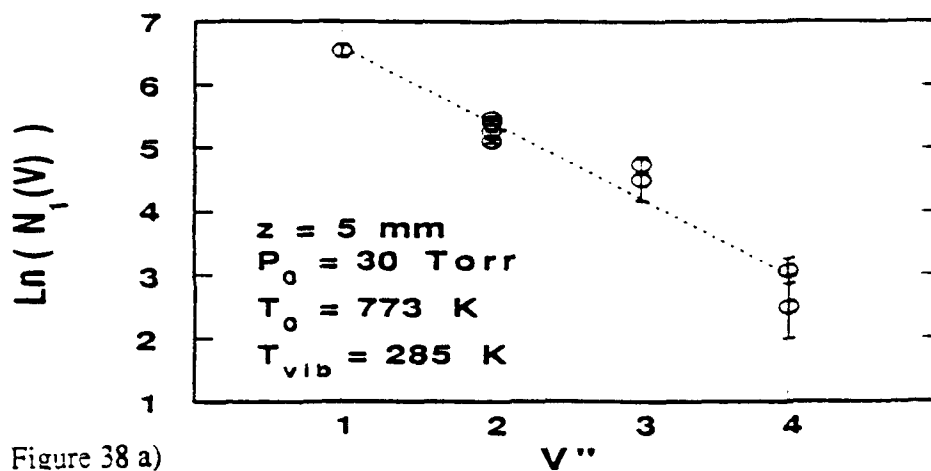


Figure 38 a)

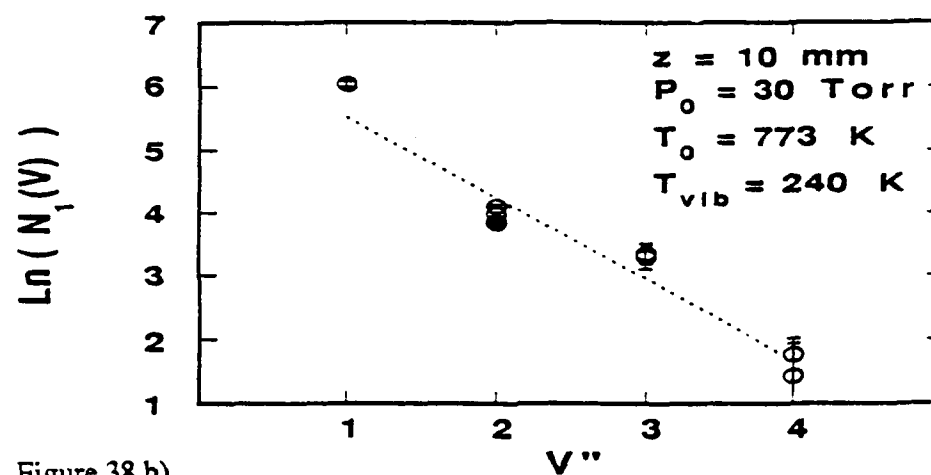


Figure 38 b)

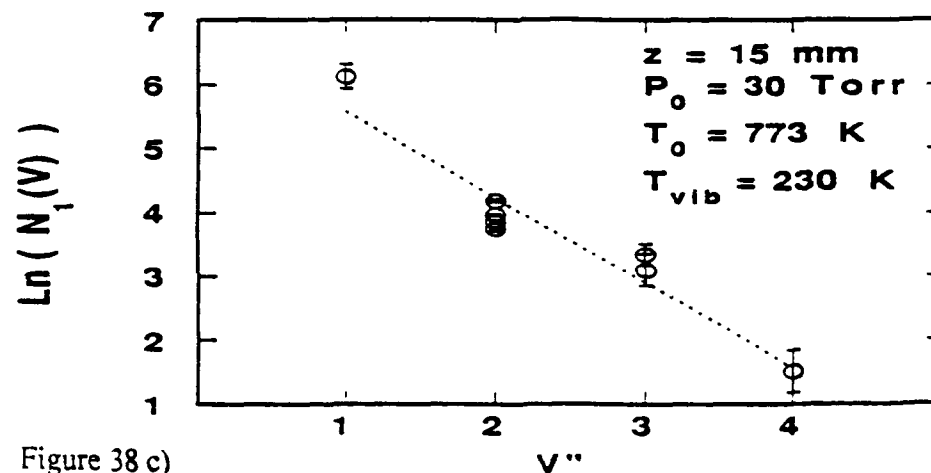


Figure 38 c)

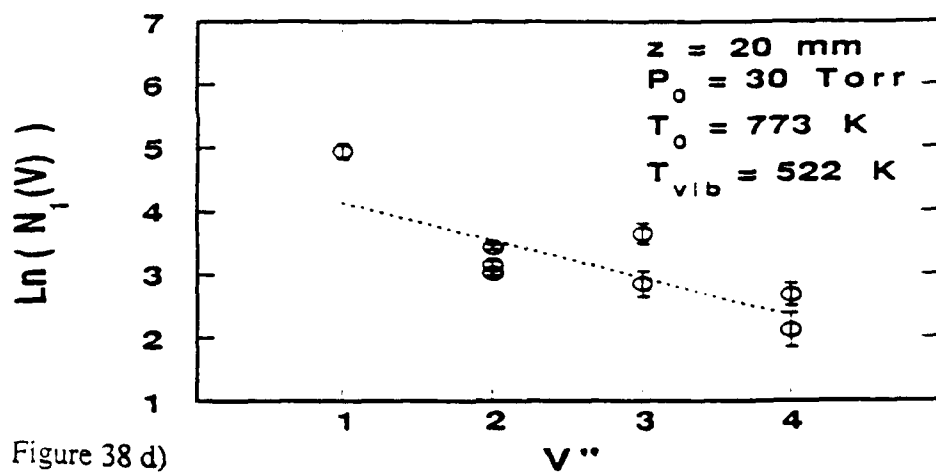


Figure 38 d)

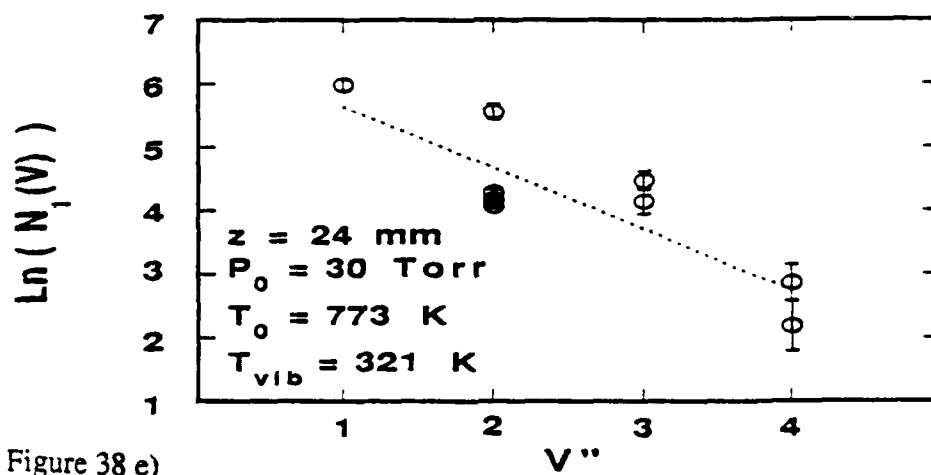


Figure 38 e)

Figure 38: Vibrational population distribution  $T_0 = 773$  K,  $P_0 = 30$  Torr for  $z =$  a) 5, b) 10, c) 15, d) 20, e) 24 mm.

Assuming that the vibrational populations are in equilibrium, a best linear fit is performed on the data of the four previous sets of figures. The slope  $S$  of the best fit is inversely proportional to the vibrational temperature  $T_{\text{vib}} = T_{0\text{vib}}/S$  where  $T_{0\text{vib}}$  is the characteristic vibrational temperature  $hc\omega_e/k = 308$  K. Vibrational temperature profiles are shown in Figure 39 and Figure 40 for a stagnation temperature of 1000 K and 773 K respectively.

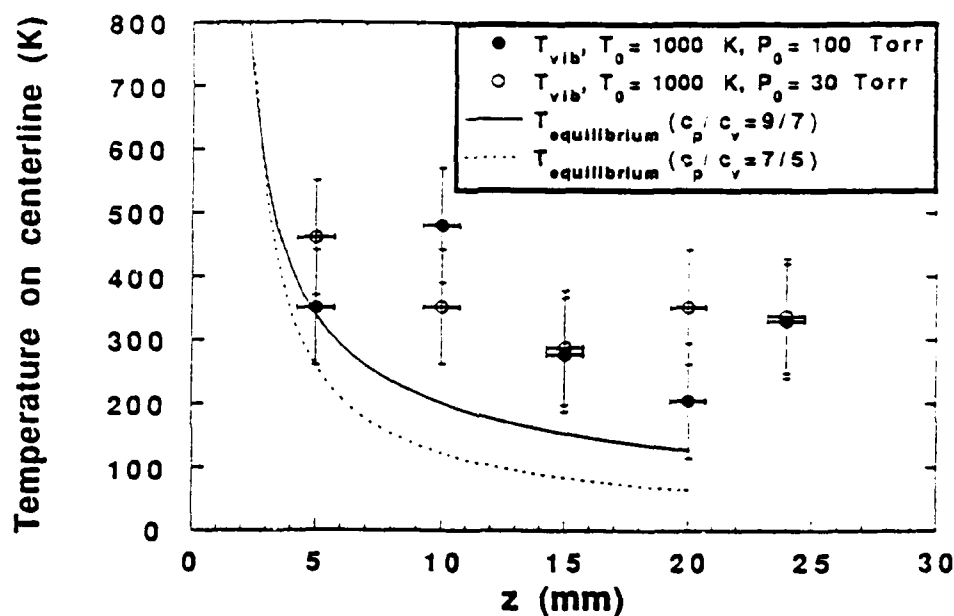


Figure 39: Vibrational temperature profiles for  $T_0 = 1000$  K,  $P_0 = 100$  and 30 Torr.

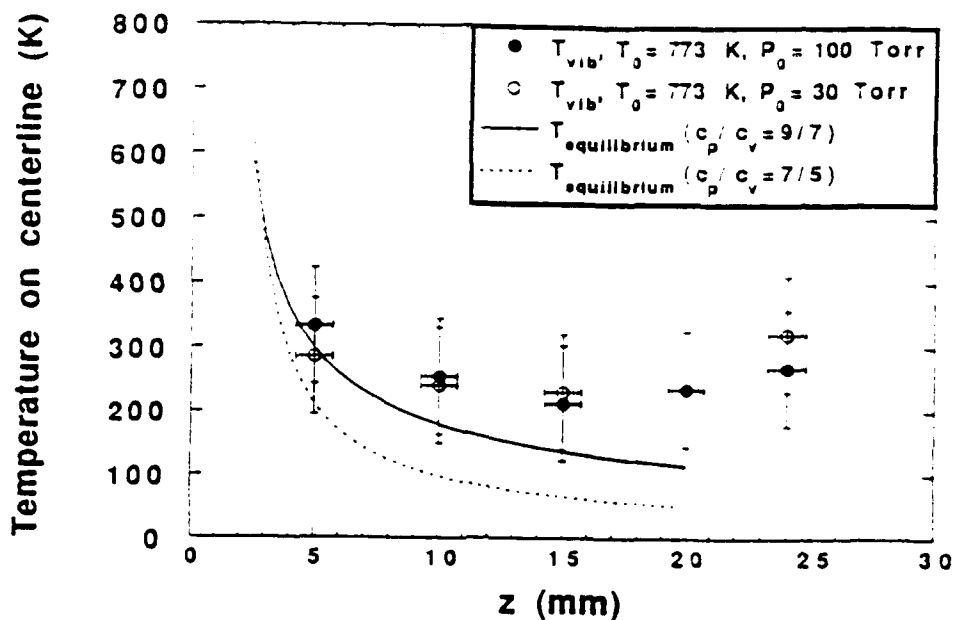


Figure 40: Vibrational temperature profiles for  $T_0 = 773$  K,  $P_0 = 100$  and 30 Torr.

#### 5.4.3 Error estimates

The error bars shown in the Boltzmann plots of and Figure 35 through Figure 38 are estimated by evaluating the scatter involved in repeating the same spectral scan for the same flow conditions. The horizontal error bars indicated on the rotational and vibrational temperature profiles are deduced from the size of the spectrometer entrance orifice which has a diameter of 1.5 mm. The errors in temperature are calculated by estimating the maximum slope variation of the linear fit obtained by taking population errors into account. Note that the temperature scatter shown in Figure 34 for the case of transitions in the vicinity of 5208 Å is rather significant because in this case, the rotational temperature is determined with only

two transitions. The vibrational temperature error bars shown in Figure 39 and Figure 40 are also relatively large: ( $\approx \pm 90$  K) this is due to the relatively large characteristic vibrational temperature 308 K which produces large changes in vibrational temperature for small changes in the slope of the linear fits. Scatter in vibrational temperatures is also due to the relatively small number of vibrational levels probed.

## 5.5 Discussion and recommendations

### 5.5.1 Rotational data

The rotational temperature measurements obtained by the LIF technique used in this work are satisfactory and behave as expected; a gradual cooling of the flow occurs as the gas expands, subsequently, the temperature increases rapidly as the flow encounters the front surface of the disk and forms a shock. The shape of the temperature profile just upstream of the disk leading edge indicates that the shock is merged. The rotational temperature downstream of the shock seems to be highly dependent on the disk surface temperature because the measured rotational temperature does not reach stagnation temperature.

The measured rotational temperature profiles shown in Figure 33 ( $T_0 = 1000$  K) agree rather well with the isentropic expansion curve for  $\gamma = 9/7$ . This indicates that both rotational and vibrational degrees of freedom of the molecule are activated. It may also be noted that in the low pressure case ( $P_0 = 30$  Torr) the rotational temperature freezes at about 180 K starting at  $z = 10$  mm while the rotational temperature corresponding to the higher pressure case ( $P_0 = 100$  Torr) continues to decrease with increasing axial positions. This is probably due to the

larger number of collisions occurring in the high pressure case which allows the rotational energy to relax while for  $P_0 = 30$  Torr, the collision number is low enough to freeze the rotational energy transfer between molecules.

The rotational temperatures of Figure 32 ( $T_0 = 773$  K) show the freezing characteristics observed in Figure 33 ( $T_0 = 1000$  K) however, the effect is less obvious. Figure 32 indicates that the measured temperatures are somewhat lower than the isentropic expansion prediction for  $\gamma = 9/7$ . This may be due to a slight misalignment of the laser sheet with the axis of the expansion. Temperatures obtained at positions that are close to the orifice exit plane ( $z = 3, 4$  &  $5$  mm) are indeed lower than expected and consequently, seem to support this hypothesis.

#### 5.5.2 Vibrational data

The Boltzmann plots of Figure 35 through Figure 38 show significant scatter in vibrational population measurements. This is believed to be due to either low transition strengths that decrease the signal to noise ratio, or systematic errors in data analysis such as the use of faulty transitions rates to calculate the correction factors of Equations (57) and (58). In certain cases the population in a given level seems to display a systematic offset; for example the population in level  $V'' = 3$  for  $P_0 = 1000$  K,  $T_0 = 30$  Torr and  $z = 5, 10$  and  $15$  mm appears to be too large (Ref. Figure 36). This would imply that the rate  $A_{23}$  or the absorption coefficient  $B_{12}$  has been underestimated. One must remember that these coefficients have been calculated using as an input, observed decay rates of transitions pumped by a broad band laser.<sup>34</sup> Until individual and state specific measurements of lifetimes are available, it seems that the present data will remain subject to uncertainties such as those observed here.

Another source of error may be the net depletion of upper state population due to predissociation. This has been taken into account in the data analysis, but predissociation rates could only be grossly approximated (Ref. Section 3.2) because most the available experimental data are not state specific<sup>34</sup> or if the measurements are performed for an individual rovibrational state, the range of states studied is limited.<sup>43</sup> Predissociation rates used in this study are suspected to be inaccurate especially in cases where the upper state is resonant with a purely dissociative state. In fact, when the pumping wavelength is resonant with the crossing point between the  $B$  state and a dissociative state, it is expected that the predissociative rates increase rapidly and correspondingly, the lifetime of the state drops significantly.<sup>33</sup> Scatter observed in the measurement of  $B$  state lifetimes<sup>34</sup> seems to support this hypothesis. By contrast, the rates used in this study are a rather smooth function of pumping wavelength. A consequence of this resides in the fact that the vibrational distributions displayed in Figure 36 through Figure 38 only show populations starting at  $V'' = 1$ . The population in  $V'' = 0$  is omitted because measurement for this level was performed in the 5683 Å range with transitions of the type (17,0). Unfortunately, level  $V' = 17$  coincides with the  $B$  and  ${}^3\Pi_{0g}$  state crossing point.<sup>44</sup> This produces an enhanced predissociation of the  $B$  state and as a results, the population in level  $V'' = 0$  appear too low and are consequently not shown. Correct measurements of the population in  $V'' = 0$  was performed in the 5208 Å range with transitions of the type (40,0). These results, shown in Figure 35, are not subject to the enhanced predissociation anomaly and the distribution functions appear to be well behaved.

Of all the vibrational distributions shown here, the distributions at  $z = 24$  mm are the most subject to errors in data analysis. This is because the compu-



tation of laser power at the probed volume is subject to attenuation, the calculation of which requires knowledge of the number density profile along the laser beam path. While the density field for a free jet expansion is fairly well known<sup>49</sup>, the disc flowfield is more complex and can only be approximated for the region of the flow behind the shock and about the blunt body. In order to estimate the number density behind the shock, the number density at  $z = 24$  mm in the free jet was calculated and the Rankine-Hugoniot relation for normal shocks was used with the local Mach number to compute the number density downstream of the shock. The radial dependence of the density (i. e. along the laser beam path) is assumed to be of the form  $(\cos)^2$  as shown in Equation (35).

In spite of the rather significant scatter, the vibrational temperature profiles shown in Figure 39 and Figure 40 indicate that the vibrational energy does not relax as fast as the rotational energy. The reason for this has been discussed in Section 4.8.2. The rather large vertical error bars make it difficult to assess whether actual freezing of the vibrational energy occurs. Nonetheless, it is clear that the temperature at which the vibrational energy ceases to evolve is higher (350 K) in the high stagnation temperature case and lower (250 K) when  $T_0 = 773$  K. The significant uncertainty in determining vibrational temperatures also makes it difficult to assess the effect of pressure on vibrational relaxation.

### 5.5.3 Recommendation for future work

A few improvements that would enhance the efficiency with which data is acquired, may be suggested. In principle, signal to noise ratios may be maximized if long run times were possible. However, given the constraints of a facility whose total steady state run time lasts about 30 minutes and since the pumping of indi-

vidual rovibrational levels with a scannable narrow band laser appears unavoidable. It seems that a significant time gain may be achieved by collecting fluorescence from entire flowfield cross sections at a time. For example a 2-D CCD array would allow an instantaneous mapping of the entire  $X$ - $Z$  plane of Figure 27. By the same token, a 1-D array would allow detection of the populations along a single axis, say the  $Z$  axis. In these two scenarios, the spectrometer would have to be replaced by an appropriate filter.

The number of transitions probed during a spectral scan is limited because for the laser used in this study, the grating and intracavity etalon gain curves have to be manually realigned for scans that are greater than a few Å. This procedure takes a few minutes and is clearly impractical given the facility's run time. A new generation of pulsed narrow band dye lasers with fairly low Amplified Spontaneous Emission (ASE) has recently been made available. These lasers have the advantage of providing for an automatic alignment of the grating and the intracavity etalon gain curves over the entire dye gain profile. This would accelerate the scanning process and thus, enable the probing of a larger number of transitions within the facility's run time. Moreover, the probed transitions would not be limited to small spectral intervals. The laser could be programmed to scan over a set of transitions which would be selected to cover a large range of quantum levels.

Several improvements in the resolution of the population distributions can be suggested. In this study, the laser lineshape  $g(\nu_L)$  has been assumed constant for all transitions, and stable at the frequency  $\nu_L$ . However it is very likely that the laser lineshape varies during the scan due to either temperature drifts or small asynchronicities in the etalon tracking mechanism. It is also possible that

the laser profile jitters about the center frequency  $\nu_L$ . These two effects produce net variations of laser pumping power which cannot be measured with the present set up but could be minimized by monitoring the laser spectral line profile during a scan with either a Fabry-Perot set up or confocal interferometer.

As discussed in Section 5.5.2 the scatter observed in both rotational and vibrational distributions is subject to the accuracy with which the factors used to correct fluorescent intensities are determined. In the present work, these factors are based on predetermined radiative rates measured by LIF produced by a broad band laser excitation.<sup>34</sup> As a results, the rates are not state specific and can only be considered as approximations in terms of individual transitions. A more precise analysis of the measured fluorescent intensities may be achieved if the decay rate for each transitions were measured experimentally. This could be done with a technique that is similar to that used to measure the laser pulse shape described in Section 5.3.3. Such a technique involves using a pulsed narrow band laser to probe iodine vapor which is maintained in a well controlled environment (for instance, a static cell with cold finger assembly, or a slow flow of iodine vapor through a tube). Preselected single transitions can be excited by a narrow band laser pulse and the upper intermediate state lifetime can be measured by scanning a narrow boxcar gate across the fluorescent pulse profile. The radiative decays measured this way include predissociation effects and should display fine structure variations due to crossing points between the outer limb of the  $B$  state and other dissociative states. The precision of the population measurement would then still be dependent on the accuracy of both the purely radiative decay rates<sup>32</sup> ( $\Sigma A_{21}$ , predissociation excluded, Ref. Section 3.2) and direct dissociation rates<sup>32</sup> ( $B_{\infty}$ , absorption into the  ${}^1\Pi_{1u}$  state, Section 3.2).

The vibrational temperatures shown in Figure 39 and Figure 40 display rather significant error bars which could be reduced by probing a wider range of vibrational levels. To compensate for the lower number density expected in these upper levels, transitions with large Franck-Condon factors have to be chosen. As shown in Figure 12, to probe a greater number of lower vibrational ( $0 \leq V'' \leq 20$ ), maximum Franck-Condon factors are found for transitions whose upper vibrational levels  $V'$  is 20 or lower. It can also be seen by correlating Figure 12 and Figure 13 that the region of maximum Franck-Condon factors requires laser pumping at about 6000 Å and above.

Attenuation of the laser beam due to absorption of laser power by gas molecules outside the probed volume was found to be a significant effect when the transition is strong (Ref. Section 3.5.1). Since an estimate of the amount laser attenuation requires an a priori knowledge of the flowfield number density, it seems preferable to deal with this issue by operating in regimes where attenuation is negligible. This can be achieved by several means: 1) Reducing the laser beam path length in region of high density by having the laser beam enter the flowfield through the model and consequently from the downstream part of the shock. 2) Limit the probed volume to regions in the flowfield where the number density is low. 3) Choose transitions whose absorption is not too strong. A measurement of the difference between the laser beam intensity before and after the test section would give an indication of the significance of attenuation.

## Chapter 6

### CONCLUSIONS

Design and construction of a pilot scale hypersonic wind tunnel has been achieved. Its operation proves a concept for generating a dissociating nonequilibrium flow for relatively long run times. The facility expands high temperature pure iodine vapor through a sonic orifice and into a vacuum. It operates on a semi-continuous basis with a run phase lasting about 1/2 hour and an iodine supply of about 1 kg. The stagnation conditions are such that significant rotational and vibrational excitation can be achieved enabling the probing of internal state distributions within the expansion. Observation of chemical nonequilibrium is also possible because 3 to 10% dissociation may be achieved at the stagnation conditions selected for this work.

For the purpose of this work, a free jet expansion was studied under four different sets of stagnation conditions. The orifice diameter was 2 mm. In order to study a zone of high nonequilibrium, a shock was generated by placing the flat surface of a disc 26 mm downstream of the orifice exit plane. A free jet expansion has the advantage of being well studied and understood. It also allows the study of a fairly simple flowfield without interference from complex boundary conditions.

Probing internal energy population distributions has been performed with Transient Laser Induced Fluorescence. A narrow band pulsed laser was used to excite individual transitions. Since the excitation process is pulsed, and detection is performed with a narrow gate centered around the maximum of the fluores-

cence time profile, the technique is quenching insensitive. Rotational and vibrational populations were measured point by point along the free jet centerline but the use of multidimensional CCD arrays would enable fast probing of entire cross sections of the flowfield within the facility's run time.

Rotational population distributions have been measured at several axial positions. Boltzmann plots of the rotational populations indicate that the rotational distributions are in equilibrium and the resulting rotational temperatures show that both vibrational and rotational degrees of freedom are activated. There seem to be evidence of rotational temperature freezing in the coldest region of the expansion just upstream of the shock. The rotational temperature increases through the shock but does not reach stagnation conditions because of blunt body temperature effects.

Vibrational population distributions have been measured for the 5 first vibrational levels of the  $X$  state. The distributions display a significant scatter probably due to uncertainties in both radiative and dissociative transition probabilities, and possibly, laser linewidth instabilities. Under the assumption that the molecules' vibrational energy is in equilibrium, the resulting vibrational temperature profiles indicate that the vibrational energy relaxes more slowly than rotational energy.

The data analysis requires an a priori knowledge of absorption, emission, predissociation and direct dissociation rates. Absorption rates have been calculated from precomputed purely radiative decay rates under the assumption that the electronic transition moment is constant. Predissociation and direct dissociation rates have been approximated from experimental data. More precision in the

data analysis may be achieved if state specific radiative decay rates are measured or calculated, and more details for the predissociative and dissociative processes are investigated. Absorption and emission rates would have to be computed taking into account the variation of electronic transition moment with R-centroid.

Attenuation is significant if the absorbing transition is strong and the number density of the probed level is large. Because an analysis including attenuation requires an a priori knowledge of the number density field, it is recommended that future work be performed in regimes where attenuation can be neglected or at least minimized. This may be achieved by probing regions of the flowfield where the number density is low, choosing transitions whose absorption is not too strong or reducing the path length of the probing beam by introducing it in the flowfield through the model.

The scanning ranges of the dye laser used in this study are small because the manual tuning of the intracavity etalon that is necessary for long scans, is impractical to perform given the facility's run time. Consequently, only a limited number of transitions can be used for determining population distributions. The recent availability of pulsed self adjusting tunable dye lasers would enable the probing of a larger number of judiciously preselected transitions. Population distributions covering a wider quantum level range would then be possible.

A valuable tool for validating prediction technique describing nonequilibrium flows of diatomic gases has been developed. Concepts for generating hypersonic flows of a chemically reacting gas have been proven and tested. A diagnostic technique for measuring rovibrational population distributions within these flows, has been developed and may be refined.

## Appendix A

Dunham expansion coefficients for the iodine molecule ( $V'' = 0-19$ ,  $V' = 0-80$ ) taken from Gerstenkorn.<sup>11</sup>

### X state

$i$	$y_{i0}$	$y_{i1}$
0		$0.3736812559337480 \cdot 10^{-1}$
1	$0.2145292253831637 \cdot 10^{-3}$	$-0.1138151197256179 \cdot 10^{-3}$
2	$-0.6129731614337341 \cdot 10^{-6}$	$-0.3061638399475614 \cdot 10^{-6}$
3	$-0.1027340004155040 \cdot 10^{-3}$	$-0.4093271255246214 \cdot 10^{-8}$
4	$-0.1427228811574466 \cdot 10^{-3}$	$0.9542617587865405 \cdot 10^{-10}$
5	$0.8765347546885206 \cdot 10^{-5}$	$-0.4664721586567808 \cdot 10^{-11}$
6	$-0.3036676438177481 \cdot 10^{-6}$	
7	$0.4241664120510493 \cdot 10^{-8}$	

$i$	$y_{i2}$	$y_{i3}$
0	$0.4535367953884840 \cdot 10^{-8}$	$-0.5020768840583991 \cdot 10^{-15}$
1	$0.2431068375316978 \cdot 10^{-10}$	$-0.2145063451171229 \cdot 10^{-16}$
2	$0.5703742464406417 \cdot 10^{-13}$	$0.2591223350872934 \cdot 10^{-18}$
3	$0.8473602349402563 \cdot 10^{-13}$	$-0.1198981745331080 \cdot 10^{-18}$
4	$-0.8528868696138535 \cdot 10^{-14}$	$0.8784525309081259 \cdot 10^{-20}$
5	$0.4572369300012694 \cdot 10^{-15}$	$-0.2941713570946923 \cdot 10^{-21}$
6	$-0.9429307706030258 \cdot 10^{-17}$	

### B state

$i$	$y_{i0}$	$y_{i1}$
0		$0.290007271083 \cdot 10^{-1}$
1	$0.12566869517813 \cdot 10^{-3}$	$-0.149437406811 \cdot 10^{-3}$



$i$	$y_{i0}$	$y_{i1}$
2	$-0.75039983603948 \cdot 10^{-0}$	$-0.126039916187 \cdot 10^{-5}$
3	$-0.41440414502073 \cdot 10^{-2}$	$0.360843852404 \cdot 10^{-7}$
4	$0.22489315808648 \cdot 10^{-3}$	$-0.118936764784 \cdot 10^{-7}$
5	$-0.32286825302082 \cdot 10^{-4}$	$0.160836460759 \cdot 10^{-6}$
6	$0.28274026782231 \cdot 10^{-5}$	$-0.140149921572 \cdot 10^{-9}$
7	$-0.16976059525912 \cdot 10^{-6}$	$0.817082273146 \cdot 10^{-11}$
8	$0.72483391984314 \cdot 10^{-8}$	$-0.329526101021 \cdot 10^{-12}$
9	$-0.22366834361621 \cdot 10^{-9}$	$0.937259316176 \cdot 10^{-14}$
10	$0.50241595329130 \cdot 10^{-11}$	$-0.189281067061 \cdot 10^{-15}$
11	$-0.81831500764874 \cdot 10^{-13}$	$0.269875228921 \cdot 10^{-17}$
12	$0.95205749185164 \cdot 10^{-15}$	$-0.2657234093551 \cdot 10^{-19}$
13	$-0.76837892433947 \cdot 10^{-17}$	$0.172032143518 \cdot 10^{-21}$
14	$0.40758033226391 \cdot 10^{-19}$	$-0.659290444078 \cdot 10^{-24}$
15	$-0.12752869307005 \cdot 10^{-21}$	$0.113349602297 \cdot 10^{-26}$
16	$0.17806207411211 \cdot 10^{-24}$	

$i$	$C_{di}$	$C_{hi}$
1	$-0.18902422336 \cdot 10^{-2}$	$-0.3371894465 \cdot 10^{-2}$
2	$0.17571610203 \cdot 10^{-1}$	$0.7770431620 \cdot 10^{-1}$
3	$0.14692600521 \cdot 10^{-3}$	$0.1042296758 \cdot 10^{-2}$
4	$0.49182430075 \cdot 10^{-4}$	$-0.2563967293 \cdot 10^{-3}$
5	$-0.73527614381 \cdot 10^{-5}$	$0.3599155253 \cdot 10^{-4}$
6	$0.73225949643 \cdot 10^{-6}$	$-0.2830661993 \cdot 10^{-5}$
7	$-0.48677766343 \cdot 10^{-7}$	$0.1369590853 \cdot 10^{-6}$
8	$0.22330462900 \cdot 10^{-8}$	$-0.4261819805 \cdot 10^{-8}$
9	$-0.72047341782 \cdot 10^{-10}$	$0.8670586347 \cdot 10^{-10}$
10	$0.16418686914 \cdot 10^{-11}$	$-0.1145240278 \cdot 10^{-11}$
11	$-0.26242668071 \cdot 10^{-13}$	$0.9460077352 \cdot 10^{-14}$

$i$	$C_{di}$	$C_{ui}$
12	$0.28783372161 \cdot 10^{-15}$	$-0.4441816037 \cdot 10^{-16}$
13	$-0.20648260620 \cdot 10^{-17}$	$0.9058576013 \cdot 10^{-19}$
14	$0.87311009715 \cdot 10^{-20}$	
15	$-0.16504695113 \cdot 10^{-22}$	

$i$	$C_{di}$	$C_{ui}$
1	$-0.473050709 \cdot 10^{-2}$	$-0.59848313 \cdot 10^{-2}$
2	$0.109273874 \cdot 10^{-0}$	$0.77278871 \cdot 10^{-1}$
3	$0.456705023 \cdot 10^{-2}$	$0.17449445 \cdot 10^{-1}$
4	$-0.802422429 \cdot 10^{-3}$	$-0.15814745 \cdot 10^{-2}$
5	$0.711468387 \cdot 10^{-4}$	$0.75476030 \cdot 10^{-4}$
6	$-0.355923537 \cdot 10^{-5}$	$-0.20318475 \cdot 10^{-5}$
7	$0.106987914 \cdot 10^{-6}$	$0.31046670 \cdot 10^{-7}$
8	$-0.197187575 \cdot 10^{-8}$	$-0.25003026 \cdot 10^{-9}$
9	$0.218610546 \cdot 10^{-10}$	$0.82535824 \cdot 10^{-12}$
10	$-0.133994869 \cdot 10^{-12}$	
11	$0.349444102 \cdot 10^{-15}$	

## Appendix B

Rates and absorption coefficients associated with the transitions studied in this work

Transition	$A_2$ ( $\text{sec}^{-1}$ )	$A_{21}$ ( $\text{sec}^{-1}$ )	$A_{23}$ ( $\text{sec}^{-1}$ )	$A_{\text{pairs}}$ ( $\text{sec}^{-1}$ )	$B_{12}$ ( $\text{m}^3/\text{J}/\text{sec}^2$ )	Wavenumber ( $\text{cm}^{-1}$ )
7,1) R27	$9.2 \cdot 10^5$	2103	36313	$7.8 \cdot 10^5$	$8.68 \cdot 10^{17}$	16341.94
9,2) P40	$8.6 \cdot 10^5$	30267	92419	$4.6 \cdot 10^5$	$1.25 \cdot 10^{18}$	16341.76
13,4) R53	$8.1 \cdot 10^5$	19811	45555	$1.4 \cdot 10^5$	$8.18 \cdot 10^{17}$	16341.32
9,2) P41	$8.6 \cdot 10^5$	30266	92417	$4.6 \cdot 10^5$	$1.25 \cdot 10^{18}$	16340.92
13,4) R54	$8.1 \cdot 10^5$	19811	45555	$1.4 \cdot 10^5$	$8.18 \cdot 10^{17}$	16340.28
9,2) P42	$8.6 \cdot 10^5$	30266	92417	$4.6 \cdot 10^5$	$1.25 \cdot 10^{18}$	16340.05
9,2) R48	$8.6 \cdot 10^5$	30265	92412	$4.6 \cdot 10^5$	$1.25 \cdot 10^{18}$	16339.79
11,3) P49	$8.3 \cdot 10^5$	91426	9581	$2.3 \cdot 10^5$	$3.77 \cdot 10^{18}$	16339.62
11,3) R55	$8.3 \cdot 10^5$	91421	9580	$2.3 \cdot 10^5$	$3.77 \cdot 10^{18}$	16339.07
11,2) P151	$8.3 \cdot 10^5$	57995	66046	$2.3 \cdot 10^5$	$2.39 \cdot 10^{18}$	16338.41
9,2) P44	$8.6 \cdot 10^5$	30266	92415	$4.6 \cdot 10^5$	$1.25 \cdot 10^{18}$	16338.27

Table 7: Transitions in the 6120 Å range and corresponding transition probabilities.

Transition	$A_2$ ( $\text{sec}^{-1}$ )	$A_{21}$ ( $\text{sec}^{-1}$ )	$A_{23}$ ( $\text{sec}^{-1}$ )	$A_{\text{pairs}}$ ( $\text{sec}^{-1}$ )	$B_{12}$ ( $\text{m}^3/\text{J}/\text{sec}^2$ )	Wavenumber ( $\text{cm}^{-1}$ )
(19,0) P129	$6.3 \cdot 10^5$	30757	43677	$5.7 \cdot 10^5$	$1.01 \cdot 10^{18}$	17595.61
(20,0) P154	$5.8 \cdot 10^5$	34476	28553	$6.3 \cdot 10^5$	$1.14 \cdot 10^{18}$	17595.13
(25,3) P81	$4.9 \cdot 10^5$	33728	13905	$8 \cdot 10^5$	$1.14 \cdot 10^{18}$	17595.02
(24,3) R27	$5.2 \cdot 10^5$	31744	7722	$7.5 \cdot 10^5$	$1.05 \cdot 10^{18}$	17594.73

Table 8: Transitions in the 5683 Å range and corresponding transition probabilities.

Transition	$A_2$ (sec <sup>-1</sup> )	$A_{21}$ (sec <sup>-1</sup> )	$A_{23}$ (sec <sup>-1</sup> )	$A_{pair}$ (sec <sup>-1</sup> )	$B_{12}$ (m <sup>3</sup> /J/ sec <sup>2</sup> )	Wavenu mber (cm <sup>-1</sup> )
(20,1) R86	5.8 10 <sup>5</sup>	74736	3760	6.3 10 <sup>5</sup>	2.47 10 <sup>18</sup>	17594.63
(17,0) R42	6.3 10 <sup>5</sup>	19091	65848	4.6 10 <sup>5</sup>	6.31 10 <sup>17</sup>	17594.48
(25,3) P85	4.9 10 <sup>5</sup>	33723	13903	8 10 <sup>5</sup>	1.11 10 <sup>18</sup>	17594.38
(20,1) P82	5.8 10 <sup>5</sup>	74743	3761	6.3 10 <sup>5</sup>	2.47 10 <sup>18</sup>	17594.22
(17,0) R38	6.310 <sup>5</sup>	19092	65851	4.6 10 <sup>5</sup>	6.3 10 <sup>17</sup>	17593.97
(17,0) R43	6.3 10 <sup>5</sup>	19091	65848	4.6 10 <sup>5</sup>	6.3 10 <sup>17</sup>	17593.55
(18,0) R101	6.3 10 <sup>5</sup>	24585	55800	5.2 10 <sup>5</sup>	8.13 10 <sup>17</sup>	17593.43
(17,0) P39	6.3 10 <sup>5</sup>	19092	65850	4.6 10 <sup>5</sup>	6.3 10 <sup>17</sup>	17593.03

Table 8: Transitions in the 5683 Å range and corresponding transition probabilities.

Transition	$A_2$ (sec <sup>-1</sup> )	$A_{21}$ (sec <sup>-1</sup> )	$A_{23}$ (sec <sup>-1</sup> )	$A_{pair}$ (sec <sup>-1</sup> )	$B_{12}$ (m <sup>3</sup> /J/ sec <sup>2</sup> )	Wavenu mber (cm <sup>-1</sup> )
(40,0) P74	2.5 10 <sup>5</sup>	36362	14769	4.5 10 <sup>5</sup>	8.95 10 <sup>17</sup>	19194.08
(39,0) R55	2.5 10 <sup>5</sup>	36362	16175	4.5 10 <sup>5</sup>	9.26 10 <sup>17</sup>	19193.63
(45,1) P74	1.4 10 <sup>5</sup>	4596	5164	2.3 10 <sup>5</sup>	1.17 10 <sup>17</sup>	19193.29
(45,1) R76	1.4 10 <sup>5</sup>	4596	5164	2.3 10 <sup>5</sup>	1.17 10 <sup>17</sup>	19192.75

Table 9: Transitions in the 5208 Å range and corresponding transition probabilities.

## Bibliography

- 1 K. A. Fisco and D. R. Chapman. *Comparison of Shock Structure Solution Using Independent Continuum and Kinetic Theory Approaches*. SPIE Symp. Innovative Sci. and Technol., Los Angeles, 1988.
- 2 H. K. Cheng. *Problems of Inviscid-Viscous Interaction in Hypersonic Flows*. in Progress in Aeronautics and Astronautics, edited by M. M. Hafez, AIAA, New York, 1988.
- 3 G. A. Bird. *Molecular Gas Dynamics*. Clarendon Press, Oxford, 1976.
- 4 E. P. Muntz. *The Electron Beam Fluorescence Technique*. AGARDograph 132, 1968.
- 5 H. Alsmeyer. *Density Profiles in Argon and Nitrogen Shock Waves Measured by the Absorption of an Electron Beam*. J. Fluid Mech., 74, pp. 497-513, 1976.
- 6 J. A. Kunc, E. P. Muntz, and D. P. Weaver. *Model Gases for the Detailed Study of Microscopic Chemical Nonequilibrium in Diatomic Gas Flows*. AIAA-90-1662, 1990.
- 7 W. Holzer, W. F. Murphy, and H. J. Bernstein. *Resonance Raman Effect and Resonance Fluorescence in Halogen Gases*. J. Chem. Phys., 52, 1, pp. 399-408, 1970.
- 8 R. L. St. Peters, S. D. Silverstein, M. Lapp and C. M. Penney. *Resonant Raman Scattering or Resonance Fluorescence in I<sub>2</sub> Vapor?* Phys. Rev. Let., 3, 6, pp. 191-92, 1972.
- 9 W. Kiefer and H. J. Bernstein. *Vibrational- Rotational Structure in the Resonance Raman Effect of Iodine vapor*. J. Mol. Spec., 43, pp. 366-81, 1972.
- 10 D. L. Rousseau and P. F. Williams. *Resonance Raman Scattering of Light from a Diatomic molecule*. J. Chem. Phys., 64, 9, pp. 3519-37, 1975.
- 11 S. Gerstenkorn and P. Luc. *Description of the Absorption spectrum of Iodine Recorded by Means of Fourier Transform Spectrometry: the (B-X) system*. J. Physique, 46, pp. 867-81, 1985.
- 12 F. Martin, R. Bacis, S. Churassy, and J. Vergès. *Laser-Induced-Fluorescence Fourier Transform Spectrometry of the XO<sup>+</sup> State of the I<sub>2</sub>. Extensive Analysis of the BO<sup>+</sup><sub>u</sub> - XO<sup>+</sup><sub>g</sub> Fluorescence Spectrum of <sup>252</sup>I<sub>2</sub>*. J. Mol. Spec., 116, pp. 71-100, 1986.
- 13 G. W. McClelland, K. L. Saenger, J. J. Valentini. *Vibrational and Rotational Relaxation of Iodine in Seeded Supersonic Beams*. J. Phys. Chem., 83, 8, pp. 947-59, 1979.
- 14 J. Tusa, M. Sulkes, and S. A. Rice. *Low Energy Collisional Relaxation of I<sub>2</sub> in He: Evidence for Resonance Enhanced Vibrational Deactivation*. J. Chem. Phys., 70, 6, pp. 3136-37, 1978.
- 15 J. C. McDaniel. *Investigation of Laser-Induced Fluorescence for the Measure-*

*ments of Densities in Compressible Flows*. Ph.D. thesis, Stanford University, 1982.

16 R. Schilder, G. Adomeit, G. Worthberg. *Theoretical and Experimental Investigation of the Knudsen Layer Produced by Intensive Evaporation of Iodine*. 13<sup>th</sup> RGD, pp. 577-84, 1985.

17 G. A. Bird. *Nonequilibrium Radiation During Reentry at 10 Km/sec*. AIAA-87-1543, 1987.

18 G.C. Pham-Van-Diep, D. A. Erwin, E. P. Muntz. *Nonequilibrium Molecular Motion in a Hypersonic Shock Wave*. Science, 245, pp. 624-26, 1989.

19 G. C. Pham-Van-Diep, D. A. Erwin, E. P. Muntz. *A Review of the Microkinetic Details Required for Accurate Predictions of Normal Shock Waves*. 17<sup>th</sup> RGD, Ed.A. B. Beylich, Aachen, 1990.

20 D. A. Erwin, G. C. Pham-Van-Diep, E. P. Muntz. *A Detailed Validation of Monte Carlo Direct Simulation for Monatomic Gases*. Phys. Fluids A, 3, 4, pp. 697-705, 1991.

21 G. C. Pham-Van-Diep, D. A. Erwin and E. P. Muntz. *Testing Continuum Descriptions of the Low-Mach-Number Shock Structures*. J. Fluid Mech., 232, pp. 403-413, 1991.

22 G. C. Pham-Van-Diep, E. P. Muntz, D. A. Erwin. *A Study of the Microkinetic Adjustments Required to Match Shock Wave Experiments and Monte Carlo Direct Simulation for a Wide Mach Number Range*. AIAA-90-1689, 1990.

23 E. P. Muntz, L. N. Harnett. *Molecular Velocity Distribution Function Measurement in a Normal Shock Wave*. Phys. Fluids, 12, pp. 2027-35, 1969.

24 T. Holtz, E. P. Muntz. *Molecular Velocity Distribution Functions in an Argon Normal Shock Wave at Mach Number 7*. Phys. Fluids, 26, 9, pp. 2425-36, 1983.

25 S. Gerstenkorn and P. Luc. *Assignment of Several Groups of Iodine ( $I_2$ ) Lines in the B-X System*. J. Mol. Spec. 77, pp. 310-21, 1979.

26 G. C. Maitland, M. Rigby, E. B. Smith, W. A. Wakeham. *Intermolecular Forces*. Clarendon, Oxford, 1981.

27 S. F. Gimelshein, and M. S. Ivanov. *Investigation of Shock Wave Structures by Majorant Cell and Free Schemes of DSMC*. 17<sup>th</sup> RGD, Aachen. Ed.A. B. Beylich, 1990.

28 J. K. Harvey. Unpublished

29 S. P. Sharma, and S. M. Ruffin. *Nonequilibrium Vibrational Population Measurements in an Expanding Flow Using Spontaneous Raman Spectroscopy*. AIAA-92-2855, 1992.

30 G. Hertzberg. *Molecular spectra and Molecular Structure*. Robert E. Krieger Pub-

lishing Co. Malabar, Florida, 1989.

31 B. Barnault. *Etude Experimental et Théorique de la Réaction Iode-Oxygène Singulet en Vue de la Réalisation d'un Laser Chimique de Puissance*. Office National d'Etude et de Recherche Aérospatiales. Publication 1992-3.

32 L. Brewer and J. Tellinghuisen. *Quantum Yield for Unimolecular Dissociation of  $I_2$  in the Visible Absorption*. J. Chem. Phys., 56, 8, pp. 3929-38, 1971.

33 R. Mulliken. *Iodine revisited*. J. Chem. Phys., 55, 1, pp. 288-309, 1970.

34 G. E. Capelle and H. P. Broida. *Lifetimes and Quenching Cross Section of  $I_2$* . J. Chem. Physics. 58, pp. 4212-22, 1972.

35 P. A. Fraser. *A Method of Determining the Electronic Transition Moment for a Diatomic Molecules*. Can. J. Phys., 32, pp. 515-512, 1954.

36 A. Chutjian, J. K. Link, and L. Brewer. *Measurement of Lifetimes and Quenching Cross Sections of the B State of  $I_2$* . J. Chem. Phys., 46, 7, pp 2666-75, 1966.

37 K. Sakurai, G. Capelle, and H. P. Broida. *Measurements of Lifetimes and Quenching Cross Sections of the B State of Iodine Using a Tunable Dye Laser*. J. Chem. Phys., 54, 3, pp 1220-23, 1976.

38 J. Tellinghuisen. *Intensity Factors for the  $I_2$  ( $B \leftrightarrow X$ ) Band System*. J. Quant. Spectrosc., 19. pp. 149-61, 1977.

39 B. Hiller and R. Hanson. *Properties of the Iodine Molecule Relevant to Laser-Induced Fluorescence Experiments in Gas Flows*. Exp. Fluids, 10, pp. 1-11, 1990.

40 A. L. Suris. *Handbook of Thermodynamic High Temperature Process Data*. Ed. W. Begell. Hemisphere Publishing Corp. Washington, 1987.

41 J. Tellinghuisen. *Spontaneous Predissociation in  $I_2$* . J. Chem. Phys., 57, 6, pp 2397-402, 1972.

42 J. A. Paisner and R. Wallenstein. *Rotational Lifetimes and Self-Quenching Cross Sections in the B State of  $I_2$* . J. Chem Phys., 61, 10, pp 4317-20, 1974.

43 M. Broyer, J. Vigué, and J. C. Lehmann. *Direct Evidence of the Natural Predissociation of the  $I_2$  B State through Systematic Measurements of Lifetimes*. J. Chem. Phys., 63, 12, pp 5428-31, 1975.

44 J. I. Steinfeld. *Wavelength Dependence of the Quenching of Iodine Fluorescence*. J. Chem. Phys., 44, 7, pp 2740-49, 1965.

45 J. H. Perry. *Chemical Engineers's Handbook*. Mc Graw-Hill Book Company, Inc. 1950.

46 W. G. Vincenty and C. H. Kruger. *Introduction to Physical Gas Dynamics*. Robert

E. Kreiger Publishing Company. Malabar, Florida, 1965.

47 S. Dushman. *Scientific Foundations of Vacuum Technique*. John Wiley & Sons, Inc. 1949.

48 R. C. Weast. *CRC Handbook of Chemistry and Physics*. CRC Press, Inc. 1984.

49 E. P. Muntz. *Partial Pressure Condensation Pump*. U. S. Patent No. 4 185 966, January 1980.

50 J. Brook, V. Calia, B. Hanel, E. P. Muntz, P. B. Scott and T. Deglow. *Jet Membrane Process for Aerodynamic Separation of Mixtures and Isotopes*. AIAA J. Energy, 4, 5, p. 199, 1980.

51 M. Lapp, C. M. Penney and J. A. Asher. *Application of Light-Scattering Techniques for the Measurements of Density, Temperature and Velocity in Gasdynamics*. National Technical Information services Clearinghouse, Springfield, 1973.

52 H. Ashkenas and F. S. Sherman. *Structure and Utilization of Supersonic Free Jets in Low Density Wind Tunnels*. 4<sup>th</sup> International Symposium on Rarefied Gas Dynamics. J. H. de Leeuw ed. Vol. 2. Academic Press, Toronto, 1966.

53 S. H. Kang and J. A. Kunc. *Viscosity of High-Temperature Iodine*. Phys. Rev. A, 44, 6, pp. 3596-605. 1991.

54 K. N. C. Bray. *Atomic Recombination in a Hypersonic Wind-Tunnel Nozzle*. J. Fluid Mech., 6, pp. 1-32. 1958.

55 F. T. Smith. *On the Analysis of Recombination Reactions in an Expanding Gas Stream*. 7th Symp. on Combustion. Butterworths, London, 1958.

56 P. A. Blythe. *Nonequilibrium Flow through a Nozzle*. J. Fluid. Mech., 17, p. 196, 1962.

57 H. K. Cheng and R. S. Lee. *Freezing of Dissociation and Recombination in Supersonic Nozzle Flows: Part I. General Discussion and Special Analysis*. AIAA J. 6, 5, pp 823-31, 1968.

58 H. K. Cheng and R. S. Lee. *Freezing of Dissociation and Recombination in Supersonic Nozzle Flows: Part II. More General Analysis and Numerical Example*. AIAA J. 6, 5, pp 831-37, 1968.

59 J. W. L. Lewis, W. D. Williams, L. L. Price and H. M. Powell. *Nitrogen Condensation in a Sonic Orifice Expansion Flow*. AEDC-TR-74-36. 1974.

60 J. W. L. Lewis, W. D. Williams. *Argon Concentration in Free jet Expansions*. AEDC-TR-74-32. 1974.

61 O. F. Hagena and W. Obert. *Cluster Formation in Expanding Supersonic Jets: Effect of Pressure, Temperature, Nozzle Size, and Test Gas*. J. Chem. Phys., 56, 5, pp



1793-1802, 1971.

62 D. R. Stull. *Vapor pressure of Pure Substances*. Industrial Engineering Chemistry.  
39, 4, p 540, 1947.

## ATTACHMENT 4

# Analytical dependence of the viscosity cross sections and viscosity coefficients on parameters of intermolecular potentials

Joseph A. Kunc<sup>a)</sup>

*Institute for Theoretical Atomic and Molecular Physics, Harvard University and Smithsonian Astrophysical Observatory, Cambridge, Massachusetts 02138*

(Received 21 December 1992; accepted 10 June 1993)

General analytical expressions for viscosity cross sections and viscosity coefficients of gases as functions of the parameters of intermolecular potentials are derived from the first principle using the classical scattering theory. Two types (one repulsive-attractive and one purely repulsive) of the central-force potentials, suitable to represent molecule-molecule, atom-molecule and atom-atom interactions, are considered. The expressions for viscosity show good agreement with results of numerical calculations in high-temperature single-component gases (above 2000 K) where viscosity measurements are not available.

## I. INTRODUCTION

The viscosity cross sections and viscosity coefficients of gases depend on the properties of the intermolecular potentials for binary collisions dominating transport of linear momentum in the gases. [In a single-component gas (a gas consisting of one kind of nonreacting and nondissociating particles) the potentials can be approximated by a single intermolecular potential.] The existing expressions for the viscosity cross sections and for the viscosity coefficients of gases do not show explicitly the dependence on *all* parameters of the intermolecular potentials for the collisions dominating the gas viscosity. In numerical calculations of the viscosity cross sections and viscosity coefficients for neutral gases, this dependence is always "hidden" in the collision integrals.<sup>1</sup> This is very inconvenient especially when studying transport properties of gases for which the viscosity cross sections and viscosity coefficients are not available. Therefore, the main goal of this work is to evaluate *from the first principle* reliable analytical expressions for viscosity cross sections and viscosity coefficients for gases where a reasonable representation of the intermolecular potentials through well-defined central-force potentials can be provided. Two such potentials are considered: one repulsive-attractive [Lennard-Jones (12,6)] potential and one purely repulsive [ $U(r) \sim r^{-7}$ ] potential. The approach of this work is general and can be applied in a straightforward way to other types of intermolecular potentials. The viscosity cross sections are derived below using the classical scattering theory. [It has been demonstrated repeatedly (see Ref. 2 and references therein) that the classical approach leads quite often to accurate predictions of gas viscosity if the orbiting collisions in the gas are handled in a realistic way—see Sec. IV.] The expressions of this work for the viscosity coefficients are valid in single-component gases which are not far from thermal equilibrium and which have particle density below  $10^{20} \text{ cm}^{-3}$  (so that the gas kinetic processes are controlled by binary collisions).

## II. APPROACH

The viscosity  $\eta$  of a single-component gas in complete (or local) thermal equilibrium with temperature  $T$  can be given as<sup>2</sup>

$$\eta(T) = \frac{5kT}{8\Omega(T)}, \quad (1)$$

where  $k$  is the Boltzmann constant, and  $\Omega$  is the transport collision integral,

$$\Omega(T) = \frac{1}{2\pi^{1/2}} \left( \frac{\mu}{2kT} \right)^{7/2} \times \int_0^\infty \exp(-\mu w^2/2kT) Q(w) w^7 dw, \quad (2)$$

where  $E = \mu w^2/2$  is the impact energy,  $w$  is the relative speed, and  $\mu$  is the reduced mass of the particles in binary collisions, and  $Q(w)$  is the viscosity cross section for the collisions,

$$Q(w) = 2\pi \int_0^\infty \{1 - \cos^2[\chi(b, w)]\} b db, \quad (3)$$

and where  $\chi$  and  $b$  are collision deflection angle and impact parameter, respectively. If the interaction potential for binary collisions is a central-force potential  $U(r)$  ( $r$  is the distance between the particles) then the deflection function  $\chi(b, w)$  can be given as

$$\chi(b, w) = \pi - 2b \int_{r_{\min}}^\infty \frac{dr}{r^2 [1 - b^2/r^2 - U(r)/E]^{1/2}}, \quad (4)$$

where  $r_{\min}$  is the classical turning point.

In a gas of neutral particles, the potentials  $U(r)$  may be approximated by two types of functions (other possibilities are discussed below):

(a) repulsive-attractive Lennard-Jones potential,

$$U_a(r) = 4\epsilon \left[ \left( \frac{\sigma}{r} \right)^{12} - \left( \frac{\sigma}{r} \right)^6 \right], \quad (5)$$

(b) purely repulsive potential such as

<sup>a)</sup>Present address: Departments of Aerospace Engineering and Physics, University of Southern California, Los Angeles, California 90089-1191.

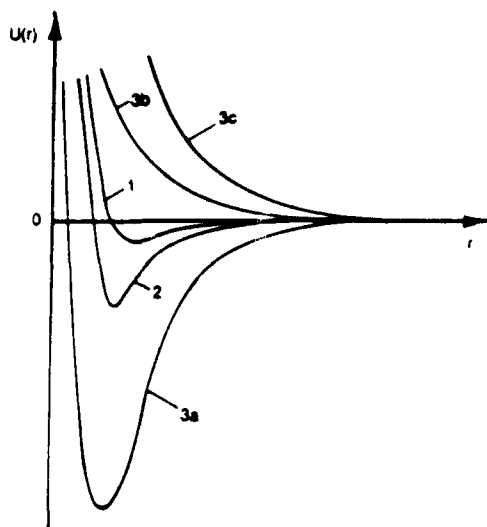


FIG. 1. Examples of typical central-force potentials for molecule-molecule interaction (curve 1), for atom-molecule (overall) interaction (curve 2), and for atom-atom interaction (curves 3a, 3b, and 3c) when the collision impact parameter is zero. The well depth for the potential 3a can be much greater (by orders of magnitude) than the well depths of the potentials 1 and 2.

$$U_b(r) = \frac{C_s}{r^s}, \quad (6)$$

where  $\epsilon$ ,  $\sigma$ ,  $C_s$ , and  $s$  are some positive constants hereafter called the parameters of the potentials. Examples of the potential curves are given in Fig. 1. Approximation of the potentials by the repulsive-attractive potential of type (5) is usually sufficient for recovering of the major features of the momentum transfer during the molecule-molecule interactions, and during some (especially, in noble gases) atom-atom interactions. An example of such potential is shown in Fig. 1 as curve 1. Some atom-atom interactions can follow several, often quite different, potential curves even when both atoms are in their ground states. Three such curves are shown in Fig. 1 as curves 3a, 3b, and 3c. The repulsive-attractive potential 3a can be approximated, for the purpose of this work, by function (5). The repulsive potentials 3b and 3c can be approximated by function (6) with the exponent  $s$  increasing with increase of the "steepness" of the curves. In other words,  $s_{3c}$  (the value of  $s$  for the curve 3c) is greater than  $s_{3b}$  (the value of  $s$  for curve 3b). The potential  $U(r)$  for atom-molecule interaction can be quite complex, but the overall effect of such interaction can sometimes be approximated<sup>3</sup> by a repulsive-attractive potential (5); an example of such a potential is given in Fig. 1 as curve 2.

We do not consider in this work the momentum-transfer collisions in the field of potentials having multiple barriers which arise from the interaction of states with the same symmetry (for example, curve crossing interactions). This, however, should not introduce any meaningful error to our considerations because the number of such collisions is usually much smaller than the total number of the momentum-transfer collisions in the gas. Also, we neglect

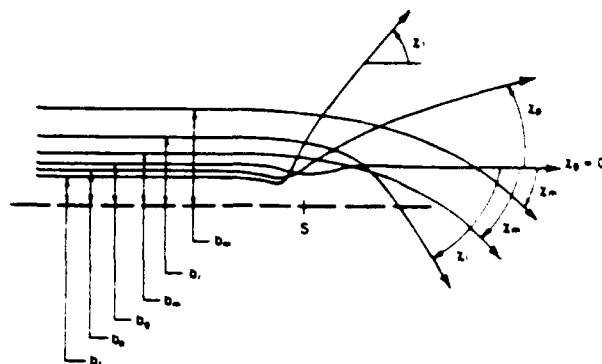


FIG. 2. Examples of trajectories of the reduced mass  $\mu$  of a binary collision system scattered on the center  $S$  which is the origin of a repulsive-attractive central-force potential. The deflection angles  $\chi$  and corresponding impact parameters  $b$  for particular trajectories are shown in the figure. The small-angle approximation is used for description of scatterings when  $\chi_m < \chi < \chi_p$ , while the trajectories with  $\chi > \chi_p$  are described by the large-angle approximation; the scattering with  $\chi = \chi_r = 0$  is the glory scattering, the trajectory with  $\chi = \chi_r$  (and with the impact parameter  $b_r$ ) is the trajectory corresponding to the rainbow scattering.

the tunneling through the barrier of the effective potential energy and the resonance scattering associated with metastable energy levels of the inner potential well and with virtual energy levels above the barrier. (In most cases, inclusion of these processes in calculations of the viscosity coefficients is not of a significant importance<sup>4</sup>).

Integrals (4), (3), and (2) cannot be obtained in closed form. We solve the problem by dividing all binary collisions between gas particles into two (see Fig. 2) groups: (1) the collisions resulting in scattering in "small angles," and (2) the collisions resulting in scattering in "large angles." The first group includes all the collisions with  $\chi_m < \chi(b) < \chi_p$ , where  $\chi_p = \pi/n$  and  $\chi_m = -\pi/n$ , and where the "smallness" of the angles  $|\chi_m|$  and  $|\chi_p|$  requires  $n$  to be greater than five. (Value of  $n=6$  is chosen in the present work because it allows to make a number of convenient simplifications.) The second group of the collisions includes all the collisions with  $\chi(b) > \chi_p$  and  $\chi_r < \chi(b) < \chi_m$ , which reflects the fact that some collisions in the field of the repulsive-attractive potential can result in the negative deflection angles  $\chi$  smaller than  $\chi_m$  but not smaller than the rainbow angle  $\chi_r$ . (The orbiting collisions are discussed in Sec. IV.)

Taking the above into account, the classical viscosity cross section (3) for a binary collision in the field of the repulsive-attractive potential (5) can be written as follows: (1) in the case when  $\chi_r > \chi_m$ ;

$$Q_a(w) = 2\pi \left[ \int_0^{b_p} \{1 - \cos^2[\chi_a^{(1)}(b, w)]\} b db + \int_{b_p}^{\infty} \{1 - \cos^2[\chi_a^{(2)}(b, w)]\} b db \right], \quad (7)$$

(2) in the case when  $\chi_r < \chi_m$ ;

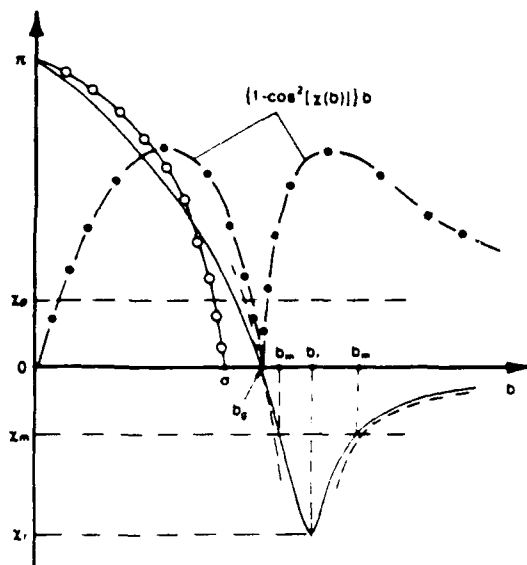


FIG. 3. Typical deflection function  $\chi(b)$  (solid line) for elastic collision of two particles (of a given relative velocity  $w$ ) in the field of the repulsive-attractive potential of type (5). The meaning of the symbols is the same as in Fig. 2. The dash-circle curve is the deflection function for the particles interacting through a rigid-sphere potential with collision diameter  $d=\sigma$ . The dashed curve is the small-angle approximation to the deflection function  $\chi(b)$  for the collisions leading to scattering into the angles  $\chi_m < \chi < \chi_p$ . The dash-dot curve represents the integrand in Eq. (3).

$$Q_a(w) = 2\pi \left[ \int_0^{b_p} \{1 - \cos^2[\chi_a^{(l)}(b, w)]\} b db + \int_{b_p}^{b'_m} \{1 - \cos^2[\chi_a^{(s)}(b, w)]\} b db + \int_{b'_m}^{b''_m} \{1 - \cos^2[\chi_a^{(l)}(b, w)]\} b db + \int_{b''_m}^{\infty} \{1 - \cos^2[\chi_a^{(s)}(b, w)]\} b db \right], \quad (8)$$

where  $\chi_a^{(l)}(b, w)$  and  $\chi_a^{(s)}(b, w)$  denote the large-angle approximation and the small-angle approximation, respectively, to the deflection function  $\chi(b, w)$  given by relationship (4) when  $U(r)$  is given by Eq. (5). The impact parameter  $b_p$  corresponds to the scatterings into the angle  $\chi_p$ . The impact parameters  $b'_m$  and  $b''_m$  are the lower and the upper limits, respectively, of the impact parameter in collisions resulting in deflection angles  $\chi < \chi_m$ .

In the case of binary collisions in the field of the repulsive potential (6), the viscosity cross section is

$$Q_b(w) = 2\pi \left[ \int_0^{b_p} \{1 - \cos^2[\chi_b^{(l)}(b, w)]\} b db + \int_{b_p}^{\infty} \{1 - \cos^2[\chi_b^{(s)}(b, w)]\} b db \right], \quad (9)$$

where  $\chi_b^{(l)}(b, w)$  and  $\chi_b^{(s)}(b, w)$  are the large-angle and the

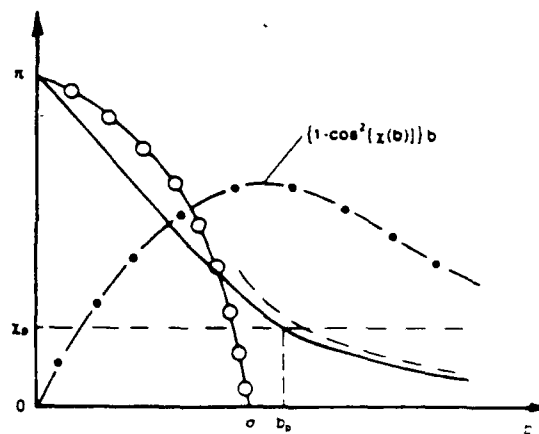


FIG. 4. Typical deflection function  $\chi(b)$  (solid line) for elastic collision of two particles (of a given relative velocity  $w$ ) in the field of the repulsive potential of type (6). The meaning of the symbols is the same as in Fig. 2 and Fig. 3. The dash-circle curve is the deflection function for the particles interacting through a rigid-sphere potential with collision diameter  $d=\sigma$ . The dashed curve is the small-angle approximation to the deflection function  $\chi(b)$  for the collisions leading to scattering into the angles  $\chi_m < \chi < \chi_p$ . The dash-dot curve represents the integrand in Eq. (3).

small-angle approximations, respectively, to the deflection function  $\chi(b, w)$  given by relationship (4) when  $U(r)$  is given by Eq. (6) (see also Figs. 3 and 4).

### III. THE DEFLECTION FUNCTION IN THE SMALL-ANGLE APPROXIMATION

In the case of small-angle scattering, the function  $1 - \cos^2[\chi(b, w)]$  in integral (3) can be expanded in the following rapidly converging series,

$$1 - \cos^2[\chi(b, w)] = \chi^2(b, w) - \frac{\chi^4(b, w)}{3} + \frac{2\chi^6(b, w)}{45} - \frac{\chi^8(b, w)}{315} + \dots, \quad (10)$$

which in the case when  $n > 6$  can be approximated by the first term of the expansion.

If the reduced mass  $\mu$  representing the binary collision system is moving before the collision in a direction  $z$  with linear momentum  $p$ , then the momentum  $(\Delta p)_y$  transferred during the collision in the direction  $y$  perpendicular to  $z$  is

$$(\Delta p)_y = |p| \sin \chi = \mu w \sin \chi, \quad (11)$$

where, as before,  $\chi$  is the deflection angle of the collision. In the case of scattering in small angles one can assume that  $\sin \chi \approx \chi$ . The amount  $(\Delta p)_y$  of the momentum transferred in the direction  $y$  can be given by integrating the  $F_y$  component of the force acting between the particles. This component is

$$F_y = -\frac{\partial U(r)}{\partial y} = -\frac{\partial U(r)}{\partial r} \frac{\partial r}{\partial y} \approx -\frac{\partial U(r)}{\partial r} \frac{b}{r}, \quad (12)$$

because in the small-angle approximation  $y \approx b$ . Thus

$$\chi(b, \omega) = \frac{(\Delta p)_y}{(2\mu E)^{1/2}} = -\frac{b}{(2\mu E)^{1/2}} \int_{-\infty}^{+\infty} \frac{\partial U(r)}{\partial r} \cdot \frac{dr}{r} \quad (13)$$

Assuming further that in small-angle approximation  $z \approx \omega t$ , and remembering that  $r$  varies from  $+\infty$  to  $b$  and back when  $z$  varies from  $-\infty$  to  $+\infty$ , Eq. (13) becomes

$$\chi(b, \omega) = -\frac{2b}{\mu \omega^2} \int_b^{\infty} \frac{\partial U(r)}{\partial r} \frac{1}{(r^2 - b^2)^{1/2}} dr. \quad (14)$$

### A. Repulsive-attractive interactions

Using Eqs. (14) and (5) one obtains the deflection function  $\chi_a(b, \omega)$  for the small-angle elastic scattering in the field of the repulsive-attractive potential  $U_a(r)$ ,

$$\chi_a(b, \omega) = \frac{3\pi\epsilon}{2\mu\omega^2} \left[ \frac{231}{32} \left( \frac{\sigma}{b} \right)^{12} - 5 \left( \frac{\sigma}{b} \right)^6 \right]. \quad (15)$$

The impact parameter  $b_p$  corresponding to the value of  $\chi_a = \chi_p$  can be obtained from solution of the equation

$$\chi_a(b, \omega) - \chi_p = 0, \quad (16)$$

because we assume that the small-angle deflection function is satisfactory approximation of the real deflection function when  $\chi$  is close to  $\chi_p$ . Assuming that  $\chi_p = \pi/n$  and using Eq. (15) one obtains from Eq. (16)

$$b_p = \left[ \frac{15n\epsilon}{8E} \left[ \left( 1 + \frac{77E}{50n\epsilon} \right)^{1/2} - 1 \right] \right]^{1/6} \sigma \\ \approx \left[ \frac{3}{u} [ (1+u)^{1/2} - 1 ] \right]^{1/6} \sigma, \quad (17)$$

where  $u = 77E/(50n\epsilon)$  and where we assumed that  $(77/80)^{1/6} = 1$  instead of the accurate value 0.994.

For small-angle scattering in the field of the repulsive-attractive potential  $U_a(r)$  one has from Eq.  $\chi_a(b) = 0$  [where the function  $\chi_a(b)$  is given by Eq. (15)] that  $b_g = (231/160)^{1/6} \sigma$ , where  $b_g$  is the forward glory impact parameter (the impact parameter corresponding to  $\chi = 0$ ). Because

$$\left( 1 + \frac{77E}{50n\epsilon} \right)^{1/2} - 1 + \frac{77E}{100n\epsilon} \quad \text{when } u \rightarrow 0, \quad (18)$$

one obtains from Eq. (17) that  $b_p \rightarrow (231/160)^{1/6} \sigma = b_g$  when  $u \rightarrow 0$ . In the case of large values of  $u$  one has  $b_p \rightarrow 0$  when  $u \rightarrow \infty$ . As can be seen from Fig. 5, the value of  $b_p$  in Eq. (17) differs only slightly from  $\sigma$  in collisions with  $u \leq 10$ . Therefore, we assume below that  $b_p = \sigma$  whenever  $u \leq 10$ .

When  $u > 10$ , the difference between  $\sigma$  and  $b_p$  increases slowly with  $u$  (see Fig. 5). Then,  $(1+u)^{1/2} \approx u^{1/2}$  and using relationships (17) one obtains  $b_p = [u(u^{1/2} - 1)/3]^{1/6} \sigma$ .

The impact parameters  $b'_m$  and  $b''_m$  corresponding to value of  $\chi_a = \chi_m$  can be obtained from equation

$$\chi_a(b, \omega) - \chi_m = 0, \quad (19)$$

because we assume that the small-angle deflection function is satisfactory approximation of the exact deflection func-

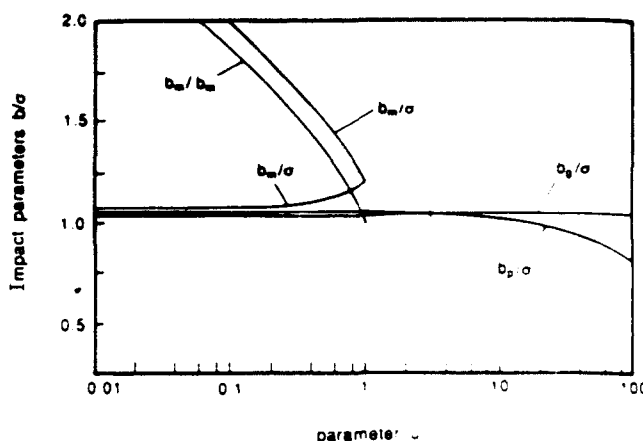


FIG. 5. Dependence of the characteristic impact parameters of a binary elastic collision in the field of potential (5) on the parameter  $u$ .  $b_p$  is the impact parameter at which the collision deflection angle  $\chi$  is equal to  $\chi_p = \pi/6$ .  $b_g$  is the forward glory impact parameter.  $b'_m$  and  $b''_m$  are impact parameters at which the collision deflection angle is equal to  $\chi_m = -\pi/6$ , and  $\sigma$  is the distance between the colliding particles at which the intermolecular potential vanishes.

tion  $\chi(b, \omega)$  when the deflection angles are close to  $\chi_m$ . Assuming further that  $\chi_m = -\pi/n$ ,  $n=6$ , and using Eqs. (15) and (19) one obtains

$$b'_m = \left[ \frac{15n\epsilon}{8E} \left[ 1 - \left( 1 - \frac{77E}{50n\epsilon} \right)^{1/2} \right] \right]^{1/6} \sigma \\ \approx \left[ \frac{3}{u} [1 - (1-u)^{1/2}] \right]^{1/6} \sigma, \quad (20)$$

and

$$b''_m = \left[ \frac{15n\epsilon}{8E} \left[ 1 + \left( 1 - \frac{77E}{50n\epsilon} \right)^{1/2} \right] \right]^{1/6} \sigma \\ \approx \left[ \frac{3}{u} [1 + (1-u)^{1/2}] \right]^{1/6} \sigma \quad (21)$$

When  $u > 1$ , the smallest angle  $\chi_s$  is greater than  $\chi_m = -\pi/6$  and the deflection angle  $\chi_a(b, \omega)$  is always greater than  $\chi_m$  for any value of  $b$ . Then, the small-angle deflection function  $\chi_a(b, \omega)$  can be used whenever  $b$  is greater than  $b_p$ .

### B. Repulsive interactions

Using Eqs. (14) and (6) one obtains the deflection function  $\chi_b(b, \omega)$  for small-angle scattering in field of the repulsive potential  $U_b(r)$ ,

$$\chi_b(b, \omega) = \frac{\pi^{1/2} s C_s \Gamma(s/2 + 1/2)}{\mu \omega^2 b^s \Gamma(s/2 + 1)}. \quad (22)$$

In order to obtain an analytical dependence of  $\chi_b$  on the exponent  $s$  we assume that  $s$  is an integer greater than one. Subsequently, we simplify Eq. (22) by introducing a parameter  $p = s/2 + 1/2$  and by noting that  $\Gamma(p)$  increases monotonically with  $p$  as long as  $p > 3/2$ . Then, the  $s$  dependence of the ratio of the gamma functions in relationship (22) can be written as

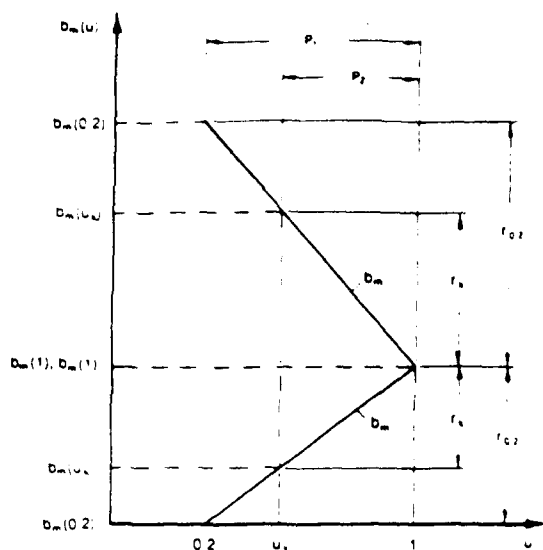


FIG. 6. Linear approximations (the thick solid lines) to the functions  $b'_m(u)$  and  $b''_m(u)$  (shown in Fig. 5) in the interval  $0.2 < u < 1$ .

$$g_h = \frac{\Gamma(s/2 + 1/2)}{\Gamma(s/2 + 1)} = \frac{\Gamma(p)}{\Gamma(p + 1/2)} \quad (23)$$

In most applications  $p$  is less than five,  $g_h$  is weakly dependent on  $p$  and close to 0.56.

#### IV. THE DEFLECTION FUNCTION IN THE LARGE-ANGLE APPROXIMATION

##### A. Repulsive-attractive interactions

##### 1. Collisions with $b < b_p$

The scattering in angles  $\chi$  greater than  $\chi_p$  ( $b < b_p$ ) can be represented by the rigid-sphere deflection function  $\chi_0(b, w) = 2 \arccos(b/d)$  ( $d$  is the kinetic "collision diameter"). Subsequently, the viscosity cross section for the large-angle scattering when  $b < b_p$  is

$$Q_0(w) = 2\pi \int_0^{b_p} \{1 - \cos^2[\chi_0(b, w)]\} b db = 2\pi b_p^2/3. \quad (24)$$

##### 2. Collisions with $b'_m < b < b''_m$

Scattering into negative angles smaller than  $\chi_m = -\pi/n$  occurs when  $u < 1$ . In principle, the impact parameter  $b_r$  corresponding to the minimum value of the angle  $\chi$  (which is the rainbow angle  $\chi_r$ ) can be found from solution of the equation

$$\frac{\partial \chi(b, w)}{\partial b} = 0, \quad (25)$$

when  $\chi(b, w) < \chi_m$ . The function  $\chi(b, w)$  in Eq. (25) should be the exact deflection function for the repulsive-attractive potential (5) because the small-angle deflection function  $\chi_a(b, w)$  is inaccurate when  $\chi < \chi_m$ . Unfortunately, the solution of Eq. (25) can not be obtained in an analytical form. However, it can be seen from Fig. 5 that  $b'_m$  and  $b''_m$  can be approximated by linear functions of  $u$  when  $0.2 \lesssim u \lesssim 1$ . It is obvious from Fig. 6 showing these

functions that

$$\frac{r'_{0.2}}{r'_k} = \frac{p_1}{p_2} \quad \text{and} \quad \frac{r''_{0.2}}{r''_k} = \frac{p_1}{p_2}, \quad (26)$$

which leads to conclusion that the ratio

$$\frac{b'_m(1) - b'_m(0.2)}{b''_m(0.2) - b''_m(1)} = \frac{b'_m(1) - b'_m(u_k)}{b''_m(u_k) - b''_m(1)} \quad (27)$$

is practically constant for an arbitrary  $u_k$  greater than 0.2 but smaller than 1. This means that in collisions with  $0.2 < u < 1$  there is a value of the impact parameter which is almost constant regardless of the values of  $u$ ,  $b'_m$ , and  $b''_m$ , including the case when  $b'_m = b''_m$  and  $u = 1$ . Since there is only one extremum (the rainbow angle  $\chi_r$ ) of the deflection function  $\chi_r$  (the subscript  $r$  indicates the deflection function when  $b'_m < b < b''_m$  and  $0.2 < u < 1$ ) this constant value of the impact parameter must be close to the rainbow impact parameter  $b_r$ . At  $u = 1$ ,  $b_r = b'_m = b''_m$ , and  $b_r = (231.80)^{1/6} \sigma = 6\sigma/5$ . Subsequently, Eq. (15) yields the rainbow angle (in radians),

$$\chi_r = -\frac{\pi}{nu} = -\frac{50\pi\epsilon}{77E} = -2.05 \frac{\epsilon}{E}. \quad (28)$$

The viscosity cross section  $Q_r(w)$  for collisions with  $0.2 < u < 1$  and  $b'_m < b < b''_m$  can be given as

$$Q_r(w) = 2\pi \int_{b'_m}^{b''_m} \{1 - \cos^2[\chi_r(b, w)]\} b db \quad (29)$$

When  $0.2 < u < 1$  one obtains from Eq. (28) that

$$-\frac{5\pi}{6} < \chi_r < -\frac{\pi}{6}. \quad (30)$$

As discussed below, when  $u > 0.2$  then  $E/\epsilon > 0.8$  and the orbiting collisions do not occur. Also, the lower limit of interval (30),  $\chi_r = -5\pi/6$ , is close to  $\chi_r = -\pi$  which, according to expression (28), corresponds to  $E/\epsilon = 0.65$  ( $u = 0.17$ ). Therefore, relationship (30) is a reasonable representation of the limits of the deflection function  $\chi_r$ .

The function  $\{1 - \cos^2[\chi_r(b, w)]\}b$  occurring in the cross section (29) can be replaced (the "pentagon" approximation) by the function indicated in Fig. 7 by the dash-dot lines. Consequently,

$$Q_r(w) = 2\pi \int_{b'_m}^{b''_m} \{1 - \cos^2[\chi_r(b, w)]\} b db \approx 2\pi A_k, \quad (31)$$

where

$$\begin{aligned} A_k = & \frac{1}{2}(b_r - b'_m) \{ [1 - \cos^2[\chi_r(b, w)]] b \}_{\max} \\ & - [1 - \cos^2 \chi_m] b'_m + \frac{1}{2}(b''_m - b_r) \\ & \times \{ [1 - \cos^2[\chi_r(b, w)]] b \}_{\max} - [1 - \cos^2 \chi_m] b''_m \\ & + (b''_m - b_r) [1 - \cos^2 \chi_m] b''_m + (b_r - b'_m) \\ & \times [1 - \cos^2 \chi_m] b'_m. \end{aligned} \quad (32)$$

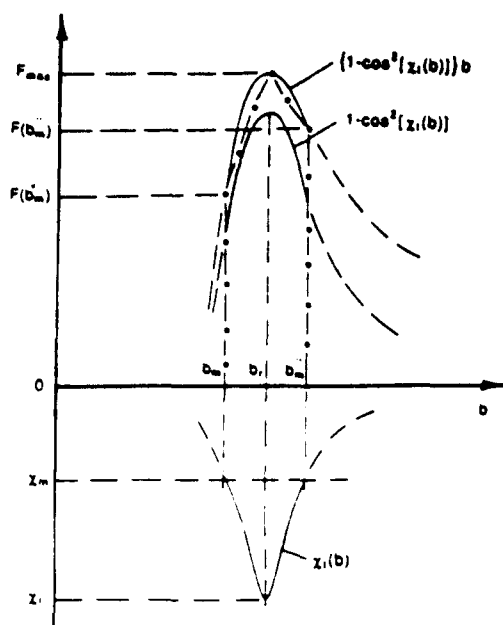


FIG. 7. The pentagon approximation, denoted by the dash-dot line, to the function  $\{1 - \cos^2[\chi_r(b, \omega)]\}b$  for collisions with impact parameters  $b_m' < b < b_m''$  which result in scattering into negative deflection angles smaller than  $\chi_m$  but greater than  $-\pi/2$ .  $F_{\max} = \{[1 - \cos^2[\chi_r(b)]\}b\}_{\max}$  is the maximum value of the function  $[1 - \cos^2[\chi_r(b)]\}b$ ,  $F(b_m'') = [1 - \cos^2[\chi_r(b_m'')]\}b_m''$  and  $F(b_m') = [1 - \cos^2[\chi_r(b_m')]\}b_m'$ .

with  $\{[1 - \cos^2[\chi_r(b, \omega)]\}b\}_{\max}$  being the maximum value of the function  $[1 - \cos^2[\chi_r(b, \omega)]\}b$ .

If  $\chi_r$  for a given collision is smaller than  $-\pi/6$  but greater than  $-\pi/2$ , then the function  $1 - \cos^2[\chi_r(b, \omega)]$  increases monotonically with  $\chi_r$ , reaching maximum when  $\chi_r$  is maximum, that is, when  $\chi_r = \chi_r$  (see Fig. 7). (The interval  $-\pi/2 < \chi_r < -\pi/6$  corresponds to  $0.33 < u < 1$ .) Thus the term  $\{[1 - \cos^2[\chi_r(b, \omega)]\}b\}_{\max}$  in Eq. (32) can be given as

$$\{[1 - \cos^2[\chi_r(b, \omega)]\}b\}_{\max} \approx [1 - \cos^2\chi_r]b_r, \quad (33)$$

because the maximum of the function  $[1 - \cos^2[\chi_r(b, \omega)]\}b$  occurs at an impact parameter which is close to  $b_r$ , a result of the fact that increase of  $b$  cannot compensate the much faster decrease of the function  $1 - \cos^2[\chi_r(b, \omega)]$  when  $b$  becomes greater than  $b_r$ .

A Fourier analysis suggests that when  $0.2 < u < 1$ , the function  $1 - \cos^2\chi_r$  can be approximated by

$$1 - \cos^2[\chi_r(u)] = \frac{\chi_r(u)}{3} [\pi - \chi_r(u)] = \frac{\pi^2}{18} \left( \frac{1}{u} - \frac{1}{6u^2} \right). \quad (34)$$

Taking the above into account, relationship (32) can be rewritten as

$$A_k = \frac{\pi^2}{72} (b_m'' - b_m') \left[ b_m' + b_m'' + b_r \left( \frac{4}{u} - \frac{2}{3u^2} - 1 \right) \right]. \quad (35)$$

Using Eqs. (20) and (21) one obtains

$$b_m'' \mp b_m' \approx \left( \frac{6}{u} \right)^{1/6} \left[ 1 \mp \left( \frac{u}{4} \right)^{1/6} \right] \sigma = \left( \frac{6}{u} \right)^{1/6} \sigma \mp \left( \frac{3}{2} \right)^{1/6} \sigma, \quad (36)$$

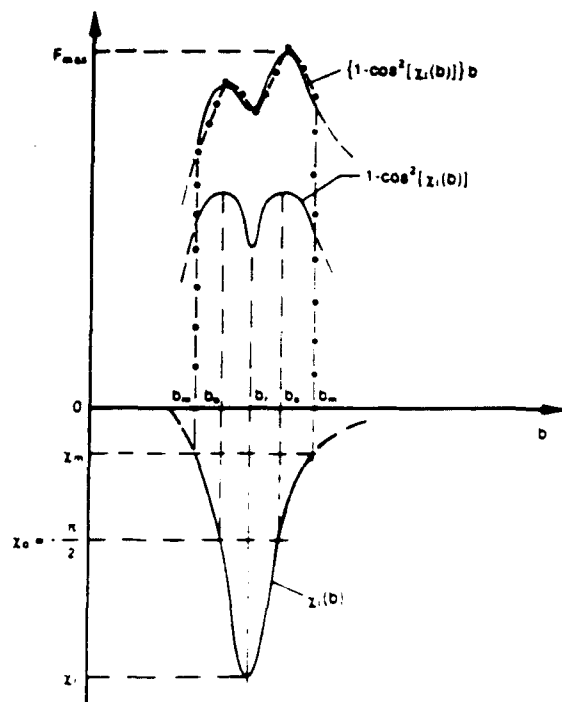


FIG. 8. The saw approximation, denoted by the dash-dot line, to the function  $\{1 - \cos^2[\chi_r(b, \omega)]\}b$  for nonorbiting collisions with impact parameters  $b_m' < b < b_m''$  which result in scattering into negative deflection angles smaller than  $\chi_0 = -\pi/2$ .  $F_{\max} = \{[1 - \cos^2[\chi_r(b)]\}b\}_{\max}$  is the maximum value of the function  $[1 - \cos^2[\chi_r(b)]\}b$ .

where we neglected the term  $u/24$  as much smaller than unity. One should notice that the difference (36) does not approach zero as  $u$  approaches unity. This results from the fact that when  $u$  is approaching unity then the one-term expansion (10) is less and less accurate. However, this fact is not of much importance in calculations of the viscosity cross section because  $A_k$  is small when  $u$  is close to one.

When  $0.33 < u < 1$  one has from Eqs. (35) and (36) that  $b_m' \approx 53\sigma/50$  and  $b_m'' \approx (6/u)^{1/6}\sigma$ . Thus relationship (35) can be rewritten as

$$A_k \approx \frac{\pi^2 (6u - 1) \sigma^2}{90u^2} \left[ \left( \frac{6}{u} \right)^{1/6} - \left( \frac{3}{2} \right)^{1/6} \right]. \quad (37)$$

Variation of the term  $(6/u)^{1/6}$  in Eq. (37) with  $u$  is much slower than the variation of the term  $(6u - 1)/u^2$ :  $(6/u)^{1/6} = 1.37$  (when  $u = 0.9$ ),  $1.50$  (when  $u = 0.5$ ), and  $1.62$  (when  $u = 0.33$ ). Assuming  $(6/u)^{1/6} = 1.50$  and replacing  $1/(20u^2)$  by its value when  $u = 0.5$  one obtains from Eq. (37)

$$A_k = \left( \frac{1}{4u} - \frac{1}{5} \right) \sigma^2. \quad (38)$$

Relationships (33) and (38) cannot be used when  $0.2 < u < 0.33$  because then the maximum value of the function  $1 - \cos^2[\chi_r(b)]$  is not equal to  $1 - \cos^2\chi_r$ , but equal to  $1 - \cos^2[\chi_r = \pi/2] = 1$ . Therefore, we replace in such a case the integral in the cross section (31) by  $A_k$  obtained from the "saw" approximation. In this approximation,  $A_k$  (the area defined in Fig. 8 by the dash-dot lines) can be given as



$$\begin{aligned}
A_k = & \frac{1}{2}(b'_0 - b'_m) \{ [1 - \cos^2 \chi_0] b'_0 - [1 - \cos^2 \chi_m] b'_m \} + \frac{1}{2}(b_r - b'_0) \{ [1 - \cos^2 \chi_0] b'_0 - [1 - \cos^2 \chi_r] b_r \} \\
& + \frac{1}{2}(b''_0 - b_r) \{ [1 - \cos^2 \chi_0] b''_0 - [1 - \cos^2 \chi_r] b_r \} + \frac{1}{2}(b''_m - b''_0) \{ [1 - \cos^2 \chi_0] b''_0 - [1 - \cos^2 \chi_m] b''_m \} + (b''_m - b''_0) \\
& \times [1 - \cos^2 \chi_m] b''_m + (b''_0 - b_r) [1 - \cos^2 \chi_r] b_r + (b_r - b'_0) [1 - \cos^2 \chi_r] b_r + (b'_0 - b'_m) [1 - \cos^2 \chi_m] b'_m
\end{aligned} \quad (39)$$

Derivation of analytical expressions for the impact parameters  $b'_0$  and  $b''_0$  occurring in Eq. (39) is difficult because the function  $\chi_i(b)$ , and subsequently the function  $[1 - \cos^2 \chi_i(b)]b$ , cannot be obtained in an analytical form. Therefore, we make in what follows a reasonable assumption that  $b'_0$  is the midpoint between  $b'_m$  and  $b_r$ , and  $b''_0$  is the midpoint between  $b_r$  and  $b''_m$ .

Because variation of  $u$  when  $0.2 < u < 0.33$  has little impact on values of  $b'_0 - b_r$  and  $b''_m - b''_0$  one has, assuming that  $u$  is a constant equal to 0.25,  $b_r - b'_m = 3\sigma/25$ ,  $b'_0 - b'_m = 3\sigma/50$ ,  $b''_m - b_r = \sigma/2$ ,  $b''_m - b''_0 = \sigma/4$ ,  $b'_m = 27\sigma/25$ ,  $b''_m = 17\sigma/10$ . Taking this into account, assuming  $\chi_0 = -\pi/2$ ,  $\chi_m = -\pi/6$ , and using Eq. (34), one obtains from Eq. (39) when  $0.2 < u < 0.33$ ,

$$A_k = \left( \frac{1}{2} + \frac{1}{10u} - \frac{1}{60u^2} \right) \sigma^2 \approx \frac{3}{5} \sigma^2 \quad (40)$$

It should also be mentioned that even when  $u = 0.33$  (as discussed below the accuracy of the viscosity cross sections at  $u \approx 0.33$  is poor when compared with the cross sections for higher values of  $u$ ) the values of  $A_k$  obtained from Eq. (38) and from Eq. (40) are close to each other (0.56 and 0.65, respectively). This suggests that the mathematical simplifications and physical approximations made during derivation of Eqs. (38) and (40) are quite reasonable.

When  $u < 0.2$  the deflection angle is close to, or smaller than,  $-\pi$ . We neglect such collisions because these collisions contribute little to the viscosity-related transfer of momentum in the gas (see discussion below).

### 3. Orbiting collisions

The effective potential  $U_{\text{eff}}(r, b)$  for a collision in the field of potential (5) with impact parameter  $b$  and with impact energy  $E$  is

$$U_{\text{eff}}(r, b) = U(r) + \frac{L^2}{2\mu r^2} = 4\epsilon \left[ \left( \frac{\sigma}{r} \right)^{12} - \left( \frac{\sigma}{r} \right)^6 \right] + \frac{b^2 E}{r^2}, \quad (41)$$

where  $L = b\mu w = b(2\mu E)^{1/2}$  is the magnitude of the angular momentum of the collision system. The distance  $r_0$  at which the maximum of the centrifugal barrier of the effective potential (41) occurs is

$$r_0 = \left( \frac{2}{b} \right)^{1/2} \left( \frac{3\epsilon}{E} \right)^{1/4} \sigma^{3/2}. \quad (42)$$

Orbiting occurs when the impact energy  $E$  is close to the height  $(U_{\text{eff}})_0$  of the centrifugal barrier. Then, the radial velocity of the reduced mass  $\mu$  is small in some range of the distance  $r$ , and the tangential component of the velocity will carry the particle several times around the scat-

tering center before the radial component of the velocity becomes significant again. In other words, for an orbiting collision to occur, the radial velocity  $\{2[E - U_{\text{eff}}(r, b)]\mu\}^{1/2}$  must be close to zero when the effective potential  $U_{\text{eff}}(r, b)$  is at a classically accessible maximum. Thus orbiting occurs at the impact parameters  $b \approx b_0$  when

$$E \approx U_{\text{eff}}(r, b) \quad \text{and} \quad \frac{\partial U_{\text{eff}}(r, b)}{\partial r} = 0 \quad (43)$$

Using Eq. (41), solution of Eqs. (43) gives two real positive roots which, in general, correspond to a minimum (at  $r = r_m$ ) and a maximum (at  $r = r_0$ ) of the function  $U_{\text{eff}}(r, b)$ . Choosing the larger root one obtains the impact parameter  $b_0$  of the orbiting collision (with impact energy  $E$ ) in the field of potential (41),

$$\begin{aligned}
b_0 = & \frac{2 \cdot 3^{1/6}}{5} \left( \frac{\epsilon}{E} \right)^{2/3} \left[ \left| 1 + \left( 1 - \frac{5E}{4\epsilon} \right)^{1/2} \right|^{1/2} \right. \\
& \times \left. \left| 1 - \left( 1 - \frac{5E}{4\epsilon} \right)^{1/2} + \frac{5E}{2\epsilon} \right|^{1/2} \right] \sigma.
\end{aligned} \quad (44)$$

One can see from Eq. (44) that orbiting will not occur when  $5E/4\epsilon > 1$ , that is, when  $u > 0.2$  ( $E/\epsilon \approx 4u$  if  $n = 6$ ).

### B. Repulsive interactions: Collisions with $b < b_p$

The viscosity cross section (24) for the large-angle scattering (when  $b < b_p$ ) in the field of the potential becomes

$$Q_0(w) = 2\pi b_p^2/3, \quad (45)$$

where  $b_p$  [obtained from Eq.  $\chi_b(b, w) - \chi_p = 0$  when  $\chi_p = \pi/6$ ] is

$$b_p = \left( \frac{3sC_{gh}}{\pi^{1/2}E} \right)^{1/3}. \quad (46)$$

## V. THE VISCOSITY CROSS SECTIONS

### A. Repulsive-attractive interactions

Using the conclusions of the previous sections and Eqs. (7) and (8) one has

(I) The viscosity cross section,  $Q_0^V(w)$  for  $0.2 < u < 0.33$  is

$$Q_a^V(w) = 2\pi \left[ \int_0^\sigma \{1 - \cos^2[\chi_0(b, w)]\} b db + \int_\sigma^{b_m'} \chi_a^2(b, w) b db + \int_{b_m'}^{b_m''} \{1 - \cos^2[\chi_1(b, w)]\} b db + \int_{b_m''}^\infty \chi_a^2(b, w) b db \right] = \frac{\pi\sigma^2}{15} \left( 28 + \frac{1}{u^2} \right), \quad (47)$$

where  $b_m' = 27\sigma/25$  and  $b_m'' = 17\sigma/10$ ;

(II) Using the pentagon approximation (38), the viscosity cross section  $Q_a^S(w)$  for  $0.33 < u < 1$  is

$$Q_a^S(w) = 2\pi \left[ \int_0^\sigma \{1 - \cos^2[\chi_0(b, w)]\} b db + \int_\sigma^{b_m'} \chi_a^2(b, w) b db + \int_{b_m'}^{b_m''} [1 - \cos^2[\chi_1(b, w)]] b db + \int_{b_m''}^\infty \chi_a^2(b, w) b db \right] = \frac{\pi\sigma^2}{30} \left( 8 + \frac{15}{u} + \frac{5}{2u^2} \right), \quad (48)$$

where  $b_m' = 53\sigma/50$  and  $b_m'' = 3\sigma/2$ ;

(III) The viscosity cross section  $Q_a^M(w)$  for  $1 < u < 10$  is

$$Q_a^M(w) = 2\pi \left[ \int_0^\sigma \{1 - \cos^2[\chi_0(b, w)]\} b db + \int_\sigma^\infty \chi_a^2(b, w) b db \right] = \frac{\pi\sigma^2}{12} \left( 8 + \frac{3}{u^2} \right), \quad (49)$$

(IV) The viscosity cross section  $Q_a^L(w)$  for  $u > 10$  is

$$Q_a^L(w) = 2\pi \left[ \int_0^{b_p} \{1 - \cos^2[\chi_0(b, w)]\} b db - \int_{b_p}^\infty \chi_a^2(b, w) b db \right] = \frac{\pi\sigma^2}{u^{1/6}}, \quad (50)$$

where  $b_p = (9/u)^{1/12}\sigma$ .

One should notice that if all the simplifications and approximations made during evaluation of Eqs. (47)–(50) are reasonable then one should have:  $Q_a^V(u=0.33) \approx Q_a^S(u=0.33)$ ,  $Q_a^S(u=1) \approx Q_a^M(u=1)$ , and  $Q_a^M(u=10) \approx Q_a^L(u=10)$ . Indeed, expressions (47)–(50) yield:  $Q_a^V(u=0.33) = 2.48\pi\sigma^2$ ,  $Q_a^S(u=0.33) = 2.54\pi\sigma^2$ ,  $Q_a^S(u=1) = 0.86\pi\sigma^2$ ,  $Q_a^M(u=1) = 0.91\pi\sigma^2$ ,  $Q_a^M(u=10) = 0.66\pi\sigma^2$ , and  $Q_a^L(u=10) = 0.68\pi\sigma^2$ .

We compared the scaled viscosity cross sections  $Q(u)/\pi\sigma^2$  obtained from Eqs. (47)–(50) with results of numerical calculations using in both cases the same Lennard-Jones interaction potential. The agreement for the cross sections  $Q_a^M$  and  $Q_a^L$  is better than one percent when  $u > 1$ .

When  $u \approx 1$ , the cross section  $Q_a^M$  agrees with numerical values within few percent. The cross sections  $Q_a^S$  and  $Q_a^V$  begin to lose their accuracy when  $u \lesssim 0.4$ ; when  $0.2 < u < 0.33$  the difference between our cross section  $Q_a^S$  and that obtained from numerical calculations can be as much as 50%. However, collisions with  $u \lesssim 1$  can be important only in low- and moderate-temperature gases (below 2000 K) where transfer of linear momentum in the gas is insignificant).

## B. Repulsive interactions

The viscosity cross section  $Q_b(w)$  for scattering in the field of the potential  $U_b(r)$  is [see Eq. (9)]

$$Q_b(w) = 2\pi \left[ \int_0^{b_p} \{1 - \cos^2[\chi_0(b, w)]\} b db + \int_{b_p}^\infty \chi_b^2(b, w) b db \right] = \frac{\pi}{3} \left[ 2 + \frac{\pi^2}{12(s-1)} \right] b_p^2, \quad (51)$$

where  $b_p$  is given in Eq. (46).

## VI. THE COLLISION INTEGRALS

### A. Repulsive-attractive interactions

In derivation of the viscosity cross sections we identified five intervals of the parameter  $u$

$$(1) \quad 0 < u < u_1 \quad \text{with } u_1 = 0.2 \quad \text{and } y_1 = 4x/5, \quad (52)$$

$$(2) \quad u_1 < u < u_2 \quad \text{with } u_2 = 0.33 \quad \text{and } y_1 = 4x/3, \quad (53)$$

$$(3) \quad u_2 < u < u_3 \quad \text{with } u_3 = 1 \quad \text{and } y_1 = 4x, \quad (54)$$

$$(4) \quad u_3 < u < u_4 \quad \text{with } u_4 = 10 \quad \text{and } y_1 = 39x, \quad (55)$$

$$(5) \quad u > u_4, \quad (56)$$

where  $y = E/kT$  and  $x = \epsilon/kT$ . The collision integral (2) can now be written as

$$\Omega_a = \left( \frac{kT}{8\pi\mu} \right)^{1/2} \int_0^\infty y^3 \exp(-y) Q_a(y) dy, \quad (57)$$

where, as before,  $Q_a$  is the viscosity cross section for a collision driven by potential (5).

The function  $g(y) = y^3 \exp(-y)$  plays in integral (57) a role of a "weight function" for the cross section  $Q_a(y)$ . The most probable value of  $y$  is  $y_p = 3$ . When  $y \ll 1$ , the function  $g(y)$  decreases rapidly with decrease of  $y$ , and at large values of  $y$ ,  $g(y)$  decreases also rapidly with increase of  $y$ .

Particles of molecular and noble gases interact through shallow potentials, that is, potentials with values of  $\epsilon/k$  less than few hundred Kelvin degrees. When  $kT > \epsilon$  and  $u < u_1 = 0.2$ ,  $y_1$  is less than one. In addition, typical low-energy viscosity cross section  $Q(y)$  is not unusually high and it varies with the impact energy less rapidly than the function  $g(y)$ . Therefore, in gases where  $kT > \epsilon$ , the contribution of collisions with energies less than  $E_1$  to the collision integral

(57) can indeed be neglected. Thus

$$\begin{aligned}\Omega_a &= \left(\frac{kT}{8\pi\mu}\right)^{1/2} \pi\sigma^2 \omega_a(x) \\ &= \left(\frac{kT}{8\pi\mu}\right)^{1/2} \pi\sigma^2 [\omega_a^V(x) + \omega_a^S(x) + \omega_a^M(x) + \omega_a^L(x)],\end{aligned}\quad (58)$$

where

$$\omega_a^V(x) = \int_{y_1}^{y_2} y^3 \exp(-y) Q_a^V(y) dy / \pi\sigma^2,$$

$$\omega_a^S(x) = \int_{y_2}^{y_3} y^3 \exp(-y) Q_a^S(y) dy / \pi\sigma^2, \quad (59)$$

$$\omega_a^M(x) = \int_{y_3}^{y_4} y^3 \exp(-y) Q_a^M(y) dy / \pi\sigma^2,$$

$$\omega_a^L(x) = \int_{y_4}^{\infty} y^3 \exp(-y) Q_a^L(y) dy / \pi\sigma^2. \quad (60)$$

Expressions (59)–(60) can be evaluated exactly using methods of symbolic computations. However, the resulting formulas are lengthy and cumbersome. Because the exact formulas do not appear explicitly in the following analysis, we are not giving them here.

As mentioned previously, interactions of some atoms produced by dissociative processes can be driven by very deep repulsive–attractive potentials (similar to the potential 3a in Fig. 1). The well depth  $\epsilon$  of such potentials can be much greater than  $kT$ —in some cases it can be as high as several electron volts. Relationship (28) indicates that such collisions will mainly be the orbiting collisions. Therefore, we do not evaluate in the present work expressions for viscosity for gases of atoms interacting through the very deep repulsive–attractive potentials. Another reason for doing so comes from the conclusions of work of Levin *et al.*<sup>5</sup> They showed that the higher-lying electronic states of binary systems formed by two interacting atoms produced in the gas by molecular dissociation provide the major contribution to the average collision integrals. [The repulsive–attractive diatomic states with the very large (several electronvolts) well depths are usually the ground state and the lowest excited states of the binary systems formed by two colliding atoms.] The higher-lying states, driven by the shallow repulsive–attractive potentials, can be treated in the way described in this and in the following sections discussing the repulsive–attractive interactions when  $\epsilon < kT$ .

## B. Repulsive Interactions

Using Eq. (51), the collision integral  $\Omega_b$  for a single-component gas of particles interacting through the repulsive potential  $U_b(r)$  given in Eq. (6) can be given as

$$\begin{aligned}\Omega_b &= \left(\frac{kT}{8\pi\mu}\right)^{1/2} \int_0^{\infty} y^3 \exp(-y) Q_b(y) dy \\ &= \frac{1}{6} \left(\frac{\pi}{2\mu}\right)^{1/2} \left[2 + \frac{\pi^2 z}{12(1-z)}\right] \left(\frac{3C_{g,h}}{\pi^{1/2} z}\right)^{2z} \Gamma(4-2z) \\ &\quad \times (kT)^{1/2-2z},\end{aligned}\quad (61)$$

where  $\Gamma(x)$  is the gamma function, and  $z = 1/5$

## C. Viscosity coefficient: Repulsive–attractive interactions

Taking into account relationships (1) and (58)–(60), the viscosity  $\eta_a$  of a single-component gas in which particles interact through the potential  $U_a(r)$  given in Eq. (5) can be given as

$$\eta_a = \frac{5}{4\sigma^2 \omega_a(x)} \left(\frac{2\mu kT}{\pi}\right)^{1/2}, \quad (62)$$

where, as before,  $x = \epsilon/kT$ .

When  $0.02 \leq x \leq 0.2$  the function  $\omega_a(x)$  in Eq. (62) reduces to

$$\omega_a(x) \approx \frac{13}{2} x^{1/4}, \quad (63)$$

so that the collision integral (58) becomes

$$\Omega_a = 3.25\sigma^2 \epsilon^{1/4} \left(\frac{\pi}{2\mu}\right)^{1/2} (kT)^{1/4}, \quad (64)$$

and viscosity (62) is

$$\eta_a = \frac{5}{26\sigma^2 \epsilon^{1/4}} \left(\frac{2\mu}{\pi}\right)^{1/2} (kT)^{3/4}. \quad (65)$$

When  $0.2 < x < 2$ , the function  $\omega_a(x)$  first slightly decreases with  $x$ , then reaches (at  $x \approx 0.7$ ) a very shallow minimum, then increases again as  $x$  becomes greater than about 0.7. In the vicinity of the minimum, the integrals  $\omega_a^S$  and  $\omega_a^M$  are the two major contributors to the collision integral  $\omega_a(x)$ , and the viscosity cross sections  $Q_a^S$  and  $Q_a^M$  are also the two major contributors to the viscosity cross section  $Q_a$ . As mentioned in Sec. V A the accuracy of the cross section  $Q_a$  is poorer at  $x \approx 0.7$  than at smaller values of  $x$  corresponding to higher temperatures. In addition, there is no physical reason for the function  $\omega_a(x)$  not to increase monotonically with  $x$  when  $0.2 \leq x \leq 2$ . Thus the local shallow minimum of  $\omega_a(x)$  at  $x \approx 0.7$  does not reflect physical properties of the gas, but it is rather a result of simplifications made during evaluation of the cross sections  $Q_a^S$  and  $Q_a^M$  and the integrals  $\omega_a^S$  and  $\omega_a^M$ . Therefore, relationship (65) can be used when  $0.2 \leq x \leq 1$  and even, as a rough approximation, when  $1 \leq x \leq 2$  (however, the latter interval of  $x$  is usually of little importance in moderate- and high-temperature gases).

We compared the viscosities obtained from Eq. (65) with existing measured viscosities of the Ar, He, Ne, H<sub>2</sub>, N<sub>2</sub>, O<sub>2</sub>, CH<sub>4</sub>, and CO<sub>2</sub> gases. The agreement between the predicted and measured viscosities for some of the gases at  $T \approx 300$  K is not better than 10%–15%, but, as expected, it improves (almost linearly) with increase of gas temper-

ature. Measured values of the viscosity coefficients at  $T < 2000$  K can be obtained with an accuracy from  $\pm 0.2\%$  to  $\pm 0.5\%$  at temperatures between 300 K and 1000 K, and with accuracy  $\pm 1-2\%$  at temperatures above 1000 K. Thus one can say that, in general, at low and moderate temperatures (below 1500–2000 K), the accuracy of the present expressions for viscosity coefficients is not better than the accuracy of the corresponding measured values. Therefore, at low and moderate temperatures, expression (65) is of a limited value and its main advantage is the fact that it provides an explicit analytical dependence of  $\eta_0$  on the parameters of the interaction potentials. However, at higher temperatures where measured viscosity coefficients are not available, the analytical viscosity coefficients of the present work show good agreement (better than 2%) with the corresponding numerical results. Therefore, the viscosity coefficients of the present work have great practical value in kinetic studies of high-temperature gases. The explicit dependence of the viscosity (65) on the parameters of the interaction potentials allows one to quickly draw important qualitative and quantitative conclusions needed in the process of formulation of detail quantum-mechanical or classical models of transport phenomena in the gases, including gases for which neither experimental nor theoretical viscosities are available.

The experimental viscosities used in the comparison discussed above are those recently recommended in the literature.<sup>6,7</sup> The viscosities differ (often significantly) from the early measurements compiled in Ref. 1. Comparison of these early measurements with numerical predictions of the viscosities (using the potential parameters compiled in Ref. 1) is made in Fig. 8.4-6 in Ref. 1. One should keep in mind when referring to this figure, that the dimensionless quantity  $\eta^*/\sqrt{T^*}$  was obtained assuming that the reduced viscosity  $\eta^* = \eta\sigma^2/\sqrt{\mu\epsilon}$  and that the reduced temperature  $T^* = kT/\epsilon$ . Thus the viscosities shown in the figure are proportional at a given temperature to  $\mu^{1/2}\epsilon^{1/2}/\sigma^2$  and are independent of  $\epsilon$  ( $\eta \sim \mu^{1/2}T^{1/2}/\sigma^2$ ) when plotted as functions of  $kT/\epsilon$ ; the  $T$  dependence of the plotted viscosities is the same (for all values of  $T$  and  $\epsilon$ ) as that of the rigid-sphere viscosity. Therefore, the scaling law used in Fig. 8.4-6 of Ref. 1 for viscosity coefficients is incorrect, which causes the discrepancy and inconsistency, at lower temperatures where  $T \approx \epsilon/k$ , in the agreement between the measured and predicted viscosities shown in the figure.

The  $\epsilon^{-1/4}$  dependence of the viscosity (65) on the well-depth  $\epsilon$  can be tested by comparing this dependence with the one obtained from measured values of the viscosities. This can be done in straightforward way for the gases where collisions are driven by repulsive-attractive potentials because various studies<sup>1</sup> suggest that the viscosity of such gases can be expressed by the following relationship:

$$\eta = \frac{\mu^{1/2}}{\sigma^2} p(\epsilon, T), \quad (66)$$

where  $\mu$  is the reduced mass of the particles participating in the binary collisions,  $\sigma$  is the intermolecular distance at which the intermolecular potential vanishes, and  $p(\epsilon, T)$  is

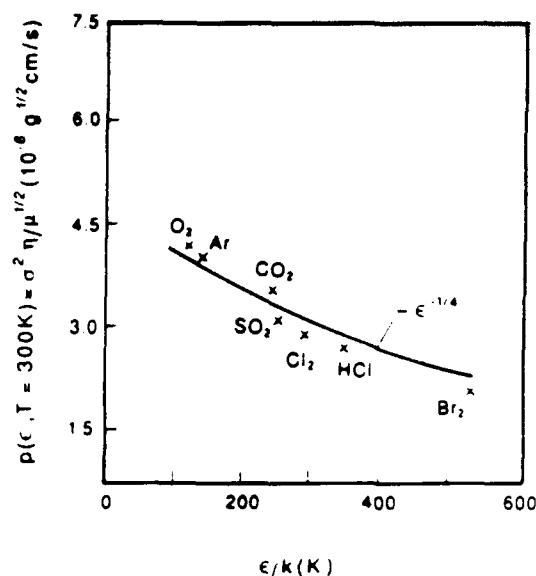


FIG. 9. The function  $p(\epsilon, T) = \sigma^2 \eta / \mu^{1/2}$  [Eq. (67)] for several single-component gases at room temperature;  $\eta$  is the gas viscosity,  $\epsilon$  is the well depth of the interaction potential for binary collisions of particles,  $\sigma$  is the intermolecular distance at which the potential vanishes,  $\mu$  is the reduced mass of the gas particles participating in the binary collisions,  $T$  is the gas temperature, and  $k$  is the Boltzmann constant. The crosses represent the values of the function  $p(\epsilon, T)$  when  $\eta$  is obtained from measurements and the solid line represents the function when  $\eta$  is calculated from expression (65).

a function representing the dependence of the gas viscosity on the potential well-depth  $\epsilon$  and on the gas temperature  $T$ . In order to isolate the dependence of the viscosity  $\eta$  on the well-depth  $\epsilon$  from the viscosity dependence on temperature  $T$  we studied the function

$$p(\epsilon, T) = \frac{\sigma^2 \eta}{\mu^{1/2}}. \quad (67)$$

for several single-component gases at room temperature. (At room temperature viscosity measurements are available for number of gases, the gases are poorly dissociated and poorly ionized, and the magnitude of the potential well-depth  $\epsilon$  is usually important for transport of momentum in the gas). At fixed temperature, function (67) depends on only one parameter—the well-depth  $\epsilon$  of the intermolecular potential representing the binary interactions in the gas. Function (67) is shown in Fig. 9 for number of gases (representing a broad range of the potential well-depth  $\epsilon$ ) at room temperature. One can see from the figure that  $p(\epsilon, T = 300 \text{ K}) \sim \epsilon^{-1/4}$  in the  $\text{O}_2$ , Ar,  $\text{CO}_2$ ,  $\text{SO}_2$ , and  $\text{Cl}_2$  gases (where  $0.02 \leq \epsilon/kT \leq 1$ ), and even in the HCl and  $\text{Br}_2$  gases (where  $1 \leq \epsilon/kT \leq 2$ ).

We test the  $T$  dependence of expression (65) by comparing it with the corresponding expressions for gas of particles interacting through purely attractive part of the LJ potential and for gas of particles interacting through purely repulsive part of the LJ potential. If particles of a single-component gas interact through repulsive-attractive potential, then both repulsive part and attractive part must be taken into account in description of collisions in the gas. Therefore, the exponent  $3/4$  describing the  $T$  dependence

in formula (65) should be between the corresponding exponent for viscosity of the gas of particles interacting through the purely repulsive part of the LJ potential and the exponent for the gas where the particles interact through the purely attractive part of the potential. If two particles interact through a repulsive potential  $U(r) \sim r^{-4}$ , then the differential cross section for an elastic scattering into an angle  $\theta = |\chi|$ , when the relative speed of the particles is  $w$ , is  $dq/d\theta \sim w^{-4/3}$ . Thus one has for the repulsive part [ $U(r) \sim r^{-12}$ ] and for the attractive part [ $U(r) \sim -r^{-6}$ ] of the Lennard-Jones potential, respectively,

$$\frac{dq}{d\theta} \sim w^{-1/3} \quad \text{and} \quad \frac{dq}{d\theta} \sim w^{-2/3} \quad (68)$$

Consequently, since Eq. (3) can be written as

$$Q(w) = \int (1 - \cos^2 \theta) dq, \quad (69)$$

one obtains for the collisions driven by the attractive part of the Lennard-Jones potential,

$$Q(w) \sim w^{-2/3}, \quad \Omega \sim T^{1/6}, \quad \eta \sim T^{5/6} = T^{10/12}. \quad (70)$$

The last relationship results from the fact that in the most important region of the variable  $y$ , integral (57) is  $\Omega \sim T^{1/2} g(y=y_p) Q(y=y_p)$ , where  $g(y=y_p)$  is a constant and  $Q(y=y_p) = Q(E=3kT) = Q[w=(6kT/\mu)^{1/2}]$ . Then,  $\Omega \sim T^{1/2} (T^{1/2})^{-2/3} = T^{1/6}$  because the mean relative speed  $w$  of the colliding particles is proportional to  $T^{1/2}$ .

Considerations similar to those leading to relationships (70) yield the following viscosity cross section, collision integral, and viscosity when binary collisions in the gas are driven by the repulsive part of the Lennard-Jones potential:

$$Q(w) \sim w^{-1/3}, \quad \Omega \sim T^{1/3}, \quad \eta \sim T^{2/3} = T^{8/12}. \quad (71)$$

One should notice that the  $T$  dependence of the viscosity given by relationship (71) is similar to that given by Eq. (76), and that the value of the exponent describing the  $T$  dependence of viscosity (65) lies, as it should, between the corresponding exponents in relationships (70) and (71); in other words,  $8/12 < 3/4 < 10/12$ .

The common rigid-sphere formula for viscosity of a single-component gas is

$$\eta_0 = \frac{5}{16d^2} \left( \frac{2\mu kT}{\pi} \right)^{1/2}, \quad (72)$$

where  $d$  is the hard-sphere collision diameter which is often assumed in literature as equal to the parameter  $\sigma$  of the LJ potential for the actual intermolecular interactions. The ratio of viscosity (65) to viscosity (72) is

$$\frac{\eta_a}{\eta_0} = \frac{8}{13} \left( \frac{d}{\sigma} \right)^2 \left( \frac{kT}{\epsilon} \right)^{1/4}. \quad (73)$$

At very high temperatures ( $x < 0.02$ ), relationship (65) cannot be used. However, at very high temperatures,  $\omega_a(x)$  is a weak function of  $x$  and can be given as  $\omega_a(x) \approx 3$ . (One should keep in mind that when  $x \rightarrow 0$  then  $T \rightarrow \infty$  and the gas under consideration becomes fully ionized.) Therefore, at very high temperatures viscosity (62)

of a single-component neutral, or weakly ionized, gas of particles interacting through Lennard-Jones potential can be written as

$$\eta_{nh} = \frac{5}{12\sigma^2} \left( \frac{2\mu kT}{\pi} \right)^{1/2} \quad (74)$$

This equation has the same  $T$  dependence as the rigid-sphere viscosity given in Eq. (72), and both relationships are identical when

$$d = \frac{3^{1/2}}{2} \sigma = 0.87\sigma. \quad (75)$$

Relationship (75) is in agreement with the fact that an increase of the short-range part of the LJ potential with decrease of the intermolecular distance is slower than the (infinite) increase of the rigid-sphere potential. Thus, replacement of the LJ potential by a rigid-sphere potential of collision diameter  $d = 0.87\sigma$  makes the interaction potential softer (that is, more realistic) than the rigid-sphere potential with  $d = \sigma$ .

Cubley and Mason<sup>8</sup> calculated the transport collision integrals for several single-component gases using intermolecular potentials of Jordan *et al.*<sup>9</sup> The collision integrals were then adjusted to connect smoothly with low-temperature measurements of viscosity. The resulting viscosities for molecular nitrogen and oxygen at temperatures up to 15 000 K were  $\eta(T) \sim T^f$  with  $f = 0.73$  (nitrogen) and  $f = 0.7$  (oxygen); these values would be different if the intermolecular potentials used by the Cubley and Mason were different from those of Jordan's *et al.* Since  $\epsilon_{N_2}/k = 103$  K and  $\epsilon_{O_2}/k = 128$  K, the viscosities of the present work for nitrogen and oxygen gases at  $T \leq 5000$  K can be calculated from Eq. (65), which gives  $f = 0.75$  for both gases. The approximation Cubley and Mason is said to be valid in a very broad range of temperature,  $300 < T < 15\,000$  K. The assumption of constant value of  $f$  in such a broad range of temperature can be invalid at  $T \geq 10\,000$  K because then all gases are highly dissociated and some are also well-ionized; such gases cannot be treated as single-component gases in which collisional processes are driven by a single interaction potential. One should also add, that viscosity of oxygen at  $T > 1000$  K (no data are available for nitrogen) obtained from the approach of Cubley and Mason when using the collision integrals calculated by Yun and Mason<sup>10</sup> shows  $T$  dependence closer to that given by expression (65) than to the one predicted by Cubley and Mason. Also, the high-temperature  $T$  dependence of viscosity predicted by expression (65) is in good agreement with the  $T$  dependence obtained from the collision integrals calculated recently, using a semiclassical approach by Levin *et al.*<sup>5</sup>

As said previously, in most high-temperature ( $T \geq 2000$  K) nonpolar, single-component gases, expression (65) predicts viscosity coefficients with accuracy better than 2% when compared to the accuracy of the coefficients obtained from direct numerical calculations based on classical formalism. [Interaction of polar molecules possessing permanent electric dipole moment is quite different

from interaction of nonpolar molecules;<sup>11,2</sup> the interaction of polar molecules contains strongly angular dependent term of long range ( $\sim r^{-3}$ ). The viscosity coefficients obtained from Eq. (65) for strongly polar gases at high temperature will be, in most cases, within 10% of values obtained from numerical calculations.

In general, the accuracy of formula (65) would improve if the interaction potential used during derivation of the formula was more accurate representation of reality than the Lennard-Jones potential. Also, it has been shown (see Ref. 12, and references therein) that anisotropy and long-range terms (other than the  $r^{-6}$  term) of the interaction potential can be of some importance for momentum transfer in the gas. In most gases, viscosity is not very sensitive to the shapes of the gas particles. However, in some gases containing highly nonsymmetric molecules having large value of ratio of the molecule length to its diameter, the interaction between the molecules will have significant dependence not only on the intermolecular distance but also on the relative orientation of the colliding particles.

The central-force repulsive-attractive potentials studied in this work are those for molecules in rotational-vibrational ground states. Rotational-vibrational excitation of molecules participating in a collision changes the parameters of the intermolecular potential; it decreases the potential well-depth  $\epsilon$  and increases the potential vanishing distance  $\sigma$ .<sup>13,14</sup> The magnitudes of these two effects depend on the degree of the rotational-vibrational excitation, and therefore, they increase with temperature.

The potential parameters  $\epsilon$  and  $\sigma$  used in the present calculations are those recommended in Ref. 15. These parameters agree well with the parameters obtained from elastic scattering measurements by Lee and co-workers.<sup>16,17</sup> Another set of the Lennard-Jones parameters often used in the literature of the subject is that recommended by Sherwood and Prausnitz<sup>18</sup> and their values are close to those compiled from early works by Hirschfelder, Curtiss, and Bird.<sup>1</sup> (A critical review of all the Lennard-Jones potential parameters used in this work is given in Ref. 12.) In general, the values of  $\sigma$  recommended by Sherwood and Prausnitz are greater than the values of  $\sigma$  recommended in Ref. 15, while the opposite is true about the corresponding well-depths  $\epsilon$ . This is one of the reasons that the quality of the analytical expressions of the present work is tested against results of numerical calculations.

#### D. Repulsive interactions

According to Eqs. (1) and (61), the viscosity  $\eta_b$  of single-component gas in which particles interact through the potential  $U_b(r)$  given in Eq. (6) is

$$\eta_b = \frac{15}{4} \left( \frac{2\mu}{\pi} \right)^{1/2} \Gamma^{-1}(4-2z) \left[ 2 + \frac{\pi^2 z}{12(1-z)} \right]^{-1} \times \left( \frac{\pi^{1/2} z}{3C_g h} \right)^{2z} (kT)^{2z+1/2}, \quad (76)$$

where  $\Gamma(x)$  is the gamma function of argument  $x$ , and  $z = 1/s$ .

The steepness of the repulsive potentials  $U_i(r) = C_i/r^s$  shown in Fig. 1 increases with increase of the exponent  $s$ . When  $s$  increases,  $z$  in Eq. (76) decreases and, subsequently, the viscosity  $\eta_b$  also decreases. (Therefore, the higher-lying repulsive diatomic states formed by atoms resulting from dissociation of molecules contribute to lowering of the gas viscosity.) However, one must verify this conclusion by investigating the *simultaneous* dependence of the viscosity  $\eta_b$  on the exponent  $s$  and on the potential parameter  $C_i$  because in general the value of  $C_i$  depends on  $s$ . This can be done by noting that the dependence of the steepness of the repulsive potential (6) on  $C_i$  and  $s$  can be found from the properties of potential (6) at  $r = \sigma$  (or, at any other distance at which two repulsive potentials with different sets of  $s$  and  $C_i$  can be easily distinguished). At  $r = \sigma$ , potential (6) is

$$U_i(\sigma) = \frac{C_i}{\sigma^s} \quad (77)$$

Thus the term  $C_i^{-2z}$  in Eq. (76) can be written as

$$\left( \frac{1}{C_i} \right)^{2z} = \frac{1}{\sigma^2} \left[ \frac{1}{U_i(\sigma)} \right]^{2z} \quad (78)$$

Therefore, an increase of steepness of the potentials of the repulsive states of the diatoms causes an increase of value of  $U_i(\sigma)$ , and, subsequently, a decrease of the gas viscosity  $\eta_b$  given in Eq. (76).

#### E. Role of inelastic collisions

So far, we did not consider the impact of the inelastic collisional channels on magnitude of the viscosity coefficient. In gases with temperatures less than several thousand degrees, the large-gap (bound-bound and bound-free) electronic transitions are usually not important for the transport of momentum in the gases. However, molecular vibration and especially molecular rotation can be well developed in many situations.

In general, the vibrational and rotational transitions can be neglected if the molecular collisions are nearly adiabatic. The requirement for a molecular collision to be nearly adiabatic with respect to a vibrational transition can be written as<sup>4</sup>

$$\frac{10\sigma}{\pi R_e} \left( \frac{m_i \Delta E_v}{\mu kT} \right)^{1/2} \gg 1, \quad (79)$$

where  $\Delta E_v$  is the energy of the transition,  $m_i$  is the mass of the lighter molecule participating in the collision,  $\mu$  is the reduced mass and  $R_e$  is the internuclear equilibrium separation in the target molecule. Criterion (79) was evaluated under assumption that the amplitude of vibration of the molecule in the lower vibrational states is about  $0.1R_e$ , and that the range of the most important interaction between the colliding molecules is close to the potential vanishing distance  $\sigma$ .

The condition for a molecular collision to be nearly adiabatic with respect to a rotational transition can be given as<sup>4</sup>

$$\frac{\sigma \Delta E}{h} \left( \frac{m_i}{kT} \right)^{1/2} \gg 1, \quad (80)$$

where  $\Delta E$ , is the energy of the transition, and  $h$  is Planck's constant.

In weakly dissociated gases,  $(\Delta E/kT)^{1/2}$  is order of unity. Therefore, the vibrational excitation in such gases has usually insignificant impact on gas viscosity. At higher temperatures when dissociation degree is significant and both atomic and molecular collisions contribute to the gas viscosity, the present approach has to be modified in the way discussed in Ref. 3.

In the case of rotational excitation, condition (80) is rarely satisfied in weakly dissociated gases. It seems, however, that the main effect<sup>19</sup> of the rotational transitions on the gas viscosity is shifting the value of the rainbow angle to larger angles with increasing value of  $\Delta J$  ( $J$  is the molecular rotational quantum number). Most likely, the overall effect of the rotational transitions on viscosity of high-temperature, but weakly dissociated, gases is not profound, especially in gases of homonuclear diatomic molecules.

#### ACKNOWLEDGMENTS

The author wish to thank H. K. Cheng, Alex Dalgarno and Evgenii Nikitin for valuable comments. This work was supported by the National Science Foundation through a grant for the Institute for Theoretical Atomic and Molec-

ular Physics at Harvard University and Smithsonian Astrophysical Observatory, and by the Air Force Office for Scientific Research, Grants Nos. 90-0170 and 91-1-0373

- <sup>1</sup>J. O. Hirschfelder, C. F. Curtiss, and R. B. Bird, *Molecular Theory of Gases and Liquids* (Wiley, New York, 1964)
- <sup>2</sup>E. A. Mason, in *Kinetic Processes in Gases and Plasmas*, edited by A. R. Hochstim (Academic, New York, 1969), p. 60
- <sup>3</sup>S. H. Kang and J. A. Kunc, *Phys. Rev. A* **44**, 3596 (1991)
- <sup>4</sup>E. E. Nikitin, *Theory of Elementary Atomic and Molecular Processes in Gases* (Clarendon, Oxford, 1974)
- <sup>5</sup>E. Levin, H. Partidge, and J. R. Stallcop, *J. Thermophys.* **4**, 469 (1990)
- <sup>6</sup>G. C. Maitland and E. B. Smith, *J. Chem. Eng. Data* **17**, 150 (1972)
- <sup>7</sup>D. R. Lide, *Handbook of Chemistry and Physics* (CRC, Boston, 1992)
- <sup>8</sup>S. J. Cubley and E. A. Mason, *Phys. Fluids* **18**, 1109 (1975)
- <sup>9</sup>J. E. Jordan, S. O. Colgate, I. Amdur, and E. A. Mason, *J. Chem. Phys.* **52**, 1143 (1970)
- <sup>10</sup>K. S. Yun and E. A. Mason, *Phys. Fluids* **5**, 380 (1962)
- <sup>11</sup>L. Monchick and E. A. Mason, *J. Chem. Phys.* **35**, 1676 (1961)
- <sup>12</sup>G. C. Maitland, M. Rigby, E. B. Smith, and W. A. Wakeham, *Intermolecular Forces* (Clarendon, Oxford, 1981)
- <sup>13</sup>J. A. Kunc, *J. Phys. B* **23**, 2553 (1990)
- <sup>14</sup>S. H. Kang and J. A. Kunc, *J. Phys. Chem.* **95**, 6971 (1991)
- <sup>15</sup>A. A. Clifford, P. Gray, and N. Platts, *J. Chem. Soc. Faraday Trans. 2* **73**, 381 (1977)
- <sup>16</sup>P. E. C. H. Chen, G. Siska, and Y. T. Lee, *J. Chem. Phys.* **59**, 601 (1973)
- <sup>17</sup>J. A. Barker, R. O. Watts, J. K. Lee, and Y. T. Lee, *J. Chem. Phys.* **61**, 3081 (1974)
- <sup>18</sup>A. E. Sherwood and J. M. Prausnitz, *J. Chem. Phys.* **41**, 429 (1964)
- <sup>19</sup>D. Beck, V. Ross, and W. Schepper, *Z. Phys. A* **293**, 107 (1979)

**ATTACHMENT 5**



# Viscosity of high-temperature iodine

Steve H. Kang and Joseph A. Kunc

*Department of Aerospace Engineering and Department of Physics, University of Southern California,  
Los Angeles, California 90089-1191*

(Received 6 March 1991)

The viscosity coefficient of iodine in the temperature range  $500 \leq T \leq 3000$  K is calculated. Because of the low dissociation energy of the  $I_2$  molecules, the dissociation degree of the gas increases quickly with temperature, and  $I-I_2$  and  $I-I$  collisions must be taken into account in calculations of viscosity at temperatures greater than  $1000^\circ$ . Several possible channels for atom-atom interaction are considered, and the resulting collision integrals are averaged over all the important channels. It is also shown that the rigid-sphere model is inaccurate in predictions of the viscosity. The approach of the present work is general and can be used for other diatomic gases with arbitrary dissociation degree.

Look at Fig. 1, what dissociation does to viscosity ☹☹☹

## INTRODUCTION

Because a significant dissociation of iodine can be achieved at low temperature, it is a particularly attractive candidate for theoretical and experimental studies of chemical nonequilibrium in continuous flows. However, viscosity and other transport coefficients of iodine have neither been measured nor calculated. Therefore, in this paper, we calculate the viscosity of high-temperature ( $500 \leq T \leq 3000$  K) iodine in equilibrium by considering the fact that the gas dissociation degree, and subsequently the frequency of atom-atom and atom-molecule collisions, increases rapidly with temperature.

Viscosity of gas with particles of mass  $m$  at temperature  $T$  can be calculated as [1,2]

$$\eta = \frac{5}{16} \frac{(\pi m k T)^{1/2}}{\pi \sigma^2 \Omega^{(2,2)*}}, \quad (1)$$

where  $k$  is Boltzmann's constant and  $\sigma$  is the particle collision diameter. The so-called collision integral  $\Omega^{(2,2)*}$  is a dimensionless quantity that depends on the temperature and on the force law (for the interparticle potential) through the collision scattering angle  $\chi$ . The scattering angle is averaged over all possible initial impact velocities  $g$  and all possible impact parameters  $b$  to produce the collision integral which has the following form when inelastic collisions are neglected:

$$\Omega^{(2,2)*} = \sigma^{-2} \int_0^\infty \gamma^2 \exp(-\gamma^2) d\gamma \int_0^\pi (1 - \cos^2 \chi) b db, \quad (2)$$

where  $\gamma^2 = mg^2/4kT$ . If inelastic collisions are taken into account, the expression for the viscosity is the same as Eq. (1), but the collision integral for viscosity is more complicated [3]:

$$\begin{aligned} \Omega^{(2,2)*} = & (2\pi)^{-1} (\sigma Q_{\text{int}})^{-2} \sum_{i,j,k,l} \exp(-\epsilon_i - \epsilon_j) \\ & \times \int_0^\infty \gamma^3 \exp(-\gamma^2) d\gamma \int_0^\pi \int_0^{2\pi} \sin \chi [\gamma^4 (1 - \cos^2 \chi) + \frac{1}{3} (\Delta \epsilon)^2 - \frac{1}{3} (\Delta \epsilon)^2 \sin^2 \chi] \\ & \times I_{ij}^{kl}(g, \chi, \phi) d\chi d\phi, \end{aligned} \quad (3)$$

where the internal partition function for the target particle is

$$Q_{\text{int}} = \sum_i \exp(-\epsilon_i), \quad (4)$$

and where the internal quantum states of the colliding particles are denoted by the subscripts  $i, j, k, l$ , and  $\epsilon_i \equiv E_i/kT$ , with  $E_i$  being the energy of the  $i$ th quantum state. A binary collision of two particles initially in states  $i$  and  $j$  results in scattering of particles through the polar angle  $\chi$  and the azimuthal angle  $\phi$ , with the particles ending up in states  $k$  and  $l$ , respectively. The differential cross section for the scattering is  $I_{ij}^{kl}(g, \chi, \phi)$ , and  $\Delta \epsilon = \epsilon_k + \epsilon_l - \epsilon_i - \epsilon_j = \gamma'^2 - \gamma^2$ , where the prime refers to

the relative kinetic energy of the particles after the collision.

Since momentum is conserved in elastic as well as inelastic collisions, both types of interactions can contribute to transport of momentum and hence viscosity of the gas. However, taking the following discussion into account, one can say that the contribution of inelastic processes can be neglected in iodine gas at temperatures below 3000 K.

The three lowest electronic states of the  $I_2$  molecule are the ground state  $X^1\Sigma_g^+$ , the  $B^3\Pi_u$  state, and the  $D^1\Sigma_u^+$  state, with energies of the excited states equal to 1.95 and 5.09 eV, respectively. The three lowest electronic states of the I atom are  $5p^5 2P_{3/2}^o$ ,  $5p^5 2P_{1/2}^o$  and  $6s^4 P_{5/2}$ , with

the excitation energies of the excited states equal to 0.94 and 6.77 eV, respectively.

The ionization potential of the  $I_2$  molecule is 9.31 eV, which is high enough to maintain a low ionization degree of the gas under the conditions considered here. The atomic ionization can also be neglected under these conditions because of the relatively high atomic ionization potential (10.45 eV). In addition, the relative number of excited atomic and molecular ions in the gas is very small. A crude measure of the ionic excitation efficiency is the value of half of the ground-state ionization potential, which is relatively high in ions considered here; this is equal to 10 eV [ $I_2^+(X^2\Pi_g)$ ] and 9.55 eV [ $I^+(5p^4\ ^3P_2)$ ].

In iodine, the typical amount of energy  $\Delta E_{in}/k$  transferred during inelastic collisions to molecular rotation and vibration is very small: less than 100 K in case of the translation-rotation exchange and less than 300 K in case of the translation-vibration exchange. Thus, at higher temperatures, the average ratio  $\Delta\epsilon/\gamma^2 = 2\Delta E_{in}/E_{tr}$  ( $E_{tr}$  is the impact energy) is always distinctively less than 1. Therefore, the terms with  $\Delta\epsilon$  can be neglected in Eq. (3) and one can approximate the differential cross section for inelastic scattering  $I_{ij}^{kl}$  by the cross section for elastic scattering  $I_{el}$ . In addition, the summation over internal states can be carried out independently from the translational states. Taking this into account and assuming that the intermolecular potential is a central-force potential, one obtains

$$\Omega^{(2,2)*} = \sigma^{-2} \int_0^\pi \gamma^2 \exp(-\gamma^2) d\gamma \times \int_0^\pi (1 - \cos^2\chi) I_{el} \sin\chi d\chi, \quad (5)$$

where  $I_{el} \sin\chi d\chi = b db$ . The approximation (5) can be verified by investigation of the ratio of the gas viscosity when inelastic collisions are included to the viscosity when the inelastic collisions are neglected. This ratio can be given as [3]

$$\frac{\eta}{\eta_{el}} = \left[ 1 - \frac{4}{15} \left[ \frac{\eta_{el}}{p\tau} \right] \left[ \frac{c_{int}}{k} \right] (1 - \frac{1}{2} \langle \sin^2\chi \rangle) \right]^{-1}, \quad (6)$$

where  $\langle \sin^2\chi \rangle$  is the average value of  $\sin^2\chi$ ,  $c_{int}$  is the internal heat capacity per molecule,  $p$  is the gas pressure, and  $\tau$  is the relaxation time for the energy transfer between translation and internal states. When the scattering is isotropic ( $\langle \sin^2\chi \rangle = \frac{2}{3}$ ), the correction term in Eq. (6) vanishes. In other words, inelastic collisions have a small effect on the gas viscosity if the anisotropy of the scattering is not significant.

Since the degree of ionization in iodine at  $T < 3000$  K is very small, we neglect in what follows any effects caused by charge exchange during collisions. [It is well known that resonant charge transfer between an ion and a molecule (atom) of the parent gas can significantly affect some transport properties (especially the ion diffusion coefficient and conductivity coefficient, much less gas viscosity).] A similar remark applies to collisions between identical atoms in different states in which resonant transfer of a quantum of internal energy can occur. We neglect the contribution of the resonant processes to

the gas viscosity because the atomic excitation in iodine is inefficient under the conditions considered in this work.

## VISCOSITY OF DISSOCIATING IODINE

The viscosity of mixture of several components depends on viscosities of the pure components; in the case of a gas being a mixture of  $N$  components, the gas viscosity can be expressed as the ratio of two determinants [4-6],

$$\eta_{mix} = - \frac{\begin{vmatrix} H_{qq} & x_q \\ x_q & 0 \end{vmatrix}}{\begin{vmatrix} H_{qq} \end{vmatrix}}, \quad (7)$$

where

$$\begin{vmatrix} H_{qq} & x_q \\ x_q & 0 \end{vmatrix} \equiv \begin{vmatrix} H_{11} & \cdots & H_{1N} & x_1 \\ \vdots & & \vdots & \vdots \\ H_{N1} & \cdots & H_{NN} & x_N \\ x_1 & \cdots & x_N & 0 \end{vmatrix}, \quad (8)$$

$$\begin{vmatrix} H_{qq} \end{vmatrix} \equiv \begin{vmatrix} H_{11} & \cdots & H_{1N} \\ \vdots & & \vdots \\ H_{N1} & \cdots & H_{NN} \end{vmatrix}, \quad (9)$$

and  $x_q$  is the mole fraction (depending on the gas dissociation degree) of the  $q$ th component of the mixture. The elements  $H_{qq}$  are given by the expressions

$$H_{qq} = \frac{x_q^2}{\eta_q} + \sum_{r=1, r \neq q}^N \frac{RT}{pD_{qr}} \left[ \frac{2x_q x_r}{M_q + M_r} \right] \left[ 1 + \frac{3}{5} \frac{M_r}{M_q} A_{qr}^* \right] \quad (10)$$

and

$$H_{qq'} (q' \neq q) = - \frac{RT}{pD_{qq'}} \left[ \frac{2x_q x_{q'}}{M_q + M_{q'}} \right] (1 - \frac{1}{5} A_{qq'}^*), \quad (11)$$

where  $M_q$  is the molecular weight of the  $q$ th component,  $\eta_q$  is the viscosity of the pure  $q$ th component,  $D_{qq'}$  is the coefficient of mutual diffusion of the components  $q$  and  $q'$ ,  $R$  is the universal gas constant, and  $p$  is the total gas pressure. The units of  $D_{qq'}$  are usually  $\text{cm}^2/\text{sec}$ . Before calculating  $D_{qq'}$  one must define  $R$  and  $p$  in consistent units. If  $p$  is in atmospheres,  $R$  must be in  $\text{cm}^3 \text{atm}/\text{mol}^\circ\text{K}$  (82.056); if  $R$  is taken as  $8.3143 \times 10^7$  erg/mol $^\circ\text{K}$ , then  $p$  must be in dyn/cm $^2$ . The ratio  $A_{qq'}^*$  is defined as the ratio of the average values of the products  $\sigma_{qq'}^2 \Omega_{qq'}^{(1,1)*}$ ,

$$A_{qq'}^* = \frac{\langle \sigma_{qq'}^2 \Omega_{qq'}^{(2,2)*} \rangle}{\langle \sigma_{qq'}^2 \Omega_{qq'}^{(1,1)*} \rangle}, \quad (12)$$

where  $\sigma_{qq'}^2$  is the collision diameter for interaction of species  $q$  and  $q'$ .  $\Omega_{qq'}^{(2,2)*}$  is given by an expression similar to Eq. (3) except that it now refers to a collision between two unlike molecules  $q$  and  $q'$ ;  $\Omega_{qq'}^{(1,1)*}$  is the collision integral for diffusion (see below). The expression for  $\eta_{mix}$  given by Eq. (7) has the same form regardless of whether

molecular collisions are elastic or inelastic [4]. In the first-order approximation, the corrections to  $A_{qq}^*$  accounting for inelastic collisions are negligible and one can use calculated  $A_{qq}^*$  for elastic interactions between the particles.

The viscosity of a binary mixture such as high-temperature dissociating iodine (mixture of I atoms and  $I_2$  molecules) can be obtained from Eq. (7) as

$$\eta_{\text{mix}} = \left[ \frac{x_1^2}{H_{11}} + \frac{x_2^2}{H_{22}} - \frac{2x_1x_2H_{12}}{H_{11}H_{22}} \right] \left[ 1 - \frac{H_{12}^2}{H_{11}H_{22}} \right]^{-1}, \quad (13)$$

where the subscripts 1 and 2 denote properties of the  $I_2$  and I components, respectively,

$$H_{12} = -\frac{2x_1x_2RT}{pD_{12}(M_1+M_2)} \left( 1 - \frac{1}{3}A_{12}^* \right), \quad (14)$$

$$H_{11} = \frac{x_1^2}{\eta_1} + \frac{2x_1x_2RT}{pD_{12}(M_1+M_2)} \left[ 1 + \frac{3M_2A_{12}^*}{5M_1} \right], \quad (15)$$

and

$$H_{22} = \frac{x_2^2}{\eta_2} + \frac{2x_1x_2RT}{pD_{12}(M_1+M_2)} \left[ 1 + \frac{3M_1A_{12}^*}{5M_2} \right], \quad (16)$$

where

$$D_{12} = 2.628 \times 10^{-3} T^{3/2} (p \langle \sigma_{12}^2 \Omega_{12}^{(1,1)*} \rangle)^{-1} \times \left[ \frac{M_1+M_2}{2M_1M_2} \right]^{1/2}, \quad (17)$$

where  $D_{12}$  is in  $\text{cm}^2/\text{sec}$ ,  $p$  is in atm, and  $\sigma_{12}$  is in Å.

### VISCOSITY CONTRIBUTION OF $I_2+I_2$ COLLISIONS

We assume in this section that the  $I_2+I_2$  interactions are governed by a single force law specified by the Lennard-Jones (12-6) potential,

$$U_{LJ}(r) = 4\epsilon \left[ \left( \frac{\sigma}{r} \right)^{12} - \left( \frac{\sigma}{r} \right)^6 \right], \quad (18)$$

where  $\epsilon$  is the potential well depth and  $\sigma$  is the intermolecular distance, other than infinity, at which the potential vanishes.

The potential parameters  $\epsilon$  and  $\sigma$  for collision systems involving atoms and molecules are denoted by subscripts  $mm$  (molecule-molecule interaction),  $aa$  (atom-atom interaction), and  $am$  (atom-molecule interaction); for example,  $\epsilon_{am}$  means the potential well depth for the  $I+I_2$  interaction.

The collision diameter for interaction of two identical diatomic molecules can be given as [7]

$$\sigma_{mm} = \frac{c}{J} \langle R \rangle + c, \quad (19)$$

where  $c$  is a constant and  $\langle R \rangle$  is the mean internuclear distance (a function of the rotational and vibrational quantum numbers) in the molecules [8,9],

$$\langle R \rangle = R_0 - (2\beta)^{-1} \ln \left[ 1 - \frac{E - A_0}{D} \right], \quad (20)$$

where  $D$  (equal to  $12\,582\text{ cm}^{-1}$ ) is the dissociation energy referred to the minimum of the intramolecular potential, and  $\beta$  (equal to  $1.799\text{ Å}^{-1}$ ) is the constant in the Morse function,

$$V(R) = D(1 - e^{-\beta(R-R_e)})^2, \quad (21)$$

which approximates the intramolecular potential of the rotationless molecules.

The position of the minimum of the rotational-vibrational intramolecular potential is

$$R_0 = R_e - 4I_e^2 J(J+1)/R_e^3, \quad (22)$$

where  $R_e$  (equal to  $2.667\text{ Å}$ ) is the molecular bond length,  $J$  is the rotational quantum number,

$$I_e^2 = \frac{\hbar}{2B(2\mu D)^{1/2}}, \quad (23)$$

$$A_0 = \frac{\hbar^2 J(J+1)}{2\mu R_0^2}, \quad (24)$$

and

$$E = hc \left[ \omega_e \left( v + \frac{1}{2} \right) - \omega_e x_e \left( v + \frac{1}{2} \right)^2 + B_e J(J+1) - D_e J^2(J+1)^2 \right], \quad (25)$$

where  $E$  is the rotational-vibrational energy of molecule excited to the  $v, J$ th vibrational-rotational level and where the other constants have their usual meaning.

Hirschfelder and Eliason suggested [7] that  $c$  in Eq. (19) is equal to  $1.8\text{ Å}$ . However, a comparison of collision diameters obtained from Eq. (19) with corresponding measured values [10,11] for various collision systems suggests that a more accurate value is  $c = 1.6\text{ Å}$ , which is consistent with the conclusions of Pauling [12]. Using  $c = 1.6\text{ Å}$  and  $\langle R \rangle = R_e$  one obtains from Eq. (19) that  $\sigma_{mm} = 5.156\text{ Å}$  when the colliding molecules are in the ground rotational-vibrational-electronic states.

One finds from Eq. (56) that the mean radius [13] of the iodine atom in the ground electronic state is  $\langle r_a \rangle = 1.324\text{ Å}$ . This value is close to that obtained from the relationship  $\langle r_a \rangle = R_e/2$  suggested by Hirschfelder and Eliason [7] for diatomic homonuclear molecules in the ground electronic state. Consequently, using  $c = 1.6\text{ Å}$  and  $\langle r_a \rangle = 1.324\text{ Å}$  one obtains from Eq. (19) that  $\sigma_{mm} = 5.13\text{ Å}$ .

The intermolecular potential function for interaction of diatomic molecules can be obtained from the Slater-Kirkwood theory [14]. According to the original formulation of the theory, the parameters of the LJ potential for interaction of a particle  $i$  and a particle  $j$  are [14,15]

$$\epsilon_{ij} = \frac{b_{ij}}{2(r_i + r_j)^6}, \quad (26)$$

where

$$b_{ij} = \frac{3e\hbar\alpha_i\alpha_j}{2m_e^{1/2}[(\alpha_i/N_i)^{1/2} + (\alpha_j/N_j)^{1/2}]}, \quad (27)$$

and where  $e$  is the electronic charge,  $m_e$  is the electronic mass,  $r_i$  is the van der Waals radius of the  $i$ th particle,  $\alpha_i$  is the polarizability of the  $i$ th particle, and  $N_i$  is the number of the valence-shell electrons in the  $i$ th particle. A study [16] of intermolecular forces in a number of systems (including the halogen system  $\text{Cl}_2-\text{Cl}_2$ ) showed that more accurate potential parameters are obtained when using the so-called "modified" Slater-Kirkwood method. In the latter approach the potential well depth is obtained by multiplying the value obtained from the original formula (26) by a factor  $\beta_c$  that depends on the product  $N_i\alpha_i^3$ . In the case of the  $\text{I}_2-\text{I}_2$  interaction  $N_i\alpha_i^3 = 5306 \text{ \AA}^9$  ( $N_i = 5$  and  $\alpha_i = 10.2 \text{ \AA}^3$ ), which gives  $\beta_c = 2.2$ .

The van der Waals radius  $r_i$  for the  $\text{I}_2$  molecule is obtained by assuming that  $2r_i/2r_i' \approx \sigma_{mm}/\sigma_{aa}$ , where  $r_i'$  is the van der Waals radius for the I atom [15,17] and the collision diameter  $\sigma_{aa}$  for two iodine atoms is given by Eq. (55). Consequently, one obtains from Eq. (26) that  $\epsilon_{mm}/k = 557 \text{ K}$ .

The values of the collision diameter  $\sigma_{mm} = 5.156 \text{ \AA}$  and the potential well depth  $\epsilon_{mm}/k = 557 \text{ K}$  obtained from the "modified" Slater-Kirkwood theory agree well with the corresponding values obtained from viscosity measurements [2],  $\sigma_{mm} = 4.982 \text{ \AA}$  and  $\epsilon_{mm}/k = 550 \text{ K}$ . The latter values of the potential parameters are assumed in the present work for interaction of two iodine molecules in the ground electronic states.

Using the potential (18), it is possible to derive an expression [18] for the reduced collision cross sections  $S^{(l)}(K)$ ,

$$S^{(l)}(K) = \left[ 2 - \frac{1+(-1)^l}{1+l} \right]^{-1} \int_0^\infty (1 - \cos^{(l)}\chi) \delta d\delta, \quad (28)$$

$$V(x) = \left[ 1 + \frac{b_{12}^2}{b_{11}b_{22} - b_{12}^2} + \frac{b_{11}(b_{12}b_{23} - b_{22}b_{13})^2}{(b_{11}b_{22} - b_{12}^2)^2(b_{11}b_{22}b_{33} + 2b_{12}b_{13}b_{23} - b_{12}^2b_{33} - b_{23}^2b_{11} - b_{13}^2b_{22})} \right], \quad (34)$$

and

$$b_{11} = 4W^{(2,2)}(x), \quad (36)$$

$$b_{12} = 7W^{(2,2)}(x) - 2W^{(2,3)}(x), \quad (37)$$

$$b_{22} = \left(\frac{301}{12}\right)W^{(2,2)}(x) - 7W^{(2,3)}(x) + W^{(2,4)}(x), \quad (38)$$

$$b_{13} = \left(\frac{61}{8}\right)W^{(2,2)}(x) - \left(\frac{9}{2}\right)W^{(2,3)}(x) + \left(\frac{1}{2}\right)W^{(2,4)}(x), \quad (39)$$

$$b_{23} = \left(\frac{1363}{32}\right)W^{(2,2)}(x) - \left(\frac{121}{16}\right)W^{(2,3)}(x) + \left(\frac{25}{8}\right)W^{(2,4)}(x) - \left(\frac{1}{4}\right)W^{(2,5)}(x), \quad (40)$$

$$b_{33} = \left(\frac{25137}{256}\right)W^{(2,2)}(x) - \left(\frac{1755}{32}\right)W^{(2,3)}(x) + \left(\frac{381}{32}\right)W^{(2,4)}(x) - \left(\frac{9}{8}\right)W^{(2,5)}(x) + \left(\frac{1}{16}\right)W^{(2,6)}(x) + \left(\frac{1}{2}\right)W^{(4,4)}(x). \quad (41)$$

where  $K$  is the impact kinetic energy in units of  $\epsilon$ , and  $\delta$  is the collision impact parameter in units of  $\sigma$ . Subsequently, the collision integrals  $\Omega^{(l,s)}$  of Chapman and Cowling [1] are obtained from

$$\Omega^{(l,s)} = \sigma^2 \left[ \frac{2\pi kT}{\mu} \right]^{1/2} W^{(l,s)}(x), \quad (29)$$

where

$$W^{(l,s)}(x) = \frac{1}{8} \left[ 2 - \frac{1+(-1)^l}{1+l} \right] x^{s-2} \times \int_0^\infty \exp(-xK) K^{s-1} S^{(l)}(K) dK, \quad (30)$$

with  $x = \epsilon/kT$ . The analytic fits to the function  $W^{(l,s)}(x)$  are given in the Appendix.

The collision integrals of rigid spheres with collision diameter  $\sigma$  are

$$(\Omega^{(l,s)})_{\text{RS}} = \left[ \frac{\pi kT}{2\mu} \right]^{1/2} \sigma^2 (s+1)! \frac{[1-2l+(-1)^l]}{[4(1+l)]}, \quad (31)$$

and the dimensionless collision integrals  $\Omega^{(l,s)*}$  are defined as

$$\Omega^{(l,s)*} = \frac{\Omega^{(l,s)}}{(\Omega^{(l,s)})_{\text{RS}}}. \quad (32)$$

The viscosity  $\eta$  of a pure component can now be written in the form

$$\eta = \frac{5}{8\sigma^2} \left[ \frac{\mu kT}{2\pi} \right]^{1/2} \frac{V(x)}{W^{(2,2)}(x)}, \quad (33)$$

where  $V(x)$  is a slowly varying function of  $x$ .

## VISCOSITY CONTRIBUTION OF I+I COLLISIONS

Atoms of partially dissociated gases interact according to multiple force laws, each law corresponding to a different alignment of the electronic spins during the atom-atom interaction. In principle, the Chapman-Enskog kinetic-theory problem should be solved when the multiple force interactions are included. It was shown by Mason, Vanderslice, and Yos [19] that the formula (1) retains its original form (and is valid for all degrees of the Chapman-Enskog approximation for mixtures of any complexity) in such a case, but each collision integral must be replaced by a statistical average over the different possible force laws. In other words, for a given pair of colliding atoms, the following replacement is necessary in Eq. (1):

$$\sigma^2 \Omega^{(l,s)} \rightarrow \langle \sigma^2 \Omega^{(l,s)} \rangle = \sum p_i \sigma_i^2 \Omega_i^{(l,s)}, \quad (42)$$

where  $\sigma_i$  and  $\Omega_i^{(l,s)}$  are the collision diameter and the collision integral, respectively, for the  $i$ th force law, and  $p_i$  is the probability that the colliding atoms will follow the  $i$ th potential curve. This probability is obtained as the ratio of the degeneracy of the molecular electronic state corresponding to the  $i$ th potential curve to the sum of the degeneracies of all molecular states that can result from interaction (along different potential curves) of these two atoms. The possible potential curves for the interaction of two atoms in particular electronic states can be determined from the Wigner-Witmer rules. The two lowest electronic states in iodine atoms are  $5p^5 2P_{3/2}$  (the ground state) and  $5p^5 2P_{1/2}$ . According to the Wigner-Witmer rules, an interaction of two  $2P$  atoms can lead to the following molecular states:  $^1\Sigma_g^+$ ,  $^1\Sigma_u^+$ ,  $^1\Pi_g$ ,  $^1\Pi_u$ ,  $^1\Delta_g$ ,  $^3\Sigma_g^+$ ,  $^3\Sigma_g^-$ ,  $^3\Pi_g$ ,  $^3\Pi_u$ , and  $^3\Delta_u$ . The potential curves for the possible molecular states for  $2P_{3/2}-2P_{3/2}$ ,  $2P_{3/2}-2P_{1/2}$ , and  $2P_{1/2}-2P_{1/2}$  atom-atom interactions were given by Mulliken [20]. The excitation energies of the first ( $5p^5 2P_{1/2}$ ) and the second ( $5p^4 6s^2 P_{3/2}$ ) excited atomic states are 0.94 and 6.77 eV, respectively. Thus, in the range of temperatures considered here, one can assume that most of the atoms are in the ground state, and the dominant atom-atom interactions are those between atoms in the ground ( $2P_{3/2}$ ) electronic states. Therefore, we take into account in averaging (42) only the interactions between two ground-state iodine atoms. The corresponding potentials (a total of ten; see Fig. 1 in Ref. [20]) represent the molecular states that dissociate into two  $2P_{3/2}$  iodine atoms.

When the atom-atom potentials have a minimum (three curves out of the ten Mulliken's potentials mentioned above), the collision integrals of I+I interactions are calculated (fitting first the particular I+I potential curve to a Lennard-Jones curve) in the same way as the collision integrals for  $I_2-I_2$  interactions.

In the cases of the atom-atom interactions following a repulsive potential,

$$U_i(r) = \frac{c_i}{r^{t_i}} \quad (43)$$

( $r$  is an interatomic distance, and  $c_i$  and  $t_i$  are constants), the collision integrals are [7]

$$\Omega^{(l,s)} = \left[ \frac{\pi k T}{2\mu} \right]^{1/2} \left[ \frac{t_i c_i}{k T} \right]^{2/t_i} A^{(l)} \Gamma[s-2-(2/t_i)], \quad (44)$$

where  $\mu$  is the reduced mass of the collision system,

$$A^{(l)} = \int_0^\pi (1 - \cos^l \chi) \beta d\beta, \quad (45)$$

and

$$\beta = \left[ \frac{\mu g^2}{2t_i c_i} \right]^{1/t_i}. \quad (46)$$

The values of the integrals  $A^{(l)}$  are finite for all values of  $t_i$  greater than 1 (see Table I), and the relationship be-

TABLE I. The integrals  $A^{(1)}$  and  $A^{(2)}$  given in Eq. 45 for several values of the exponent  $t_i$  of Eq. 43.

$t_i$	$A^{(1)}$	$A^{(2)}$
2	0.397	0.527
3	0.311	0.353
4	0.298	0.308
6	0.306	0.283
8	0.321	0.279
10	0.333	0.278
12	0.346	0.279
14	0.356	0.280
$\infty$	0.500	0.333

tween  $\chi$  and  $\beta$  can be obtained from the equation of binary collision trajectory [21]

$$\chi(\beta) = \pi - 2 \int_0^{\beta} \left[ 1 - z^2 - \frac{1}{t_i} \left( \frac{z}{\beta} \right)^{t_i} \right]^{-1/2} dz, \quad (47)$$

where the upper limit of the integral is the smallest positive root of the expression in the brackets.

For the repulsive potentials, it has been shown [22,23] that only the region of potential energy near  $U_i(r) \approx kT$  is important in calculating transport coefficients at the temperature  $T$ . Furthermore, Hirschfelder and Eliason [7] made a conceivable supposition that the separation between two atoms  $r$  is related to the effective collision diameter  $\sigma$  in such a way that the average kinetic energy  $kT$  is comparable to the potential energy  $U_i(\sigma)$ . By using that supposition, the adjusted values of  $\sigma$  and  $\sigma^2 \Omega^{(l,s)}$  are derived. In order to express the rigid-sphere collision diameter in terms of constants  $c_i$  and  $t_i$ , the collision integral (44) is equated to the collision integral (31), which gives

$$\sigma^2 = \frac{A^{(l)} 4(1+l)(t_i c_i / kT)^{2/t_i} \Gamma[s-2-(2/t_i)]}{(s+1)! [1-2l-(l-1)^2]}. \quad (48)$$

If this  $\sigma$  is substituted into Eq. (43), the constant  $c_i$  of repulsive potential cancels out, and

$$U_i(\sigma) = \frac{kT}{t_i} \left[ \frac{(s-1)! [1+2l-(l-1)^2]}{4(1-l) A^{(l)} \Gamma[s-2-(2/t_i)]} \right]^{t_i/2}, \quad (49)$$

where  $t_i$  can be obtained from

$$t_i = \left[ -\frac{r}{U_i(r)} \frac{dU_i(r)}{dr} \right]_{r=r_0} \quad (50)$$

[ $r_0$  is the distance between the two atoms when  $U_i(r) = kT$ ]. Because the coefficient of viscosity is defined in terms of  $\Omega^{(2,2)}$ , Eq. (49) can be rewritten, since  $s = l = 2$ , as

$$U_i(\sigma) = \theta_{\text{visc}} kT, \quad (51)$$

where

$$\theta_{\text{visc}} = \left[ \frac{1}{2} A^{(2)} \Gamma \left[ 4 - \frac{2}{t_i} \right] \right]^{-1/2} / t_i. \quad (52)$$

Summarizing the above, one can say that the first step to determine the adjusted values of  $\sigma$  from the particular repulsive potential curve is computing the effective value of  $\sigma$ . After that, the appropriate value of  $\theta_{visc}$  is calculated, and  $\theta_{visc}$  is substituted into Eq. (51) to determine  $\Omega(\sigma)$ . The corresponding value of  $\sigma$ , obtained from the potential curve, is the effective (adjusted) value of the collision diameter. Since the collision integral  $\Omega^{(1,2)}$  of the hard sphere is equal to 1, the value of  $\sigma^2 \Omega^{(1,2)}$  of the repulsive potentials is equal to  $\sigma^2$ .

Procedures of calculating  $\sigma_i$  and  $\Omega_i^{(1,2)}$  are applied to each potential curve of I-I interactions, and the contribution to the gas viscosity coming from I-I interactions is obtained from

$$\eta = \frac{5}{16} \frac{(\pi mkT)^{1/2}}{\pi \sigma^2 \sum p_i \sigma_i^2 \Omega_i^{(1,2)}} \quad (53)$$

where the sum is taken over all I-I potential curves taken into consideration.

### VISCOSITY CONTRIBUTION OF I+I<sub>2</sub> COLLISIONS

The usual mixture rule for evaluation of the collision diameter for unlike particles in terms of the diameters for like particles is

$$\sigma_{jm} = (\sigma_{ja} + \sigma_{mm})/2, \quad (54)$$

where the collision diameter for interaction of two ground-state iodine atoms can be given as [7]

$$\sigma_{ja} = 2\langle r_j \rangle + c, \quad (55)$$

where  $c = 1.6 \text{ \AA}$  and  $\langle r_j \rangle$  is the mean radius of the atoms participating in the collision,

$$\langle r_j \rangle = \int_0^\infty r_j^3 \psi^2 dr_j. \quad (56)$$

The wave function  $\psi$  is given by a series expansion on the basis-set Slater orbitals [24,25] (with constants  $C_i, n, \zeta_i$ ),

$$\psi_{n,l,m}(r_j, \theta, \phi) = \sum C_i R_{n,l}(r_j) Y_{lm}(\theta, \phi), \quad (57)$$

where  $n$ ,  $l$ , and  $m$  are the quantum numbers of the outer-shell electron,  $Y_{lm}(\theta, \phi)$  is a normalized spherical harmonic, and the radial part of the wave function is

$$R_{n,l}(r_j) = [(2n_l)!]^{-1/2} (2\zeta_l)^{n_l+1/2} r_j^{n_l-1} \exp(-\zeta_l r_j). \quad (58)$$

Assuming that  $\langle r_j \rangle = 1.324 \text{ \AA}$  and  $c = 1.6 \text{ \AA}$ , one finds from Eq. (55) that  $\sigma_{ja} = 4.248 \text{ \AA}$ ; this value differs from the value of  $\sigma_{Xe-Xe} = 3.888 \text{ \AA}$ , which is sometimes assumed [10,11] for the I-I interaction because xenon is iodine's neighbor in the Periodic Table.

The collision diameter for the atom-molecule interaction, when the atom and the molecule are in the electronic ground states, can now be obtained from the expressions (19), (54), and (55) as

$$\sigma_{jm} = c + \langle r_j \rangle + 2\langle R \rangle/3, \quad (59)$$

so that  $\sigma_{jm} = 4.702 \text{ \AA}$  if the molecule is in the ground

rotational-vibrational state.

Using the radical molecule complex (RMC) mechanism [26,27], Blake and Burns calculated [28] the potential parameters for iodine-atom-iodine-molecule interaction. Their result for the potential well depth for the hard-sphere interaction between I and I<sub>2</sub> was  $\epsilon_{jm}/k = 3069 \text{ K}$ , while for the Sutherland interaction  $\epsilon_{jm}/k = 2767 \text{ K}$  the latter value was recommended for the well depth for the I-I<sub>2</sub> interaction. Similar values, 2968 and 2600 K, respectively, were obtained by Thompson [29] from the Monte Carlo quasiclassical trajectory calculations and by Bunker and Davidson [30] from thermodynamic considerations; these values are in agreement with the conclusions of Porter [31]. The geometrical average of the potential well depths obtained by Thompson and by Bunker and Davidson gives  $\epsilon_{jm}/k = 2813 \text{ K}$ .

The I-I<sub>2</sub> interaction can have some channels (for example, atomic exchange [29]) that may have some importance when viscosity of iodine is considered. Unfortunately, the efficiency of these channels is not accurately known [32-34]. However, the studies of Blake and Burns [28] and of Thompson [29] have suggested that the Lennard-Jones potential with parameters discussed above is an acceptable approximation of the overall forces dominating the I-I<sub>2</sub> interaction, even though it ignores such effects as, for example, the quadrupole-quadrupole  $r^{-5}$  term in the interaction. Keeping this in mind, we use in this work the Lennard-Jones potential with  $\sigma_{jm} = 4.702 \text{ \AA}$  and  $\epsilon_{jm}/k = 2800 \text{ K}$  as an acceptable representation of the overall forces dominating the I-I<sub>2</sub> interaction.

### DISSOCIATION DEGREE IN LOCAL THERMAL EQUILIBRIUM

The law of mass action for a gas of homogeneous diatomic molecules leads to [35]

$$\frac{y^2}{1-y} = \frac{m}{2\rho V} \frac{Q_d^2}{Q_m} \exp(-\Theta_d/T), \quad (60)$$

where  $\Theta_d = D_0/k$ ,  $D_0$  is the dissociation energy,  $m$  is the mass of the atoms forming the molecules,  $\rho$  and  $V$  are the mass density and volume of the gas, respectively, and the dissociation degree  $y = N_2/N$ ,  $N = N_2 + 2N_m$ ,  $N_2$  and  $N_m$  are numbers of free atoms and free molecules in the gas, respectively) is a constant number of atoms, both free and those bound in the molecules, available in the gas with ongoing dissociation. Here,  $Q_d = Q_d^t Q_d^r$  and  $Q_m = Q_m^t Q_m^r Q_m^v Q_m^e$  are total partition functions of atomic and molecular components of the gas, respectively, with the superscripts  $t$ ,  $r$ ,  $v$ , and  $e$  referring to translational, rotational, vibrational, and electronic freedom degrees of the species, respectively. The last relationship is valid if all four kinds of energies are independent of one another; such an assumption is well justified in iodine at  $T < 3000 \text{ K}$ . Here  $Q_m^t = 2^{3/2} Q_d^t$ ,  $Q_d^r = V(2\pi mkT/h^2)^{3/2}$ , the rotational partition function  $Q_m^r = T/2\Theta_r$ ,  $\Theta_r = hcB_r/k$ , and the vibrational partition function  $Q_m^v = [1 - \exp(-\Theta_v/T)]^{-1}$ , where  $\Theta_v = hc\omega_v/k$ ;  $Q_d^e \approx g_{d,0} + g_{d,1} \exp(-E_{d,1}/kT)$  and  $Q_m^e \approx g_{m,0} - g_{m,1} \exp(-E_{m,1}/kT)$ , where  $E_{d,1}$  and  $E_{m,1}$  are the exci-

tation energies of the first excited electronic states in iodine atom and molecule, respectively. Using the above and assuming that the relationship  $pV = (N_a + N_m)kT$  is valid, the expression (60) can be written as

$$\frac{y^2}{1-y} = C$$

or

$$y = \frac{C(\sqrt{1+4/C} - 1)}{2} \quad (61)$$

where

$$C = n^{-1} \exp(-\Theta_d/T) \times \left[ \left( \frac{\pi mk}{h^2} \right)^{3/2} \Theta_d T^{1/2} [1 - \exp(-\Theta_v/T)] \frac{(Q_v')^2}{Q_v''} \right] \quad (62)$$

with  $n = N/V$ , where  $V$  is the volume of the gas.

## RESULTS AND DISCUSSION

The viscosity coefficient of dissociating iodine in local thermal equilibrium was calculated in a broad range of temperature, and the results are shown in Fig. 1. (The approach of this work can also be used to predict viscosity of the gas in thermal nonequilibrium if the dependence of the dissociation degree on the gas parameters is known.) At low temperature, the dissociation degree is low, and collisions involving atoms have no impact on the viscosity of the gas. As the temperature of the gas increases, the collisions involving atoms become important, and at temperatures greater than about 1000 K, these collisions start to dominate the transport properties of iodine. The decrease of the viscosity of iodine (see Fig. 1) at temperatures about 1000–2000 K is caused by a rapid increase of dissociation and, subsequently, a rapid increase of the  $I+I_2$  and  $I+I$  collision frequencies at those temperatures. The potential well depths  $\epsilon$  for the  $I+I_2$  and  $I+I$  interactions are much larger than the well depth for the  $I_2+I_2$  collisions which are dominant at lower temperatures. It was shown [36] that the viscosity of gas consisting of particles interacting according to a potential characterized by well depth  $\epsilon$  and collision diameter  $\sigma$  can be given as

$$\eta \sim \frac{\sigma^2}{\mu^{1/2} \epsilon^{1/2}} \quad (63)$$

Therefore, at temperatures 1000–2000 K, the increase of the viscosity resulting from the increase in temperature competes with the decrease of the viscosity, resulting, as indicated by the relationship (63), from the significant increase in the potential well depth of the  $I+I_2$  and  $I+I$  interactions. As the temperature of the gas continues to increase, the gas becomes highly dissociated, and  $I+I$  collisions dominate the kinetic properties of the gas. The

gas viscosity then increases monotonically with temperature, as expected for gas containing only one kind of particle.

A numerical analysis shows that the contribution of the rotational-vibrational excitation of molecules to the viscosity of iodine in local thermal equilibrium is very small. (This contribution depends on the collision diameters which in turn depend on the mean internuclear distances of the rotationally and vibrationally excited  $I_2$  molecules.) This is because in most cases the degree of dissociation of iodine in local thermal equilibrium is high when the gas temperature is close to or higher than 1500 K. Therefore, the impact of the rotational-vibrational excitation of molecules on the gas viscosity would be meaningful only at temperatures less than about 1500 K. However, at these temperatures the contribution of the rotational-vibrational excitation of iodine to the gas viscosity is negligible.

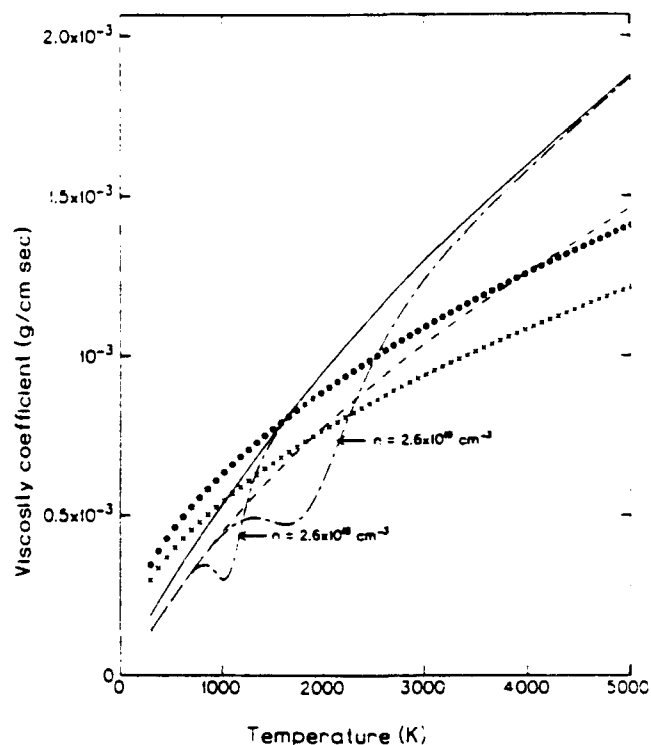


FIG. 1. The viscosity of iodine as function of gas temperature. Solid and dashed line represent viscosities of pure atomic (fully dissociated) and pure diatomic (undissociated) iodine, respectively. The dash-dotted curves represent the viscosities of iodine of particle density  $n$  when atom-atom ( $I+I$ ), atom-molecule ( $I+I_2$ ), and molecule-molecule ( $I_2+I_2$ ) collisions are taken into account; the dissociation degree of the gas is taken as that of the gas in the local thermal equilibrium. ( $n = n_a + 2n_m$ , where  $n_a$  and  $n_m$  are particle densities of free atoms and free molecules, respectively.) The circles and crosses denote the values of viscosity of fully dissociated and undissociated iodine, respectively, as predicted by the rigid-sphere model.

A quick estimate of the role of the rotational-vibrational excitation of molecules to the viscosity of iodine can be made by use of a simple approximate expression for the mean internuclear distance  $\langle R \rangle$  in a "typical" (that is, representing majority of the gas molecules) molecule in iodine of temperature  $T$ . Such an expression can be obtained in the following way. In local thermal equilibrium the ratio of the population of the first excited vibrational level ( $v=1$ ) to the population of the vibrational ground state ( $v=0$ ) is equal to 0.36 (at  $T=300$  K), 0.74 (at  $T=1000$  K), and equal to about 1 (at  $T=1500$  K). Thus, the majority of molecules in iodine at  $T \leq 1500$  K is in the  $v=0$  and 1 vibrational states. Therefore, the vibrational quantum number of the typical molecule in such gas is a weak function of temperature  $T$ . Consequently, it is reasonable to assume, when calculating the rotational-vibrational energy  $E$  in the relationship (20), that the vibrational quantum number of the typical molecule is  $v_p=1$ . (The choice of  $v_p=1$  over  $v_p=0$  makes the contribution of the vibrational excitation to the gas viscosity slightly greater than it is in reality.)

The rotational quantum number of the typical  $I_2$  molecule can be taken as the most probable rotational quantum number  $J_p$  in the gas in the local thermal equilibrium at temperature  $T$ . The value  $J_p$  can be obtained from the LTE distribution of the rotational levels after approximation of the distribution by a continuous function of  $J$ ; such a procedure is justified because the rotational levels in iodine are closely spaced. Then, the most probable rotational quantum number  $J_p$  is an integer nearest to

$$J_p' = \left[ \frac{kT}{2B_e hc} \right]^{1/2} - \frac{1}{2} \approx \left[ \frac{kT}{2B_e hc} \right]^{1/2}, \quad (64)$$

where  $B_e$  is the rotational spectroscopic constant; one can see from Eq. (64) that the  $T$  dependence of the rotational quantum number  $J_p$  is stronger than the  $T$  dependence of the vibrational quantum number  $v_p$ .

Using  $v_p=1$  and  $J_p$  given by the relationship (64), one obtains from Eqs. (24) and (25) that

$$\frac{E - A_0}{D} = \frac{6\omega_e x_e}{\omega_e} \left[ 1 - \frac{kT}{3hc\omega_e} \left[ 1 - \left[ \frac{R_e}{R_0} \right]^2 \right] \right], \quad (65)$$

where we neglected the higher terms in the expression (25), used the fact that  $J_p(J_p+1) \approx J_p^2$ , and used the expressions

$$D = \frac{hc\omega_e^2}{4\omega_e x_e} \quad (66)$$

and

$$B_e = \frac{\hbar}{4\pi c \mu R_e^2} \quad (67)$$

The  $\ln(1-x)$  in Eq. (20) can be expanded into a series:

$$\ln(1-x) = - \sum_{n=1}^{\infty} x^n / n \approx -x, \quad (68)$$

because  $x = (E - A_0)/D$  is much less than unity at temperatures less than about 1500 K. Consequently, Eq. (22) gives the following expression acceptable at temperatures less than about 1500 K:

$$R_0 \approx R_e + \frac{4\omega_e x_e kT}{hcR_e \beta^2 \omega_e^2}, \quad (69)$$

where we used the fact that  $1 - (R_e/R_0)^2 \ll 4/\beta R_e$ . In the case of iodine one obtains from Eq. (69)

$$\frac{\langle R \rangle}{R_e} \approx 1 + 1.62 \times 10^{-6} T, \quad (70)$$

where  $T$  is in degrees Kelvin. This linear dependence becomes a crude estimate when the gas temperature is close or greater than about 1500 K. Then the dependence of  $\langle R \rangle/R_e$  on temperature is much stronger, but is still not strong enough to affect the viscosity of iodine significantly [37]. At temperatures higher than 2500 K the relationship (70) is invalid. In such a case the ratio  $\langle R \rangle/R_e$  departs substantially from unity [8,9,37], but this fact is practically meaningless because the number of diatomic molecules in iodine is insignificant at the higher temperatures.

We also show in Fig. 1 the viscosities  $\eta_0$  of pure diatomic (no I atoms are present) and pure atomic (no  $I_2$  molecules are present) iodine calculated from the rigid-sphere model, where

$$\eta_0 = \frac{5}{16} \frac{(\pi m k T)^{1/2}}{\pi \sigma^2} \quad (71)$$

Summarizing the results of the present work, one can say that in high-temperature ( $\geq 1000$  K) iodine (1) dissociation processes should not be ignored in calculations of viscosity, (2) the viscosity of atomic iodine is greater than the viscosity of molecular (diatomic) iodine, and (3) the rigid-sphere model is inappropriate for calculations of the gas viscosity.

One should add that the decrease of viscosity with temperature takes place, to a different degree, in most dissociating gases. However, in most cases it happens at temperatures well above 3000 K.

#### ACKNOWLEDGMENTS

One of us (J.A.K.) thanks Alex Dalgarno and Evgeni Nikitin for valuable comments. This work was supported by the National Aeronautics and Space Administration, Grant No. NAGW-1061, by the Air Force Office of Scientific Research, Grant No. 88-0119, and URI Grant No. 90-0170.

#### APPENDIX

The analytic fits to the integrals  $W^{(l,s)}(x)$  [Eq. (30)] are

$$W^{1,1}(x) = \frac{1}{2} x^3 [2.11114x^{-2.845} + 1.43329(x+0.439)^{-2.5} + 566.494x + 3.675]^{-5.126} \\ - 0.02077 \exp(-0.8093x) - 0.2159 \exp(-0.5867x) + 0.003726 \exp(-0.2552x) ] .$$



$$\begin{aligned}
W^{(1,2)}(x) &= \frac{1}{2}x^4[6.00619x^{-3.845} - 3.58323(x+0.439)^{-3.5} + 2903.85(x+3.675)^{-6.126} \\
&\quad - 0.01681\exp(-0.8144x) - 0.01267\exp(-0.6089x) + 0.0009506\exp(-0.2895x)], \\
W^{(1,3)}(x) &= \frac{1}{2}x^5[23.0938x^{-4.845} - 12.5413(x+0.439)^{-4.5} - 17789(x+3.675)^{-7.126} \\
&\quad - 0.01369\exp(-0.8196x) + 0.0002752\exp(-0.3239x) - 0.007714\exp(-0.6311x)], \\
W^{(2,2)}(x) &= \frac{1}{6}x^4[6.88155x^{-3.855} - 2.89488(x+0.19)^{-3.211} + 7.33242(x+0.67742)^{-3.303} \\
&\quad - 660079(x+6.7461)^{-7.01} + 0.03950\exp(-0.9274x) \\
&\quad + 0.03732\exp(-0.8291x) + 0.03888\exp(-0.6161x) - 0.009625\exp(-0.2211x)], \\
W^{(2,3)}(x) &= \frac{1}{6}x^5[26.528x^{-4.855} + 9.29546(x+0.19)^{-4.211} + 24.2190(x+0.67742)^{-4.303} \\
&\quad - 4627150(x+6.7461)^{-8.01} + 0.03663\exp(-0.9349x) \\
&\quad - 0.03094\exp(-0.8314x) + 0.02395\exp(-0.6232x) - 0.002128\exp(-0.2489x)], \\
W^{(2,4)}(x) &= \frac{1}{6}x^6[128.795x^{-5.858} - 39.1432(x+0.19)^{-5.211} + 104.214(x+0.67742)^{-5.303} \\
&\quad - 37063500(x+6.7461)^{-9.01} + 0.03425\exp(-0.9425x) \\
&\quad + 0.02573\exp(-0.8336x) + 0.01493\exp(-0.6303x) - 0.0005298\exp(-0.2767x)], \\
W^{(2,5)}(x) &= \frac{1}{6}x^7[754.095x^{-6.855} - 203.975(x+0.19)^{-6.211} + 552.647(x+0.67742)^{-6.303} \\
&\quad - 333942000(x+6.7461)^{-10.01} + 0.03228\exp(-0.9501x) \\
&\quad + 0.02145\exp(-0.8359x) + 0.009408\exp(-0.6374x) - 0.0001466\exp(-0.3045x)], \\
W^{(2,6)}(x) &= \frac{1}{6}x^8[5169.32x^{-7.855} + 1266.89(x+0.19)^{-7.211} + 3483.33(x+0.67742)^{-7.303} \\
&\quad - 3342750000(x+6.7461)^{-11.01} + 0.03067\exp(-0.9576x) \\
&\quad + 0.01793\exp(-0.8381x) + 0.005997\exp(-0.6446x) - 0.00004463\exp(-0.3323x)], \\
W^{(4,4)}(x) &= \frac{1}{3}x^6[132.154x^{-5.86} + 29.9505(x+0.1350)^{-5.5} + 175.386(x+0.49593)^{-5.58915} \\
&\quad - 737383000000(x+7.5377)^{-13.3} - 0.09163\exp(-1.0424x) \\
&\quad - 0.002420\exp(-0.9133x) - 0.001657\exp(-0.4796x) \\
&\quad - 0.003243\exp(-0.4646x) - 0.01629\exp(-0.6493x) - 0.008924\exp(-0.8070x)].
\end{aligned}$$

- 
- [1] S. Chapman and T. G. Cowling, *The Mathematical Theory of Non-Uniform Gases* (Cambridge University, New York, 1952).
- [2] J. O. Hirschfelder, C. F. Curtiss, and R. B. Bird, *Molecular Theory of Gases and Liquids* (Wiley, New York, 1964).
- [3] E. A. Mason, in *Kinetic Processes in Gases and Plasmas*, edited by A. R. Hochstim (Academic, New York, 1969), p. 60.
- [4] L. Monchick, K. S. Yun, and E. A. Mason, *J. Chem. Phys.* **39**, 654 (1963).
- [5] S. C. Saxena and R. K. Joshi, *Physica* **29**, 870 (1963).
- [6] T. S. Storvick and E. A. Mason, *J. Chem. Phys.* **45**, 3752 (1966).
- [7] J. O. Hirschfelder and M. A. Eliason, *Ann. N.Y. Acad. Sci.* **67**, 451 (1957).
- [8] J. A. Kunc, *J. Phys. B* **23**, 2553 (1990).
- [9] J. A. Kunc, *J. Phys. B* (to be published).
- [10] C. H. Chen, P. E. Siska, and Y. T. Lee, *J. Chem. Phys.* **59**, 601 (1973).
- [11] J. A. Barker, R. O. Watts, J. K. Lee, and Y. T. Lee, *J. Chem. Phys.* **61**, 3081 (1974).
- [12] L. Pauling, *Nature of the Chemical Bond* (Cornell University Press, New York, 1939), p. 178.
- [13] A. A. Radzig and B. M. Smirnov, *Reference Data on Atoms, Molecules, and Ions* (Springer, Berlin, 1985).
- [14] J. C. Slater and J. G. Kirkwood, *Phys. Rev.* **37**, 682 (1931).
- [15] R. A. Scott and H. A. Scheraga, *J. Chem. Phys.* **45**, 2091 (1966).
- [16] W. Brandt, *J. Chem. Phys.* **24**, 501 (1956).
- [17] A. Bondi, *J. Phys. Chem.* **68**, 441 (1964).
- [18] J. O. Hirschfelder, R. B. Bird, and E. L. Spotz, *J. Chem. Phys.* **16**, 968 (1948).
- [19] E. A. Mason, J. T. Vanderslice, and J. M. Yos, *Phys. Fluids* **2**, 688 (1959).
- [20] R. S. Mulliken, *J. Chem. Phys.* **55**, 288 (1971).

- [21] M. A. Eliason, D. E. Stogryn, and J. O. Hirschfelder, *Proc. Natl. Acad. Sci. U.S.A.* **42**, 546 (1956).
- [22] D. D. Konowalow, J. O. Hirschfelder, and B. Linder, *J. Chem. Phys.* **31**, 1575 (1959).
- [23] P. H. Krupenie, E. A. Mason, and J. T. Vanderslice, *J. Chem. Phys.* **10**, 2399 (1963).
- [24] E. Clementi and C. Roetti, *At. Data Nucl. Data Tables* **14**, 177 (1974).
- [25] A. D. McLean and R. S. McLean, *At. Data Nucl. Data Tables* **26**, 197 (1981).
- [26] J. K. Ip and G. Burns, *J. Chem. Phys.* **51**, 3414 (1969).
- [27] J. A. Blake, R. J. Browne, and G. Burns, *J. Chem. Phys.* **53**, 3320 (1970).
- [28] J. A. Blake and G. Burns, *J. Chem. Phys.* **54**, 1480 (1971).
- [29] D. L. Thompson, *J. Chem. Phys.* **60**, 4557 (1974).
- [30] D. L. Bunker and N. Davidson, *J. Am. Chem. Soc.* **80**, 5090 (1958).
- [31] G. Porter, *Discuss. Faraday Soc.* **33**, 198 (1962).
- [32] R. M. Noyes and J. Zimmerman, *J. Chem. Phys.* **18**, 656 (1950).
- [33] I. D. Clark and R. P. Wayne, in *Comprehensive Chemical Kinetics*, edited by C. H. Bamford and C. F. Tipper (Elsevier, New York, 1969), p. 4.
- [34] M. A. Clyne and H. W. Cruse, *J. Chem. Soc. Faraday Trans.* **68**, 1377 (1972).
- [35] M. J. Lighthill, *J. Fluid Mech.* **2**, 1 (1957).
- [36] J. De Boer and J. van Kranendonk, *Physica* **14**, 442 (1948).
- [37] S. H. Kang and J. A. Kunc, *J. Phys. Chem.* (to be published).

**ATTACHMENT 6**

## Molecular Diameters in High-Temperature Gases

Steve H. Kang and Joseph A. Kunc\*

Departments of Aerospace Engineering and Physics, University of Southern California,  
Los Angeles, California 90089-1191 (Received: March 5, 1991)

The kinetic molecular diameters of rotationally and vibrationally excited diatomic molecules and molecular ions are derived. The diameters are functions of the rotational and vibrational quantum numbers of the incident and target molecules. As an example, "typical" molecular diameters in several diatomic gases of temperature  $T$  are calculated.

## Introduction

Calculating some properties of gases requires constants, called the "molecular diameters", representing the "size" of the gas molecules. (For example, the concept of the molecular diameter is especially useful in Monte-Carlo probabilistic simulations of molecular collisions in high-temperature gases.) In low-temperature ("cold") gas the molecular diameters can be taken as the diameters of the molecules in the ground vibrational-rotational states. In high-temperature ("hot") gas, a large portion of molecules is rotationally and vibrationally excited and the values of the molecular diameters are greater than in unexcited (cold) gas. Since the molecular scattering cross sections are proportional (roughly) to the square of molecular diameters, the rotational-vibrational excitation of molecules can have a meaningful effect on the kinetic properties of high-temperature gases. This fact raises a question concerning what is the typical value of the molecular diameter in high-temperature gas.

In this work, we study molecular diameters in high-temperature gases, taking into account the rotational-vibrational excitation of molecules. Two cases are considered: (a) the "cold" gas, where the molecular diameter  $d_c$  is independent of the degree of rotational-vibrational excitation of the molecules, and (b) the "hot" gas, where the molecular diameter  $d_h$  depends on the degree of rotational-vibrational excitation of the molecules, that is, on vibrational ( $v$ ) and rotational ( $J$ ) quantum numbers of the molecules.

## "Cold" Gas

The mean value of the molecular diameter  $d_c$  in "cold" gas of diatomic molecules can be obtained from an empirical rule proposed by Hirschfelder and Eliason:<sup>2</sup>

$$d_c = \frac{1}{3}(r_a + r_b) + 1.8 \quad (1)$$

where all quantities are measured in angstroms, and  $r_a$  and  $r_b$  are mean radii of the Slater orbitals of the outer-shell electrons in the atoms forming the molecule

$$r_{ab} = \frac{n_{ab}^*(2n_{ab}^* + 1)}{2(Z_{ab} - S_{ab})} a_0 \quad (2)$$

where  $Z$  is the atomic number,  $a_0$  is the Bohr radius,  $n^*$  is the effective principal quantum number for the orbital electrons, and  $S$  is their screening constant. Also, a review of the molecular diameters obtained from measured transport coefficients for gases of homonuclear diatomic molecules indicates that  $d_c \approx R_e + b_c$ ;  $R_e$  is the equilibrium bond length of the molecule (Å) and the constant  $b_c \approx 2.3$  Å.

## "Hot" Gas

The diameter  $d_h(v, J)$  of a diatomic molecule excited to a  $v$ th vibrational level and a  $J$ th rotational level is proportional to the mean values of the internuclear distance ( $R_{vJ}$ )

$$d_h(v, J) \approx \langle R_{vJ} \rangle + c_v \quad (3)$$

where it is reasonable to assume that  $c_v = b_c$  if the degree of vibrational-rotational excitation of the molecule is not very high.

In general, the mean internuclear distance can be found (through numerical calculations) from the eigenfunctions obtained from solution of the Schrodinger equation for a rotating anharmonic oscillator.<sup>3</sup> A simple and convenient approximation (limited, however, to levels with low and moderate values of the vibrational quantum number) to the mean internuclear distance can be obtained by using<sup>4</sup> the following anharmonic potential, which includes the centrifugal rotational term:

$$U_{\text{anh}}(s) = U_{\text{anh}}(0) + B_0 s^2 + C_0 s^3 + D_0 s^4 \quad (4)$$

where

$$s = B_0^{1/2}(R - R_0) \quad (5)$$

$$B_0 = \left[ \frac{1}{2} \left( \frac{\partial^2 U_{\text{anh}}}{\partial R^2} \right)_{R=R_0} \right]^{1/2} \quad (6)$$

$$C_0 = \left[ \frac{1}{6} \left( \frac{\partial^3 U_{\text{anh}}}{\partial R^3} \right)_{R=R_0} \right] \left[ \frac{1}{2} \left( \frac{\partial^2 U_{\text{anh}}}{\partial R^2} \right)_{R=R_0} \right]^{-3/4} \quad (7)$$

$$D_0 = \left[ \frac{1}{24} \left( \frac{\partial^4 U_{\text{anh}}}{\partial R^4} \right)_{R=R_0} \right] \left[ \frac{1}{2} \left( \frac{\partial^2 U_{\text{anh}}}{\partial R^2} \right)_{R=R_0} \right]^{-1} \quad (8)$$

and  $R_0$ , the position of the minimum of the intramolecular rotational-vibrational potential, is

$$R_0 = R_e + 4l_e^4 J(J+1)/R_e^3 \quad (9)$$

$$l_e^2 = 16.863/\omega_e \mu \quad (10)$$

where  $l_e$  is in angstroms if the reduced mass  $\mu$  of the molecule is in atomic units and the vibrational constant  $\omega_e$  is in  $\text{cm}^{-1}$ .

By use of the above and the second-order time-independent perturbation theory,<sup>4</sup> the eigenfunctions  $S_{vJ}$  of the rotating anharmonic oscillator can be expressed as a function

$$S_{vJ}(s) = f(B_0, C_0, D_0, v, J, S_{vJ}^0) \quad (11)$$

where  $S_{vJ}^0$  are eigenfunctions for an unperturbed rotating harmonic oscillator. Consequently, the mean internuclear distance ( $R_{vJ}$ ) in a diatomic molecule excited to the  $v, J$ th vibrational-rotational level is

$$\begin{aligned} \langle R_{vJ} \rangle = & R_e + \frac{3}{2} B l_e^2 (2v+1) - \frac{\beta^3 l_e^4}{192} (1091 + 2282v + \\ & 1675v^2 - 1214v^3 - 607v^4) + \frac{4l_e^4}{R_e^3} J(J+1) + \\ & \frac{l_e^4}{R_e^3} \left( 13\beta^2 - \frac{27\beta}{R_e} + \frac{24}{R_e^2} \right) (2v+1)J(J+1) - \frac{l_e^4}{18R_e^3} \left( 95\beta^4 - \right. \\ & \left. \frac{189\beta^3}{R_e} + \frac{84\beta^2}{R_e^2} + \frac{180\beta}{R_e^3} \right) (31 + 78v + 78v^2)J(J+1) + \\ & \frac{l_e^4}{48R_e^3} \left( 5\beta^4 - \frac{12\beta^3}{R_e} + \frac{12\beta^2}{R_e^2} \right) \times \\ & (645 + 2086v + 2693v^2 + 1214v^3 + 607v^4)J(J+1) \quad (12) \end{aligned}$$

(1) Hirschfelder, J. O.; Curtiss, C. F.; Bird, R. B. *Molecular Theory of Gases and Liquids* John Wiley: New York, 1964.

(2) Hirschfelder, J. O.; Eliason, M. A. *Ann. N. Y. Acad. Sci.* 1957, 67, 451.

(3) Kunc, J. A. *J. Phys. B* 1990, 23, 2553.

(4) Bonham, R. A.; Peacher, J. L. *J. Chem. Phys.* 1963, 38, 2319.

where  $\beta$  is the Morse constant in the Morse function approximating the intramolecular potential. Neglecting small quantities and reducing (using the symbolic algebra) the second and the third terms in relationship 12 to  $9\beta l_a^2 \exp[2(\beta l_a)^{1/2}(v-1)]/2$ , one obtains

$$(R_{av}) \approx R_e - \frac{9}{2} \beta l_a^2 \exp[2(\beta l_a)^{1/2}(v-1)] + \frac{4l_a^4}{R_e^3} f \quad (13)$$

If the molecule is not excited ( $v = 0$ ,  $J = 0$ ) then the mean internuclear distance is slightly different from  $R_e$  because the  $v = 0$  vibrations are slightly anharmonic. One should also remember that some vibrational-rotational levels do not exist in stable diatomic molecules even though the rotationless vibrational states with the same vibrational quantum number do exist.

#### "Typical" Molecular Diameters in High-Temperature Gas

The value of the "typical" molecular diameter for a diatomic gas of temperature  $T$  can be taken as one for the molecule excited to the vibrational-rotational level with "typical" quantum numbers  $v_p$  and  $J_p$ . (An attempt in ref 4 to average eq 12 over equilibrium distributions of vibrational and rotational levels produced long and cumbersome formulas containing some misprints.) We choose the values  $v_p$  and  $J_p$  as the gas mean vibrational quantum number and the most probable rotational quantum number, respectively. Such choice is well justified, as representation of the corresponding distributions of rotational and vibrational levels, in gases of homonuclear diatomic molecules.

The most probable rotational quantum number  $J_p$  can be estimated from the equilibrium distribution  $g_r(J)$  of the rotational levels because the rotational temperature is usually very close to the gas translational temperature while typical relaxation times for translational energy are usually very short. This distribution is

$$g_r(J) dJ = C_r J(J+1) \exp[-B_r J(J+1)hc/kT] dJ \quad (14)$$

where  $C_r$  is a normalization constant and  $B_r$  (in  $\text{cm}^{-1}$ ) is the rotational spectroscopic constant. Since the rotational energy levels in diatomic molecules are closely spaced, the distribution (14) can be approximated by a continuous function of  $J$  with  $J_p$  being an integer close to

$$J_p' = \left( \frac{kT}{2B_r hc} \right)^{1/2} - \frac{1}{2} \approx \left( \frac{kT}{2B_r hc} \right)^{1/2} \quad (15)$$

In stationary gases the value of  $v_p$  can often be obtained from the local thermal equilibrium (LTE) distribution (or from the Treanor distribution) of vibrational states at translational temperature  $T$ . It should be emphasized that in a gas where low and medium vibrational states are in the LTE with translational temperature other modes of energy distribution (including dissociation) does not have to be in the LTE. For example, the population of the higher vibrational levels (the most important for the process of dissociation) can strongly deviate from the LTE population;<sup>5</sup> as a result, the overall dissociation process can easily maintain a state of nonequilibrium in the gas.

The LTE distribution  $g_v(v)$  of vibrational states has the following form if the vibrational energy is measured from the ground vibrational state

$$g_v(v) dv = Q_v^{-1} \exp(-E_v/kT) dv \quad (16)$$

where  $E_v$  is the energy of the  $v$ th state, and  $Q_v$  is the vibrational partition function

$$Q_v = \sum_{v=0}^{v_m} \exp(-E_v/kT) \quad (17)$$

where  $v_m$  is the number of vibrational states taken into account. Since the statistical weights of these states are equal to 1 and since

$E_v \gg kT$  when  $v$  is high, the contribution of the upper states to the partition function  $Q_v$  and to the first moment of the distribution  $g_v(v)$  is very small. Consequently,  $v_p$  is much smaller than  $v_m$ . Thus, one can assume (but only for the purpose of calculating  $v_p$ ) that the partition function  $Q_v$  and vibrational eigenvalues are close to their values given by the model of harmonic oscillator. Then

$$Q_v \approx Q_v^h = [1 - \exp(-hc\omega_e/kT)]^{-1} \quad (18)$$

where  $h$ ,  $c$ , and  $k$  are Planck's constant, the speed of light, and Boltzmann's constant, respectively.

The number of the vibrational states of the anharmonic oscillator can be given as

$$v_m \approx \frac{1}{2} \left\{ \frac{\omega_e}{\omega_e x_e} - \left[ 1 + \left[ \left( \frac{\omega_e}{\omega_e x_e} - 1 \right)^2 - \frac{4D_0}{\omega_e x_e} \right]^{1/2} \right] \right\} \quad (19)$$

where  $\omega_e x_e$  is the anharmonicity constant ( $\text{cm}^{-1}$ ), and  $D_0$  is the dissociation energy ( $\text{cm}^{-1}$ ) measured from the ground vibrational state.

A simple and acceptably accurate expression for  $v_p$  can be obtained by assuming that  $v_m = D/hc\omega_e$ , where  $D$  is the dissociation energy (ergs) measured from the bottom of the intramolecular potential curve. Then, neglecting small quantities one obtains

$$v_p = \int_0^{v_m} v g_v(v) dv \approx (Q_v^h)^{-1} \int_0^{v_m} v \exp(-E_v/kT) dv = \left( \frac{kT}{hc\omega_e} \right)^2 \gamma \quad (20)$$

where the energy of the first excited vibrational state is

$$E_1 = hc\omega_e \quad (21)$$

and

$$\gamma = [1 - (D/kT) \exp(-D/kT)][1 - \exp(-hc\omega_e/kT)] \quad (22)$$

In most cases, the ratio  $D/kT$  is much greater than 1. (The case when the ratio  $D/kT$  is less than 1 corresponds to the situation when degree of dissociation of the gas is high. Then, atom-atom, not molecule-molecule, interactions dominate kinetic properties of the gas.) The assumption that  $D/kT$  is significantly greater than 1 gives  $\gamma \approx hc\omega_e/kT$  (if  $hc\omega_e/kT < 1$ ) or  $\gamma \approx hc\omega_e/2kT$  (if  $hc\omega_e/kT \geq 1$ ); we used the expansion  $e^x = \sum x^n/n!$  (neglecting the higher order terms) in the former relationship. Consequently

$$v_p \approx \eta(kT/hc\omega_e) \quad (23)$$

where in the case when the vibrational states have the LTE distribution

$$\eta = 1 \quad \text{when } hc\omega_e/kT < 1 \\ \eta = 1/2 \quad \text{when } hc\omega_e/kT \geq 1 \quad (24)$$

As said above, the "typical" molecular diameter  $d_b'(T)$  in a gas of temperature  $T$  can be taken as the diameter of a molecule in the  $v_p$ th vibrational and  $J_p$ th rotational level. Then, using relationships 13, 15, and 23, one obtains

$$d_b'(T) = d_e + \frac{9}{2} \beta l_a^2 \exp[2\sqrt{\beta l_a}(\eta kT/hc\omega_e - 1)] + \frac{2l_a^4 kT}{B_r hc R_e^3} \quad (25)$$

where  $d_e = R_e + c_e$ , and  $\omega_e$  and  $B_r$  are in  $\text{cm}^{-1}$  if  $h$ ,  $c$ , and  $k$  are in centimeter-gram-second units. Equation 25 is of course valid for anharmonic molecules too (as is eq 12) because the molecular anharmonicity is contained in the Morse constant  $\beta$ .

As can be seen from eq 25, heating of a gas with a distribution of vibrational states close to the LTE distribution can have a significant effect on molecular diameters in gases with molecules having low values of the spectroscopic constants  $\omega_e$  and  $B_r$ .

At low and moderate temperatures with the V-V exchange processes dominating at the lower vibrational states, the distribution of the states is close to the Treanor distribution.<sup>6</sup> Then

(5) Nikitun, E. E. *Theory of Elementary Atomic and Molecular Processes in Gases*; Clarendon: Oxford, U.K., 1974.

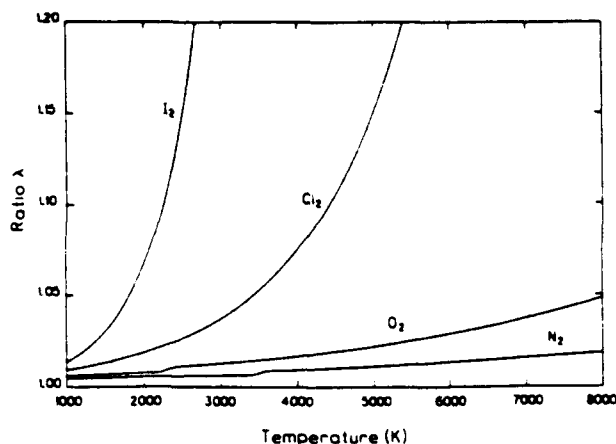


Figure 1.  $T$  dependence of the ratio  $\lambda$  (eq 28) in nitrogen, oxygen, chlorine, and iodine when the low and intermediate vibrational states are in local thermal equilibrium with translational temperature. The "bumps" on the  $N_2$  and  $O_2$  curves are in vicinity of  $\eta = 1$ , and they result from approximation 24.

$v_p$  can be taken as the vibrational quantum number corresponding to the minimum of the distribution. If  $T < T_v$

$$v_p \approx (E_1 / 2hc\omega_e x_e)(T/T_v) \quad (26)$$

where  $T_v$  is the vibrational temperature. In the same case, but with  $T > T_v$ , the quantum number  $v_p$  can be obtained from eq 23 by replacing  $T$  with  $T_v$ .

Comparison of expressions 26 and 23 indicates that relationship 25 also can be used when the distribution of the vibrational states is the Treanor distribution. In such a case the factor  $\eta$  is

$$\eta = (\omega_e^2 / 2\omega_e x_e)(hc/kT_v) \quad (27)$$

(6) Treanor, C.; Rich, J.; Rehm, R. *J. Chem. Phys.* 1968, 48, 1798.

Thus, in gases with the Treanor distribution of vibrational states, the value of the typical molecular diameter depends on the rotational constant  $B_v$  and the ratios  $\omega_e/\omega_e x_e$  and  $T/T_v$ ; at higher temperatures, the diameter can be a strong, increasing function of these two ratios.

As an example illustrating the impact of the rotational-vibrational excitation on the molecular diameters we calculated  $T$  dependence of the ratio

$$\lambda = (d_h'/d_c)^2 \quad (28)$$

for several gases of homonuclear diatomic molecules with an LTE distribution of low and intermediate vibrational states. Ratio 28 is roughly proportional to the ratio of the "typical" kinetic cross section  $Q_h$  in "hot" gas to the corresponding cross section  $Q_c$  in "cold" gas.

Examples of  $T$  dependence of ratio 28 are given in Figure 1. As can be seen from the figure, the rotational-vibrational excitation of molecules can have a meaningful effect on the collisional properties of gases. This effect is stronger in gases of weakly bound molecules (molecules with low values of the dissociation energy). (The dissociation energies of the molecules considered in Figure 1 are as follows: 9.76 ( $N_2$ ), 5.12 ( $O_2$ ), 2.48 ( $Cl_2$ ), and 1.54 eV ( $I_2$ ).)

The assumptions made during the evaluation of the analytical approximation 25 limit its validity (if accuracy better than a few percent is required) to temperatures  $T \leq 9000$  ( $N_2$ ), 8000 ( $O_2$ ), 6000 ( $Cl_2$ ), and 3000 K ( $I_2$ ). However, because all diatomic gases are usually well-dissociated and atom-atom, not molecule-molecule, collisions dominate the gas properties at temperatures higher than those temperatures, this limitation is not important.

**Acknowledgment.** This work was supported by the National Aeronautics and Space Administration, Grant NAGW-1061, by the Air Force Office of Scientific Research, Grant 88-0119, and the URI Grant 90-0170.

**Registry No.**  $I_2$ , 7553-56-2;  $Cl_2$ , 7782-50-5;  $O_2$ , 7782-44-7;  $N_2$ , 7727-37-9.

**ATTACHMENT 7**

## Vibration-translation exchange in diatom-diatom collisions

Joseph A Kunc

Departments of Aerospace Engineering and Physics, University of Southern California,  
Los Angeles, CA 90089-1191

Received 31 January 1991, in final form 28 March 1991

**Abstract.** A general and computationally efficient (analytical) approach evaluating the transition probabilities for vibration-translation (VT) exchange, involving higher vibrational states, in diatomic gases is presented. The role of the slope of the repulsive part of the intermolecular potential on the transition probability is also investigated. Examples of numerical results are given for a number of transitions in nitrogen and oxygen molecules in the ground electronic states. The approach can be used for VT exchange involving diatomic molecular ions.

### 1. Introduction

Energy transfer in molecular collisions is of fundamental importance for kinetic studies of high-temperature gases. In particular, one is often interested in collisions in which vibrational and/or rotational energy of one collision partner is transferred to translational energy of the other partner (V,R-T exchange). In most situations the distribution of rotational levels equilibrates quickly with gas temperature and the VT processes play a dominant role in establishing kinetic non-equilibrium in the gas.

A general and computationally efficient approach predicting accurate VT transition probabilities for both lower and upper vibrational states in diatomic gases is not available. The most commonly used theory (the so-called SSH theory) of VT energy transfer in a diatomic gas was developed by Schwartz *et al* (1952) and Schwartz and Herzfeld (1954). The theory was based on the Jackson and Mott (1934) distorted wave approximation (DWA) simplified by the modified wavenumber approximation (MWA) due to Takayanagi (1952). The SSH theory predicts reasonable  $T$ -dependence at moderate and high temperatures but inaccurate magnitudes of the VT transition probabilities (Rapp and Kassal 1969). However, scaling the probabilities with respect to the  $1 \rightarrow 0$  transition probability (obtained from a reliable theory of experiment) makes the SSH theory a useful method of estimating of the probabilities for VT transitions with low values of the vibrational quantum numbers. Unfortunately, at moderate and high vibrational quantum numbers the 'scaled' SSH theory gives inaccurate values of transition probabilities (see table 4.1 in Billing 1986). The higher vibrational states can be important (for example, in a dissociating gas) and knowledge of accurate probabilities for the transitions involving these levels is often essential for kinetic studies of chemical non-equilibrium. One should add that the common procedure of calculating the VT probabilities from the vv (vibration-vibration) probabilities can be inaccurate.

We study in this paper the vibration-translation (VT) energy transfer between diatomic molecules with the target molecule undergoing a vibrational transition. We



Formally, these spatially averaged potentials are not justified for the vt energy exchange between molecules because it is the final product (the vt probabilities), and not an intermediate result (the intermolecular potentials), that should be spatially averaged. However, possible negative consequences of the use of these potentials are 'neutralized' by the 'dynamic effects factor' (see discussion below).

We use in the present work the wkb semiclassical approach of Shin (1966, 1976) and the  $v$ ,  $J$ -independent intermolecular potentials (5) to evaluate the state-to-state temperature-dependent transition probabilities  $P_{ij}(T)$  for the vt energy transfer in collisions of diatomics. An excellent review of the wkb approach was given by Shin (1976). Therefore, we give below only a brief summary of the method. One should mention that the wkb semiclassical approach used here does not take into account several factors that can be of importance in some situations. For example, it assumes that the Maslov index (the number of times quantum mechanics fails at the turning points) does not affect transition probabilities, that the collisions are collinear and that the collision impact parameter is zero. (These issues are discussed in the paper and concluded in the last section.) Therefore, in the final step of the present work we use the wkb expression for the vt transition probability multiplied by a 'dynamic effects factor'  $g$  (a constant) that is expected to represent contributions of these, and possibly other, effects. Verification of the factor is made by comparison of the final transition probabilities with existing measurements.

Numerical examples of the transition probabilities for the vt energy exchange are given for the  $N_2$ - $N_2$  and  $O_2$ - $O_2$  systems with the molecules in the ground electronic states.

## 2. The approach

We consider a one-dimensional collision of two diatomic molecules in a potential field of  $V(x, r)$ , where  $r$  is the intermolecular distance and  $x$  is the displacement of the target oscillator from its equilibrium position. (The effect of the three-dimensional character of the interaction is accounted for by the factor  $g$  (see below).) Assuming that the amplitude of vibration of the target molecule is distinctively smaller than the range of the potential, the interaction energy can be given (Widom 1962) by the following sum of two independent functions (the potential  $U(r)$  and the perturbing force  $F(r)$ ),

$$V(x, r) = U(r) - xF(r). \quad (6)$$

When the deviation of the oscillator from its equilibrium position is not large, the perturbing force can be given (Shin 1976) as

$$F(r) \approx \frac{m_a}{m_a + m_b} \left( \frac{\partial V}{\partial r} \right)_{x=0} \quad (7)$$

where  $m_a$  and  $m_b$  are masses of the incident and target particles, respectively.

We assume in what follows that the initial state of the collision system is defined by a real wavefunction  $\psi(E)$ , where  $E$  is the relative translational energy. The final state (after the vt ( $i \rightarrow j$ ) transition; where  $i$  and  $j$  are the initial and final vibrational quantum numbers of the target molecule, respectively) is characterized by a real wavefunction  $\psi(E + \epsilon_{ij})$  and a new energy  $E + \epsilon_{ij}$ , where  $\epsilon_{ij}$  is the change in the internal

The method of Landau and Lifshitz was formulated for monotonic, with respect to  $r$ , potentials. Widom (1962) applied the method to a couple of repulsive potentials and averaged the obtained probabilities  $P_{ij}(E)$  over energy distribution. Shin (1965) generalized the approach and evaluated the integral  $I_{ij}$  for almost any central force potential, including the repulsive-attractive potentials. Two such potentials are considered in the present work: the Lennard-Jones potential (for interaction of two diatomic molecules), and the Lennard-Jones potential with an additional term  $-\alpha^2/2r^4$  (for interaction of a diatomic molecular ion with a diatomic molecule). In either case the singular point (at  $r=0$ ) of the potential coincides with the singular point of the wavefunctions  $\psi$ . Therefore, the perturbation integral (11) can be evaluated in the limit  $U_x = U(r) \rightarrow \infty$ ,

$$I_{ij} = \exp \left[ -\frac{(2\bar{\mu})^{1/2}}{\hbar} \left( \int_{E+\epsilon_{ij}}^{U_x} [U(r) - (E + \epsilon_{ij})]^{1/2} \frac{dr}{dU} dU - \int_E^{U_x} [U(r) - E]^{1/2} \frac{dr}{dU} dU \right) \right]. \quad (13)$$

The integral (13), evaluated for the two repulsive-attractive intermolecular potentials, will be used below to calculate the vt probability  $P_{ij}(E)$ .

Using a central-force intermolecular potential is easily understood in the case of some systems such as, for example, the  $(N_2)_2$  complex. However, some systems can have more than one potential surface. For instance, the ground state of  $O_2$  is triplet  $^3\Sigma_g^-$  and the  $(O_2)_2$  complex has three potential surfaces that correspond to total spins 0, 1 and 2. Because we do not consider transitions between these surfaces, it is reasonable to replace them, for our purposes, by one surface. In a more rigorous approach one can evaluate transition probabilities for each surface and then average them.

The pre-exponential constant in the relationship (12) has been evaluated by Shin (1976) leading to the following energy-dependent probability per collision for the  $i \rightarrow j$  vibrational transition,

$$P_{ij}(E) = \frac{4c_i^2 c_j^2 x_{ij}^2}{\hbar^2 [E(E + \epsilon_{ij})]^{1/2}} \left( \int_{-x}^x \frac{F(r) dr}{[U(r) - E]^{1/4} [U(r) - (E + \epsilon_{ij})]^{1/4}} \right) \times \exp \left\{ -\frac{(2\bar{\mu})^{1/2}}{\hbar} \left[ \int_{E+\epsilon_{ij}}^{U(r)} [U(r) - (E + \epsilon_{ij})]^{1/2} \left( \frac{dr}{dU} \right) dU - \int_E^{U(r)} [U(r) - E]^{1/2} \left( \frac{dr}{dU} \right) dU \right] \right\}^2 \quad (14)$$

where  $c_i$  and  $c_j$  are constants evaluated as  $(2\bar{\mu}|U(r) - E|)^{1/4}$  and  $(2\bar{\mu}|U(r) - (E + \epsilon_{ij})|)^{1/4}$  at  $r \rightarrow \infty$ , respectively.

Since the relaxation of translation energy is usually very fast one can often assume an equilibrium distribution of the initial kinetic energies of the colliding particles. Averaging the probability (14) over the equilibrium distribution of energies for one-dimensional collisions one obtains (Herzfeld 1965) the temperature-dependent probability  $P_{ij}(T)$ ,

$$P_{ij}(T) = (kT)^{-1} \int_0^x P_{ij}(E) \exp(-E/kT) dE. \quad (15)$$

The assumption that the rotational transitions do not significantly affect the probabilities of the discussed  $\nu\tau$  vibrational transitions in diatomic systems should be true for most homonuclear diatomic molecules, except the hydrogen molecule where such an assumption can be inaccurate. A simultaneous  $\Delta J$  transition in the direction opposite to the  $\Delta v$  transition decreases the amount of internal energy transferred to translation (Lambert 1977). Subsequently, it tends to favour the transitions with larger values of  $\Delta J$ . However, this effect is limited by the requirement of conservation of total angular momentum during collision, which favours small values of  $\Delta J$ . In small and medium homonuclear molecules,  $\Delta J = \pm 0$  and  $\Delta J = \pm 2$  are the most probable transitions when  $\Delta v = \pm 1$ . In heavy molecules  $\Delta J$  is larger because the angular momentum is easily conserved (Kurzel *et al* 1971) in collisions of heavy molecules; for example, the most probable transitions in the  $I_2$  molecule are those with  $\Delta J = \pm(6-8)$  (Kurzel *et al* 1971). Since the energy gaps of the rotational transitions are much smaller than the energy gaps of the vibrational transitions, inclusion of the rotational excitation in our model would increase the  $\nu\tau$  probabilities only slightly.

A constant value of the factor  $g$  in equation (17) is suggested by a comparison of the theoretical probabilities  $P_{ij}$  with existing experimental data (see below) and by the fact that two important effects accounted for by the factor are rather weak functions of temperature. The first effect (the 'steric' effect) results from the necessity of taking into account the contribution of non-collinear collisions (the wkb approach discussed above was formulated for collinear interactions). Since collisions between two diatomic molecules may not be linear, consideration of a 'steric' effect (that is, accounting for the fact that some collision orientations are more effective in energy exchange than others) becomes necessary. In general, estimation of the 'steric' effect for three-dimensional scattering is a difficult problem. Shin (1976) investigated the effect for collisions of diatomic molecules with various intermolecular potentials; his study of several diatomic systems indicated that the presence of non-collinear collisions decreases the  $\nu\tau$  transition probabilities, but the effect is a weak (decreasing) function of gas temperature. The second important effect accounted for by the factor  $g$  is caused by the non-zero-impact-parameter collisions. These collisions decrease the  $\nu\tau$  probabilities but this effect is also a weak (increasing) function of temperature (Shin 1976). Thus, the overall dependence of the two effects (the contributions of the non-linear and non-zero-impact parameter collisions) on temperature should indeed be very weak.

The assumption of the zero Maslov index (Maslov and Fedoriuk 1981, Delos 1986) in the wkb approach can be justified as follows. The wavefunctions for the one-dimensional motion are

$$\psi_{i,f} \sim \sin\left(\hbar^{-1} \int_{r_i}^r p_{i,f} dr + \varphi_{i,f}\right) \equiv \sin(A_{i,f} + \varphi_{i,f}) \quad (20)$$

where the subscripts  $i$  and  $f$  denote initial and final states of the system, respectively,  $p$  is the classical momentum,  $r_i$  is the turning point and  $\varphi$  is a constant related to the Maslov index. The product  $\sin(A_i + \varphi_i) \sin(A_f + \varphi_f)$  can then be written as

$$[\cos(A_i - A_f + \varphi_i - \varphi_f) - \cos(A_i + A_f + \varphi_i + \varphi_f)]/2 \quad (21)$$

where the second cosine term is rapidly oscillating, which is opposite to the behaviour of the first cosine term, and can be neglected. Presumably, the Maslov indices for the initial and final translational states of the systems considered here are close to each other. In such a case the first term would be weakly dependent on the Maslov indices and this may be the reason why a non-zero Maslov index does not have to be introduced

where  $\sigma'$  and  $U'_m$  (the potential well depth) can be obtained from the approach discussed in I and summarized in section 1.

Substituting the constants (23)–(25) into equation (17) one obtains a more transparent form of the equation,

$$\begin{aligned}
 P_{ii}(T) = & \frac{4\pi^2 \hbar n_1 g \rho^2 [C(\sigma')^{n_1}]^{3/2} j \left( \frac{2\pi\bar{\mu}n_1}{2+3n_1} \right)^{1/2} \left[ \frac{\epsilon_{ij}}{n_1+2} \left( \frac{2\bar{\mu}}{C(\sigma')^{n_1} \hbar^2} \right)^{1/2} \right]^{(3n_1+2)/(n_1+2)}}{M\epsilon_{ij}^2} \\
 & \times \left( \frac{\chi'}{kT} \right)^{1/2} \exp \left[ - \left( \frac{2+3n_1}{2+n_1} \right) \frac{\chi'}{kT} - \frac{\Gamma(1+1/n_1)\Gamma(\frac{3}{2}-5/n_1)}{\Gamma(\frac{3}{2}+1/n_1)\Gamma(1-5/n_1)} C^{1-6/n_1} \frac{(\chi')^{6/n_1}}{kT} \right. \\
 & - \frac{\Gamma(1+1/n_1)\Gamma(\frac{3}{2}-3/n_1)}{\Gamma(\frac{3}{2}+1/n_1)\Gamma(1-3/n_1)} \frac{C^{1/3}}{C^4 n_1 (\sigma')^4} \frac{(\chi')^{4/n_1}}{kT} \\
 & + \left[ \left( \frac{n_1}{2+3n_1} \right) \left( \frac{\Gamma(2+1/n_1)\Gamma(\frac{5}{2}-5/n_1)}{\Gamma(\frac{3}{2}+1/n_1)\Gamma(1-5/n_1)} \right)^2 \right. \\
 & \left. \left. - \left( \frac{3n_1-10}{4n_1} \right) \left( \frac{\Gamma(1+1/n_1)\Gamma(\frac{3}{2}-11/n_1)}{\Gamma(\frac{3}{2}+1/n_1)\Gamma(1-11/n_1)} \right) \right] C^{1-6/n_1} \right] \\
 & \times \left[ \frac{(\chi')^{12/n_1-1}}{kT} + \frac{\epsilon_{ij}}{2kT} \right] \quad (28)
 \end{aligned}$$

where  $g = 0.2$ ,  $j$  is, as before, the initial value of the vibrational quantum number of the target molecule, and

$$\chi' = \left( \frac{\Gamma(\frac{3}{2}+1/n_1)(4U'_m)^{1/n_1} \sqrt{2\pi\bar{\mu}} \sigma' \epsilon_{ij} kT}{\Gamma(1+1/n_1) n_1 \hbar} \right)^{2n_1/(2+3n_1)} \quad (29)$$

### 3. Some analytical approximations

In order to obtain analytical expressions for the temperature-dependent transition probabilities (see the next section) one has to introduce several approximations.

An approximate value of the mean internuclear distance  $\langle R_{v,J} \rangle$  in a diatomic molecule excited to the  $v, J$ th vibrational-rotational level can be obtained from the quantum-classical model of the rotating Morse oscillator discussed in I. The effective intramolecular potential of the oscillator is

$$U_{\text{eff}}(R) = U_v(R) + U_J(R) \quad (30)$$

where  $U_v(R)$  is the vibrational part and  $U_J(R)$  is the rotational part of the potential,

$$U_v(R) = D\{1 - \exp[-\beta(R - R_e)]\}^2 \quad (31)$$

and

$$U_J(R) = \frac{\hbar^2 [J(J+1) - \Lambda^2]}{2\mu R^2} \quad (32)$$

where  $D$  is the dissociation energy, referred to the potential minimum, of the rotationless oscillator,  $R$  is the internuclear distance,  $R_e$  is the equilibrium bond length,  $\beta$  is a constant,  $\mu$  is the reduced mass of the oscillator and  $\Lambda$  is the quantum number for the axial component of electronic angular momentum. Typically,  $J_p^2 \gg \Lambda^2$  ( $J_p$  is the most

one factor obtainable from the distribution normalization condition. Taking this into account the normalized distribution  $p(z)$  for the Morse oscillator of energy  $E_{v,J}$  is

$$p(z) dz = \pi^{-1} (1-u^2)^{-1/2} (1-z)^{-1} (u^2-z^2)^{-1/2} dz. \quad (43)$$

(It should be noted that  $p(z)$  becomes infinite at the oscillator turning points because the velocities  $dR/dt$  at these points are zero.) The mean internuclear distance of such an oscillator is

$$\langle z \rangle = \int_{z_1}^{z_2} zp(z) dz = 1 - (1-u^2)^{1/2} \quad (44)$$

so that

$$\langle R_{v,J} \rangle = R_e - (2\beta)^{-1} \ln \left( 1 - \frac{E_{v,J} - A_0}{D} \right). \quad (45)$$

We assumed above that the stretching term  $U_J(R) = A_0$  is independent of  $R$ . This assumption can be improved by replacing  $R_e$  by  $R_0$  in equation (45).

A more accurate analytical expression for the mean internuclear distance  $\langle R_{v,J} \rangle$  can be obtained by using the first nine terms of the expansion (I)

$$\begin{aligned} \left( \frac{R_e}{R} \right)^2 &= \frac{1}{[1 - \ln y / \beta R_e]^2} = 1 + \frac{2}{\beta R_e} (y-1) - \left( \frac{1}{\beta R_e} - \frac{3}{\beta^2 R_e^2} \right) (y-1)^2 \\ &+ \left( \frac{2}{3\beta R_e} - \frac{3}{\beta^2 R_e^2} + \frac{4}{\beta^3 R_e^3} \right) (y-1)^3 \dots \end{aligned} \quad (46)$$

where  $y = \exp[-\beta(R - R_e)]$ . Then, equation (30) can be rewritten as

$$E_{v,J} - U_{\text{eff}}(R) = D(Fy^2 + Gy + H) \quad (47)$$

where

$$F = \frac{A(\beta R_e - 3)}{D\beta^2 R_e^2} - 1 \quad (48)$$

$$G = -\frac{2A(2\beta R_e - 3)}{D\beta^2 R_e^2} + 2 \quad (49)$$

$$H = \frac{A(3\beta R_e - 3)}{D\beta^2 R_e^2} - \frac{D + A - E_{v,J}}{D} \quad (50)$$

and

$$A = \frac{\hbar^2 J(J+1)}{2\mu R_e^2}. \quad (51)$$

The relationships (30)–(32), (41), (44), (46) and (47) can be used, in the way similar to that leading to equation (45), to obtain an analytical expression for the mean internuclear distance  $\langle R_{v,J} \rangle$ . However, the expression is complicated and gives results that are close to the results obtained from the expression (45) when  $R_e$  is replaced by  $R_0$ .

The dependence of the intermolecular potential  $U(r)$  on the degree of rotational-vibrational excitation of the colliding molecules is given by the coefficients  $\Phi_p$  (I)

the 12-6 (or 12-6-4) form, then the resulting intermolecular potential  $U'(r)$  will have a similar functional form if the colliding molecules are homonuclear or 'almost' homonuclear. Thus, the assumed potential  $U'(r)$  of two homonuclear molecules that are excited vibrationally and/or rotationally is

$$U'(r) = 4U'_m \left[ \left( \frac{\sigma'}{r} \right)^{12} - \left( \frac{\sigma'}{r} \right)^6 \right] \quad (59)$$

while in the case of the interaction of a homonuclear molecular ion with its parent molecule it is

$$U'(r) = 4U'_m \left[ \left( \frac{\sigma'}{r} \right)^{12} - \left( \frac{\sigma'}{r} \right)^6 \right] - \frac{\alpha e^2}{2r^4}. \quad (60)$$

In most cases it is reasonable to assume that the initial (before collision) rotational quantum numbers ( $J_a$  for the incident particle and  $J_b$  for the target particle) of the colliding molecules can be taken as equal to their most probable rotational quantum numbers ( $(J_p)_a$  and  $(J_p)_b$ , respectively) at a given temperature. The most probable rotational quantum numbers in a gas of temperature  $T$  can be obtained from the equilibrium distribution of the rotational levels (the rotational temperature is usually very close to gas translational temperature),

$$N_J \sim (2J+1) \exp[-B_e J(J+1)hc/kT]. \quad (61)$$

The distribution (61) can be approximated by a continuous function of  $J$  with maximum at  $J = J_p$ , where  $J_p$  is an integer nearest to

$$J'_p = \left( \frac{kT}{2B_e hc} \right)^{1/2} - \frac{1}{2}. \quad (62)$$

Thus, the most probable initial rotational quantum numbers for the incident and the target molecules can be taken as integers nearest to

$$(J'_p)_{a,b} \approx \left( \frac{kT}{2(B_e)_{a,b}hc} \right)^{1/2}. \quad (63)$$

Since the value of  $J_p$  is obtained from differentiation of the continuum (classical) distribution  $N_J$ , it is somewhat inaccurate; the absolute inaccuracy is  $|\Delta J_p| \leq 1$  and the relative inaccuracy is less than a few per cent (usually  $J_p \gg 1$ ). Inclusion of the nuclear spin degeneracy in the distribution (61) causes disappearance of odd or even rotational levels of homonuclear diatomics. Therefore, the inaccuracy in  $J_p$  resulting from using the continuum distribution  $N_J$  is comparable with the inaccuracy resulting from neglecting the dependence of  $N_J$  on the nuclear spin statistics. Thus, neglecting, as we have done, the nuclear spin degeneracy factors in the distribution (61) has no meaningful impact on the final results of our calculations.

The transition probability for a binary collision in which the target molecule  $b$  (initially in the  $v_b = j$ ,  $J_b$  vibrational-rotational state) undergoes a VT transition  $v_b = j \rightarrow v_b = i$  upon the impact of an incident molecular ion  $a$  (being initially in the  $v_a$ ,  $J_a$  state) can be obtained from equation (28) assuming intermolecular potential (60). This probability is (if both colliding particles are neutral molecules then the expression (64) will also be valid but then the term including  $\alpha$  should be neglected)

$$P_{ji}(T) = 1.612 g m_b^{-1} (U'_m)^{1/2} \bar{\mu}^{13/7} \epsilon_{ij}^{5/7} \left( \frac{\sigma'}{h} \right)^{12/7} \left( \frac{\chi'}{kT} \right)^{1/2} j \exp \left( -2.714 \frac{\chi'}{kT} \right. \\ \left. + 1.346 \frac{(\chi' U'_m)^{1/2}}{kT} + 0.254 \frac{\alpha e^2}{(U'_m)^{1/3} (\sigma')^4} \frac{(\chi')^{1/3}}{kT} + 0.362 \frac{U'_m}{kT} + \frac{\epsilon_{ij}}{2kT} \right) \quad (64)$$

The collision numbers  $Z_{10}$  obtained from equations (22) and (28) are compared in figure 1 with the SSH theory (Schwartz *et al* 1952) and with the existing experimental data (Blackman 1956, Camac 1961, Millikan and White 1963, White and Millikan 1963, Hurle 1964). The agreement between the present results and the measurements is very good in the considered range of temperature. The collision number  $Z_{10}$  is a strong decreasing function of temperature  $T$  and logarithm of  $Z_{10}$  varies as  $T^{-1/3}$  which is close to the  $T$  dependence ( $T^{-1/3}$ ) predicted by the Landau-Teller theory (Landau and Teller 1936). The collision numbers obtained from the SSH theory do not include several correction factors due to effects discovered since the original publication (Rapp and Kassal 1969, Yardley 1980). The product of these correction factors was estimated by Rapp and Kassal (1969) as equal to about a hundred. Multiplying the SSH results (the broken curves in figure 1) by a hundred brings these results much closer to the experimental data.

Examples of the  $\nu\tau$  transition probabilities  $P_{j,j-1}(T)$  for the  $j \rightarrow j-1$  vibrational de-excitation of nitrogen and oxygen molecules are given in figures 2 and 3, respectively. The probabilities, obtained from equation (28) using the intermolecular potentials of I, are strong increasing functions of temperature  $T$ , and strong increasing functions of the vibrational quantum number  $j$ .

Experimental data for transitions other than  $1 \rightarrow 0$  are not available. To verify the present approach for the  $j > 1$  transitions we compare our results with the existing results of numerical calculations for nitrogen (Billing and Fisher 1979, Capitelli *et al* 1980, Billing 1980, Bogdanov *et al* 1989). Since the numerical results of Billing *et al* and Bogdanov *et al* are given in form of rate constants  $k_{j,j-1}^{\text{BB}}$  (in  $\text{cm}^3 \text{s}^{-1}$ ) we calculated

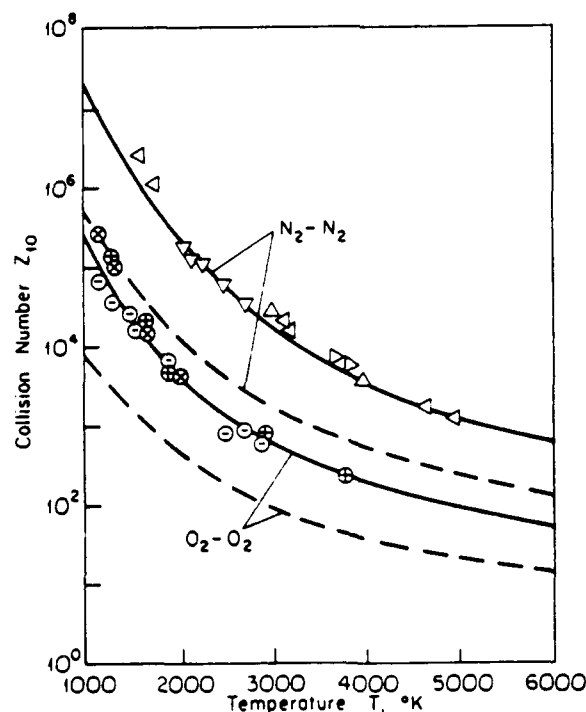


**Figure 1.** The collision numbers  $Z_{10}$  for the  $\nu\tau$   $1 \rightarrow 0$  transitions in  $\text{N}_2 + \text{N}_2(\text{X}^1\Sigma_g^+, v=1) \rightarrow \text{N}_2 + \text{N}_2(\text{X}^1\Sigma_g^+, v=0)$  and  $\text{O}_2 + \text{O}_2(\text{X}^3\Sigma_g^-, v=1) \rightarrow \text{O}_2 + \text{O}_2(\text{X}^3\Sigma_g^-, v=0)$  collisions. The incident molecules are in the ground electronic and ground vibrational states. The full and broken curves represent the results of the present work and the SSH (Schwartz *et al*) theory, respectively. The circles and triangles denote the experimental data obtained by Blackman (1956), Camac (1961), Millikan and White (1963), White and Millikan (1963) and Hurle (1964). The exponent characterizing the short-range interaction is  $n_1 = 12$ .

the corresponding transition probabilities  $P_{j,j-1}^{BB}$  using the following relationship

$$P_{j,j-1}^{BB}(T) = P_{10}^{exp}(T) \frac{k_{j,j-1}^{BB}(T)}{k_{10}^{BB}(T)} \quad (74)$$

where the superscript BB denotes the results of Billing *et al* and Bogdanov *et al*,  $P_{10}^{exp}(T)$  is the probability obtained from the measured collision number  $Z_{10}(T)$  (figure 1); note that  $P_{10}^{exp}(T)$  is very close to  $P_{10}(T)$  of the present approach.

Comparison of the probabilities  $P_{j,j-1}^{BB}$  with the results of the present work is shown in figure 2. As can be seen from there, the agreement between the compared probabilities is quite good in the entire range of temperatures considered. One should add, however, that at temperatures  $T \geq 6000$  some probabilities of the present work can become close to, or greater than, unity for higher values of  $j$ . In such a case, our first-order wkb approach becomes inaccurate and other methods should be used for calculating the transition probabilities.

The  $\Delta v = 1$  transition probabilities of the present work are close to the 'scaled' (with respect to the probability  $P_{10}$ ) results of the SSH theory for the lowest transitions. At higher vibrational quantum numbers of the target molecule the difference between our results and the SSH results becomes large, which is in agreement with conclusions of Billing (1986); for example, at  $T = 300$  K and  $j > 10$  the difference is greater than one order of magnitude.

As discussed above, the present approach seems to give accurate values of the  $v \rightarrow j \rightarrow j-1$  transition probabilities. This first-order perturbation approach can be used in a straightforward way to calculate the probabilities for transitions with  $\Delta v > 1$ . As discussed in section 1, applying the present approach to such transitions may lead to inaccurate values of the corresponding probabilities  $P_{j,j}$ . The accuracy of our approach for  $\Delta v > 1$  transitions cannot be estimated at present. However, it seems that the approach gives reasonable estimates of the  $\Delta v = 2(j \rightarrow j-2)$  transition probabilities provided we drop the  $\delta$ -function in equation (9). In the case of transitions with  $\Delta v > 2$  the inaccuracy of the approach may be significant.

Examples of the probabilities  $P_{j,j-2}$  for nitrogen and oxygen are given in figure 4 and figure 5, respectively. As expected, the probabilities are strong increasing functions of temperature and they are orders of magnitude smaller than the probabilities  $P_{j,j-1}$ .

The role of the short-range part of the intermolecular potential was investigated assuming different values (10, 12 (Lennard-Jones) and 14) of the exponent  $n_1$ . The dependence of the transition probability  $P_{j,j}(T)$  on  $n_1$  is shown in figures 6 and 7. As can be seen from there, the differences between the probabilities when  $n_1 = 10$  and when  $n_1 = 14$  are within a factor of two, regardless of the value of vibrational quantum number  $j$ .

The transition probabilities  $P_{j,j}(T)$  obtained from the simple expression (64) are in good agreement (in most cases better than 10%, and not exceeding 20% in a few 'bad' cases) with the discussed above transition probabilities obtained from equation (28) using the intermolecular potentials of I.

In Shin's wkb approach the molecular anharmonicity is accounted for only by taking  $\epsilon_{jj}$  as the energy gap between the levels of an anharmonic oscillator (the vibrational matrix element was assumed in that approach to be the matrix element of the harmonic oscillator,  $x_{jj}^h$ ). In the present approach the anharmonicity of the target oscillator is accounted for through three quantities: the transition energy gap  $\epsilon_{jj}$  of the Morse oscillator, the 'corrected' matrix element  $x_{jj}$  and the intermolecular potential  $U'(r)$  which was calculated under the assumption that the colliding molecules are



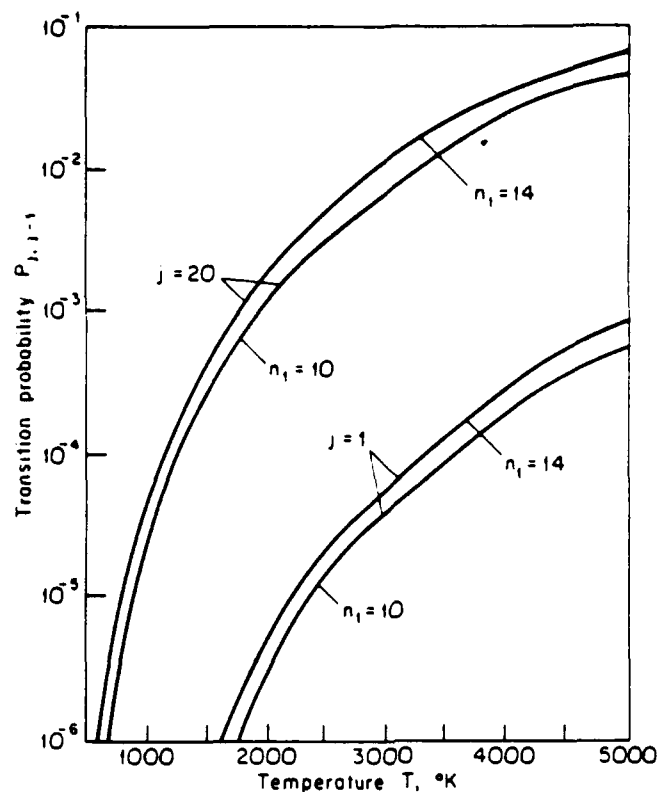


Figure 6. The dependence of the transition probabilities  $P_{j,j-1}$  for the  $N_2(X^1\Sigma_g^+, v_a=0) + N_2(X^1\Sigma_g^+, v_b=j)$  collision on the slope (represented by the exponent  $n_1$ ) of the short-range part of the intermolecular potential.

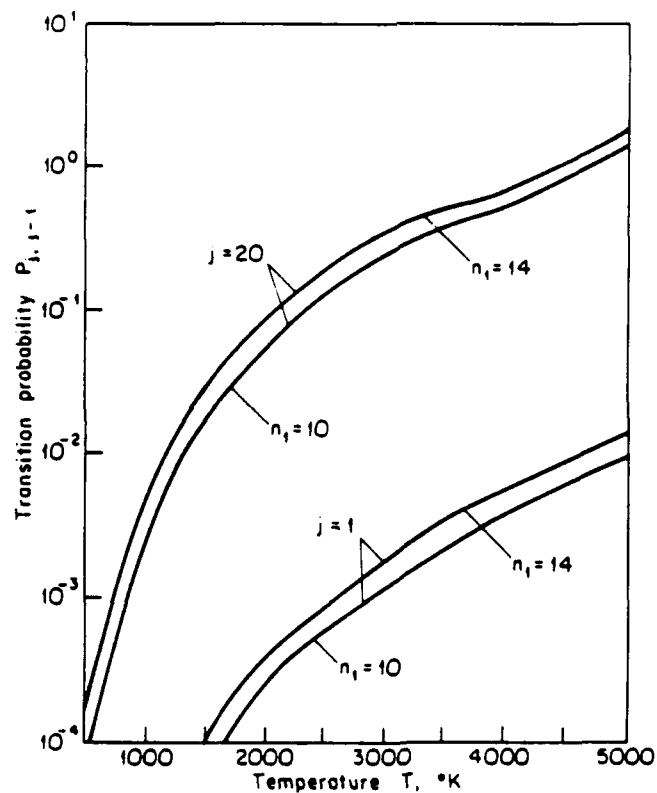


Figure 7. The dependence of the transition probabilities  $P_{j,j-1}$  for the  $O_2(X^1\Sigma_g^-, v_a=0) + O_2(X^3\Sigma_g^-, v_b=j)$  collision on the slope (represented by the exponent  $n_1$ ) of the short-range part of the intermolecular potential.

- Bonham R A and Peacher J L 1963 *J. Chem. Phys.* **38** 2319  
Camac M 1961 *J. Chem. Phys.* **34** 448  
Capitelli M, Gorse C and Billing G D 1980 *Chem. Phys.* **52** 299  
Delos J B 1986 *Adv. Chem. Phys.* **65** 161  
Herzberg G 1961 *Spectra of Diatomic Molecules* (New York: Van Nostrand Reinhold)  
Herzfeld K F 1965 *Thermodynamics and Physics of Matter* ed F D Rossini (Princeton, NJ: Princeton University Press) p 111  
Hurle I R 1964 *J. Chem. Phys.* **41** 3911  
Jackson J M and Mott N F 1932 *Proc. R. Soc. A* **137** 703  
Kunc J A 1990 *J. Phys. B: At. Mol. Opt. Phys.* **23** 2553  
Kurzweil R B, Steinfeld J I, Hatzenbuehler D A and Leroy G E 1971 *J. Chem. Phys.* **55** 4822  
Lambert J D 1977 *Vibrational and Rotational Relaxation in Gases* (Oxford: Clarendon)  
Landau L 1932 *Phys. Z. Sowjetunion* **2** 46  
Landau L and Lifshitz E M 1959 *Quantum Mechanics* (New York: Pergamon)  
Landau L and Teller E 1936 *Phys. Z. Sowjetunion* **10** 34  
Maslov V P and Fedoriuk M V 1981 *Semiclassical Approximation in Quantum Mechanics* (Boston: Reidel)  
Millikan R C and White D R 1963 *J. Chem. Phys.* **39** 98  
Nikitin E E 1974 *Theory of Elementary Atomic and Molecular Processes in Gases* (Oxford: Clarendon)  
Rapp D and Kassal T 1969 *Chem. Rev.* **69** 61  
Schwartz R N and Herzfeld K F 1954 *J. Chem. Phys.* **22** 767  
Schwartz R N, Slawsky Z I and Herzfeld K F 1952 *J. Chem. Phys.* **20** 1591  
Shin H K 1965 *J. Chem. Phys.* **42** 59  
— 1966 *Adv. Chem.* **58** 44  
— 1976 *Dynamics of Molecular Collisions* vol 1, ed W H Miller (New York: Plenum) p 131  
Takayanagi K 1952 *Prog. Theor. Phys., Kyoto* **8** 497  
White D R and Millikan R C 1963 *J. Chem. Phys.* **39** 1803  
Widom B 1962 *Disc. Faraday Soc.* **33** 37  
Yardley J T 1980 *Introduction to Molecular Energy Transfer* (New York: Academic)  
Zener C 1931 *Phys. Rev.* **37** 556

**ATTACHMENT 8**



**AIAA 93-2996**

**Measurement of Rotational and Vibrational Population  
Distributions in a Hypersonic Flow of Chemically Reacting  
Iodine Vapor**

Gerald C. Pham-Van-Diep and E. Phil Muntz  
University of Southern California, Los Angeles, CA 90089-1191

Iain D. Boyd  
Cornell University, Ithaca, NY 14853

**AIAA 24th  
Fluid Dynamics Conference  
July 6-9, 1993 / Orlando, FL**

# Measurement of Rotational and Vibrational Population Distributions in a Hypersonic Flow of Chemically Reacting Iodine Vapor

Gerald C. Pham-Van-Diep<sup>1</sup> and E. Phil Muntz<sup>2</sup>

University of Southern California, Los Angeles, CA 90089-1191

Iain D. Boyd<sup>3</sup>

Cornell University, Ithaca, NY 14853

## 1 Abstract

Rotational and vibrational population distributions are measured at several positions along the central axis of a free jet of iodine vapor impinging on the flat surface of a disc. The probing technique is described and the procedure used to determine populations of vibrational and rotational energy levels from fluorescent signal intensities is outlined. The procedure accounts for both dissociation and predissociation of the molecules during the pulsed laser excitation process. The measured rotational and vibrational population distributions are compared to Direct Simulation Monte Carlo predictions. The precision of the measurements and possible improvements of the diagnostic technique are discussed.

## 2 Introduction

Nonequilibrium flows are encountered in a significant number of natural and technological settings. A few examples are material plasma processing, ion or cluster deposition schemes, arc jet or chemical rocket exhaust plumes, and gas dynamic or chemical lasers. Of particular interest to the aerospace engineering community are the nonequilibrium phenomena associated with the flowfield around a spacecraft entering Earth's or other planet's atmospheres.

In two previous papers,<sup>1,2</sup> we proposed that iodine be used for the detailed experimental study of nonequilibrium,

chemically reacting hypersonic diatomic gas flows. In terms of dissociation, a stagnation temperature of 1500 K for iodine is equivalent to about 4000 K for oxygen or 6000 K for nitrogen.<sup>1</sup> The experimental simulation of chemically reacting air flows has traditionally been performed in transient facilities such as shock tubes or shock tunnels because of the high stagnation enthalpy required to produce significant internal excitation in nitrogen and oxygen.<sup>3</sup> In order to avoid the drawbacks associated with these pulsed flow experiments, a semi-continuous pilot scale hypersonic wind tunnel operating on pure iodine vapor has been developed. Its performance has been reported in previous papers.<sup>4,5</sup> The wind tunnel operates intermittently by expanding iodine through a sonic orifice and into a vacuum for run times lasting approximately 30 minutes. Stagnation temperatures up to 1000 K can be achieved at stagnation pressures up to 100 Torr. This enables the production of significantly populated higher rotational and vibrational levels as well as some dissociation. The approach that we have taken does not propose to directly simulate O<sub>2</sub> or N<sub>2</sub> with I<sub>2</sub>, but rather, to study the rotational, vibrational and dissociative energy behavior of the iodine molecule when placed in a hypersonic nonequilibrium situation. Accurate measurements of the population distributions for the large number of significantly populated levels typical of a dissociating gas, will permit meaningful tests of the basic assumptions about local thermodynamic equilibrium that are made in most predictions involving finite rate chemistry.

This paper describes the experimental method developed to probe rotational and vibrational population distributions at several positions along the central axis of a free jet

1 Graduate Assistant, AIAA Member

2 Professor, AIAA Fellow

3 Assistant Professor, AIAA Member

impinging on the flat surface of a disc. Transient Laser Induced Fluorescence (TLIF) is used as a diagnostic technique. The pulsed nature of the technique makes the measurements quenching insensitive, however issues such as the sensitivity of the probed molecules to dissociation and pulsed pumping have to be addressed so that the fluorescence intensities may be interpreted. Other diagnostic considerations such as saturation and attenuation of the laser beam are discussed. Finally, typical rotational and vibrational population distributions measured at several plume axial positions are presented and compared to direct simulation Monte Carlo calculations. The accuracy of the measurements and plan for improving the technique are discussed.

### 3 Transient Laser Induced Fluorescence applied to the iodine molecule

The Transient Laser Induced Fluorescence technique is selected for the purpose of this study because it produces relatively strong signals compared to alternate scattering techniques such as Raman or Rayleigh scattering. Provided the tunable pulsed laser linewidth is small enough to permit excitation of single transitions, the chosen diagnostic technique is robust and has the additional advantage of being insensitive to quenching under the condition that the laser pulse duration and the detection time are shorter than the local quenching time.

To probe individual rovibrational levels the laser excites  $I_2$  molecules from a rovibrational level ( $V''$ ,  $J''$ ) of the ground electronic state  $X(^1\Sigma_0^+)$  to a rovibrational level ( $V'$ ,  $J'$ ) of the  $B(^3\Pi_0^-)$  state. Emission spectra are obtained by scanning the laser wavelength, i. e. successively exciting levels of the  $X$  state to levels of the  $B$  state. The fluorescence signal is observed through a fixed spectral window ( $\sim 20$  Å) of a spectrometer whose main purpose is to filter scattered photons at the laser frequency and at the overtones other than the one detected by the spectrometer. In the study presented here, only the first overtone on the Stokes side of the laser line is detected ( $\Delta V = V_{\text{final}} - V_{\text{initial}} = +2$ ). The intensity of the fluorescent signal is a measure of the population in level ( $V''$ ,  $J''$ ) provided the transition strengths for both the absorption ( $B_{12}$ ) and emission ( $A_{23}$ ) phases are known. The relative population in a rotational level  $J''$  can be calculated using

$$N(J'') \propto \frac{I_{\text{fluo}}}{f(B_{12}) A_{23} SP(J'')} \quad (\text{EQ 1})$$

where the subscripts 1, 2 and 3 correspond to the lower initial, upper intermediate and lower final state involved in the TLIF process (Ref. Fig. 1). The rotational population distributions presented in this paper were determined from transitions starting from the same lower vibrational state, consequently (EQ 1) is independent of  $V''$ . In (EQ 1)  $f(B_{12})$  is a factor which depends on the Einstein absorption coefficient  $B_{12}$ , the partial dissociation of the molecules occurring during the excitation process and the pulsed nature of the experiment.  $SP(J'')$  is a factor which accounts for the nuclear spin of the molecule, it takes a value of 7 for odd  $J''$  and 5 for even  $J''$ .

Similarly, the relative population in a vibrational level  $V''$  may be computed with

$$N(V'') \propto \frac{I_{\text{fluo}}}{f(B_{12}) A_{23} SP(J'') N(J'')} \quad (\text{EQ 2})$$

The vibrational population distributions presented in this paper were computed from transitions involving different rotational quantum levels, consequently, as indicated in (EQ 2), the fluorescent signal intensity is divided by the rotational population  $N(J'')$  calculated with (EQ 1).

#### 3.1 Upper state response to pulsed pumping

Fig. 1 shows a diagram of the three level system used to model the transitions involved in the TLIF process. The population  $N_1$  of the  $X$  state being excited by the laser and the population  $N_2$  in the  $B$  state may be described by the system of equations:

$$\frac{dN_1}{dt} = N_2(P_{21} + A_{21}) - N_1(P_{12} + P_{\text{dis}}) \quad (\text{EQ 3})$$

$$\frac{dN_2}{dt} = N_1(P_{12}) - N_2(P_{21} + \sum_{i < 2} A_{2i} + A_{p\text{dis}}) \quad (\text{EQ 4})$$

where  $P_{ij} = B_{ij} g(v_L) E_p(t)/(Ac)$  is the pumping rate from level  $i$  to level  $j$ ,  $A_{ij}$  is the spontaneous emission coefficient from level  $i$  to  $j$ ,  $B_{ij}$  is the stimulated emission or stimulated absorption factor depending on whether levels  $i$  and  $j$  are upper or lower levels.  $g(v_L)$  is the laser line shape,  $E_p(t)$  is the laser energy delivered to the probed volume per unit time.  $A$  is the laser beam cross-sectional area and  $c$

is the speed of light. Finally  $P_{dis}$  is the pumping rate which depopulates level 1 by direct absorption to the dissociative state  $^1\Pi_{1u}$ .<sup>6,7</sup>  $P_{dis}$  has the same form as  $P_{ij}$  with the only difference being that  $B_{ij}$  is replaced by an absorption coefficient  $B_{dis}$  consistent with a dissociative reaction. Spontaneous predissociation, whereby a molecule is initially absorbed into the  $B$  state and subsequently spontaneously dissociates by transitioning to the  $^1\Pi_{1u}$  state, has been taken into account in (EQ 4) with the spontaneous decay term  $A_{pdis}$ . Direct absorption and spontaneous predissociation to other dissociative states such as  $^3\Pi_{2g}$ ,  $^3\Pi_{1g}$ ,  $^3\Pi_{0g}$ ,  $^3\Sigma_{0u}$ , or  $^3\Delta_{3u}$  are ignored in this analysis because their contribution has been found to be minimal compared to the  $^1\Pi_{1u}$  state, unless the laser is resonant with the crossing point between one of these dissociative states and the  $B$  state.<sup>8</sup> In the calculations shown below, dissociative and predissociative rates are approximated from independent measurements.<sup>6,10</sup> Fig. 2 shows the intermolecular potentials of the  $I_2$  molecule<sup>7,9</sup> which are relevant to the analysis of the pulsed laser pumping process. Also indicated are the approximate crossing points between the  $B$  state and the purely dissociative states mentioned above believed to be responsible for an enhanced decay rate of level 2 when the laser is tuned close to a crossing point.

Fig. 3 shows the time response of the population in level 2 when subjected to a pulsed laser excitation successively tuned to a variety of transitions: (20,1) P82, (24,3) R27, (19,0) P129, (18,0) R101 and (17,0) P39. These transitions require laser pumping at approximately 5683 Å and are used in this paper to determine rotational population distributions. The population responses are calculated by simultaneously solving (EQ 3) and (EQ 4), and assuming a laser pulse shape whose FWHM is approximately 25 nsec as indicated in Fig. 3.  $N_2(t)$  is integrated over a time gate of 100 nsec to yield the factor  $f(B_{12})$  for each transitions selected in this study. To calculate  $N_2(t)$ , Einstein A and B coefficients are determined from calculated radiative decays rates.<sup>6</sup> The total spontaneous radiative decay rate from a single upper vibrational level  $V'$  to several lower levels  $V''$  can be written as

$$A = \alpha \cdot \sum_{V''} \nu^3 FC(V', V''), \quad (\text{EQ } 5)$$

where  $\nu$  is the frequency of the radiation emitted during the transition  $(B, V', J') \rightarrow (X, V'', J'')$ ,  $FC(V', V'')$  is the Franck-Condon factor involved in the transition and

$$\alpha = \frac{64\pi^4}{3hc^3} \cdot \frac{1}{4\pi\epsilon_0} \cdot \frac{HL(J', J'')}{g_2} \cdot |\mu(R_c)|^2. \quad (\text{EQ } 6)$$

In (EQ 6)  $HL(J', J'')$  is the Hönl-London factor corresponding to a  $J' \rightarrow J''$  transition,  $\mu(R_c)$  is the electric dipole moment taken at an average internuclear distance  $R_c$  often called the  $R$ -centroid, and  $g_2$  is the total statistical weight of the radiating level in the  $B$  state.  $\alpha$  for a specified upper level is first calculated from (EQ 5), Franck-Condon factors determined by Martin *et al*<sup>19</sup> and total radiative decay rates computed by Brewer and Tellinghuisen.<sup>6</sup> The spontaneous decay rate  $A_{23}$  in (EQ 1) and (EQ 2) may then be calculated with (EQ 5) but for a single transition (i. e. without the summation).  $A_{12}$  is calculated in the same manner as  $A_{23}$  and  $B_{12}$  can be determined with

$$\frac{A_{21}}{B_{12}} = \frac{8\pi h \nu^3}{c^3} \cdot \frac{g_1}{g_2}. \quad (\text{EQ } 7)$$

(EQ 5) is based on several assumptions:

- 1) The rotational transition probability  $HL(J', J'')$  is independent of vibrational transition probability.
- 2) The total transition probability may be decomposed into three independent parts: an overlap integral of vibrational wavefunctions  $FC(V', V'')$ , the average electronic transition moment  $|\mu(R_c)|^2$  and the rotational transition probability  $HL(J', J'')$ .
- 3) The average electronic transition moment can be represented by the electronic transition moment at an average internuclear distance  $R_c$  called the  $R$ -centroid.
- 4) The  $R$ -centroid which in principle depends on vibrational quantum number has for the purpose of this study been considered constant.

Although the last assumption has been used for convenience in a number of past studies,<sup>20, 21</sup> it was found in this work that it may result in overestimating the decay rates and absorption coefficients by up to 15% for the (17, 0) R42 transition for instance.

The accuracy of the measurements depends greatly on the precision with which the rates of dissociation and predissociation, and the absorption and emission strengths have been determined. The diagnostic technique described here could be used to measure state specific transition probabilities for iodine maintained in a fairly well controlled envi-

ronment. These measurements could in turn validate more extensive rate predictions based on first principles.

### 3.2 Saturation

Under pulsed excitation, saturation of the upper intermediate excited state (*B* state) is virtually impossible to achieve because part of the molecules in the *X* state are dissociated during the laser pumping process. Fig. 4 shows the response of the population in level 2 normalized by the initial total population  $N_1(0)$  for three laser power levels:  $7 \cdot 10^{-5}$ ,  $7 \cdot 10^{-6}$  and  $7 \cdot 10^{-7}$  Joules/pulse. These responses are calculated for the (39, 0) R55 transition. As may be noticed,  $N_2(t)$  does not reach its saturated value  $N_{2\infty}$  as the laser power is increased. The saturated value of  $N_2(t)$  is reached when stimulated absorption is counterbalanced by stimulated emission transitions if there is no significant depletion of the total population in the two levels (i. e. if dissociation can be neglected).  $N_{2\infty}$  is given by

$$N_{2\infty} = \frac{N_1(0)}{(1 + g_1/g_2)}, \quad (\text{EQ 8})$$

where  $N_1(0)$  is the population in the initial level of the *X* state before the laser pulse is turned on.  $g_1$  and  $g_2$  are the statistical weight of the initial (*X*) and intermediate (*B*) state respectively. For the *X* state  $g_1 = 2J'' + 1$  and for the *B* state  $g_2 = 3(2J' + 1)$ . This results in a normalized saturated population of  $N_{2\infty}/N_1(0) = 3/4$  assuming that  $J''$  is more or less equal to  $J'$  due to the selection rule  $\Delta J = \pm 1$ . Since saturation of the population in the upper intermediate state is difficult to achieve, the laser power used in this study was reduced so that the fluorescent signal behaved linearly with laser power.

It is interesting to note from the value of their statistical weights that both *X* and *B* states have no  $\Lambda$ -type doubling. This is quite understandable for the *X* state which is a singlet state ( $\Lambda = 0$ ,  $S = 0$ ). The *B* state, on another hand is a triplet state ( $\Lambda = 1$ ,  $S = 1$ ) and should in principle be subjected to a  $\Lambda$ -type splitting. This however does not occur because the electronic spin-orbit coupling is strong for a heavy molecule such as  $I_2$  and consequently falls into the category of Hund's case (c)<sup>16</sup> in which case states with  $\Omega = \Lambda + \Sigma = 0$  behave like states with  $\Lambda = 0$ .

### 3.3 Attenuation

As the laser beam travels in the flowfield, it is absorbed by molecules along the beam path. The absorption is more or less severe depending on the transition being excited and the number density in the level being probed. As a result the laser power deposited in the probed volume varies in an undetermined manner and consequently, the population in the probed level cannot be calculated from the fluorescent signal intensity. In this study, attenuation can be significant (up to 60%) in high density regions for strong transitions.<sup>8</sup> This is taken into account in the calculation of  $f(B_{12})$  by using a value for the laser power at the probed volume that has been corrected for attenuation. The laser power at the probed volume can be found by solving

$$\frac{dP}{P} = -n(z, r) \sigma dr, \quad (\text{EQ 9})$$

where  $P$  is the laser power,  $n(z, r)$  the number density as a function of axial ( $z$ ) and radial ( $r$ ) coordinate.  $\sigma$  is the absorption cross section given by

$$\sigma = \frac{B_{12} h g(v)}{\lambda}, \quad (\text{EQ 10})$$

where  $B_{12}$  is the absorption coefficient,  $h$  is Planck's constant,  $g(v)$  is the laser spectral profile assumed to be wide compared to the absorption profile and approximated by  $1/\Delta v = 9 \cdot 10^{-10}$  sec.  $\lambda$  is the wavelength of the transition. The number density distribution in the free jet expansion  $n(z, r)$  is calculated using expressions derived by Ashkenas and Sherman.<sup>17</sup>

The issue of attenuation becomes tricky when the number density field is not well defined. This may be the case for complex flowfields around models of various shapes. In these circumstances, attenuation can be dealt with by either choosing transitions which have equal absorption coefficients, or configure the experiment so that the laser beam path length is reduced in regions of strong absorption.

## 4 Synthetic spectra

Synthetic spectra were generated for the purpose of identifying the transitions that are excited by the laser. The spectral positions of the transitions were calculated using the Dunham expansion coefficients determined by Gerstenkorn and Luc.<sup>18</sup> The relative intensity of a transition was calculated using the following assumptions: a) the gas is in



thermodynamic equilibrium, consequently, the population in a given rovibrational level can be calculated. b) the transition probability of the transitions is mainly controlled by the Franck-Condon factors. Hönl-London factors and electronic transition moments are considered constant. c) Due to the nuclear spin degeneracy of the  $I_2$  molecule, a transition initiated from an odd  $J''$  is 7/5 stronger than a transition involving an initial rovibrational level with an even  $J''$ . d) There are no significant broadening mechanisms, consequently, the emission spectrum is obtained by convolving the intensity at each transition with the laser profile which in this work is assumed of Gaussian form with a FWHM of 0.01 Å.

Fig. 5 gives an example of a synthetic spectrum in the vicinity of 6120 Å compared to an experimental spectrum recorded in a static cell filled with iodine vapor at room temperature. The predicted spectrum was calculated for an equilibrium temperature of 300 K. The agreement between the experimental and predicted spectrum is rather good which not only indicates that the assumptions stated above are adequate, but most importantly allows unambiguous identification of the transitions excited by the laser.

## 5 Experiment

### 5.1 Pilot scale wind tunnel

The pilot scale hypersonic wind tunnel used in this study has been described in previous papers.<sup>4,5</sup> The facility operates with 1 kg of pure iodine and on a semi-continuous basis. It has a run phase which lasts approximately 30 minutes and a recycling phase lasting about 2 hours. For the purpose of this study, a free jet expansion impinging on the flat surface of a ceramic disc is investigated. The orifice diameter is 2 mm and the leading edge of the disc is placed 26 mm downstream of the orifice exit plane. The stagnation temperature tested in this paper is 1000 K and the stagnation pressure 100 Torr, at these conditions the degree of dissociation in the stagnation chamber is about 8%.

### 5.2 TLIF set up

An excimer pumped tunable dye laser of type Lambda Physik FL 3002 E is used as laser source. In order for the laser to excite individual transitions at a time, the tuning block of the laser is fitted with an intra-cavity etalon to

narrow the nominal  $0.2 \text{ cm}^{-1}$  linewidth to  $0.05 \text{ cm}^{-1}$ . The laser beam is fanned into a 1.5 mm thick sheet which illuminates the entire flowfield between the orifice exit plane and the disc's leading edge. Positions along the expansion center axis are probed by successively imaging the probed volume onto a 1.5 mm diameter orifice at the entrance a 0.85 m double spectrometer (SPEX 1404). Consequently, the probed volume is a small cylinder 1.5 mm in diameter and 1.5 mm long. The spectrometer filters the fluorescent signal from photons scattered at the laser frequency and at the overtones other than the one of interest (Usually the first overtone). The spectral band pass of the spectrometer has a width of approximately 20 Å. Photon detection is performed with a thermocooled photomultiplier tube (RCA C31034A02) and a box car integrator (Stanford Research System 250). The time gate during which the fluorescent signal is detected has a width of 100 nsec and is centered about the laser pulse maximum. The fluorescent signal is normalized by laser power. Both fluorescent signal and laser energy are averaged over 30 samples. The experiment is performed at a laser repetition rate of 30 Hz.

## 6 DSMC computations

Application of the direct Monte Carlo Method (DSMC) to the iodine wind tunnel flow is described in detail in a companion paper.<sup>11</sup> A vectorized DSMC code is employed<sup>12</sup> that simulates thermochemical nonequilibrium. In Ref. 11 physical constants are determined for simulation of translational and rotational nonequilibrium of iodine at the conditions investigated experimentally.

In the DSMC technique, the rate of vibrational relaxation is modeled using a probability of exchanging energy between the translational and vibrational energy modes. This is achieved for iodine using a high-temperature form developed for air consisting of the familiar Landau-Teller expression with a collision-limited correction.<sup>13</sup> In the present study, the parameters for the Landau-Teller term are obtained from Millikan and White.<sup>14</sup> In Ref. 14 it is shown that these parameters give good agreement with experiment for iodine at temperatures below 600 K. The high temperature correction term requires a collision-limiting vibrational excitation cross-section to be chosen. In the present work this is set to  $5 \cdot 10^{-21} \text{ m}^2$ . The vibrational mode is simulated as a harmonic oscillator with discrete energy levels using the model of Bergemann and Boyd.<sup>15</sup> Modeling vibrational energy in quantized form allows the

direct calculation of distributions that can be compared with the experimental measurements.

The simulations employ an axisymmetric grid of 230 x 80 cells. This covers the region along the axis beginning at 5 mm from the orifice and extending to 26 mm where the disc is located. In the radial direction, a distance of 50 mm is covered. The disc surface is modeled as diffuse with complete thermal accommodation to a temperature of 400 K. This value is shown in Ref. 11 to give good agreement with the rotational temperature measurements obtained close to the disc for all conditions investigated. Flow conditions input to the DSMC code are derived from analytical theory (see Ref. 11). At steady state, there are 500,000 particles in the flow domain. To obtain solutions with small statistical scatter requires 40 minutes on a Cray C-90.

## 7 Results and discussion

### 7.1 Rotational population distributions and temperatures

Relative rotational populations distributions are represented in Fig. 6 on Boltzmann plots where  $\ln(N_1(J)/(2J+1))$  is plotted against  $J(J+1)$ , the population in rotational level  $J$  being  $N_1(J)$ . The stagnation pressure and temperature of the corresponding test flow are 100 Torr and 1000 K respectively. The populations are displayed for absolute axial positions of 5, 10, 20 and 24 mm referenced from the orifice exit plane. The indicated error bars are based on variations in fluorescent signal intensities due to laser linewidth fluctuations. The plots indicate that within experimental errors the rotational energy levels are in equilibrium. A rotational temperature  $T_{rot}$  may be calculated from the slope  $S$  of the linear best fits to the data and the expression  $T_{rot} = \theta_r/S$ , where  $\theta_r$  is the characteristic rotational temperature of iodine taken as 0.05375 K. The resulting rotational temperatures at various positions along the free jet center axis are plotted in Fig. 7 along with DSMC predictions and isentropic expansion predictions<sup>17</sup> calculated for two cases of specific heat ratio  $\gamma$  of 9/7 and 7/5. The measured rotational temperature agrees well with the isentropic curve for  $\gamma = 9/7$  which indicates that the molecules in the flow are both rotationally and vibrationally activated. It may also be noticed that the DSMC, isentropic expansion curve for  $\gamma = 9/7$  and experiment agree in the expanding region. In the compression region of the

flowfield however, the DSMC prediction is in poor agreement with the experimental data. The rise in temperature computed with the DSMC technique is fairly rapid and reaches a maximum value that overshoots the measurements even when the spatial resolution of the probing technique is taken into account. This would indicate that the probability of rotational energy exchange assumed in the DSMC calculations should be smaller. Clearly, in the high temperature region of the flowfield, the relaxation of the rotational mode of the iodine molecule cannot be modelled with a single rate. Consequently, the development of a more detailed rotational relaxation model seems appropriate to describe rotational energy transfers for diatomic molecules at higher temperatures. A more complete discussion dealing with this issue may be found in a companion paper.<sup>11</sup>

### 7.2 Vibrational population distributions and temperatures

Boltzmann plots of the relative vibrational population distributions at various axial positions are shown in Fig. 8. Also represented in these figures are the corresponding DSMC computations. The figures indicate that at least for low vibrational quantum numbers, the energy levels are in equilibrium. Indeed, independent calculations performed for hypersonic iodine flows expanding in conical nozzles indicate that the vibrational population distributions become non-Maxwellian for vibrational quantum levels greater than about 10.<sup>22</sup> This provides a strong incentive for probing higher vibrational quantum levels. The population measurement in these levels is possible because strong transitions from these levels exist and can be used to compensate for the expected drop of population for increasing  $V''$ . Such probing of higher vibrational levels has been shown to required laser excitation in the red and infrared part of the spectrum.<sup>8</sup>

In Fig. 8 the measured vibrational distributions agree with the DSMC predictions for axial positions  $z = 5, 15$  and 24 mm, while at  $z = 10$  and 20 mm significant disagreement may be observed. In addition, the measurements show significant scatter in comparison to the rotational population measurements. This is certainly due to systematic errors in the probing technique caused by uncertainties in either transitions probabilities (assumption of a constant electronic transition moment), or dissociative and predissociative effects (as mentioned in Section 3.1, the decay rate of the excited state may be enhanced when the laser is reso-

nant with a crossing point between the  $B$  state and another dissociative state). Improving the probing technique is possible by either measuring the decay rate of individual excited states or calculating it from first principles. The rotational population measurements appear to be more reliable than the vibrational data because transitions used in the former belonged to the same vibrational band and consequently could be excited within a small wavelength interval. The vibrational population distributions, on the other hand, are based on transitions from different vibrational bands which require laser pumping from a broader spectrum. For example, in Fig. 8 the population in  $V'' = 0$  and 1 is measured in the 5208 Å range and the populations in  $V'' = 1, 2, 3, 4$  require laser excitation in the 6120 Å range. To obtain the total distributions shown in the figure, the populations were matched at  $V'' = 1$ . It is believed that the assumption of constant electronic transition moment may be inadequate if transitions that are spectrally too far apart are used in the measurement. A possible solution to this problem is to include the electronic transition moment dependence on the  $R$ -centroid in the calculations on transition probabilities (Ref. Section 3.1).

Vibrational temperatures determined in the same manner as the rotational temperatures with a characteristic vibrational temperature  $\theta_v = 308$  K are plotted versus various positions along the free jet center axis. These are shown in Fig. 9. The temperatures display fairly significant scatter bars due to the inherent uncertainty involved in the measurement of vibrational populations. In spite of their scatter, the vibrational temperature appears to relax more slowly than the rotational temperature. Coincidentally, the DSMC predictions indicate that the flow is essentially frozen however, since the computational domain starts at an axial position of 5 mm and the calculated temperature at this location is immediately frozen, it is possible that a computation with a more extensive grid system would predict freezing at a different vibrational temperature. Consequently, DSMC calculations with a computational domain extending as close as possible to the orifice exit plane need to be performed in future investigations. Since the number density close to the throat may be of the order of  $10^{18} \text{ cm}^{-3}$ , such simulations may be well suited for parallel computations.

## 8 Conclusions

The TLIF technique has been used to successfully measure both rotational and vibrational population distributions in

a nonequilibrium hypersonic flow of iodine vapor generated in a pilot scale wind tunnel. The developed diagnostic technique has the advantages of producing strong fluorescent signals and is insensitive to quenching. Rotational population measurements are satisfactory while the vibrational population distributions display significant scatter. The scatter appears to be due to uncertainties in the computed transition probabilities. The latter should, in future studies, include the dependence of electronic transition moment on internuclear distance, and a more precise quantification of the effects of dissociation and predissociation. Vibrational population distributions have been measured for the first five vibrational levels of the  $X$  state. The probing of higher vibrational levels appears feasible and requires laser excitation at wavelength in the red and infrared.

Rotational temperatures predicted with the DSMC technique agree fairly well with the measurements in the expansion region of the flowfield. In the compression region the agreement is poor, which indicates that more refined experiments are needed and that detailed models of rotational energy relaxation have to be included in the prediction scheme. The DSMC prediction of vibrational temperatures indicates that simulations with a larger computational domain need to be performed in order to confirm the apparent freezing trend seen in the measurements.

The work described here proves concepts for generating and probing nonequilibrium chemically reacting hypersonic flows of iodine vapor. Several improvements of the technique are feasible. Although the measurements performed in this study are preliminary, they indicate that more detailed models for internal energy exchanges are needed for accurate predictions of nonequilibrium flow properties of diatomic gases. More accurate and refined measurements are needed to improve the probing technique and confirm the need for new models.

## 9 Acknowledgments

This work was supported by URI grant # AFOSR-90-0170.

## 10 References

- 1 Kunc, J. A., Muntz, E. P., and Weaver, D. P., "Model Gases for the Detailed Study of Microscopic Chemical Nonequilibrium in Diatomic Gas Flows," AIAA 90-1662.
- 2 Muntz, E. P., Pham-Van-Diep, G. C., Bradley, M. K., Erwin, D. A., and Kunc, J. A., "A code Validation Strategy and Facility for Nonequilibrium, Reacting Flow," AIAA 92-3970.
- 3 Sharma, S. P., and Ruffin, S. M., "Nonequilibrium Vibrational Population Measurements in an Expanding Flow Using Spontaneous Raman Spectroscopy," AIAA-92-2855.
- 4 Pham-Van-Diep, G. C., Muntz, E. P., Weaver, D. P., Dewitt, T. G., Bradley, M. K., Erwin, D. A. and Kunc, J. A., "An iodine Hypersonic Wind Tunnel for the Study of Nonequilibrium Reacting Flows," AIAA 92-0566.
- 5 Pham-Van-Diep, G. C., Muntz, E. P., Erwin, D. A., and Kunc, J. A., "Measurement of Rotational Temperature in a Free Jet Flow of Chemically Reacting Iodine Vapor," 18<sup>th</sup> International Symposium on Rarefied gas Dynamics, Vancouver, July 1992.
- 6 Brewer, L., and Tellinghuisen, J., "Quantum Yield for unimolecular dissociation of  $I_2$  in the visible absorption," J. Chem. Phys., 56, 8, 1972, pp. 3929-38.
- 7 Mulliken, R., "Iodine revisited," J. Chem. Phys., 55, 1, 1970, pp. 288-309.
- 8 Pham-Van-Diep, G. C., "Chemically Reacting, Hypersonic Flows of Iodine Vapor for the Study of Nonequilibrium Phenomena in Diatomic Gases," Ph. D. Thesis, University of Southern California, August 1993.
- 9 Steinfeld, J. I., "Wavelength Dependence of the Quenching of Iodine Fluorescence," J. Chem. Phys., 44, 7, 1965, pp. 2740-49.
- 10 Capelle, G. E., and Broida, H.P., "Lifetimes and Quenching Cross Section of  $I_2$ ," J. Chem. Phys., 58, 1972, pp. 4212-22.
- 11 Boyd, I. D., Pham-Van-Diep, G. C., and Muntz, E. P., "Monte Carlo Computation of Nonequilibrium Flow in a Hypersonic Iodine Wind Tunnel," AIAA 93-2871.
- 12 Boyd, I. D., and Gökçen, T., "Computation of Axisymmetric Ionized Flows Using Particle and Continuum Methods," AIAA-93-0729.
- 13 Boyd, I. D., "Analysis of Vibrational-Dissociation-Recombination Process Behind Strong Shock Waves of Nitrogen," Phys. Fluids A, 4, 1992, pp. 178-85.
- 14 Millikan, R. C., and White, D. R., "Systematics of Vibrational Relaxation," J. Chem. Phys., 39, 12, 1963. pp. 3209-13.
- 15 Bergemann, F., and Boyd, I. D., "New Model for Discrete Vibrational Energy in the Direct Simulation Monte Carlo Method," 18<sup>th</sup> International Symposium on Rarefied gas Dynamics, Vancouver, July 1992.
- 16 Hertzberg, G., "Molecular Spectra and Molecular Structure. I. Spectra of Diatomic Molecules," Robert E. Kreger Publishing Co. Malabar, Florida, 1989.
- 17 Ashkenas, H., and Sherman, F. S., "Structure and Utilization of Supersonic Free Jets in Low Density Wind Tunnels," 4<sup>th</sup> International Symposium on Rarefied gas Dynamics, J. H. de Leeuw ed. Vol. 2. Academic Press, Toronto, 1966.
- 18 Gerstenkorn, S., and Luc, P., "Description of the Absorption Spectrum of Iodine Recorded by Means of Fourier Transform Spectrometry: the (B-X) System," J. Physique, 46, 1985, pp. 867-81.
- 19 Martin, F., Bacis, R., Churassy, S., and Vergès, J., "Laser Induced Fluorescence Fourier Transform Spectrometry of the X State of  $I_2$  Extensive Analysis of the B-X Fluorescence Spectrum of  $I_2$ ," J. Mol. Spec., 116, 1986, pp. 71-100.
- 20 Chutjian, A., Link, J. K., and Brewer, L., "Measurement of Lifetimes and Quenching Cross Sections of the B State of  $I_2$ ," J. Chem. Phys., 46, 7, 1966, pp. 2666-75.
- 21 Sakurai, K., Capelle, G., and Broida, H. P., "Measurement of Lifetimes and Quenching Cross Sections of the B State of Iodine using a Tunable Dye Laser," J. Chem. Phys., 54, 3, 1976, pp. 1220-23.
- 22 Bradley, M. K. Private communications.

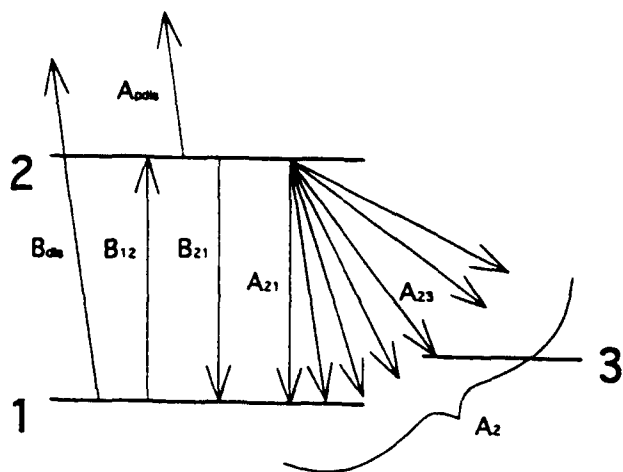


FIGURE 1: Two level energy diagram used to model TLIF process.

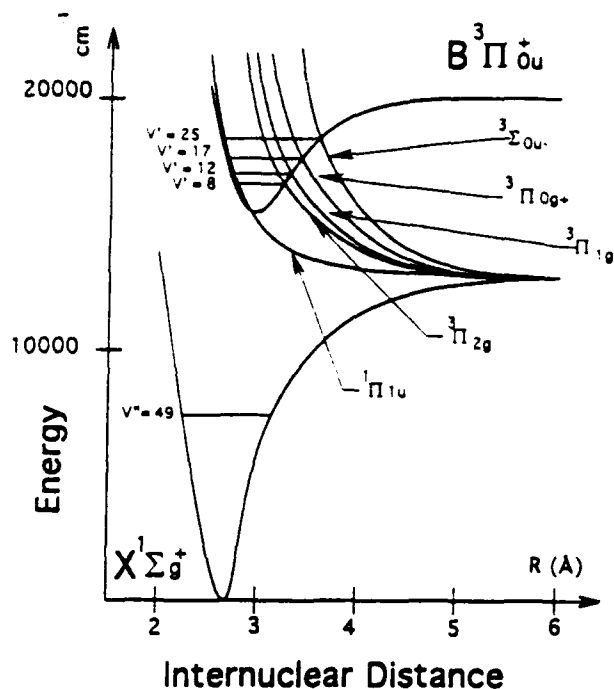


FIGURE 2: Intermolecular potentials of the iodine molecule relevant to the analysis of the TLIF technique.

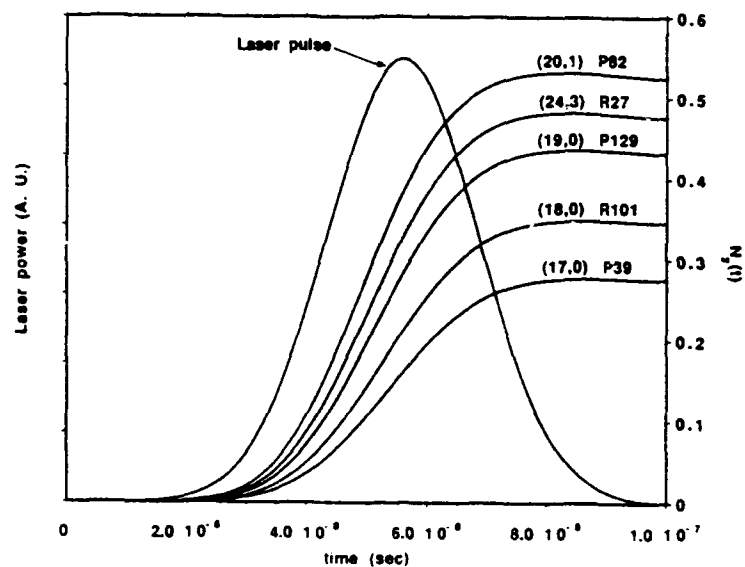


FIGURE 3: Upper state response to pulsed laser excitation for a variety of transitions. Also shown is the laser pulse shape assumed in the calculation of  $N_2(t)$ .

FIGURE 4: Upper state response to pulsed laser excitation for three cases of laser pulse energy  $E_p$ .

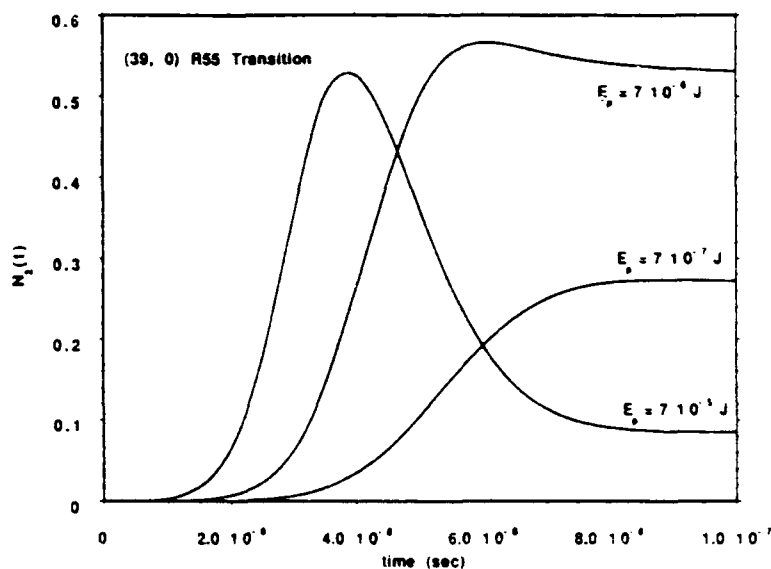
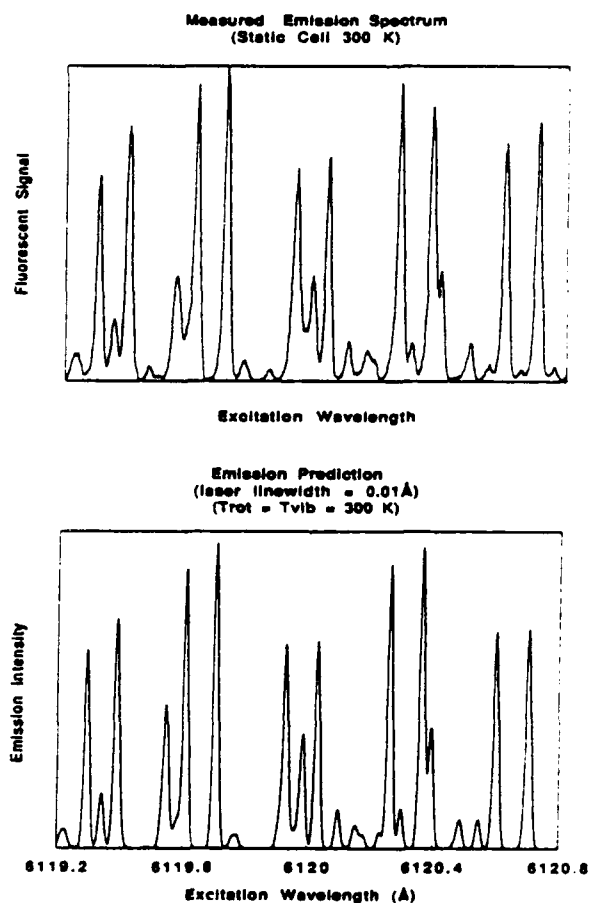
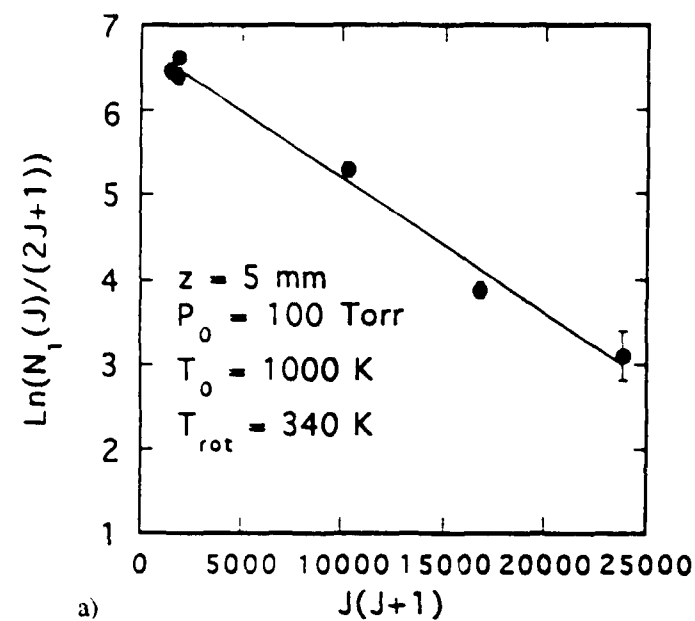
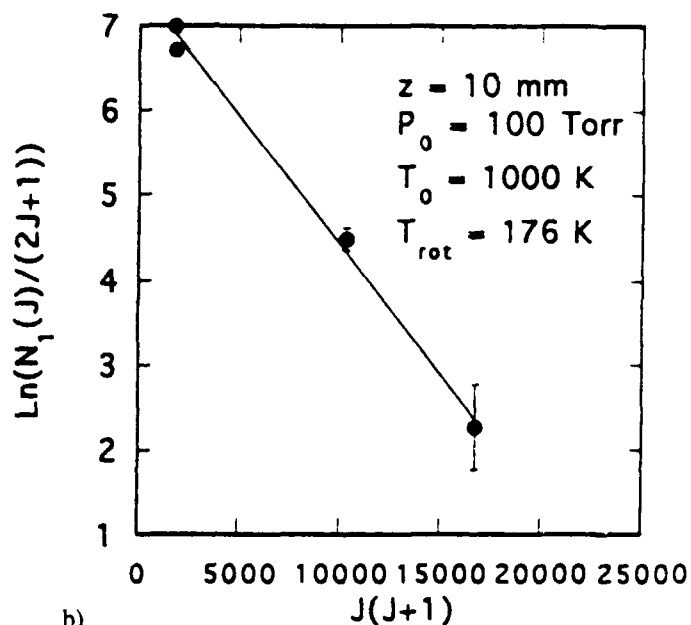


FIGURE 5: Experimental and synthetic spectra compared for the purpose of identification of transitions excited by the laser. The experiment is performed in a static cell of iodine maintained at room temperature. The synthetic spectrum is calculated to an equilibrium temperature of 300 K.

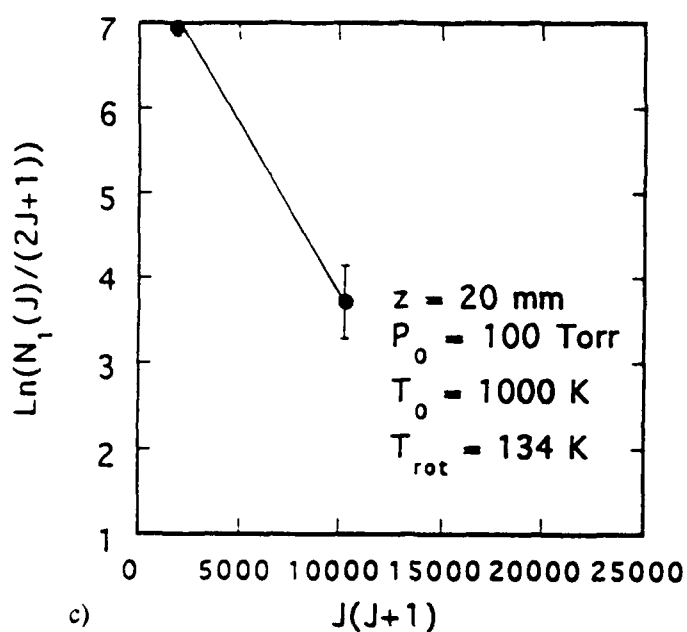




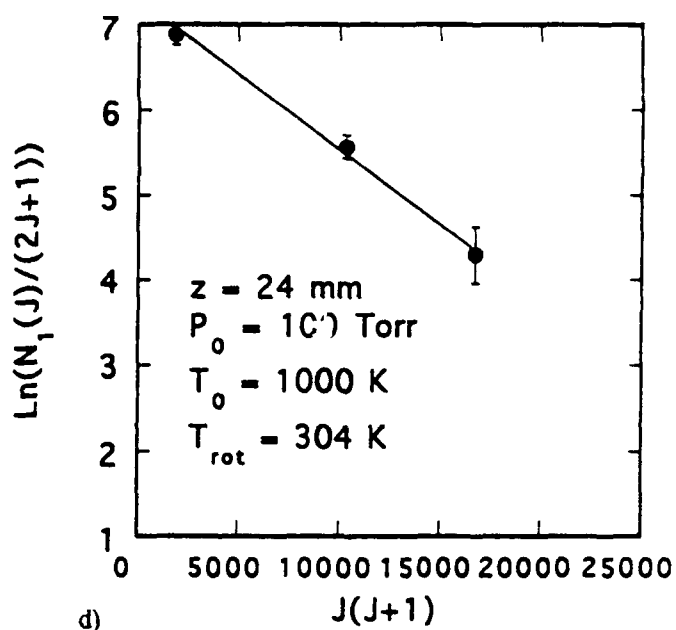
a)



b)



c)



d)

FIGURE 6: Boltzmann plots of rotational populations for  $z$  (axial distance on the free jet center axis) = a) 5, b) 10, c) 20, d) 24 mm.

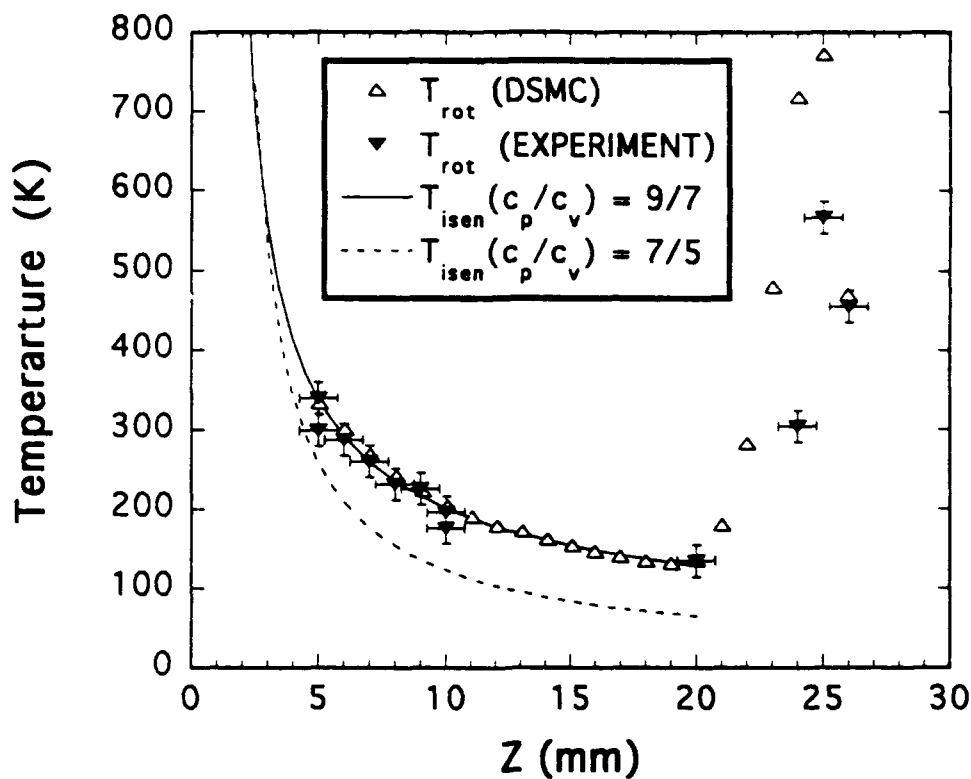


FIGURE 7: Rotational temperature along the free jet centerline for a stagnation temperature of 1000 K and a stagnation pressure 100 Torr.

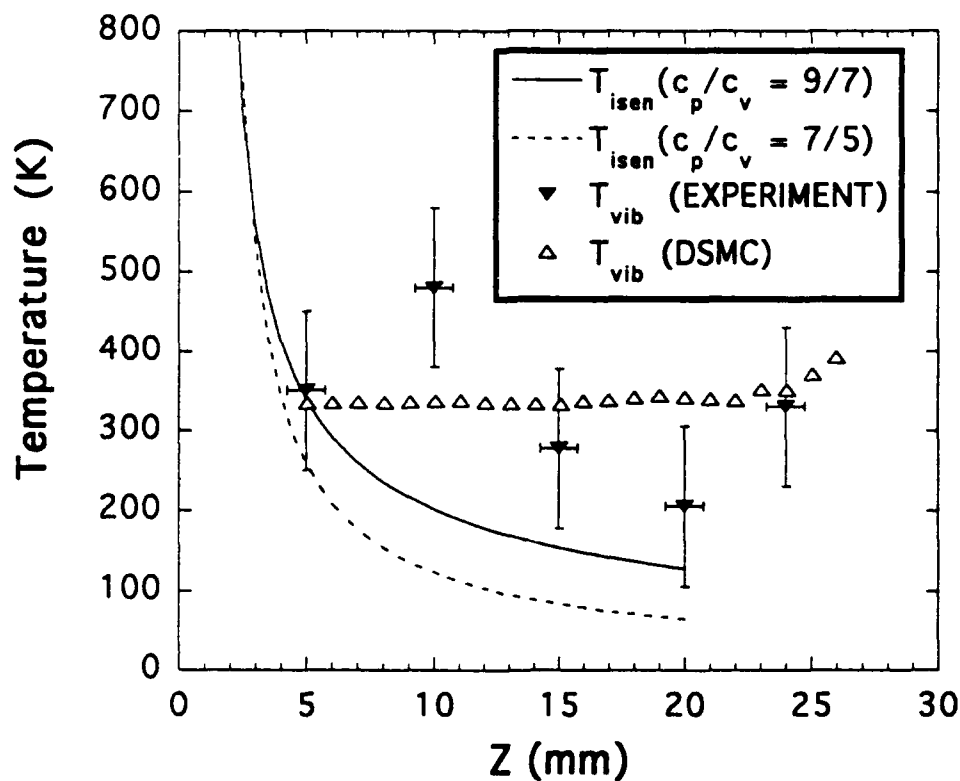


FIGURE 9: Vibrational temperature along the free jet centerline for a stagnation temperature of 1000 K and a stagnation pressure of 100 Torr.



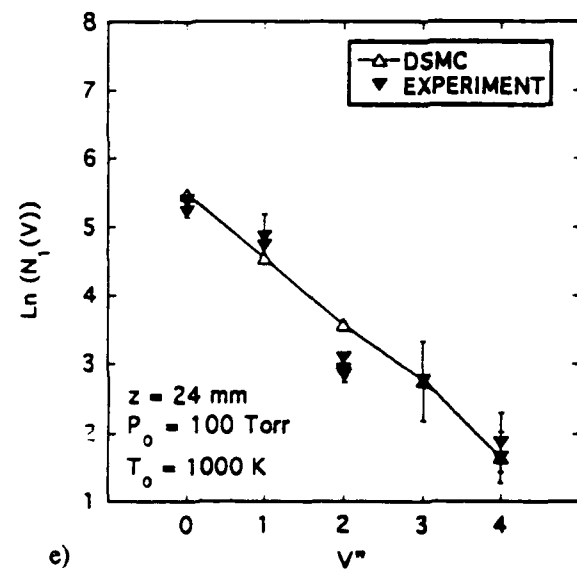
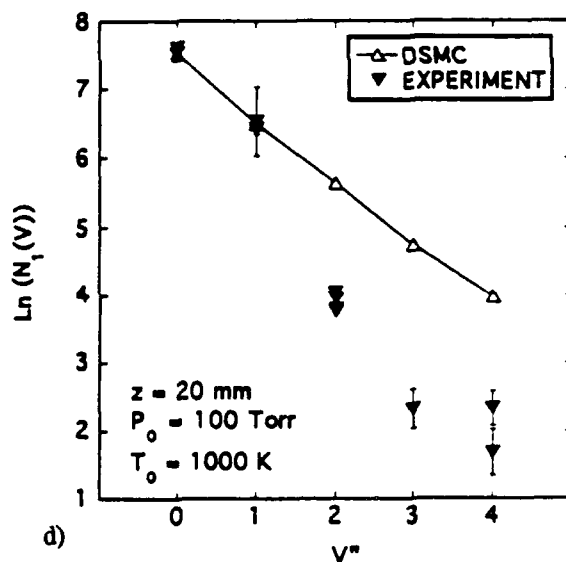
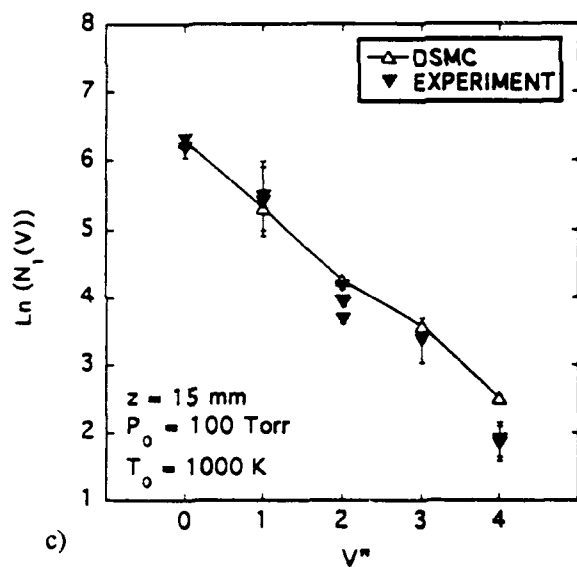
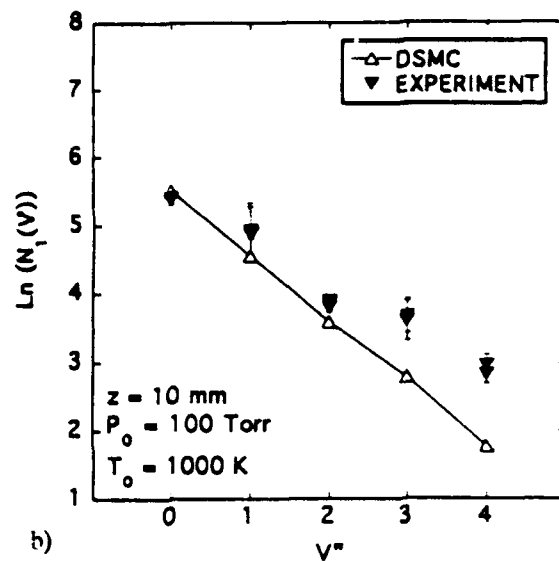
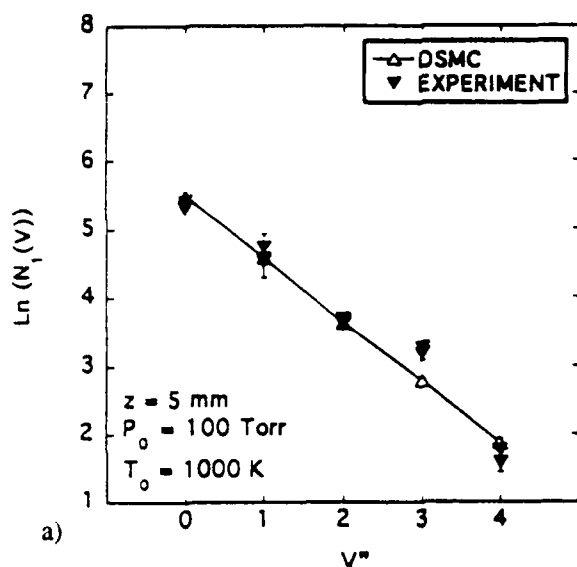


FIGURE 8: Boltzmann plots of vibrational populations for  $z$  (axial distance on the free jet center axis) = a) 5, b) 10, c) 15, d) 20, e) 24 mm.

**ATTACHMENT 9**



**AIAA-93-2871**

**Monte Carlo Computation of  
Nonequilibrium Flow in a  
Hypersonic Iodine Wind Tunnel**

**I. D. Boyd**

**Cornell University**

**Ithaca, NY 14853.**

**G. C. Pham-Van-Diep and E. P. Muntz**

**University of Southern California**

**Los Angeles, CA 90089.**

**AIAA 28th Thermophysics Conference**  
**July 6-9, 1993 / Orlando, FL**

# MONTE CARLO COMPUTATION OF NONEQUILIBRIUM FLOW IN A HYPERSONIC IODINE WIND TUNNEL

Iain D. Boyd\*

Cornell University, Ithaca, NY 14853.

Gerald C. Pham-Van-Diep† and E. Phil Muntz‡

University of Southern California, Los Angeles, CA 90089.

## **Abstract**

The nonequilibrium flow formed by the interaction of a free-jet of iodine vapor impinging on a blunt body is investigated using numerical and experimental techniques. The computational approach employs the direct simulation Monte Carlo method. The experimental measurements consist of rotational temperature obtained along the flow axis and include portions of both the free-jet expansion and blunt-body shock for four different stagnation conditions. Direct comparison of the numerical results and the experimental data are quite successful at moderate temperatures. Hence, the rotational collision time of iodine is estimated in the temperature range of 100-500 K. At higher temperatures, the agreement between simulation and measurement is less satisfactory. This demonstrates the requirement for the development of a more detailed approach to simulating rotational nonequilibrium in high-temperature flows of diatomic species.

## **Introduction**

Aerospace vehicles traveling at hypersonic speed and at high altitude produce flow fields that are in thermochemical nonequilibrium. Many years of both experimental and numerical research have been spent in the study of these flows. Detailed experimental study of hypersonic flows of air requires the latest optical diagnostic techniques. However, even when these are available, it is difficult to reproduce in ground-based facilities the high-enthalpy flow conditions experienced in flight. In the literature, there are very few experimental studies indeed that have provided much insight into the coupled physical relaxation phenomena characteristic of low-density hypersonic flow. This lack of data has severely restricted the development of more sophisticated numerical techniques and

models for computing such flow fields. Therefore there exists a very real and urgent requirement for detailed experimental investigation, and accompanying numerical analysis, of hypersonic flows in thermochemical nonequilibrium.

It has been proposed<sup>1</sup> that iodine represents a convenient model gas for investigation of hypersonic nonequilibrium flow phenomena. This is mainly due to the lower characteristic temperatures for vibration and dissociation of iodine in comparison with the diatomic constituents of air. A significant degree of thermochemical nonequilibrium is therefore observed at relatively low enthalpies. This feature of iodine presents promising possibilities for detailed experimental investigation in ground-based facilities using modern optical diagnostics techniques. A pilot scale hypersonic wind tunnel that operates on pure iodine vapor has been designed and tested at the University of Southern California<sup>2</sup>. A preliminary set of rotational temperature measurements for a free-jet of iodine impinging on a blunt body were reported in Ref. 2. This flow represents an interesting configuration as the gas first expands from the orifice, and is then compressed by the blunt body. Therefore, any numerical approach must successfully simulate each of these important flow phenomena.

A powerful numerical technique for computing low-density nonequilibrium flows is the direct simulation Monte Carlo method (DSMC). This method offers unique opportunities for simulating in great detail the thermochemical nonequilibrium that occurs in the flows of interest. In previous studies, successful comparisons between DSMC and experimentally measured distributions for velocity<sup>3</sup> and rotational energy<sup>4</sup> have been made. The main purpose of the present paper is to make comparison of numerical results obtained using the DSMC technique and new experimental data

---

\* Assistant Professor. School of Mechanical and Aerospace Engineering.

† Graduate Assistant. Aerospace Engineering.

‡ Professor. Aerospace Engineering

large, and the orifice diameter sufficiently small, to ensure continuum flow. However, the density decays rapidly as the gas expands away from the orifice. The Knudsen number associated with the shock wave formed at the blunt body is therefore relatively large. Due to this low-density nature of the expanding iodine flow, the DSMC technique is an appropriate numerical approach. The DSMC computations begin at a distance of 5 mm from the orifice exit. The computational domain extends to 26 mm along the axis and to 50 mm radially. The disc is 36.25 mm high in the axisymmetric grid. It is assumed that the surface of the disc is diffusely reflecting with full accommodation to the wall temperature. The disc is made of a ceramic material that will be heated by the compressed gas to an unknown extent. A wall temperature of 400 K is used in all simulations. Except for the inlet plane and the surface of the disc, all other boundaries are treated as expansion into a vacuum.

The flow conditions input to the DSMC code at the upstream boundary are calculated using the theory of Ashkenas and Sherman.<sup>9</sup> In Ref. 9, the Mach number,  $M$ , at a distance  $x$  along the axis of a free-jet formed from an orifice of diameter  $D$  is given by:

$$M = A \left( \frac{x - x_o}{D} \right)^{\gamma-1} - \frac{1}{2} \left( \frac{\gamma+1}{\gamma-1} \right) / A \left( \frac{x - x_o}{D} \right)^{\gamma-1} \quad (3)$$

The constants  $A$  and  $x_o$  are determined in Ref. 9 for values of the ratio of specific heats  $\gamma=5/3$ ,  $7/5$ , and  $9/7$ . These values of  $\gamma$  correspond to full equilibration of the translational, rotational, and vibrational modes of a diatomic molecule respectively. Using the Mach number defined by Eq. (3), together with the isentropic relationships and the stagnation conditions, all fluid properties are obtained as a function of distance along the jet axis. At a fixed distance from the orifice exit, the distribution of density at an angle  $\theta$  to the axis is described in Ref. 9 by the relation:

$$\frac{\rho(\theta)}{\rho(0)} = \cos^2 \frac{\pi\theta}{2\phi} \quad (4)$$

where  $\phi$  is a constant again evaluated at the 3 different values for  $\gamma$ . Using the density defined by Eq. (4), and the isentropic relationships, the angular dependence of all properties is evaluated. In this manner, Eqs. (3) and (4) are employed to derive the flow properties at the upstream boundary of the DSMC calculation. For each of the conditions investigated, the value of  $\gamma$  is varied until the temperature on the axis is equal to the

experimental measurement of rotational temperature at a distance of 5 mm from the orifice. In general, the values of  $\gamma$  employed in this way are equal to or just greater than  $9/7$ . Thus, in all cases, the gas is close to full vibrational equilibrium at the DSMC inlet plane. Linear interpolation is used to estimate the values of  $A$ ,  $x_o$ , and  $\phi$  required in the above equations for the values of  $\gamma$  lying between  $9/7$  and  $7/5$ . Of course, this approach to defining the input flow conditions is approximate. The values of  $\gamma$  employed in each of the 4 cases considered are listed in Table 1.

In the present study, a vectorized DSMC code<sup>10</sup> is employed. This code models 2-d axisymmetric flow, and includes the effects of translational, rotational, vibrational, and chemical nonequilibrium. For translational nonequilibrium, detailed calculations for the collision cross-sections of iodine reported by Kang and Kunc<sup>11</sup> are employed to obtain appropriate parameters in the Variable Hard Sphere (VHS) collision model.<sup>12</sup> Using this approach, it is found that the reference collision diameter is  $8.8 \times 10^{-10}$  m, the viscosity temperature exponent is  $\omega=0.945$ , at a reference temperature of 273 K. Comparison of the variation of viscosity with temperature obtained with these parameters in the VHS model, and the detailed calculations of Ref. 11, are shown in Fig. 2. Experimental data points are also included and indicate that the theoretical models are quite accurate. The VHS parameters reveal that iodine has a very large collision diameter, and a very soft potential that is close to the ideal Maxwellian molecule.

Rotational nonequilibrium is simulated in the DSMC code using the probability of Boyd<sup>13</sup> that depends on the total energy of each collision,  $\epsilon_c$ , in the following way:

$$\phi_r Z_\infty = 1 + \frac{\Gamma(\zeta + 2 - \omega)}{\Gamma(\zeta + \frac{3}{2} - \omega)} \left( \frac{kT^*}{\epsilon_c} \right)^{\frac{1}{2}} \frac{\pi^{\frac{1}{2}}}{2} + \frac{\Gamma(\zeta + 2 - \omega)}{\Gamma(\zeta + 1 - \omega)} \left( \frac{kT^*}{\epsilon_c} \right) \left( \frac{\pi^2}{4} + 2 \right) \quad (5)$$

where  $T^*$  is a temperature characteristic of the potential of the molecule,  $Z_\infty$  is the maximum collision number, and  $\zeta$  is the average number of degrees of freedom participating in a collision. For iodine,  $T^*$  is given in Ref. 14 as 557 K. A search in the literature revealed no previous studies of the rotational relaxation rate of iodine. In the present study,  $Z_\infty$  is therefore treated as a free parameter to be determined by comparison of the simulation results with the experimental measurements of rotational temperature.

for rotational temperature. For application to the iodine wind-tunnel, it is necessary to develop the appropriate relaxation constants to be used in the DSMC models. By successful comparison with the experimental data, a rotational relaxation time for iodine at low temperatures is estimated. General flow field properties computed with the DSMC technique are also discussed.

### Experimental Facility

The pilot facility operates at a range of stagnation chamber conditions. Two different pressures (30 and 100 Torr) and two different temperatures (773 and 1000 K) are considered. Under these conditions the degree of dissociation of iodine is less than 5%. The 4 different cases examined in this study are listed in Table 1. The iodine vapor is expanded through an orifice of diameter 2 mm into a vacuum chamber at a background pressure maintained at  $10^{-4}$  Torr. At a distance of 26 mm from the orifice a 7.25 cm diameter disc is located.

### Diagnostic Technique

The relative population of  $I_2$  molecules in a given rovibrational state is measured using Transient Laser Induced Fluorescence (TLIF). The technique has the advantage of generating strong and easily detectable signals. Moreover, because the excitation is achieved by means of a 30 nsec laser pulse, the signal is insensitive to quenching provided the fluorescence is detected during a small enough time gate (=100 nsec) centered about the maximum of the fluorescence pulse. A detailed description of the TLIF technique used in this study is the subject of a companion paper.<sup>5</sup>

To probe individual rovibrational levels of the molecules composing the flow field, a narrow band tunable dye laser excites the  $I_2$  molecules from a rovibrational level ( $V''$ ,  $J''$ ) of the ground electronic state  $X(^1\Sigma_g)$  to a rovibrational level ( $V'$ ,  $J'$ ) of the  $B(^3\Pi_0)$  state. For individual transitions to be excited, the laser line width has to be of the order of  $0.5\text{ cm}^{-1}$ . This requires installation of an air-spaced intracavity etalon in the laser tuning block. Emission spectra are obtained by scanning the laser wavelength, i.e. successively exciting levels of the  $X$  state to levels of the  $B$  state. The fluorescence signal is observed through a fixed wide spectral window ( $\approx 20\text{ \AA}$ ) of a spectrometer whose main purpose is to filter scattered photons at the laser frequency and at the overtones other than the one detected by the spectrometer. The intensity of the fluorescence signal  $I_{flu}$  is a measure of the population

in level ( $V''$ ,  $J''$ ) provided the transition strengths for both the absorption ( $B_{12}$ ) and emission ( $A_{23}$ ) phases are known. The indices 1, 2 and 3 correspond to the initial lower state, intermediate upper state, and final lower state respectively. In this study,  $B_{12}$  and  $A_{23}$  are calculated from radiative decay rates measured by Capelle and Broida.<sup>6</sup> A detailed description of how both absorption and emission transition strength are computed can be found in the companion paper.<sup>1</sup> The fluorescence signal  $I_{flu}$  is normalized by laser energy and the relative population  $N(V''$ ,  $J''$ ) is then calculated using:

$$N(V''$$
,  $J''$ )  $\propto \frac{I_{flu}}{B_{12}A_{23}SP(J'')}$ , (1)

where  $SP(J'')$  is a factor that accounts for the nuclear spin of the molecule. It takes a value of 7 if  $J''$  is odd and 5 if  $J''$  is even. The transitions chosen for rotational population measurement are: (19,0) P129, (20,0) P154, (17,0) R42, (17,0) R38, (17,0) R43, (18,0) R101, (17,0) P39. They require laser excitation at approximately  $5683\text{ \AA}$  and have been identified previously by means of Fourier spectrometry.<sup>7</sup> Although the selected transitions absorb frequencies in the vicinity of  $Kr^+$  laser lines, chosen transitions are not limited to those corresponding to common lasers. Indeed, Dunham expansion coefficients have been determined for a large number of rovibrational levels for both the  $X$  and  $B$  states.<sup>8</sup> Consequently, transitions can be chosen judiciously to cover a large number of rotational quantum numbers while requiring small spectral laser scans.<sup>5</sup>

The relative populations in a selected number of rotational levels are analyzed on a Boltzmann plot where  $N_1(V''$ ,  $J'')/(2J''+1)$  is plotted versus  $J''(J''+1)$ . An example of this is shown in Fig. 1 for the particular case of a stagnation pressure of 100 Torr, a stagnation temperature of 773 K, and an axial position in the free-jet of 5 mm from the orifice. It is found that the data is easily fitted linearly within experimental errors. Under the assumption that the rotational energy is in equilibrium, a rotational temperature  $T_{rot}$  is determined based on the slope  $S$  of the best linear fit and the characteristic rotational temperature  $\theta_r=0.053\text{ K}$  using the expression:

$$T_{rot} = \theta_r/S. \quad (2)$$

### Numerical Investigation

Near the exit of the orifice, the density is sufficiently

The expression in Eq. (5) is obtained from a temperature-dependent form proposed by Parker.<sup>15,16</sup> For application to iodine, due to the relatively large value of  $T^*$ , it is considered appropriate to include an extra term in Parker's model and thus obtain the following DSMC probability:

$$\phi_r Z_\infty = \text{Eq. (5)} + \frac{\Gamma(\zeta + 2 - \omega)}{\Gamma(\zeta + \frac{1}{2} - \omega)} \left( \frac{\pi k T^*}{\epsilon_c} \right)^{\frac{1}{2}} \quad (6)$$

In Eq. (6), it is necessary to employ a larger value of  $Z_\infty$  to be consistent with Eq. (5) at low temperatures.

Analysis of vibrational relaxation in iodine is also included in the DSMC calculation. This subject is discussed in detail in a separate study.<sup>5</sup> Dissociation rates for iodine are also implemented in the current study and are obtained from Davidson.<sup>17</sup> It is found under the flow conditions investigated, however, that almost no chemical reactions occur.

### Results and Discussion

The DSMC simulations reported in this section employ a computational grid that consists of 230 cells axially and 80 cells radially. The topology is nonuniform and accounts for local variations in the mean free path. Typical simulations employ 500,000 particles. Execution times on a Cray C-90 are of the order of 40 minutes.

To gain an idea of the flow fields involved in these studies, the high pressure and high temperature conditions of Case 1 are first considered. One reason for emphasizing this case is the fact that the continuum Ashkenas-Sherman theory is most valid for these conditions. Thus, the data along the DSMC inlet plane located at 5 mm from the orifice should be most accurate. It is also worth noting that the value of  $\gamma$  is 9/7 under these conditions. The variation in density along the jet centerline for this case is shown in Fig. 3 and compared with the theory of Ref. 9. It is found that the DSMC solution initially follows the Ashkenas-Sherman theory, then undergoes slightly faster expansion, before the effect of the blunt-body starts to form a thick, diffuse shock. Similar trends are observed for the variation in temperature along the axis. The comparison between the theory and the translational temperature computed using DSMC is shown in Fig. 4. Note the very high temperature attained by the gas in the shock. More detailed quantitative comparisons between DSMC and experiment are provided later in this section. Contours of the ratio of local to free stream density for the entire flow field are shown in Fig. 5.

The non-uniform upstream profile is clearly seen. The shock structure formed in front of the body is rather interesting. The decrease in density away from the axis causes a perceptible thickening of the shock in the radial direction. This behavior is also observed in fluorescence images generated in the experimental facility. Translational temperature contours for Case 1 are shown in Fig. 6. These again show the gradual decay due to expansion, followed by a sharp increase due to the compression of the gas at the blunt body. The expansion fan that forms immediately above the vertical plane representing the blunt body is also evident in this figure.

Detailed consideration is next given to the comparison of the DSMC results with the experimental measurements of rotational temperature along the axis. In Fig. 7 the results for case 1 (see Table 1) are shown. The two different DSMC results correspond to the use of Eqs. (5) and (6) for simulating the rate of rotational relaxation. For each of the simulations, there is very good agreement obtained in the expansion region of the flow field. These results are computed using values for  $Z_\infty$  of 75 in Eq. (5) and 150 in Eq. (6). Note that a value of  $Z_\infty=50$  is obtained using the theory of Parker.<sup>15</sup> A comparison of the rotational collision numbers obtained using Eqs. (5) and (6) using these values is shown in Fig. 8 as a function of temperature. Note that, at higher temperatures, Eq. (6) gives higher collision numbers while the two models give similar values at lower temperatures.

The computed rotational temperatures are in rather poor agreement with the experimental data in the compression region of the flow field. With either relaxation model, the rise in rotational temperature computed using DSMC is much too rapid. This indicates that the probability of rotational energy exchange should be smaller at higher temperatures. A small improvement is obtained by including the extra term in Eq. (6). Clearly, further terms of this type may improve the simulation results further. However, such analysis is purely speculative. The original theory of Parker does not permit the inclusion of further terms, so they could only be added in an artificial manner. A more satisfactory solution to the problem lies in the development of more detailed rotational relaxation models that account for high temperature effects. Almost certainly, at these higher temperatures, the relaxation of the rotational mode of a diatomic molecule cannot be described by a single rate. The observation that the rotational relaxation rate is slower at high temper-

atures than the Parker model predicts has also been made recently for nitrogen.<sup>18</sup> The fact that a similar conclusion is drawn here for iodine gives strong evidence that high temperature nonequilibrium behavior in air may be analyzed qualitatively through study of alternative molecular species such as iodine.

Comparisons of the rotational temperatures obtained along the axis by simulation and measurement are made in Figs. 9-11 respectively for the other 3 Cases. The effect of the reduced stagnation pressure in Fig. 9 is to increase the shock thickness and standoff distance considerably. Simultaneously, because of the lower densities, there is significantly less rotational relaxation, leading to a higher minimum rotational temperature. The effects of Cases 3 and 4 are mainly just direct scaling of the temperature from 1000 to 773 K; however, there are also smaller differences caused by the temperature dependence of the rotational relaxation model employed. All of the simulations employed Eq. (6) as the rotational relaxation model. The same conclusions that are drawn from Fig. 7 are again applicable to the results in Figs. 9-11. Specifically, for moderate temperatures, the rotational relaxation rate is quite accurately simulated using Eq. (6). However, once the translational temperature increases in the shock front, the simulations compute a rotational relaxation rate that is too high. In all the simulations performed, the value of the wall temperature is found to have almost no effect on the rise of the rotational temperature in the shock front. This behavior is entirely due to the compression of the gas. The wall temperature does determine the post-shock relaxation behavior at small distances from the wall. For the present studies, the value of 400 K is found to give reasonable agreement for each of the four conditions investigated.

The measurements of rotational temperature reported in the current study should be viewed with a certain degree of caution. Further investigations in a larger-scale facility are required for verification of the data. It is also desirable to study flow in a simpler configuration such as a normal shock wave. Nevertheless, it is concluded from the present comparisons of numerical results and experimental data that the rotational relaxation rate of iodine vapor is quite well described by Eq. (6) for the temperature range of 100 to 500 K. Using the parameters derived earlier for the VHS collision model the elastic collision time for iodine,  $\tau_c$ , may be evaluated as a function of temperature. Then, the rotational collision time,  $\tau_r$ , may be derived using the

definition:

$$\tau_r = Z_r \times \tau_c. \quad (7)$$

The rotational relaxation time obtained in this manner is multiplied by pressure (in Atmospheres) and shown in Fig. 12 as a function of temperature. At higher temperatures, the rotational collision time obtained from Eq. (7) is too small.

### Conclusion

Advanced numerical and experimental techniques have been applied to nonequilibrium flows of iodine vapor. Successful comparisons of rotational temperatures obtained with these methods have permitted a rotational relaxation time for iodine to be estimated for the first time. The behavior of iodine at high temperatures indicates that rotational relaxation cannot be described by a single rate under such conditions. This type of behavior almost certainly also occurs in the diatomic species of air. The present study therefore provides a first indication that iodine vapor does represent a model gas that provides experimental access for investigation of thermochemical nonequilibrium phenomena. The detailed measurements obtained in the experimental facility may now be employed for the development of more accurate rotational relaxation models. Investigation in a full-scale facility should be undertaken to verify the data reported here. Through further increases in the stagnation enthalpy, additional studies of vibrational and chemical nonequilibrium in iodine using experimental and numerical methods should yield important information on these processes for diatomic species.

### Acknowledgments

Support for G.C.P. and E.P.M. by AFOSR-90-0170 is gratefully acknowledged.

**Table 1. Flow conditions.**

Case	$p_0$ (Torr)	$T_0$ (K)	$\gamma$
1	100	1000	1.286
2	30	1000	1.320
3	100	773	1.310
4	30	773	1.325

### References

- 1 Kunc, J.A., Muntz, E.P. and Weaver, D.P., "Model Gases for the Detailed Study of Microscopic Chemical Nonequilibrium in Diatomic Gas Flows," AIAA Paper 90-1662, Seattle, Washington, June 1990.
- 2 Pham-Van-Diep, G.C., Muntz, E.P., Erwin, D.A., and Kunc, J.A., "Measurement of Rotational Temper-



ature in a Free Jet Flow of Chemically Reacting Iodine Vapor," 18th International Symposium on Rarefied Gas Dynamics, Vancouver, July 1992.

<sup>3</sup> Pham-Van-Diep, G.C., Erwin, D.A., and Muntz, E.P., "Highly Nonequilibrium Molecular Motion in a Hypersonic Shock Wave," *Science*, Vol. 245, 1989, pp. 624-627.

<sup>4</sup> Boyd, I.D., "Relaxation of Discrete Rotational Energy Distributions Using a Monte Carlo Method," *Physics of Fluids A*, in press.

<sup>5</sup> Pham-Van-Diep, G.C., Muntz, E.P., and Boyd, I.D., "Measurement of Vibrational Population Distributions in a Free-Jet Flow of Chemically Reacting Iodine Vapor and Comparison With Monte Carlo Predictions," AIAA Paper 93-2996, Orlando, Florida, July 1993.

<sup>6</sup> Capelle, G.E. and Broida, H.P., "Lifetimes and Quenching Cross Section of  $I_2$ ," *Journal of Chemical Physics*, Vol. 58, 1972, pp. 4212-4222.

<sup>7</sup> Gerstenkorn, S. and Luc, P., "Assignment of Several Groups of Iodine ( $I_2$ ) Lines in the  $B-X$  System," *Journal of Molecular Spectroscopy*, Vol. 77, 1979, pp. 310-321.

<sup>8</sup> Martin, F., Bacis, R., Churassy, S. and Verges, J., "Laser-Induced-Fluorescence Fourier Transform Spectrometry of the  $XO_g^+$  State of the  $I_2$ : Extensive Analysis of the  $BO_g^+-XO_g^+$  Fluorescence Spectrum of  $^{127}I_2$ ," *Journal of Molecular Spectroscopy*, Vol. 116, 1986, pp. 71-100.

<sup>9</sup> Ashkenas, H. and Sherman, F.S., "Structure and Utilization of Supersonic Free Jets in Low Density Wind Tunnels," 4th International Symposium on Rarefied Gas Dynamics, Academic Press, Toronto, 1966, pp. 84-105.

<sup>10</sup> Boyd, I.D. and Gökçen, T., "Computation of Axisymmetric Ionized Flows Using Particle and Continuum Methods," AIAA Paper 93-0729, Reno, Nevada, January 1993.

<sup>11</sup> Kang, S.H. and Kunc, J.A., "Viscosity of High Temperature Iodine," *Physical Review A*, Vol. 44, September 1991, pp. 3596-3605.

<sup>12</sup> Bird, G.A., "Monte Carlo Simulation in an Engineering Context," in *Rarefied Gas Dynamics*, edited by Sam S. Fisher, Volume 74 of Progress in Astronautics and Aeronautics, Part I, AIAA, New York, 1981, pp. 239-255.

<sup>13</sup> Boyd, I.D., "Analysis of Rotational Nonequilibrium in Standing Shock Waves of Nitrogen," *AIAA Journal*,

Vol. 28, No. 11, 1990, pp. 1997-1999.

<sup>14</sup> Hirschfelder, J.O., Curtiss, C.F., and Bird, R.B., *Molecular Theory of Gases and Liquids*, Wiley, New York, 1954, p. 1110.

<sup>15</sup> Parker, J.G., "Rotational and Vibrational Relaxation in Diatomic Gases," *Physics of Fluids*, Vol. 2, July 1959, pp. 449-462.

<sup>16</sup> Parker, J.G., "Comparison of Experimental and Theoretical Vibrational Relaxation Times for Diatomic Gases," *Journal of Chemical Physics*, Vol. 41, September 1964, pp. 1600-1609.

<sup>17</sup> Davidson, N., *Fundamental Data Obtained from Shock Tube Experiments*, Pergamon Press, 1961, p. 138.

<sup>18</sup> Moreau, S., Bourquin, P.Y., Chapman, D.R., and MacCormack, R.W., "Numerical Simulation of Sharma's Shock-Tube Experiment," AIAA Paper 93-0273, Reno, Nevada, January 1993.

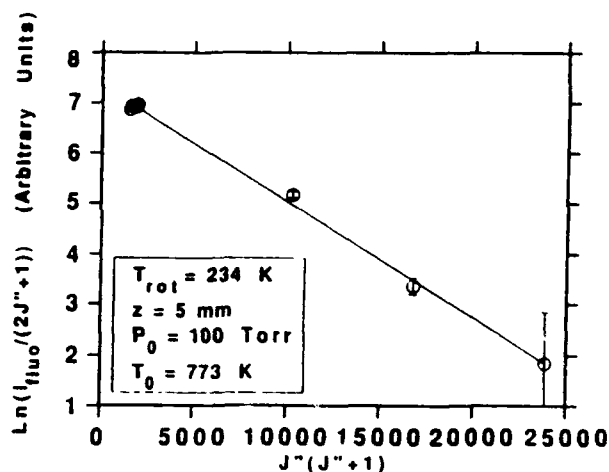


Fig. 1. Boltzmann plot for rotational temperature.

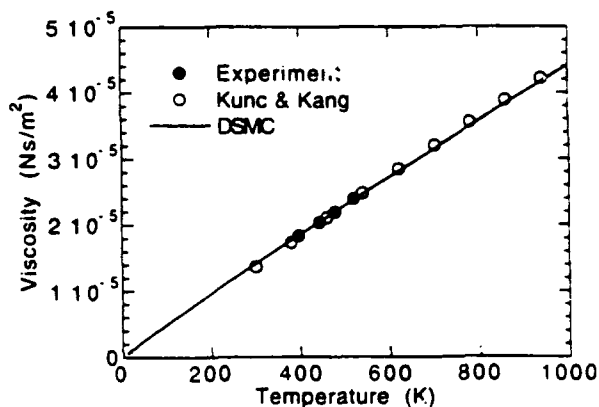


Fig. 2. Temperature dependence for the viscosity coefficient of iodine.

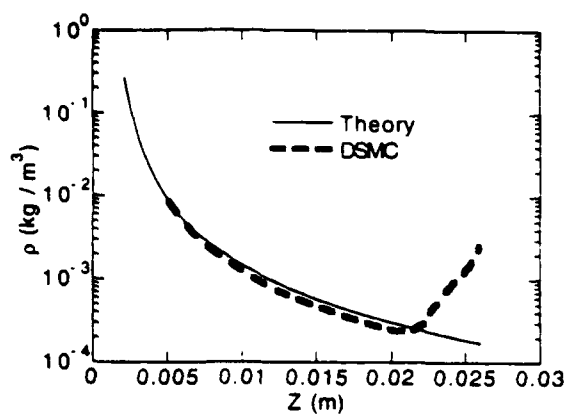


Fig. 3. Comparison of density along the axis predicted by the Ashkenas-Sherman theory and by DSMC for Case 1.

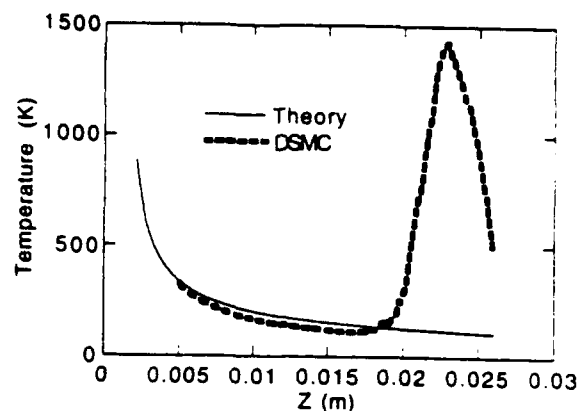


Fig. 4. Comparison of temperature along the axis predicted by the Ashkenas-Sherman theory and by DSMC for Case 1.

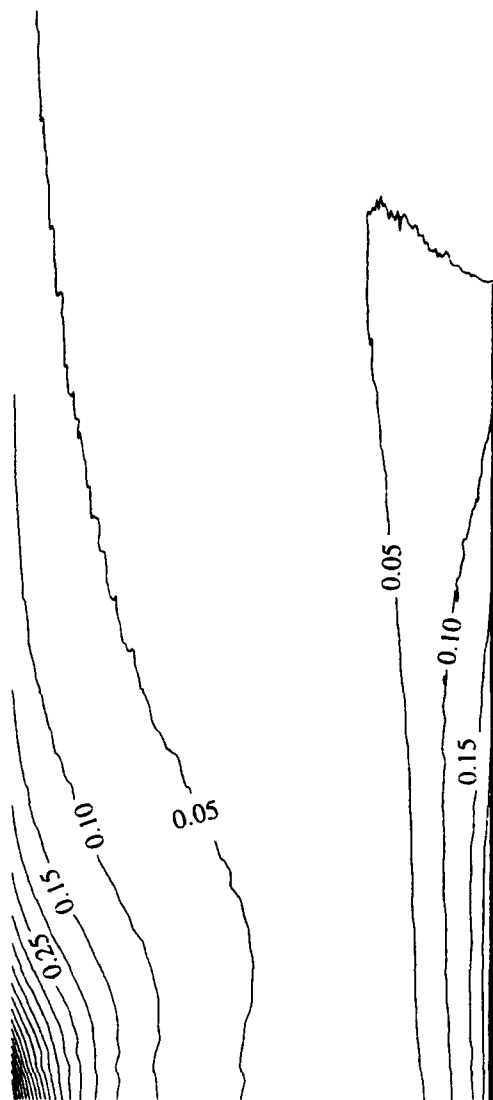


Fig. 5. Flow field contours of the ratio of local to free stream density computed using DSMC for Case 1.

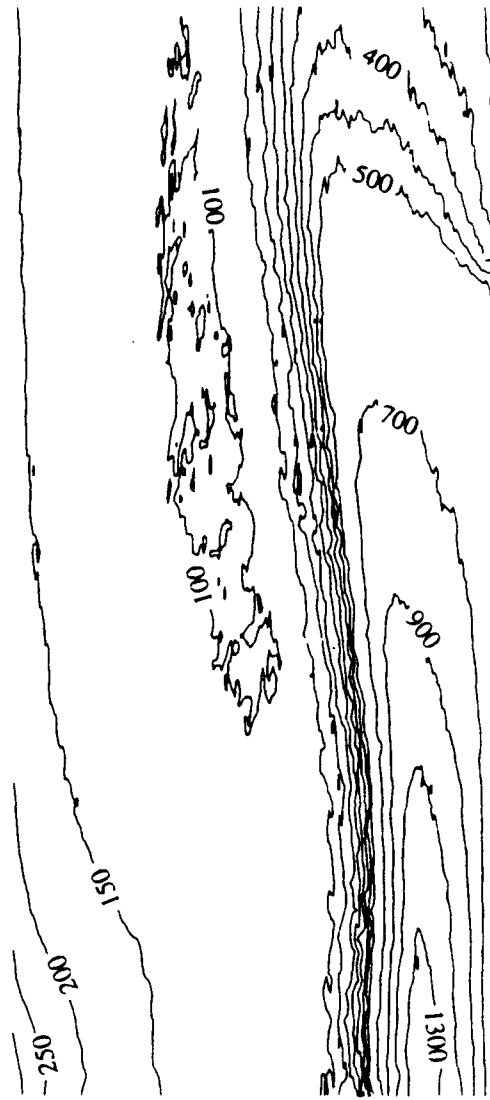


Fig. 6. Flow field contours of translational temperature computed using DSMC for Case 1.

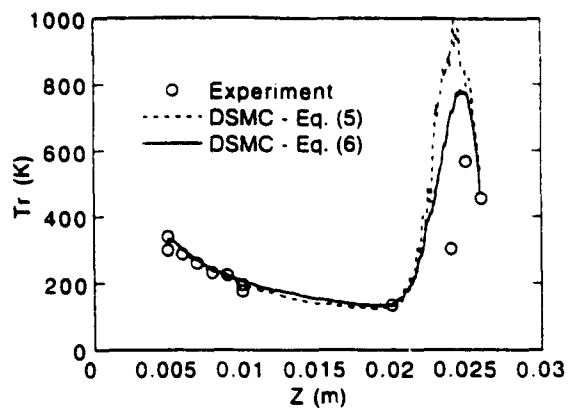


Fig. 7. Comparison of rotational temperatures computed using 2 different DSMC relaxation models and experimental data along the axis for Case 1.

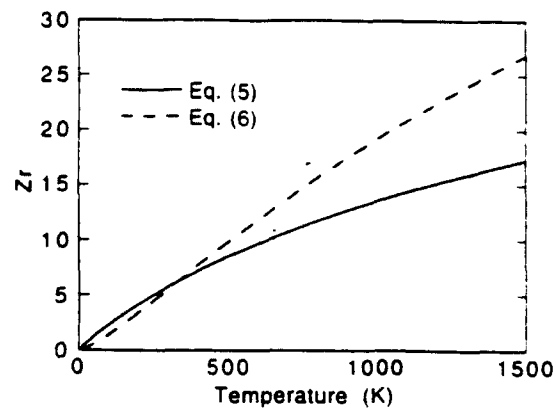


Fig. 8. Comparison of 2 different DSMC rotational relaxation models for iodine.

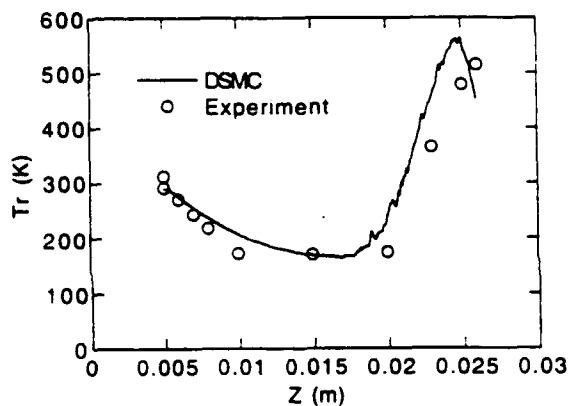


Fig. 9. Comparison of rotational temperatures along the axis obtained experimentally and numerically for Case 2.

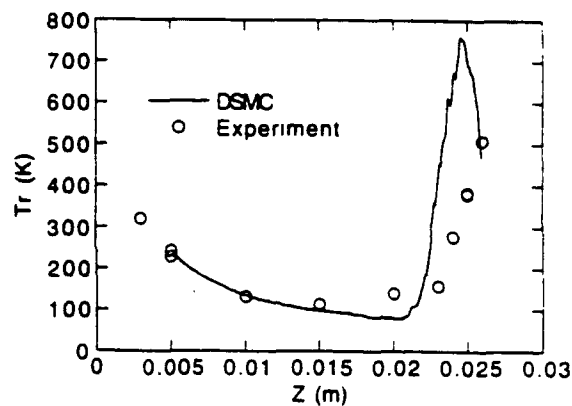


Fig. 10. Comparison of rotational temperatures along the axis obtained experimentally and numerically for Case 3.

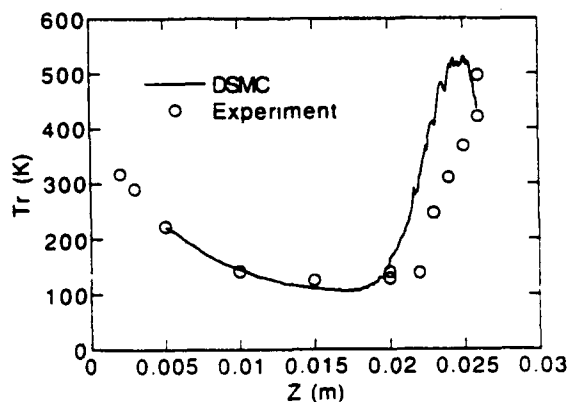


Fig. 11. Comparison of rotational temperatures along the axis obtained experimentally and numerically for Case 4.

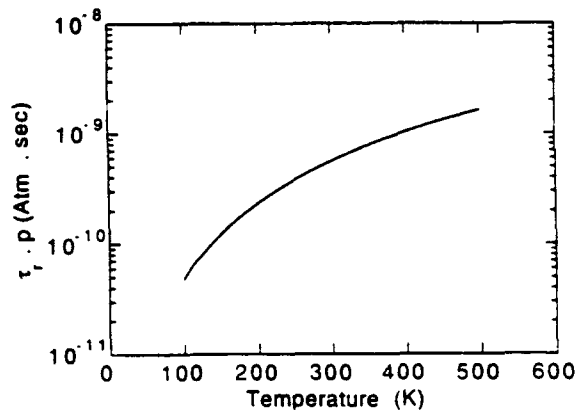


Fig. 12. Temperature dependence of the product of the rotational relaxation time for iodine and the pressure.